

Process Systems Engineering of Continuous Pharmaceutical Manufacturing

by

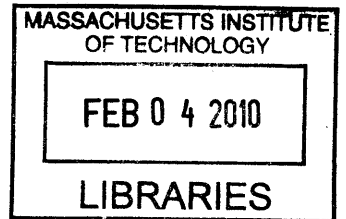
Matthew J. Abel
Stanford University, 2001

Submitted to the Department of Chemical Engineering
in partial fulfillment of the requirements for the degree of
Doctor of Philosophy in Chemical Engineering

at the

MASSACHUSETTS INSTITUTE OF TECHNOLOGY

[February 2009]
2009



ARCHIVES

© Massachusetts Institute of Technology, 2009. All rights reserved.

Author
Matthew Abel
Department of Chemical Engineering

Certified by
Charles L. Cooney
Robert T. Haslam (1911) Professor of Chemical Engineering
Thesis Supervisor

Accepted by
William M. Deen
Carbon P. Dubbs Professor
Chairman, Department Committee on Graduate Students

Process Systems Engineering of Continuous Pharmaceutical Manufacturing

by

Matthew J. Abel

Stanford University, 2001

Submitted to the Department of Chemical Engineering
in partial fulfillment of the requirements for the degree of
Doctor of Philosophy in Chemical Engineering

Abstract

Continuous manufacturing offers a number of operational and financial benefits to pharmaceutical companies. This research examines the critical blending step for continuous pharmaceutical manufacturing and the characteristics of continuous downstream pharmaceutical manufacturing systems. Discrete element method (DEM) simulations were used to develop novel insights into the mechanism of mixing for continuous blending of cohesive pharmaceutical powders and to examine the effects of particle properties, blender design and operating conditions on blend homogeneity. To place continuous blending into the context of pharmaceutical manufacturing, the scope of the analysis was expanded to process system models of continuous downstream pharmaceutical manufacturing.

DEM simulations were used to study the mechanisms of mixing in the continuous blending of pharmaceutical powders. Diffusive mixing from the avalanching particles appears to be the dominant mechanism of mixing in both the axial and radial direction for the double helical ribbon blender. This result can guide the development of future continuous pharmaceutical powder blenders by optimizing the mixing elements to increase the amount of particles transported to a position where they can avalanche/flow and diffusively mix.

A range of particle properties, blender designs and operating conditions were examined for their effects on flow behavior and blend homogeneity. Three particle properties were examined: particle size, polydispersity and cohesive force. Particle size was observed to be positively correlated to both flow rates and blend homogeneity. Polydispersity had no effect on flow rate and was negatively correlated to homogeneity. Cohesive force was negatively correlated to flow rate and had little to no effect on homogeneity. Two modifications of blender design were analyzed: changes in blender size and changes in shaft design. Blender size was observed to be positively correlated to flow rate and negatively correlated to homogeneity. The paddle shaft designs created a more homogeneous powder blend than the double helical ribbon shaft. Two operating parameters were also studied: rotation rate and fill fraction. Rotation rate was positively correlated to both flow rate and homogeneity. Fill fraction had the interesting result of being positively correlated to the absolute flow rate, but negatively correlated to the fill mass normalized flow rate. In addition, fill fraction has a clear negative correlation to homogeneity above fill fractions of 0.55, but is inconsistent for fill fractions lower than this. This research on particle properties, blender designs and operating conditions will help to guide the operation of continuous pharmaceutical blenders and the design of continuous pharmaceutical manufacturing systems.

Process simulations comparing model batch and continuous downstream pharmaceutical manufacturing systems have quantified some of the potential size, cost and performance benefits of continuous processes. The models showed significant reductions in process equipment sizes for continuous manufacturing particularly in the blending step. This reduction in equipment size translates to capital cost (CAPEX) savings for both the continuous process equipment and manufacturing facilities. The steady state operation of continuous processing also reduces the labor requirements and gives the continuous processes an operating cost (OPEX) advantage over batch processes.

This research has contributed to the understanding of continuous pharmaceutical powder blending and quantified some of the benefits of continuous downstream pharmaceutical manufacturing. This work is being continued by the Novartis-MIT Center for Continuous Manufacturing whose work is providing the foundation for future industrial scale pharmaceutical continuous manufacturing systems.

Acknowledgements

First and foremost and I would like to acknowledge and thank my advisor, Professor Charles Cooney. Professor Cooney has been a great mentor in both my research and professional development. My thesis committee at the Massachusetts Institute of Technology (Professor Paul Barton, Professor Alan Hatton and Professor Gregory McRae) has also been a great help to my research and I want to thank them for their time.

I would like to acknowledge the Consortium for the Advancement of Manufacturing of Pharmaceuticals and Novartis AG for their funding of my research. The many interactions I have had with their members and employees have proved valuable in guiding my research.

Next, I would like to thank Dr. Paul Cleary and Dr. Matthew Sinnott from the Commonwealth Scientific Research Organisation. They both have provided countless hours of support to my research and have helped me through many challenging problems. I owe much of my research success to their guidance and teaching. In addition, I would like to thank the Commonwealth Scientific and Industrial Research Organisation for the use of their discrete element method (DEM) software and their computers.

Lakshman Pernenkil and Ben Lin, my graduate student collaborators at the Massachusetts Institute of Technology, deserve many thanks as well. Lakshman and Ben were both a great help in providing the experimental grounding to my modeling efforts. The rest of the Cooney Lab was also a point of inspiration and support throughout my time and I especially want to thank Erin Bell, Samuel Ngai and Luis Perez-Breva.

Finally, I want to thank my parents (Marsha and Greg), my brother (Garrett) and Kathryn.

Table of Contents

1	INTRODUCTION.....	36
1.1	Pharmaceutical industry	36
1.2	Pharmaceutical manufacturing	37
1.3	Batch vs. continuous downstream pharmaceutical manufacturing.....	39
1.3.1	<i>Continuous manufacturing operational advantages.....</i>	40
1.3.2	<i>Continuous manufacturing material containment advantages.....</i>	40
1.3.3	<i>Continuous manufacturing scale-up advantages.....</i>	40
1.3.4	<i>Continuous manufacturing equipment size and cost advantages</i>	43
1.4	Continuous downstream pharmaceutical manufacturing systems	44
1.5	Thesis overview	45
2	LITERATURE REVIEW	47
2.1	Experimental studies of powder blending	47
2.2	Continuum studies of particle blending.....	56
2.3	Compartment model studies of powder blending.....	57
2.4	Discrete element method studies of powder blending	59
2.5	Combined models of powder blending.....	70
2.6	Process system models of downstream pharmaceutical manufacturing	71
3	THESIS OBJECTIVES.....	74
3.1	Continuous pharmaceutical powder blending objectives	74
3.1.1	<i>Discrete element method simulation of a double helical ribbon blender.....</i>	76
3.1.2	<i>Particle property effects on simulated flow behavior and mixing performance.....</i>	76

3.1.3	<i>Blender design effects on simulated flow behavior and mixing performance</i>	78
3.1.4	<i>Operating condition effects on simulated flow behavior and mixing performance.....</i>	79
3.2	Continuous downstream pharmaceutical manufacturing process systems objectives	80
4	METHOD OF APPROACH FOR DISCRETE ELEMENT METHOD SIMULATION	81
4.1	Blenders	81
4.2	Materials	86
4.2.1	<i>Particle parameters</i>	86
4.2.2	<i>Particle interaction parameters.....</i>	88
4.3	Simulations	91
4.3.1	<i>Blender objects.....</i>	91
4.3.2	<i>Blender coordinate system.....</i>	92
4.3.3	<i>Operating conditions</i>	94
4.3.4	<i>Initialization.....</i>	95
4.3.5	<i>Flow behavior measurements</i>	96
4.3.6	<i>Mixing measurements</i>	97
5	DISCRETE ELEMENT METHOD SIMULATION OF A CONTINUOUS DOUBLE HELICAL RIBBON BLENDER.....	101
5.1	Simulation.....	102
5.2	Verification	102
5.3	Flow behavior results.....	104
5.3.1	<i>Volume fraction.....</i>	105
5.3.2	<i>Particle velocities.....</i>	107

5.3.3	<i>Granular temperature</i>	114
5.3.4	<i>Flow rate</i>	116
5.4	Mixing results	119
5.4.1	<i>Centroid</i>	119
5.4.2	<i>Quantitative mixing measure</i>	151
5.5	Summary of results	153
6	EFFECTS OF PARTICLE PROPERTIES	156
6.1	Particle size simulations	156
6.2	Comparison of powder flows for particle size	157
6.2.1	<i>Particle velocities</i>	157
6.2.2	<i>Granular temperature</i>	159
6.2.3	<i>Flow rate</i>	161
6.3	Mixing results for particle size simulations	164
6.3.1	<i>Quantitative mixing measure</i>	164
6.4	Polydispersity simulations	167
6.5	Flow behavior results for polydispersity simulations	167
6.5.1	<i>Flow rate</i>	167
6.6	Mixing results for polydispersity simulations	169
6.6.1	<i>Quantitative mixing measure</i>	169
6.7	Cohesive force simulations	172
6.8	Flow behavior results for cohesive force simulations	173
6.8.1	<i>Volume fraction</i>	173
6.8.2	<i>Velocity</i>	176
6.8.3	<i>Granular temperature</i>	179

6.8.4	<i>Flow rate</i>	179
6.9	Mixing results for cohesive force simulations	183
6.9.1	<i>Quantitative mixing measure</i>	183
6.10	Summary of results	186
7	EFFECTS OF BLENDER DESIGN	188
7.1	Blender size simulations	188
7.2	Flow behavior results for blender size simulations	188
7.2.1	<i>Flow rate</i>	188
7.3	Mixing results for blender size simulations	194
7.3.1	<i>Quantitative mixing measure</i>	194
7.4	Shaft design simulations	198
7.5	Flow behavior results for shaft design simulations	199
7.5.1	<i>Volume fraction</i>	199
7.5.2	<i>Particle velocities</i>	201
7.5.3	<i>Granular temperature</i>	206
7.5.4	<i>Flow rate</i>	210
7.6	Mixing results for shaft design	213
7.6.1	<i>Color centroids</i>	213
7.6.2	<i>Quantitative mixing measure</i>	221
7.7	Summary of results	224
8	EFFECTS OF PROCESS CONDITIONS	226
8.1	Rotation rate simulations	226
8.2	Flow behavior results for rotation rate simulations	226
8.2.1	<i>Volume fraction</i>	226

8.2.2	<i>Particle velocities</i>	228
8.2.3	<i>Granular temperature</i>	230
8.2.4	<i>Flow rate</i>	232
8.3	Mixing results for rotation rate simulations	235
8.3.1	<i>Particle mixing measure</i>	235
8.4	Fill fraction simulations	238
8.5	Flow behavior results for fill fraction simulations	238
8.5.1	<i>Flow rates</i>	238
8.6	Mixing results for fill fraction simulations	241
8.6.1	<i>Quantitative mixing measure</i>	241
8.7	Summary of results	244
9	ANALYSIS OF PHARMACEUTICAL POWDER BLENDING MODELS	246
9.1	Summary of the effects of particle properties, blender designs and operating conditions	246
9.2	Dimensional analysis	253
9.2.1	<i>Scale ratio</i>	253
9.2.2	<i>Froude number</i>	255
9.2.3	<i>Avalanche velocity</i>	257
9.2.4	<i>Dimensional analysis of flow rate</i>	258
9.2.5	<i>Dimensional analysis of homogeneity</i>	261
9.3	Summary of results	263
10	CONTINUOUS DOWNSTREAM PHARMACEUTICAL MANUFACTURING SYSTEMS	265

10.1	Process models.....	265
10.2	Process model results.....	272
10.3	Summary of results.....	277
11	FUTURE WORK.....	279
11.1	Parallel discrete element method simulation.....	279
11.2	Non-spherical particles.....	279
11.3	New active pharmaceutical ingredients.....	280
11.4	Paddle blender design optimization.....	281
<i>11.4.1</i>	<i>Blender geometry.....</i>	<i>281</i>
<i>11.4.2</i>	<i>Inflow and outflow ports.....</i>	<i>282</i>
<i>11.4.3</i>	<i>Paddle design and orientation.....</i>	<i>282</i>
12	CONCLUSION.....	284
	REFERENCES.....	290

List of Figures

FIGURE 1: PROCESS SCHEMATIC FOR UPSTREAM AND DOWNSTREAM PHARMACEUTICAL MANUFACTURING. 38

FIGURE 2: SCHEMATIC OF AVALANCHING (1), ROLLING (2), CATARACTING (3) AND CENTRIFUGING (4) FLOW REGIMES IN A ROTATING DRUM. THE PARTICLE BED IS DEFINED BY THE YELLOW REGION AND THE UNOCCUPIED SPACE BY THE BLUE REGION. THE FREE SURFACE IS THE BORDER BETWEEN THE TWO REGIONS. FOR AVALANCHING, THE SOLID REGION REPRESENTS THE FREE SURFACE BEFORE AN AVALANCHE AND THE CHECKERED REGION REPRESENTS THE FREE SURFACE AFTER AN AVALANCHE. 48

FIGURE 3: SCHEMATIC FOR A COMPARTMENT MODEL OF A CONTINUOUS PHARMACEUTICAL POWDER BLENDER USING AXIAL SUBDIVISIONS. 58

FIGURE 4: INITIAL POSITION GROUP CENTROIDS CONVERGING ON THE CENTROID OF ALL OF THE PARTICLES (BLACK LINE) 67

FIGURE 5: QUANTITATIVE MIXING MEASURE FOR 4 COMPARTMENTS WITH 16 PARTICLES IN 4 INITIAL POSITION GROUPS (RED, BLUE, GREEN, ORANGE). 69

FIGURE 6: FACTORS AFFECTING MECHANISMS OF MIXING AND HOMOGENEITY 75

FIGURE 7: BLENDER SHELL 81

FIGURE 8: BLENDER FEED PORT 82

FIGURE 9: DOUBLE HELICAL RIBBON SHAFT. 82

FIGURE 10: ISOMETRIC VIEW OF PADDLE SHAFT. 84

FIGURE 11: PLAN VIEW OF PADDLE SHAFT WITH DIMENSIONS 85

FIGURE 12: SEM IMAGE OF DCL 11 LACTOSE. [DMV INTERNATIONAL GMBH. PRODUCT GROUP OVERVIEW. PHARMATOSE® AND DC LACTOSE. DELHI, NY, 2006.].....	87
FIGURE 13: ESEM IMAGE OF A CAFFEINE PARTICLE [S.H. NGAI. MULTISCALE ANALYSIS AND SIMULATION OF POWDER BLENDING IN PHARMACEUTICAL MANUFACTURING. PHD DISSERTATION, MASSACHUSETTS INSTITUTE OF TECHNOLOGY, DEPARTMENT OF CHEMICAL ENGINEERING. AUGUST 2005.].....	87
FIGURE 14: YZ COORDINATES FOR BLENDER SIMULATION.....	92
FIGURE 15: XZ COORDINATES FOR BLENDER SIMULATION.....	93
FIGURE 16: XY COORDINATES FOR BLENDER SIMULATION.....	93
FIGURE 17: MASS FLOW RATE SAMPLE PLANE POSITIONS.....	97
FIGURE 18: INITIAL POSITION GROUPS FOR MEASUREMENT OF MIXING IN THE X DIRECTION.....	97
FIGURE 19: INITIAL POSITION GROUPS FOR MEASUREMENT OF MIXING IN THE Y DIRECTION.....	98
FIGURE 20: INITIAL POSITION GROUPS FOR MEASUREMENT OF MIXING IN THE Z DIRECTION.....	98
FIGURE 21: INITIAL POSITION GROUPS FOR MEASUREMENT OF MIXING IN THE R DIRECTION.....	99
FIGURE 22: COMPARISON OF 1 REVOLUTION MOVING AVERAGE EXIT FLOW RATES (MG/S) FOR THE EIGHTH SCALE DEM SIMULATION (GREEN) AND SCALED EXPERIMENTS (BLACK) IN THE DOUBLE HELICAL RIBBON BLENDER OPERATING AT 20 RPM WITH 0.0035 G/S INFLOW MIXING LACTOSE AND CAFFEINE PARTICLES.....	103

FIGURE 23: EIGHTH SCALE DOUBLE HELICAL RIBBON BLENDER OPERATING AT 20 RPM WITH 0.0035 G/S INFLOW MIXING LACTOSE AND CAFFEINE PARTICLES..... 104

FIGURE 24: CROSS SECTIONS SHOWING VOLUME FRACTION OF GRID CELLS OF AN EIGHTH SCALE DOUBLE HELICAL RIBBON BLENDER WITH LACTOSE AND CAFFEINE PARTICLES OPERATING AT 20 RPM WITH 0.0035 G/S INFLOW. 106

FIGURE 25: CROSS SECTIONS OF THE R COMPONENT OF VELOCITY IN M/S FOR AN EIGHTH SCALE DOUBLE HELICAL RIBBON BLENDER OPERATING AT 20 RPM WITH A 0.0035 G/S INFLOW MIXING LACTOSE AND CAFFEINE PARTICLES. 109

FIGURE 26: CROSS SECTIONS SHOWING THE THETA COMPONENT OF VELOCITY IN M/S FOR AN EIGHTH SCALE DOUBLE HELICAL RIBBON BLENDER OPERATING AT 20 RPM WITH 0.0035 G/S INFLOW MIXING LACTOSE AND CAFFEINE PARTICLES..... 110

FIGURE 27: CROSS SECTIONS SHOWING THE Z COMPONENT OF VELOCITY IN M/S FOR AN EIGHTH SCALE DOUBLE HELICAL RIBBON BLENDER OPERATING AT 20 RPM WITH 0.0035 G/S INFLOW MIXING LACTOSE AND CAFFEINE PARTICLES..... 112

FIGURE 28: CROSS SECTIONS SHOWING GRANULAR TEMPERATURE FOR AN EIGHTH SCALE DOUBLE HELICAL RIBBON BLENDER OPERATING AT 20 RPM WITH 0.0035 G/S INFLOW MIXING LACTOSE AND CAFFEINE PARTICLES..... 115

FIGURE 29: INSTANTANEOUS FLOW RATE IN THE DIRECTION OF FLOW FOR THE MIDDLE AND EXIT OF AN EIGHTH SCALE DOUBLE HELICAL RIBBON BLENDER WITH LACTOSE AND CAFFEINE PARTICLES OPERATING AT 20 RPM WITH 0.0035 G/S INFLOW. 117

FIGURE 30: 1 REVOLUTION MOVING AVERAGE FLOW RATE IN THE DIRECTION OF FLOW FOR THE MIDDLE AND EXIT OF AN EIGHTH SCALE DOUBLE HELICAL RIBBON BLENDER WITH LACTOSE AND CAFFEINE PARTICLES OPERATING AT 20 RPM WITH 0.0035 G/S INFLOW. 118

FIGURE 31: MEAN PARTICLE TO PARTICLE OR PARTICLE TO OBJECT BOND STRENGTH IN N_N FOR AN EIGHTH SCALE DOUBLE HELICAL RIBBON BLENDER WITH LACTOSE AND CAFFEINE PARTICLES OPERATING AT 20 RPM WITH 0.0035 G/S INFLOW. 119

FIGURE 32: CENTROIDS OF X DIMENSION INITIAL POSITIONS (BLUE = 1, GREEN = 2, YELLOW = 3, ORANGE = 4) IN THE X DIRECTION IN AN EIGHTH SCALE DOUBLE HELICAL RIBBON BLENDER WITH LACTOSE AND CAFFEINE PARTICLES OPERATING AT 20 RPM WITH 0.0035 G/S INFLOW. 121

FIGURE 33: XY CUTAWAY WITH X DIMENSION INITIAL POSITIONS (BLUE = 1, GREEN = 2, YELLOW = 3, ORANGE = 4) IN AN EIGHTH SCALE DOUBLE HELICAL RIBBON BLENDER WITH LACTOSE AND CAFFEINE PARTICLES OPERATING AT 20 RPM WITH 0.0035 G/S INFLOW. 123

FIGURE 34: XY CUTAWAY OF X INITIAL POSITION GROUP 1 (BLUE) IN AN EIGHTH SCALE DOUBLE HELICAL RIBBON BLENDER WITH LACTOSE AND CAFFEINE PARTICLES OPERATING AT 20 RPM WITH 0.0035 G/S INFLOW. 124

FIGURE 35: XY CUTAWAY OF X INITIAL POSITION GROUP 2 (GREEN) IN AN EIGHTH SCALE DOUBLE HELICAL RIBBON BLENDER WITH LACTOSE AND CAFFEINE PARTICLES OPERATING AT 20 RPM WITH 0.0035 G/S INFLOW. 125

FIGURE 36: XY CUTAWAY OF X INITIAL POSITION GROUP 3 (YELLOW) IN AN EIGHTH SCALE DOUBLE HELICAL RIBBON BLENDER WITH LACTOSE AND CAFFEINE PARTICLES OPERATING AT 20 RPM WITH 0.0035 G/S INFLOW. 126

FIGURE 37: XY CUTAWAY OF X INITIAL POSITION GROUP 4 (ORANGE) IN AN EIGHTH SCALE DOUBLE HELICAL RIBBON BLENDER WITH LACTOSE AND CAFFEINE PARTICLES OPERATING AT 20 RPM WITH 0.0035 G/S INFLOW. 127

FIGURE 38: CENTROIDS OF Y POSITION COLORS (BLUE = 1, GREEN = 2, YELLOW = 3, ORANGE = 4) IN THE Y DIRECTION IN AN EIGHTH SCALE DOUBLE HELICAL RIBBON BLENDER WITH LACTOSE AND CAFFEINE PARTICLES OPERATING AT 20 RPM WITH 0.0035 G/S INFLOW. 128

FIGURE 39: XY CUTAWAY WITH COLORATION BY Y INITIAL POSITION GROUP (BLUE = 1, GREEN = 2, YELLOW = 3, ORANGE = 4) IN AN EIGHTH SCALE DOUBLE HELICAL RIBBON BLENDER WITH LACTOSE AND CAFFEINE PARTICLES OPERATING AT 20 RPM WITH 0.0035 G/S INFLOW..... 130

FIGURE 40: XY CUTAWAY OF Y INITIAL POSITION GROUP 1 (BLUE) IN AN EIGHTH SCALE DOUBLE HELICAL RIBBON BLENDER WITH LACTOSE AND CAFFEINE PARTICLES OPERATING AT 20 RPM WITH 0.0035 G/S INFLOW..... 131

FIGURE 41: XY CUTAWAY OF Y INITIAL POSITION GROUP 2 (GREEN) IN AN EIGHTH SCALE DOUBLE HELICAL RIBBON BLENDER WITH LACTOSE AND CAFFEINE PARTICLES OPERATING AT 20 RPM WITH 0.0035 G/S INFLOW..... 132

FIGURE 42: XY CUTAWAY OF Y INITIAL POSITION GROUP 3 (YELLOW) IN AN EIGHTH SCALE DOUBLE HELICAL RIBBON BLENDER WITH LACTOSE AND CAFFEINE PARTICLES OPERATING AT 20 RPM WITH 0.0035 G/S INFLOW..... 133

FIGURE 43: XY CUTAWAY OF Y INITIAL POSITION GROUP 4 (ORANGE) IN AN EIGHTH SCALE DOUBLE HELICAL RIBBON BLENDER WITH LACTOSE AND CAFFEINE PARTICLES OPERATING AT 20 RPM WITH 0.0035 G/S INFLOW..... 134

FIGURE 44: CENTROIDS OF Z INITIAL POSITION GROUPS (BLUE = 1, GREEN = 2, YELLOW = 3, ORANGE = 4) IN THE Z DIRECTION IN AN EIGHTH SCALE DOUBLE HELICAL RIBBON BLENDER WITH LACTOSE AND CAFFEINE PARTICLES OPERATING AT 20 RPM WITH 0.0035 G/S INFLOW..... 135

FIGURE 45: DISPLACEMENT OF CENTROIDS OF Z INITIAL POSITION GROUPS (BLUE = 1, GREEN = 2, YELLOW = 3, ORANGE = 4) IN THE Z DIRECTION IN AN EIGHTH SCALE DOUBLE HELICAL RIBBON BLENDER WITH LACTOSE AND CAFFEINE PARTICLES OPERATING AT 20 RPM WITH 0.0035 G/S INFLOW..... 136

FIGURE 46: YZ CUTAWAY WITH COLORATION BY Z INITIAL POSITION GROUP (BLUE = 1, GREEN = 2, YELLOW = 3, ORANGE/RED = 4) IN AN EIGHTH SCALE DOUBLE HELICAL RIBBON BLENDER WITH LACTOSE AND CAFFEINE PARTICLES OPERATING AT 20 RPM WITH 0.0035 G/S INFLOW..... 138

FIGURE 47: YZ CUTAWAY OF Z INITIAL POSITION GROUP 1 (BLUE) IN AN EIGHTH SCALE DOUBLE HELICAL RIBBON BLENDER WITH LACTOSE AND CAFFEINE PARTICLES OPERATING AT 20 RPM WITH 0.0035 G/S INFLOW. 139

FIGURE 48: YZ CUTAWAY OF Z INITIAL POSITION GROUP 2 (GREEN) IN AN EIGHTH SCALE DOUBLE HELICAL RIBBON BLENDER WITH LACTOSE AND CAFFEINE PARTICLES OPERATING AT 20 RPM WITH 0.0035 G/S INFLOW. 140

FIGURE 49: YZ CUTAWAY OF Z INITIAL POSITION GROUP 3 (YELLOW) IN AN EIGHTH SCALE DOUBLE HELICAL RIBBON BLENDER WITH LACTOSE AND CAFFEINE PARTICLES OPERATING AT 20 RPM WITH 0.0035 G/S INFLOW. 141

FIGURE 50: YZ CUTAWAY OF Z INITIAL POSITION GROUP 4 (ORANGE/RED) IN AN EIGHTH SCALE DOUBLE HELICAL RIBBON BLENDER WITH LACTOSE AND CAFFEINE PARTICLES OPERATING AT 20 RPM WITH 0.0035 G/S INFLOW. 142

FIGURE 51: CENTROIDS OF R INITIAL POSITION GROUPS (BLUE = 1, GREEN = 2, YELLOW = 3, ORANGE = 4) IN THE R DIRECTION IN AN EIGHTH SCALE DOUBLE HELICAL RIBBON BLENDER WITH LACTOSE AND CAFFEINE PARTICLES OPERATING AT 20 RPM WITH 0.0035 G/S INFLOW. 143

FIGURE 52: CENTROIDS OF R INITIAL POSITION GROUPS (BLUE = 1, GREEN = 2, YELLOW = 3, ORANGE = 4) IN THE Z DIRECTION IN AN EIGHTH SCALE DOUBLE HELICAL RIBBON BLENDER WITH LACTOSE AND CAFFEINE PARTICLES OPERATING AT 20 RPM WITH 0.0035 G/S INFLOW. 144

FIGURE 53: XY CUTAWAY WITH COLORATION BY RADIAL (R) INITIAL POSITION GROUP (BLUE = 1, GREEN = 2, YELLOW = 3, ORANGE = 4) IN AN EIGHTH SCALE DOUBLE HELICAL RIBBON BLENDER WITH LACTOSE AND CAFFEINE PARTICLES OPERATING AT 20 RPM WITH 0.0035 G/S INFLOW. 146

FIGURE 54: XY CUTAWAY OF R INITIAL POSITION GROUP 1 (BLUE) IN AN EIGHTH SCALE DOUBLE HELICAL RIBBON BLENDER WITH LACTOSE AND CAFFEINE PARTICLES OPERATING AT 20 RPM WITH 0.0035 G/S INFLOW. 147

FIGURE 55: XY CUTAWAY OF R INITIAL POSITION GROUP 2 (GREEN) IN AN EIGHTH SCALE DOUBLE HELICAL RIBBON BLENDER WITH LACTOSE AND CAFFEINE PARTICLES OPERATING AT 20 RPM WITH 0.0035 G/S INFLOW. 148

FIGURE 56: XY CUTAWAY OF R INITIAL POSITION GROUP 3 (YELLOW) IN AN EIGHTH SCALE DOUBLE HELICAL RIBBON BLENDER WITH LACTOSE AND CAFFEINE PARTICLES OPERATING AT 20 RPM WITH 0.0035 G/S INFLOW. 149

FIGURE 57: XY CUTAWAY OF R INITIAL POSITION GROUP 4 (ORANGE) IN AN EIGHTH SCALE DOUBLE HELICAL RIBBON BLENDER WITH LACTOSE AND CAFFEINE PARTICLES OPERATING AT 20 RPM WITH 0.0035 G/S INFLOW. 150

FIGURE 58: MIXING % FOR X, Y, Z AND R INITIAL POSITION COLORING FOR AN EIGHTH SCALE DOUBLE HELICAL RIBBON BLENDER WITH LACTOSE AND CAFFEINE PARTICLES OPERATING AT 20 RPM WITH 0.0035 G/S INFLOW. 151

FIGURE 59: RATE OF MIXING FOR X, Y, Z AND R INITIAL POSITION COLORING FOR AN EIGHTH SCALE DOUBLE HELICAL RIBBON BLENDER WITH LACTOSE AND CAFFEINE PARTICLES OPERATING AT 20 RPM WITH 0.0035 G/S INFLOW. 152

FIGURE 60: YZ CROSS SECTION SHOWING Z COMPONENT OF VELOCITY IN M/S FOR AN EIGHTH SCALE DOUBLE HELICAL RIBBON BLENDER WITH 100, 200 AND 300 MICRON LACTOSE PARTICLES OPERATING AT 20 RPM AND A 0.0033 G/S INFLOW. 158

FIGURE 61: XY CROSS SECTION SHOWING GRANULAR TEMPERATURE FOR AN EIGHTH SCALE DOUBLE HELICAL RIBBON BLENDER WITH 100, 200 AND 300 MICRON LACTOSE PARTICLES OPERATING AT 20 RPM AND A 0.0033 G/S INFLOW. 160

FIGURE 62: FLOW RATE IN MG/S AT THE MIDDLE OF AN EIGHTH SCALE DOUBLE HELICAL RIBBON BLENDER WITH 100, 200 AND 300 MICRON LACTOSE PARTICLES OPERATING AT 20 RPM AND A 0.0033 G/S INFLOW. 162

FIGURE 63: FLOW RATE IN MG/S AT THE EXIT OF AN EIGHTH SCALE DOUBLE HELICAL RIBBON BLENDER WITH 100, 200 AND 300 MICRON LACTOSE PARTICLES OPERATING AT 20 RPM AND A 0.0033 G/S INFLOW 163

FIGURE 64: HOMOGENEITY (MIXING %) FOR X AND Y INITIAL POSITION GROUPS IN AN EIGHTH SCALE DOUBLE HELICAL RIBBON BLENDER WITH 100, 200 AND 300 MICRON LACTOSE PARTICLES OPERATING AT 20 RPM AND A 0.0033 G/S INFLOW. 165

FIGURE 65: HOMOGENEITY (MIXING %) FOR Z AND R INITIAL POSITION GROUPS IN AN EIGHTH SCALE DOUBLE HELICAL RIBBON BLENDER WITH 100, 200 AND 300 MICRON LACTOSE PARTICLES OPERATING AT 20 RPM AND A 0.0033 G/S INFLOW. 166

FIGURE 66: FLOW RATE IN MG/S AT THE MIDDLE OF AN EIGHTH SCALE DOUBLE HELICAL RIBBON BLENDER WITH 200 MICRON MONODISPERSE AND 200 MICRON POLYDISPERSE LACTOSE PARTICLES OPERATING AT 20 RPM AND A 0.0033 G/S INFLOW. 168

FIGURE 67: HOMOGENEITY (MIXING %) FOR X AND Y INITIAL POSITION GROUPS IN AN EIGHTH SCALE DOUBLE HELICAL RIBBON BLENDER WITH 200 MICRON MONODISPERSE AND 200 MICRON POLYDISPERSE LACTOSE PARTICLES OPERATING AT 20 RPM AND A 0.0033 G/S INFLOW..... 170

FIGURE 68: HOMOGENEITY (MIXING %) FOR Z AND R INITIAL POSITION GROUPS IN EIGHTH SCALE DOUBLE HELICAL RIBBON BLENDER WITH 200 MICRON MONODISPERSE AND 200 MICRON POLYDISPERSE LACTOSE PARTICLES OPERATING AT 20 RPM AND A 0.0033 G/S INFLOW..... 171

FIGURE 69: FILL WEIGHT IN G OF AN EIGHTH SCALE DOUBLE HELICAL RIBBON BLENDER WITH 300 MICRON LACTOSE PARTICLES WITH 0%, 50%, 100% AND 150% OF THE STANDARD EXPERIMENTALLY MEASURED COHESION OPERATING AT 20 RPM AND A 0.0035 G/S INFLOW..... 173

FIGURE 70: YZ CROSS SECTION SHOWING VOLUME FRACTION FOR AN EIGHTH SCALE DOUBLE HELICAL RIBBON BLENDER WITH 300 MICRON LACTOSE PARTICLES OPERATING AT 20 RPM AND A 0.0035 G/S INFLOW. 174

FIGURE 71: XY CROSS SECTION SHOWING VOLUME FRACTION FOR AN EIGHTH SCALE DOUBLE HELICAL RIBBON BLENDER WITH 300 MICRON LACTOSE PARTICLES OPERATING AT 20 RPM AND A 0.0035 G/S INFLOW. 175

FIGURE 72: YZ CROSS SECTION SHOWING Z VELOCITY FOR AN EIGHTH SCALE DOUBLE HELICAL RIBBON BLENDER WITH 300 MICRON LACTOSE PARTICLES OPERATING AT 20 RPM AND A 0.0035 G/S INFLOW. 177

FIGURE 73: XY CROSS SECTION SHOWING GRANULAR TEMPERATURE FOR AN EIGHTH SCALE DOUBLE HELICAL RIBBON BLENDER WITH 300 MICRON LACTOSE PARTICLES OPERATING AT 20 RPM AND A 0.0035 G/S INFLOW. 178

FIGURE 74: FLOW RATES IN MG/S AT THE MIDDLE OF AN EIGHTH SCALE DOUBLE HELICAL RIBBON BLENDER WITH 300 MICRON LACTOSE PARTICLES WITH 0%, 50%, 100% AND 150% OF THE STANDARD EXPERIMENTALLY MEASURED COHESION OPERATING AT 20 RPM AND A 0.0035 G/S INFLOW. 180

FIGURE 75: FLOW RATE IN MG/S AT THE EXIT OF AN EIGHTH SCALE DOUBLE HELICAL RIBBON BLENDER WITH 300 MICRON LACTOSE PARTICLES WITH 0%, 50%, 100% AND 150% OF THE STANDARD EXPERIMENTALLY MEASURED COHESION OPERATING AT 20 RPM AND A 0.0035 G/S INFLOW. 181

FIGURE 76: FLOW RATE NORMALIZED BY THE FILL WEIGHT AT T = 6 SECONDS VERSUS % OF THE STANDARD EXPERIMENTALLY MEASURED COHESION FOR EXIT OF THE DOUBLE HELICAL RIBBON BLENDER WITH 200 MICRON LACTOSE PARTICLES OPERATING AT 20 RPM AND A 0.0035 G/S INFLOW. 182

FIGURE 77: HOMOGENEITY (MIXING %) FOR X AND Y INITIAL POSITION GROUPS IN AN EIGHTH SCALE DOUBLE HELICAL RIBBON BLENDER WITH 300 MICRON LACTOSE PARTICLES WITH 0%, 50%, 100% AND 150% OF THE STANDARD

EXPERIMENTALLY MEASURED COHESION OPERATING AT 20 RPM AND A 0.0035 G/S INFLOW.	184
FIGURE 78: HOMOGENEITY (MIXING %) FOR Z AND R INITIAL POSITION GROUPS IN AN EIGHTH SCALE DOUBLE HELICAL RIBBON BLENDER WITH 300 MICRON LACTOSE PARTICLES WITH 0%, 50%, 100% AND 150% OF THE STANDARD EXPERIMENTALLY MEASURED COHESION OPERATING AT 20 RPM AND A 0.0035 G/S INFLOW.	185
FIGURE 79: FLOW RATE NORMALIZED BY THE FILL WEIGHT FOR THE MIDDLE OF THE DOUBLE HELICAL RIBBON BLENDER WITH 200 MICRON LACTOSE PARTICLES OPERATING AT 20 RPM AT A SIXTEENTH SCALE WITH 0.0004 G/S INFLOW, AN EIGHTH SCALE WITH 0.0033 G/S INFLOW AND A QUARTER SCALE WITH 0.0260 G/S INFLOW.	190
FIGURE 80: FLOW RATE NORMALIZED BY THE FILL WEIGHT FOR EXIT OF THE DOUBLE HELICAL RIBBON BLENDER WITH 200 MICRON LACTOSE PARTICLES OPERATING AT 20 RPM AT A SIXTEENTH SCALE WITH 0.0004 G/S INFLOW, AN EIGHTH SCALE WITH 0.0033 G/S INFLOW AND A QUARTER SCALE WITH 0.0260 G/S INFLOW.	191
FIGURE 81: FLOW RATES NORMALIZED BY THE FILL WEIGHT AND SCALED TO THE QUARTER SCALE NORMALIZED FLOW RATE OF THE DOUBLE HELICAL RIBBON BLENDER WITH 200 MICRON LACTOSE PARTICLES OPERATING AT 20 RPM AT A SIXTEENTH SCALE WITH 0.0004 G/S INFLOW, AN EIGHTH SCALE WITH 0.0033 G/S INFLOW AND A QUARTER SCALE WITH 0.0260 G/S INFLOW.	192
FIGURE 82: HOMOGENEITY (MIXING %) FOR X AND Y INITIAL POSITION GROUPS IN THE DOUBLE HELICAL RIBBON BLENDER WITH 200 MICRON LACTOSE PARTICLES OPERATING AT 20 RPM AT A SIXTEENTH SCALE WITH 0.0004 G/S INFLOW, AN EIGHTH SCALE WITH 0.0033 G/S INFLOW AND A QUARTER SCALE WITH 0.0260 G/S INFLOW.....	195

FIGURE 83: HOMOGENEITY (MIXING %) FOR Z AND R INITIAL POSITION GROUPS IN THE DOUBLE HELICAL RIBBON BLENDER WITH 200 MICRON LACTOSE PARTICLES OPERATING AT 20 RPM AT A SIXTEENTH SCALE WITH 0.0004 G/S INFLOW, AN EIGHTH SCALE WITH 0.0033 G/S INFLOW AND A QUARTER SCALE WITH 0.0260 G/S INFLOW..... 196

FIGURE 84: YZ CROSS SECTION SHOWING VOLUME FRACTION FOR AN EIGHTH SCALE BLENDER WITH 300 MICRON LACTOSE PARTICLES AND A 0.0035 G/S INFLOW. 200

FIGURE 85: XY CROSS SECTION SHOWING R COMPONENT OF VELOCITY IN M/S FOR AN EIGHTH SCALE BLENDER WITH 300 MICRON LACTOSE PARTICLES AND A 0.0035 G/S INFLOW. 202

FIGURE 86: XY CROSS SECTION SHOWING THE THETA COMPONENT OF VELOCITY IN M/S FOR AN EIGHTH SCALE BLENDER 300 MICRON LACTOSE PARTICLES AND A 0.0035 G/S INFLOW. 203

FIGURE 87: XY CROSS SECTION SHOWING THE Z COMPONENT OF VELOCITY IN M/S FOR AN EIGHTH SCALE BLENDER WITH 300 MICRON LACTOSE PARTICLES AND A 0.0035 G/S INFLOW..... 204

FIGURE 88: YZ CROSS SECTION SHOWING THE Z COMPONENT OF VELOCITY IN M/S FOR AN EIGHTH SCALE BLENDER WITH 300 MICRON LACTOSE PARTICLES AND A 0.0035 G/S INFLOW. 205

FIGURE 89: XY CROSS SECTION SHOWING GRANULAR TEMPERATURE FOR AN EIGHTH SCALE BLENDER WITH 300 MICRON LACTOSE PARTICLES AND A 0.0035 G/S INFLOW. 207

FIGURE 90: XZ CROSS SECTION SHOWING GRANULAR TEMPERATURE FOR AN EIGHTH SCALE BLENDER WITH 300 MICRON LACTOSE PARTICLES AND A 0.0035 G/S INFLOW. 208

FIGURE 91: YZ CROSS SECTION SHOWING GRANULAR TEMPERATURE FOR AN EIGHTH SCALE BLENDER WITH 300 MICRON LACTOSE PARTICLES AND A 0.0035 G/S INFLOW. 209

FIGURE 92: FLOW RATE IN MG/S AT THE MIDDLE OF AN EIGHTH SCALE DOUBLE HELICAL RIBBON BLENDER OPERATING AT 20 RPM OR A PADDLE BLENDER OPERATING AT 40 RPM WITH 300 MICRON LACTOSE PARTICLES AND A 0.0035 G/S INFLOW. 211

FIGURE 93: FLOW RATE IN MG/S AT THE EXIT OF AN EIGHTH SCALE DOUBLE HELICAL RIBBON BLENDER OPERATING AT 20 RPM OR A PADDLE BLENDER OPERATING AT 40 RPM WITH 300 MICRON LACTOSE PARTICLES AND A 0.0035 G/S INFLOW. 212

FIGURE 94: CENTROIDS OF X INITIAL POSITION GROUPS (BLUE = 1, GREEN = 2, YELLOW = 3, ORANGE = 4) IN THE X DIRECTION FOR AN EIGHTH SCALE PADDLE BLENDER OPERATING AT 40 RPM WITH 300 MICRON LACTOSE PARTICLES AND A 0.0035 G/S INFLOW. 214

FIGURE 95: CENTROIDS OF Y INITIAL POSITION GROUPS (BLUE = 1, GREEN = 2, YELLOW = 3, ORANGE = 4) IN THE Y DIRECTION FOR AN EIGHTH SCALE PADDLE BLENDER OPERATING AT 40 RPM WITH 300 MICRON LACTOSE PARTICLES AND A 0.0035 G/S INFLOW. 215

FIGURE 96: CENTROIDS OF X AND Y INITIAL POSITION GROUP 1 (BLUE) IN THE Y DIRECTION FOR AN EIGHTH SCALE DOUBLE HELICAL RIBBON BLENDER OPERATING AT 20 RPM OR A PADDLE BLENDER OPERATING AT 40 RPM WITH 300 MICRON LACTOSE PARTICLES AND A 0.0035 G/S INFLOW..... 216

FIGURE 97: CENTROIDS OF Z INITIAL POSITION GROUPS (BLUE = 1, GREEN = 2, YELLOW = 3, ORANGE = 4) IN THE Z DIRECTION FOR AN EIGHTH SCALE PADDLE BLENDER OPERATING AT 40 RPM WITH 300 MICRON LACTOSE PARTICLES AND A 0.0035 G/S INFLOW. 218

FIGURE 98: CENTROIDS OF R INITIAL POSITION GROUPS (BLUE = 1, GREEN = 2, YELLOW = 3, ORANGE = 4) IN THE R DIRECTION FOR AN EIGHTH SCALE

PADDLE BLENDER OPERATING AT 40 RPM WITH 300 MICRON LACTOSE PARTICLES AND A 0.0035 G/S INFLOW.	219
FIGURE 99: CENTROIDS OF Z INITIAL POSITION GROUP 2 (GREEN) AND R INITIAL POSITION GROUP 1 (BLUE) IN THE R DIRECTION FOR AN EIGHTH SCALE DOUBLE HELICAL RIBBON BLENDER OPERATING AT 20 RPM OR A PADDLE BLENDER OPERATING AT 40 RPM WITH 300 MICRON LACTOSE PARTICLES AND A 0.0035 G/S INFLOW.	220
FIGURE 100: HOMOGENEITY (MIXING %) FOR X AND Y INITIAL POSITION GROUPS IN EIGHTH SCALE BLENDERS WITH 300 MICRON LACTOSE PARTICLES AND A 0.0035 G/S INFLOW.	222
FIGURE 101: HOMOGENEITY (MIXING %) FOR Z AND R INITIAL POSITION GROUPS IN EIGHTH SCALE BLENDERS WITH 300 MICRON LACTOSE PARTICLES AND A 0.0035 G/S INFLOW.	223
FIGURE 102: YZ SLICE SHOWING VOLUME FRACTION FOR AN EIGHTH SCALE DOUBLE HELICAL RIBBON BLENDER WITH 300 MICRON LACTOSE PARTICLES AT 10, 20 AND 30 RPM AND A 0.0043 G/S INFLOW.	227
FIGURE 103: YZ SLICE SHOWING THE Z COMPONENT OF VELOCITY FOR AN EIGHTH SCALE DOUBLE HELICAL RIBBON BLENDER WITH 300 MICRON LACTOSE PARTICLES AT 10, 20 AND 30 RPM AND A 0.0043 G/S INFLOW.	229
FIGURE 104: XY SLICE SHOWING GRANULAR TEMPERATURE FOR AN EIGHTH SCALE DOUBLE HELICAL RIBBON BLENDER WITH 300 MICRON LACTOSE PARTICLES AT 10, 20 AND 30 RPM AND A 0.0043 G/S INFLOW.	231
FIGURE 105: FLOW RATE IN MG/S AT THE MIDDLE OF AN EIGHTH SCALE DOUBLE HELICAL RIBBON BLENDER WITH 300 MICRON LACTOSE PARTICLES OPERATING BETWEEN 10 RPM AND 30 RPM AND A 0.0043 G/S INFLOW.	233

FIGURE 106: FLOW RATE IN MG/S AT THE EXIT OF AN EIGHTH SCALE DOUBLE HELICAL RIBBON BLENDER WITH 300 MICRON LACTOSE PARTICLES OPERATING BETWEEN 10 RPM AND 30 RPM AND A 0.0043 G/S INFLOW. 234

FIGURE 107: HOMOGENEITY (MIXING %) FOR X AND Y INITIAL POSITION GROUPS IN AN EIGHTH SCALE DOUBLE HELICAL RIBBON BLENDER WITH 300 MICRON LACTOSE PARTICLES OPERATING BETWEEN 10 RPM AND 30 RPM AND A 0.0043 G/S INFLOW. 236

FIGURE 108: HOMOGENEITY (MIXING %) FOR Z AND R INITIAL POSITION GROUPS IN AN EIGHTH SCALE DOUBLE HELICAL RIBBON BLENDER WITH 300 MICRON LACTOSE PARTICLES OPERATING BETWEEN 10 RPM AND 30 RPM AND A 0.0043 G/S INFLOW. 237

FIGURE 109: FLOW RATE IN MG/S AT THE MIDDLE OF AN EIGHTH SCALE DOUBLE HELICAL RIBBON BLENDER WITH 300 MICRON LACTOSE PARTICLES OPERATING WITH VARYING INFLOW, ROTATION RATE AND FILL FRACTION. 239

FIGURE 110: FLOW RATE IN MG/S AT THE EXIT OF AN EIGHTH SCALE DOUBLE HELICAL RIBBON BLENDER WITH 300 MICRON LACTOSE PARTICLES OPERATING WITH VARYING INFLOW, ROTATION RATE AND FILL FRACTION. 240

FIGURE 111: HOMOGENEITY (MIXING %) FOR X AND Y INITIAL POSITION GROUPS IN AN EIGHTH SCALE DOUBLE HELICAL RIBBON BLENDER WITH 300 MICRON LACTOSE PARTICLES OPERATING WITH VARYING INFLOW, ROTATION RATE AND FILL FRACTION..... 242

FIGURE 112: HOMOGENEITY (MIXING %) FOR Z AND R INITIAL POSITION GROUPS IN AN EIGHTH SCALE DOUBLE HELICAL RIBBON BLENDER WITH 300 MICRON LACTOSE PARTICLES OPERATING WITH VARYING INFLOW, ROTATION RATE AND FILL FRACTION..... 243

FIGURE 113: EFFECT OF PARTICLE PROPERTIES ON 3 SECOND MOVING AVERAGE MASS NORMALIZED FLOW RATE AT $T = 2$ REVOLUTIONS FOR A DOUBLE HELICAL RIBBON BLENDER. TREND LINE FITTED TO Q_{MIDDLE} 248

FIGURE 114: EFFECT OF PARTICLE PROPERTIES ON INITIAL POSITION GROUP HOMOGENEITY (MIXING STATE %) AT T = 2 REVOLUTIONS FOR A DOUBLE HELICAL RIBBON BLENDER. TREND LINE FITTED TO Z INITIAL POSITION GROUP HOMOGENEITY.....	249
FIGURE 115: EFFECT OF BLENDER SIZE ON 3 SECOND MOVING AVERAGE MASS NORMALIZED FLOW RATE AT T = 2 REVOLUTIONS FOR A DOUBLE HELICAL RIBBON BLENDER. TREND LINE FITTED TO Q_{MIDDLE}	250
FIGURE 116: EFFECT OF BLENDER SIZE ON INITIAL POSITION GROUP HOMOGENEITY (MIXING STATE %) AT T = 2 REVOLUTIONS FOR A DOUBLE HELICAL RIBBON BLENDER. TREND LINE FITTED TO Z INITIAL POSITION GROUP HOMOGENEITY.	250
FIGURE 117: EFFECT OF OPERATING CONDITIONS ON 3 SECOND MOVING AVERAGE MASS NORMALIZED FLOW RATE AT T = 2 REVOLUTIONS FOR A DOUBLE HELICAL RIBBON BLENDER. TREND LINE FITTED TO Q_{MIDDLE}	251
FIGURE 118: EFFECT OF OPERATING CONDITIONS ON INITIAL POSITION GROUP HOMOGENEITY (MIXING STATE %) AT T = 2 REVOLUTIONS FOR A DOUBLE HELICAL RIBBON BLENDER. TREND LINE FITTED TO Z INITIAL POSITION GROUP HOMOGENEITY.....	252
FIGURE 119: 3 SECOND MOVING AVERAGE MASS NORMALIZED FLOW RATE AND SCALE RATIO FOR A DOUBLE HELICAL RIBBON BLENDER WITH LACTOSE PARTICLES OPERATING AT 20 RPM.....	253
FIGURE 120: 3 MIXING % AND SCALE RATIO FOR A DOUBLE HELICAL RIBBON BLENDER WITH LACTOSE PARTICLES OPERATING AT 20 RPM.....	254
FIGURE 121: 3 SECOND MOVING AVERAGE MASS NORMALIZED FLOW RATE AND SCALE RATIO FOR A DOUBLE HELICAL RIBBON BLENDER WITH LACTOSE PARTICLES.....	255
FIGURE 122: MIXING % AND FROUDE NUMBER FOR A DOUBLE HELICAL RIBBON BLENDER WITH LACTOSE PARTICLES.	256

FIGURE 123: 3 SECOND MOVING AVERAGE MASS NORMALIZED FLOW RATE AND AVALANCHE VELOCITY FOR A DOUBLE HELICAL RIBBON BLENDER WITH LACTOSE PARTICLES..... 257

FIGURE 124: MIXING % AND AVALANCHE FOR A DOUBLE HELICAL RIBBON BLENDER WITH LACTOSE PARTICLES..... 258

FIGURE 125: 1 REVOLUTION MOVING AVERAGE MASS NORMALIZED FLOW RATE FROM DISCRETE ELEMENT METHOD MEASUREMENT AND DIMENSIONAL ANALYSIS MODEL FOR A DOUBLE HELICAL RIBBON BLENDER WITH LACTOSE PARTICLES..... 260

FIGURE 126: HOMOGENEITY OF INITIAL POSITION GROUPS FROM DEM MEASUREMENT AND DIMENSIONAL ANALYSIS MODEL FOR A DOUBLE HELICAL RIBBON BLENDER WITH LACTOSE PARTICLES. 262

FIGURE 127: SUPERPRO DESIGNER FLOW SHEET FOR WET GRANULATION PROCESSES. 266

FIGURE 128: SUPERPRO DESIGNER FLOW SHEET FOR DIRECT COMPRESSION PROCESSES. 267

FIGURE 129: GANTT CHART OF PROCESS STEPS FOR BATCH DIRECT COMPRESSION PROCESS..... 270

FIGURE 130: GANTT CHART OF PROCESS STEPS FOR BATCH WET GRANULATION PROCESS..... 271

FIGURE 131: CAPITAL (CAPEX) AND OPERATING (OPEX) COSTS FOR BATCH AND CONTINUOUS WET GRANULATION AND DIRECT COMPRESSION PROCESSES. 274

FIGURE 132: PRESENT VALUE (PV) COSTS FOR CAPEX AND 10 YEARS OF OPEX WITH A WACC OF 10%. 275

FIGURE 133: CAPITAL (CAPEX) AND OPERATING (OPEX) COMPARISON FOR BATCH AND CONTINUOUS WET GRANULATION AND DIRECT COMPRESSION PROCESSES. 276

List of Tables

TABLE 1: 12 LARGEST PHARMACEUTICAL COMPANIES BY REVENUE. [FORTUNE. GLOBAL 500 2009: INDUSTRY: PHARMACEUTICALS.].....	36
TABLE 2: CLINICAL TRIAL PHASE WITH NUMBER OF PATIENTS AND EQUIVALENT ANNUAL PRODUCTION OF TABLETS (1 TABLET PER PATIENT PER DAY) AND TABLET MASS (500 MG TABLET).....	41
TABLE 3: CLINICAL TRIAL PHASE WITH CORRESPONDING ANNUAL PRODUCTION OF TABLET MASS (500 MG TABLET) AND EQUIVALENT OPERATING TIME FOR 10KG/HR CONTINUOUS MANUFACTURING.....	42
TABLE 4: EXPENSES AND NET INCOME FOR PFIZER INC. [PFIZER 10-K (PERIOD: DECEMBER 31, 2008)]	43
TABLE 5: DESIGN, OPERATIONAL AND MATERIAL RELATIONSHIPS TO AXIAL DISPERSION COEFFICIENT IN A ROTATED DRUM. [R.G. SHERRITT, J. CHAOUKI, A.K. MEHROTRA AND L.A. BEHIE. AXIAL DISPERSION IN THE THREE-DIMENSIONAL MIXING OF PARTICLES IN A ROTATING DRUM REACTOR. CHEMICAL ENGINEERING SCIENCE 58 (2003) 401-415.].....	50
TABLE 6: REFERENCES FOR DEM SIMULATIONS OF VARIOUS BLENDERS.....	64
TABLE 7: SUMMARY OF MODEL CONDITIONS FOR DEM SIMULATION OF THE DOUBLE HELICAL RIBBON BLENDER.	76
TABLE 8: SUMMARY OF MODEL CONDITIONS FOR DEM SIMULATIONS STUDYING PARTICLE SIZE EFFECTS.	77
TABLE 9: SUMMARY OF MODEL CONDITIONS FOR DEM SIMULATIONS STUDYING POLYDISPERSITY EFFECTS.	77
TABLE 10: SUMMARY OF MODEL CONDITIONS FOR DEM SIMULATIONS STUDYING PARTICLE COHESIVE FORCE EFFECTS.	78

TABLE 11: SUMMARY OF MODEL CONDITIONS FOR DEM SIMULATIONS STUDYING BLENDER SIZE EFFECTS.....	78
TABLE 12: SUMMARY OF MODEL CONDITIONS FOR DEM SIMULATIONS STUDYING SHAFT DESIGN EFFECTS.	79
TABLE 13: SUMMARY OF MODEL CONDITIONS FOR DEM SIMULATIONS STUDYING ROTATION RATE EFFECTS.	79
TABLE 14: SUMMARY OF MODEL CONDITIONS FOR DEM SIMULATIONS STUDYING FILL FRACTION EFFECTS.	80
TABLE 15: PARTICLE PROPERTIES OF SIMULATED MATERIALS.	86
TABLE 16: SPRING CONSTANT (K) IN N/M FOR SIMULATION FORCE LAW FOR EACH PARTICLE SYSTEM.	88
TABLE 17: MEAN SURFACE ENERGY (γ) IN MJ/M ² FOR COHESIVE PARTICLE INTERACTIONS [S.H. NGAI. MULTISCALE ANALYSIS AND SIMULATION OF POWDER BLENDING IN PHARMACEUTICAL MANUFACTURING. PHD DISSERTATION, MASSACHUSETTS INSTITUTE OF TECHNOLOGY, DEPARTMENT OF CHEMICAL ENGINEERING. AUGUST 2005.].....	90
TABLE 18: SURFACE ENERGY STANDARD DEVIATION (γ) IN MJ/M ² FOR COHESIVE PARTICLE INTERACTIONS [S.H. NGAI. MULTISCALE ANALYSIS AND SIMULATION OF POWDER BLENDING IN PHARMACEUTICAL MANUFACTURING. PHD DISSERTATION, MASSACHUSETTS INSTITUTE OF TECHNOLOGY, DEPARTMENT OF CHEMICAL ENGINEERING. AUGUST 2005.].....	90
TABLE 19: APPROXIMATE PARTICLE NUMBERS FOR LINEAR SIZE REDUCTIONS IN BLENDER SCALE. PARTICLES HAVE 100 μ M DIAMETERS WITH A PACKING FRACTION OF 0.63.	91
TABLE 20: INITIAL FILL CONDITIONS FOR BLENDER SIZE, INFLOW AND ROTATION RATE.	95

TABLE 21: SUMMARY OF MODEL CONDITIONS FOR DEM SIMULATION OF THE DOUBLE HELICAL RIBBON BLENDER.	102
TABLE 22: SUMMARY OF MODEL CONDITIONS FOR DEM SIMULATIONS COMPARING THE EFFECTS OF PARTICLE SIZE.	156
TABLE 23: SUMMARY OF MODEL CONDITIONS FOR DEM SIMULATIONS COMPARING THE EFFECTS OF POLYDISPERSITY.	167
TABLE 24: SUMMARY OF MODEL CONDITIONS FOR DEM SIMULATIONS COMPARING THE EFFECTS OF COHESIVE FORCES.	172
TABLE 25: SUMMARY OF MODEL CONDITIONS FOR DEM SIMULATIONS COMPARING THE SIZE OF DOUBLE HELICAL RIBBON BLENDERS.	188
TABLE 26: OBSERVED (T = 6 SECONDS) AND CALCULATED FLOW RATES RATIO NORMALIZED TO THE QUARTER SCALE BLENDER.	193
TABLE 27: SUMMARY OF MODEL CONDITIONS FOR DEM SIMULATIONS COMPARING THE EFFECTS OF SHAFT DESIGN.	198
TABLE 28: SUMMARY OF MODEL CONDITIONS FOR DEM SIMULATIONS COMPARING ROTATION RATE.	226
TABLE 29: SUMMARY OF MODEL CONDITIONS FOR DEM SIMULATIONS COMPARING FILL FRACTION.	238
TABLE 30: SUMMARY OF TESTED PROPERTIES AND THEIR CORRELATION TO FLOW RATE.	246
TABLE 31: SUMMARY OF TESTED PROPERTIES AND THEIR CORRELATION TO HOMOGENEITY.	247
TABLE 32: COMPARISON OF DEM MODEL HOMOGENEITY FOR Z INITIAL POSITION GROUPS (MIXING %) AND DIMENSIONAL ANALYSIS MODEL Z HOMOGENEITY.	263

TABLE 33: BATCH PROCESS UNITS WITH PROCESS TIMES AND COSTS FOR A 1 BILLION
TABLET/YR MANUFACTURING SYSTEM. 269

TABLE 34: CONTINUOUS PROCESS UNITS WITH PROCESS TIMES AND COSTS FOR A 1
BILLION TABLET/YR MANUFACTURING SYSTEM..... 270

TABLE 35: LABOR HOURS PER OPERATING HOUR FOR BATCH PROCESS STEPS. 272

TABLE 36: PROCESS EQUIPMENT VOLUMES AND THROUGHPUTS FOR A 1 BILLION
TABLET/YR MANUFACTURING SYSTEM. 273

List of Equations

EQUATION 1: FROUDE NUMBER IN TERMS OF BLENDER DIAMETER (D), ROTATION RATE (Ω) AND THE ACCELERATION OF GRAVITY (G)..... 48

EQUATION 2: AXIAL DISPERSION COEFFICIENT FOR VARIANCE OF TRACER DISPLACEMENT IN TERMS THE STANDARD DEVIATION OF AXIAL POSITION (Σ_z)..... 49

EQUATION 3: BODENSTEIN NUMBER (Bo) IN TERMS OF CHARACTERISTIC LENGTH (L), MEAN VELOCITY (U) AND THE AXIAL DISPERSION COEFFICIENT (D_z). 49

EQUATION 4: CONCENTRATION (C) AT THE EXIT OF A BLENDER AT TIME T FOR A UNIT IMPULSE AT T = 0 IN TERMS OF SPACE TIME (T) AND BODENSTEIN NUMBER (Bo)..... 49

EQUATION 5: AVALANCHE VELOCITY WITH DIMENSIONALLY HOMOGENOUS EXPONENTS AND PROPORTIONALITY CONSTANT (K)..... 52

EQUATION 6: AVALANCHE VELOCITY WITH EXPERIMENTALLY FITTED EXPONENTS AND PROPORTIONALITY CONSTANT (K). 52

EQUATION 7: BEVERLOO LAW FOR MASS FLOW RATE (Q) IN GRAVITY DRIVEN FLOW THROUGH AN ORIFICE OF DIAMETER (D) BASED ON DENSITY (P), ACCELERATION OF GRAVITY (G), PARTICLE DIAMETER (D), DISCHARGE CONSTANT (C) AND SHAPE CONSTANT (K)..... 53

EQUATION 8: SIZE RATIO (SR) COMPARING ORIFICE DIAMETER (D) TO PARTICLE DIAMETER (D). 54

EQUATION 9: MODIFIED BEVERLOO LAW FOR MASS FLOW RATE WITH AN EXPONENTIAL CORRECTIVE FACTOR IN TERMS OF SIZE RATIO (SR) AND CONSTANTS (C' AND B)..... 54

EQUATION 10: DAMPING COEFFICIENT (C) BASED ON COEFFICIENT OF RESTITUTION (ϵ) AND MASSES (M_i, M_j) OF THE TWO COLLIDING PARTICLES..... 60

EQUATION 11: NORMAL FORCE FOR A DEM MODEL WITH A LINEAR SPRING TO PROVIDE A REPULSIVE FORCE AND A DASHPOT TO DISSIPATE A PORTION OF THE KINETIC ENERGY. 60

EQUATION 12: TANGENTIAL FORCE FOR A DEM MODEL WITH THE INTEGRAL OF V_T SERVING AS AN INCREMENTAL SPRING THAT STORES ENERGY AND A DASHPOT TO DISSIPATE ENERGY FROM THE TANGENTIAL MOTION..... 61

EQUATION 13: POSITION EQUATION FOR SPHERICAL PARTICLE I..... 63

EQUATION 14: VELOCITY EQUATION FOR SPHERICAL PARTICLE I. 63

EQUATION 15: ORIENTATION EQUATION FOR SPHERICAL PARTICLE I..... 63

EQUATION 16: SPIN EQUATION FOR SPHERICAL PARTICLE I WITH MOMENT OF INERTIA I. 63

EQUATION 17: THERMODYNAMIC TEMPERATURE (T) FOR GASSES. 65

EQUATION 18: GRANULAR TEMPERATURE (T) FOR PARTICLES WHERE B IS AVERAGE (OVER ALL PARTICLES) OF THE SQUARE OF THE RATIO OF THE PARTICLE RADIUS OF GYRATION TO THE PARTICLE RADIUS. 65

EQUATION 19: QUANTITATIVE MIXING MEASUREMENT BASED ON COEFFICIENT OF VARIATION, THE FULLY SEGREGATED COEFFICIENT OF VARIATION AND THE PERFECTLY MIXED COEFFICIENT OF VARIATION..... 68

EQUATION 20: JKR CONTACT MODEL RELATING COHESIVE FORCE (F) TO SURFACE ENERGY (Γ) AND REDUCED RADIUS (R). 89

EQUATION 21: REDUCED RADIUS (R) FOR TWO SPHERES A AND B WITH DIAMETER D. 89

EQUATION 22: PROPORTIONALITY BETWEEN BLENDER DIAMETER OR EXIT PORT DIAMETER AND FLOW RATE..... 193

EQUATION 23: OBSERVED RELATIONSHIPS FOR MASS FLOW RATE..... 259

EQUATION 24: UNITS FOR THE MASS NORMALIZED FLOW RATE..... 259

EQUATION 25: DIMENSIONAL ANALYSIS MODEL FOR FLOW RATE..... 259

EQUATION 26: DIMENSIONAL ANALYSIS MODEL FOR FLOW RATE WITH FITTED
EXONENTS. 259

EQUATION 27: OBSERVED RELATIONSHIPS FOR MIXING STATE..... 261

EQUATION 28: DIMENSIONAL ANALYSIS MODEL FOR HOMOGENEITY. 261

EQUATION 29: DIMENSIONAL ANALYSIS MODEL FOR HOMOGENEITY WITH EXPONENTS
FITTED FROM DEM SIMULATIONS. 261

EQUATION 30: PRICE OF THE MODELED CONTINUOUS PHARMACEUTICAL POWDER
BLENDER. 268

1 INTRODUCTION

1.1 Pharmaceutical industry

The pharmaceutical industry develops, manufactures and markets products that have been proven to have a therapeutic effect on patients. Pharmaceuticals are a significant industry globally with the 12 largest pharmaceutical companies producing revenues of \$434 billion and profits of \$78 billion in 2008 (Table 1) [1].

Table 1: 12 largest pharmaceutical companies by revenue. [Fortune. Global 500 2009: Industry: Pharmaceuticals.]

Company	Country	2008 Revenue <i>\$ millions</i>	2008 Profits <i>\$ millions</i>
Johnson & Johnson	United States	63,747	12,949
Pfizer	United States	48,296	8,104
GlaxoSmithKline	United Kingdom	44,654	8,439
Roche Group	Switzerland	44,268	8,288
Sanofi-Aventis	France	42,179	5,637
Novartis	Switzerland	41,459	8,195
AstraZeneca	United Kingdom	31,601	6,101
Abbott Laboratories	United States	29,528	4,881
Merck	United States	23,850	7,808
Wyeth	United States	22,834	4,418
Bristol-Myers Squibb	United States	21,366	5,247
Eli Lilly	United States	20,378	-2,072
Total		434,160	77,995

The pharmaceutical industry also enjoys healthy margins with the 12 companies listed in Table 1 achieving a profit margin of 18% as a whole, even with Eli Lilly taking a loss in 2008. The pharmaceutical industry is also heavily regulated with government bodies, like the Food and

Drug Administration (FDA) in the United States, overseeing both the approval and manufacturing standards of drug products.

1.2 Pharmaceutical manufacturing

The reliable and cost effective manufacturing of drug products is essential to the business success of large pharmaceutical companies. Pharmaceutical manufacturing typically consists of two distinct areas:

1. Primary or upstream manufacturing where the active pharmaceutical ingredient (API) is synthesized,
2. Secondary or downstream manufacturing where the active pharmaceutical ingredient is formulated into a useful drug product.

While both upstream and downstream pharmaceutical manufacturing have the potential for increasing the understanding of unit operations and economic improvement, the focus of this research is limited to downstream manufacturing.

Downstream manufacturing takes the active pharmaceutical ingredients and combines them with other materials, commonly referred to as excipients, to create drug products that can be administered to patients. Downstream pharmaceutical manufacturing frequently consists of a multistep process with granulation, drying, milling, blending, compression and coating unit operations as can be seen in Figure 1.

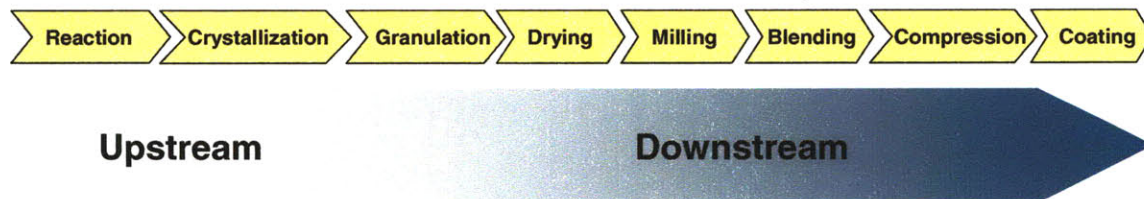


Figure 1: Process schematic for upstream and downstream pharmaceutical manufacturing.

The purpose of the granulation and milling steps are to modify and control the size distribution of pharmaceutical powders to adjust their properties for more efficient blending and compression. The granulation step increases the size of the pharmaceutical powder particles and the milling step decreases the size of the pharmaceutical powder particles. The drying step removes liquids added in the granulation step. Blending steps combine the API with excipients to create the desired drug formulation. The compression step forms the solid dosage (tablet) that is the drug product. Finally, the coating step coats the drug product to modify its color, flavor and pharmacokinetics.

The typical material inputs for the downstream manufacturing process are dry powdered APIs and dry powdered excipients. The most common final drug products are oral solid dosage forms, such as capsules and tablets. A primary advantage of the oral solid dosage is that it provides a simple way to meter the prescribed dose (multiples of tablets) to the patient. In addition, oral solid dosage forms are very consumer friendly, with easy handling, storage and administration. The oral solid dosage form can be optimized to increase the effectiveness of the active pharmaceutical ingredient by providing greater stability for the API or changing (increasing or decreasing) the rate of dissolution for the API. Given the popularity and fundamental advantages of oral solid dosage forms, the focus of this research will be limited to the manufacturing of tablets.

1.3 Batch vs. continuous downstream pharmaceutical manufacturing

The majority of pharmaceutical manufacturing is accomplished with batch operations [2] that can be defined as the processing of material in a step-wise manner, where each step is run to completion before material is moved to the next step. Besides prior capital investment in batch equipment and institutional familiarity with batch processes, there have been important regulatory and operational reasons for batch processing. First, there is the need in pharmaceutical manufacturing to separate the product into lots for regulatory compliance. Batch processing offers a natural operational synergy with this task with the single batch providing a distinct unit. Second, there is a lack of continuous processing equipment or continuous processing equipment at the appropriate scale for some pharmaceutical manufacturing unit operations. Currently, this makes it unfeasible to deploy continuous manufacturing systems for pharmaceuticals.

Recent guidance from the Food and Drug Administration (FDA) [3] and current research in continuous pharmaceutical processing equipment [4] have begun to remove some of the justifications for batch manufacturing and have provided support for continuous manufacturing in the pharmaceutical industry. The Consortium for the Advancement of Manufacturing of Pharmaceuticals (CAMP) has defined continuous manufacturing as, “Processing of raw materials without interruption and with continuity of production over a sustained period of time” [5]. With the barriers to continuous pharmaceutical manufacturing lowered, researchers, like Mollan and Lodoya of Pfizer Inc. [6] and Pernenkil [4] of the Massachusetts Institute of Technology, have begun to explore continuous manufacturing’s potential advantages.

1.3.1 Continuous manufacturing operational advantages

During the bulk of its operations, a continuous process should operate at steady state. Instead of operating to set process times and then testing for quality as one would do in a batch process, the continuous process can be maintained at its set steady state operating conditions using appropriate control schemes to address critical product qualities. Once at steady state operating conditions, it can be run with minimal attention. This allows operations to more easily shift from an 8/5 schedule to a 24/7 schedule creating more efficient use of the manufacturing facilities and less labor intensive operations.

1.3.2 Continuous manufacturing material containment advantages

By design, a continuous manufacturing system needs to have closed connections between its various unit operations. This decreases the risk of employee exposure to dangerous products by removing much of the need to interact with the product between unit operations. This also decreases the risk of cross contamination by other products in a multi-product manufacturing facility.

1.3.3 Continuous manufacturing scale-up advantages

One of the key challenges of pharmaceutical manufacturing is the need to perform a number of scale-ups as a process moves through the various clinical trial phases on to commercialization [7]. This is best understood through an example using a hypothetical drug product with a tablet mass of 500 mg and a dose frequency of 1 tablet per day. Table 2 summarizes the number of patients in each clinical trial phase, the corresponding number of

tablets per year and the mass of tablets per year that would need to be produced in order to meet this demand.

Table 2: Clinical trial phase with number of patients and equivalent annual production of tablets (1 tablet per patient per day) and tablet mass (500 mg tablet).

Phase	Patients <i>number</i>	Tablets <i>number/yr</i>	Mass <i>kg/yr</i>
Phase I	10	3,650	2
Phase II	100	36,500	18
Phase III	1,000	365,000	183
Commercialization	1,000,000	365,000,000	182,500

With batch processing, each of these transitions between phases would require at least a 10X scale-up by volume as the number of patients increases. Continuous manufacturing offers ways to scale-up, either scaling by time or parallel units, which reduces the need to make significant changes in the processing equipment volume.

The first scale-up advantage of continuous manufacturing is the ability to scale-up by time rather than volume. As an example, take the continuous pharmaceutical powder blender successfully used in experiments by Pernenkil [4] and the manufacturing volumes calculated for the hypothetical pharmaceutical product in Table 2. This blender can operate at a throughput of 10 kg/hr. If one were to use this blender for manufacturing in the various clinical trial phases instead of scaling the size of the blender for each phase, one could simply extend operating time (Table 3).

Table 3: Clinical trial phase with corresponding annual production of tablet mass (500 mg tablet) and equivalent operating time for 10kg/hr continuous manufacturing.

Phase	Mass <i>kg/yr</i>	Operation Time @ 10 kg/hr <i>hr</i>
Phase I	2	0.2
Phase III	18	1.8
Phase III	183	18

The second scale-up advantage of continuous manufacturing is the ability to scale-up by adding parallel units. Returning to the 10 kg/hr blender used by Pernenkil [4] and the hypothetical pharmaceutical product from Table 2, it is possible to achieve this commercial manufacturing scale using 3 of these blenders in parallel and operating them 24/7 with 80% uptime. In both of the previously cited scale-up examples, the physical manufacturing equipment is the same at all scales and thus any risk of changes in process behavior as one moves between scales is removed. Ultimately, this should speed the development of pharmaceutical manufacturing processes as well as remove the uncertainties associated with scale-up.

1.3.4 Continuous manufacturing equipment size and cost advantages

Pharmaceutical companies spend significant sums of money developing, manufacturing and marketing their drugs. The expenses of Pfizer Inc. were in excess of \$40 billion in 2008 (Table 4) [8].

Table 4: Expenses and net income for Pfizer Inc. [Pfizer 10-K (period: December 31, 2008)]

Pfizer Inc.	\$ millions	% of Revenue
Cost of Goods Sold	8,112	17%
Selling, General and Administrative	14,537	30%
Research and Development	7,945	16%
Other	9,598	20%
Net Income	8,104	17%

Two of the major expenses for Pfizer were research and development (the expenses associated with discovering and developing the pharmaceuticals) and costs of goods sold (the expenses associated with manufacturing the pharmaceuticals) with each valued at approximately \$8 billion in 2008. Other pharmaceutical companies spend an even greater percentage of their sales on manufacturing with the cost of goods sold for brand-name pharmaceutical companies averaging 26% of sales [9]. While large in magnitude, these expenses would be manageable if they were static, but they are not. Research and development costs have been increasing significantly for a number of years. Based on an estimate of the average research and development costs per new drug brought to market in 1987 (\$231 million in 1987 dollars) and 2000 (\$802 million in 2000 dollars), the capitalized drug development cost has been rising at an annual rate of 7.4% above general price inflation [7]. Ultimately, with the rising costs of research and development, the pharmaceutical industry will need to find ways to reduce their other expenses to maintain their

profitability. Pharmaceutical manufacturing represents an attractive area to seek possible cost savings.

Continuous processing equipment can be much smaller than the equivalent batch processing equipment. This comes from increased equipment utilization from both the operational improvements mentioned previously and by removing the downtime associated with loading and unloading batch process equipment. The smaller equipment creates capital cost savings both from the equipment itself and from the added effect that the manufacturing facility where it is housed can be smaller.

1.4 Continuous downstream pharmaceutical manufacturing systems

In order to realize all of the potential benefits of continuous downstream pharmaceutical manufacturing, it is necessary to develop fully continuous process systems. Mollan and Lodaya [6] recognized that much of the current pharmaceutical process equipment is “continuous by design” and is merely being operated in batch mode. Unit operations like roller compaction, milling and compression that operate on a “first in/first out” principle are continuous devices that could be easily integrated into a fully continuous manufacturing system. Most pharmaceutical powder blenders, however, are inherently batch devices.

In order to transition to a fully continuous downstream pharmaceutical manufacturing system, it is necessary to develop and implement new continuous powder blending devices. Powder blending is a key process in pharmaceutical manufacturing that is essential for assuring the uniformity of the final drug product. An efficacious drug product formulation often incorporates numerous excipients in a blending step. In a tablet manufacturing process (Figure 1), blending is typically the last step before compression. Thus, blending is the last opportunity

in the process system to influence the uniformity of the API before it is finalized by the tablet formation. This makes consistent blending the essential step for homogenous drug products and reliable continuous downstream pharmaceutical manufacturing. Ultimately, continuous downstream pharmaceutical manufacturing can be a reality with a continuous blending solution.

1.5 Thesis overview

This thesis begins with a literature review in Chapter 2 that covers simulation of downstream pharmaceutical processes at both a process system and unit operation scale. Particular emphasis is placed on techniques for understanding flow behavior and mixing performance for granular materials in blending operations using the discrete element method.

Chapter 3 defines the objectives of the thesis to be accomplished in the subsequent chapters. Chapter 4 details the methods used for subsequent simulations and explains the rationale for the choice of systems.

The results of the discrete element method simulation of a double helical ribbon blender begin in Chapter 5 with a detailed examination of its flow behavior and mixing performance. Chapter 6 examines the effects of changing particle properties in the double helical ribbon blender. The particle properties examined are particle size, polydispersity and cohesive force. Chapter 7 examines the effects of blender design by changing the size of the double helical ribbon blender and comparing a ribbon and paddle type blender design. Finally, Chapter 8 looks at changing the blender's operating conditions to understand their effects.

Chapter 9 brings together the discrete element method simulation results from Chapters 5 to 8 to evaluate techniques for predicting flow rates and blend homogeneity during scale-up. Models from the literature as well as models developed by the author are examined.

Chapter 10 examines the design of continuous pharmaceutical manufacturing systems. In this chapter, potential benefits for continuous manufacturing are examined using process system simulations.

The suggestions for further research in the modeling of continuous downstream pharmaceutical manufacturing are detailed in Chapter 11. Finally, Chapter 12 is the conclusion of this thesis.

2 LITERATURE REVIEW

This review of continuous powder blending begins with the experimental work on continuous blending and the governing factors of blend homogeneity. Additionally, various computational techniques for studying continuous powder blending are explored. This review concludes with an examination of modeling techniques for downstream pharmaceutical manufacturing processes.

2.1 Experimental studies of powder blending

One of the simplest blending devices is the rotating drum. Its flow behavior and mixing performance have been studied extensively [10, 11, 12, 13]. A rotating drum is a cylinder that is rotated radially; it can be operated in either batch or continuous modes. Continuous operation is typically handled by angling the device downward toward the outflow. As rotation rate increases, flow in rotating drums can be classified into distinct regimes (Figure 2):

1. **Avalanching:** In the avalanching regime, flowing material is limited to a layer on the surface, the avalanching region. The rest of the particles rotate as a solid body in the particle bed.
Each avalanche is a discrete event where a wedge of particles moves across the surface of the particle bed.
2. **Rolling:** In the rolling regime, a layer of steady flowing particles exists at the surface of the particle bed with the rest of the particles rotating as a solid body.
3. **Cataracting:** In the cataracting regime, some particles become airborne and separate from the main body of particles.

4. Centrifuging: In the centrifuging regime, particles become a mostly stationary body in an annular region.

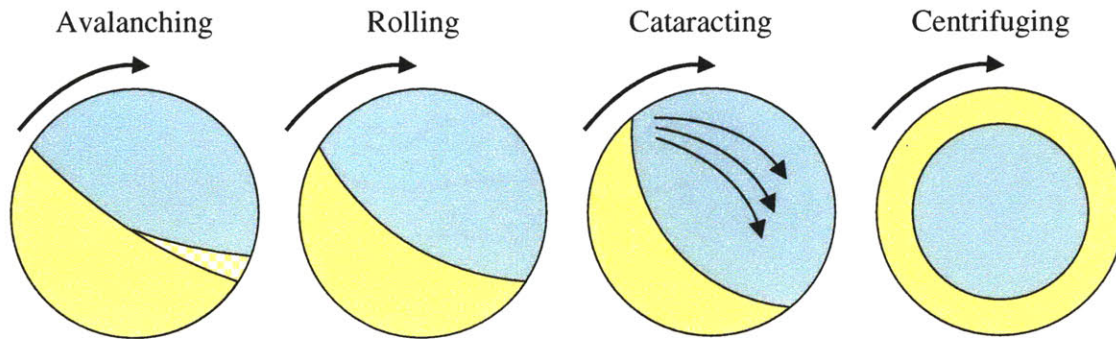


Figure 2: Schematic of avalanching (1), rolling (2), cataracting (3) and centrifuging (4) flow regimes in a rotating drum. The particle bed is defined by the yellow region and the unoccupied space by the blue region. The free surface is the border between the two regions. For avalanching, the solid region represents the free surface before an avalanche and the checkered region represents the free surface after an avalanche.

The operational conditions that define these flow regimes are often designated by the Froude number (Equation 1), a dimensionless parameter that relates gravitational forces to inertial forces.

$$Fr = \frac{\Omega^2(D/2)}{g}$$

Equation 1: Froude number in terms of blender diameter (D), rotation rate (Ω) and the acceleration of gravity (g).

Sherritt et al. [10] used radioactive particle tracers with non-cohesive spherical glass beads to study powder mixing in a rotating drum across these different flow regimes. The variance of the tracer displacement in the axial direction was related to an axial dispersion coefficient (D_z) (Equation 2).

$$D_z = \frac{\sigma_z^2}{2\Delta t}$$

Equation 2: Axial dispersion coefficient for variance of tracer displacement in terms the standard deviation of axial position (σ_z).

The axial dispersion coefficient (D_z) and the related Bodenstein number (Bo) (Equation 3) was used to model the output concentration of components in a continuous blending process using an open-open boundary axial dispersion model (Equation 4) by Pernenkil [4].

$$Bo = \frac{\bar{u}L}{D_z}$$

Equation 3: Bodenstein number (Bo) in terms of characteristic length (L), mean velocity (u) and the axial dispersion coefficient (D_z).

$$C(t) = \frac{1}{2\tau \sqrt{\left(\frac{\pi}{Bo}\right)\left(\frac{t}{\tau}\right)^3}} \exp\left(-\frac{\left(1 - \left(\frac{t}{\tau}\right)\right)^2}{\left(\frac{4}{Bo}\right)\left(\frac{t}{\tau}\right)}\right)$$

Equation 4: Concentration (C) at the exit of a blender at time t for a unit impulse at $t = 0$ in terms of space time (τ) and Bodenstein number (Bo).

This axial dispersion model was also used by Pernenkil [4] to calculate a theoretical variance reduction ratio (VRR) and was used as a predictor for homogeneity in continuous blenders. The axial dispersion coefficients measured by Sherritt et al. [10] were then correlated to rotation rate, particle diameter, drum diameter and fill fraction for the avalanching, rolling and cataracting flow regimes (Table 5).

Table 5: Design, operational and material relationships to axial dispersion coefficient in a rotated drum.
[R.G. Sherritt, J. Chaouki, A.K. Mehrotra and L.A. Behie. Axial dispersion in the three-dimensional mixing of particles in a rotating drum reactor. Chemical Engineering Science 58 (2003) 401-415.]

Flow Regime	Blender diameter (D)	Particle diameter (d)	Rotation rate (Ω)	Fill fraction (χ)
Avalanching	$D_z \propto D$	$D_z \propto d$	$D_z \propto 1/\Omega$	$D_z \propto \chi^{-0.5}$
Rolling	$D_z \propto D$	$D_z \propto d$	$D_z \propto \Omega^{0.5}$	$D_z \propto \chi^{-0.5}$
Cataracting	$D_z \propto D$	$D_z \propto d$	$D_z \propto \Omega$	<i>None</i>

The axial dispersion coefficient was found to be approximately proportional to drum diameter for all flow regimes and was found to be proportional to the square root of particle size for all flow regimes. For the avalanching flow regime, the axial dispersion coefficient tends to decrease with increasing rotation rate. However, the axial dispersion coefficient is proportional to the square root of the rotation rate for the rolling regime and to the rotation rate for the cataracting regime. Finally, for the avalanching and rolling regime, the axial dispersion coefficient tends to be inversely proportional to the square root of the fill fraction; for the cataracting regime, the axial-dispersion coefficient is unrelated to fill fraction.

Sudah et al. [11] studied the continuous blending of 0.30 cm by 0.15 cm zeolite pellets using colored tracer particles and by visually observing the surface concentration of colored tracers. It was observed in these experiments that mean residence time was inversely proportional to rotation rate, but independent of inflow rate. They also found that the mass of material in the blender was inversely proportional to rotational speed and directly proportional to inflow rate. When the residence time distribution (RTD) data were used to calculate axial dispersion coefficients, it was found that the axial dispersion coefficient strongly depends on rotation rate and weakly depends on inflow rate. This agrees with Sherritt et al.'s [10] findings

that the axial dispersion coefficient is proportional to either the square root of the rotation rate or the rotation rate itself in the rolling and cataracting regime respectively.

Ingram et al. [12] used positron emission particle tracking (PEPT) to study the continuous mixing of sand in rotated drums. Their experiments consisted of tracking the position of a single particle from the entrance of the blender to the exit. They found that axial displacement of tracked particles agreed well with a Gaussian distribution when the drum was operated in the rolling regime. In addition to the axial motion of the particle, they were able to track the motion of the particle in the radial direction and calculate a radial dispersion coefficient. Like the axial displacement, the radial displacements of the tracer particle also formed a Gaussian distribution. This radial motion in the rotating drum was demonstrated to be caused by particles entering and leaving the flowing region at different radiuses. The radial dispersion was found to increase slightly with increasing rotation rate. Finally, it was found that the radial dispersion coefficient for continuous blending was similar to batch blending in the same type of device.

The results of Sherritt et al. [10], Sudah et al. [11] and Ingram et al. [12] highlight a number of important parameters in continuous powder blending and the mechanisms of mixing in the rotating drum blender. Particle size, blender size, rotation rate and fill fraction all had a discernible effect on axial dispersion for blenders operated in either the avalanching or rolling regime. Sherritt et al. stated that axial mixing for the rotating drum is caused by random collisions in the flowing regions of the various operating regimes. Sherritt et al. concluded that mixing in the rotating drum is limited to these flowing regions and is a purely diffusive mechanism. This theory is supported by Ingram et al.'s findings that the axial displacements of tracer particles are normally distributed. It is unclear from these results, however, what effect cohesive particles and a more complex blender geometry would have had on the relationships

between the axial dispersion coefficient and particle size, blender size and operating conditions. In addition, this research demonstrates that further study of the mechanisms through which the changes in particle size, blender size and operating conditions affect blending is warranted.

Like the previously mentioned researchers, Alexander and Muzzio [14] also recognized the primacy of the flowing region for mixing in rotating drums. They derived a relationship between rotation rate, drum radius, particle diameter and acceleration from gravity to velocity for particles in the avalanching region of a tumbling blender using the rules of dimensional homogeneity (Equation 5) [15].

$$V_{avalanche} = k(D)^{1-c-e} \Omega^{1-2e} d^c g^e$$

Equation 5: Avalanche velocity with dimensionally homogenous exponents and proportionality constant (k).

By measuring velocity in rotating drums with different diameters and rotational rates, Alexander and Muzzio were able to fit the exponents for the model (Equation 6).

$$V_{avalanche} = k(D/2)\Omega^{2/3}\left(\frac{g}{d}\right)^{1/6}$$

Equation 6: Avalanche velocity with experimentally fitted exponents and proportionality constant (k).

The avalanche velocity model was demonstrated to have good agreement with experimental results for velocity magnitude over a range of 4X blender size (D) and 3X rotation rate (Ω).

Even with continuous processing's ability to avoid scale-up steps, it is inevitable that pharmaceutical manufacturers will need to occasionally change scales in process equipment. Alexander and Muzzio [14] believed that maintaining a constant surface avalanche velocity would allow for consistent scale-up in rotating blenders. Little testing has been done to validate

whether avalanche velocity or Froude number, which is also used for scaling powder blending, is a reliable technique for scale-up in continuous powder blending.

Sherritt et al. [10] demonstrated the importance of fill fraction on axial dispersion. Controlling fill fraction is important to blend homogeneity and requires an understanding of the flow behavior at the outlet of a continuous blender. Kehlenbeck and Sommer [16] examined the use of a rotating star shaped blending device to increase the consistency of exit mass flow rates with a continuous volumetric powder feeder. There was a considerable improvement in the standard deviation of the mass flow rate with cohesive calcium carbonate when using the rotating star device. Marikh et al. [17] researched the continuous blending of couscous and semolina in a ribbon/paddle blender. In their work, they were able to show that mean residence time and fill fraction were correlated to the square root of rotation rate. In both of the previous examples, the exit flow rate was controlled by a rotating mixing device, however, some blenders may use a gravity driven outlet. For gravity driven flows, the mass flow rate of powders through outlets has been shown to be governed by the Beverloo law (Equation 7) [18].

$$Q = C\rho\sqrt{g}(D - kd)^{5/2}$$

Equation 7: Beverloo law for mass flow rate (Q) in gravity driven flow through an orifice of diameter (D) based on density (ρ), acceleration of gravity (g), particle diameter (d), discharge constant (C) and shape constant (k).

Good agreement between the Beverloo law and experiments has been shown for particles with diameters greater than 600 μm and for the case where $D \gg d$ [19, 20, 21]. The Beverloo law was developed for powders without strong cohesive forces so care must be taken when using it with pharmaceutical powders, like lactose and microcrystalline cellulose (MCC), which can cause significant deviations from the model in some geometries [22]. Recent work examining a

wide range of outlet sizes has recast the Beverloo equation in terms of a ratio of the outlet diameter to the particle diameter (Equation 8) [23] with an exponential corrective factor (Equation 9).

$$Sr = \frac{D}{d}$$

Equation 8: Size ratio (Sr) comparing orifice diameter (D) to particle diameter (d).

$$Q = C' \left(1 - \frac{1}{2} e^{-b(Sr-1)} \right) (Sr-1)^{5/2}$$

Equation 9: Modified Beverloo law for mass flow rate with an exponential corrective factor in terms of size ratio (Sr) and constants (C' and b).

This modified Beverloo law predicts the same flow behavior as the standard Beverloo law for large Sr with $Q \propto Sr^{5/2}$, but corrects for the errors in the Beverloo law at small Sr . These relationships between particle properties, outlet diameter and operating conditions to flow rate are essential for designing effective continuous pharmaceutical powder blenders and processes.

Pernenkil [4] studied the mixing performance of two different continuous powder blenders and five materials. The experiments were conducted on a “plant scale” Zigzag blender manufactured by Patterson-Kelley & Co. and a “laboratory scale” double helical ribbon blender of Pernenkil’s design using lactose, MCC and magnesium stearate (MgSt) for excipients and caffeine and acetaminophen for APIs. Pernenkil systematically studied the effects of material type, particle size, rotation rate and inflow rate on residence time distribution (RTD) and variance reduction ratio (VRR). The APIs were used as tracers in the experiments with their concentration measured at the outlet of the blenders using both light induced fluorescence (LIF)

and near infrared spectroscopy (NIR). Pernenkil abstracted his residence time distributions to a single axial dispersion coefficient (D_z) that he was able to compare with VRR for similar materials and operating conditions.

Pernenkil found that mean residence time was positively correlated with VRR and that operational parameters (rotation rate and inflow rate) were primarily correlated to VRR through their effect on mean residence time. When examining the effects of particle properties, Pernenkil found that increasing particle size increased homogeneity, while increasing cohesive forces decreased homogeneity. Pernenkil was unable, however, to relate his operational and material parameters to an axial dispersion coefficient. Further, Pernenkil found the axial dispersion coefficient to be unrelated to VRR.

Portillo et al. [24] have examined powder mixing in a continuous paddle blender using lactose and acetaminophen. Operational parameters (process angle and rotation rate), design parameters (number of paddles and paddle angle) and material parameters (particle size) were evaluated for their effect on RTD and relative standard deviation (RSD). RTD and RSD were evaluated by measuring the concentration of acetaminophen at the exit of the blender using NIR. The process angles evaluated were either upward (30°), horizontal (0°) or downward (-30°). Mean residence time decreased with decreasing process angle and RSD increased with decreasing process angle. This agrees with Pernenkil's [4] finding that homogeneity increases with increasing the mean residence time. Two rotation rates, 16 RPM and 78 RPM, were evaluated. Increasing rotation rate decreased mean residence time and increased RSD. The blenders used by Portillo et al. were operated in either a 29 paddle or a 34 paddle configuration. Increasing the number of paddles decreased RSD. Five blade angles were evaluated with 0° , 15° , 45° , 60° and 90° offsets from perpendicular to the central shaft. Portillo et al. found the lowest

RSD and the best mixing performance with the 60° paddle offset. Particle size effects were evaluated using two grades of lactose, one with a mean particle size of 130 μm and another with a mean particle size of 55 μm. This change in particle size did not affect the mixing performance.

The experimental work of Pernenkil [4] and Portillo et al. [24] both demonstrated a number of important particle properties and operating conditions that could effect blend homogeneity in a continuous pharmaceutical powder blender. Using two very different blender designs, these works highlight the potential for continuous blending in the pharmaceutical industry. A comparison of the two blender designs would be worthwhile to guide the further development of continuous pharmaceutical powder blending. Ultimately, these experimental efforts were unable to link changes in particle properties and operating conditions to the mechanisms of mixing that were driving the changes in homogeneity. The review of continuous blending by Pernenkil and Cooney [25] also found an absence of prior work on the mechanisms of mixing for continuous blending of cohesive powders.

2.2 Continuum studies of particle blending

Continuum models ignore the individual particles in a granular material and treat the material as a continuous region or set of regions [26]. Continuum models are based on conservation equations for mass and momentum and constitutive relationships to describe the stress. One of the many challenges of continuum modeling of granular flows is that they can exhibit fluid-like or solid-like behavior depending on the stress environment [27]. In the simple geometry of rolling flow of a non-cohesive material in a rotated drum, Gray [28] was able to create a steady state continuum model that treated the fluid region and the solid rotating region separately. Gray's solution allowed the two regions to interact across a non-material singular

interface and demonstrated qualitative agreement with experimental results using the displacement of colored regions from their initial position. Another successful application of continuum models is their use by Ding et al. [29] to create more meaningful dimensionless parameters that govern granular flow in rotating drums. Ding et al. [30] have used these techniques to create a modified Froude number based on bed turnover frequency that allowed them to align changes in flow regime for sand and titanium dioxide. Ultimately, granular materials are not truly continuous with inhomogeneous behavior down to the particle level [31] and continuum models will always fail to capture these behaviors. This limits their use in studying powder mixing and, in particular, for cohesive powders.

2.3 Compartment model studies of powder blending

Compartment models divide the geometry of interest into compartments where particle movement between compartments is governed by probabilistic fluxes. One advantage of this technique is that it can treat each particle distinctly through a population balance approach [32]. Berthiaux et al. used a 1-D 10 compartment model using axial subdivisions to study a continuous powder blender (Figure 3) [33].

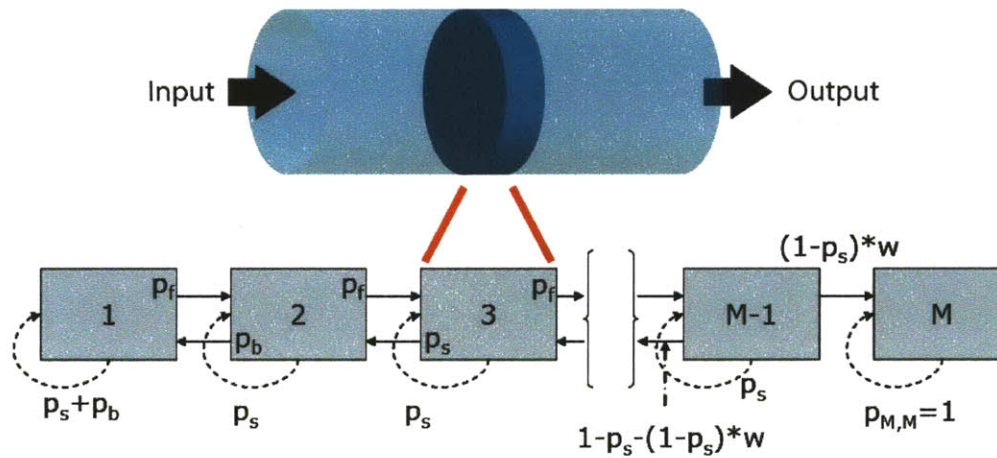


Figure 3: Schematic for a compartment model of a continuous pharmaceutical powder blender using axial subdivisions.

The probabilistic fluxes are the probability of a particle moving forward (P_f) or backward (P_b) respectively in a given time step. Berthiaux et al. made the assumption that each blender compartment has the same probabilistic fluxes as all of the other sections. Particles are contained in a state vector with each compartment represented by a corresponding element of a state vector. A final element of the state vector is an absorbing state and represents the material output from the blender. Berthiaux et al. did not compare their model to experimental result, but did investigate the sensitivity to probabilistic fluxes on residence time distributions and variance reduction ratio. Portillo et al. [34] have applied a similar technique to a batch V-blender by dividing it into a 1-D model of 5 compartments. While it is unclear how Portillo et al. derived the probabilistic fluxes for their V-blender, the model demonstrated reasonable agreement to a previous experimental study by Brone et al. [35]. Portillo et al. [36] subsequently pursued a far more complex compartmental model of a continuous powder blender using both radial and axial subdivisions. The compartmental model had on average similar relative standard deviations to

experimental results at different axial points in the blender, but failed to capture variability observed in the experimental results.

Compartment models are conceptually attractive and have demonstrated that they can be used to model continuous powder blenders. The main challenge in their use is building a reasonable set of compartments for a device's geometry and correctly defining the probabilistic fluxes between compartments.

2.4 Discrete element method studies of powder blending

In the discrete element method (DEM), each particle is treated as a discrete entity where the motion of every particle is tracked and all collisions between particles and between particles and objects are modeled [37]. While DEM was originally developed by Cundall and Strack [38] to study rock mechanics, it has since been used to model a number of industrially relevant granular flows reviewed by Cleary [39] and Ketterhagen et al. [40].

The particles in DEM are soft and are allowed to overlap when collisions occur and may collide with multiple other particles simultaneously. This overlap is used in conjunction with a contact force law to calculate instantaneous forces based on the particle's current position, orientation, velocity and spin. While many contact force laws have been used in discrete element method models, the most common is a linear spring and dashpot [41]. In the linear spring and dashpot force law, the spring provides a repulsive force and the dashpot is used to dissipate a portion of the kinetic energy [42]. The repulsive component of the force law is governed by a spring constant (k); the dissipative component is governed by a damping coefficient (C). The spring constant is chosen to maintain reasonable mean particle overlaps, typically less than 1.0%. The physical results of DEM simulations are not significantly affected by changes in the spring

constant as shown in the work of Silbert et al. [43]. The damping coefficient (C) is determined from the specified coefficient of restitution (ϵ) for each combination of colliding materials in the simulation (Equation 10) [44].

$$C = -2 \frac{\ln(\epsilon)}{\sqrt{\pi^2 + \ln^2(\epsilon)}} \sqrt{k \left(\frac{m_i m_j}{m_i + m_j} \right)}$$

Equation 10: Damping coefficient (C) based on coefficient of restitution (ϵ) and masses (m_i, m_j) of the two colliding particles.

The force law in the normal direction (Equation 11) is defined by a repulsive component (the product of the overlap of the particles (Δx) and spring constant (k)) and a dissipative component (the product of the damping coefficient (C) and the normal component of the relative velocity at the contact point (v_n)).

$$F_n = -k\Delta x + Cv_n$$

Equation 11: Normal force for a DEM model with a linear spring to provide a repulsive force and a dashpot to dissipate a portion of the kinetic energy.

The force law in the tangential direction (Equation 12) is defined by a repulsive component (the integral of the spring constant (k) and the tangential component of the relative velocity at the contact point (v_t)) and a dissipative component (the product of the damping coefficient (C) and the tangential component of the relative velocity at the contact point (v_t)).

$$F_t = \min \left\{ \mu F_n, \int k v_t dt + C v_t \right\}$$

Equation 12: Tangential force for a DEM model with the integral of v_t serving as an incremental spring that stores energy and a dashpot to dissipate energy from the tangential motion.

The tangential force is also subject to the sliding Coulomb friction limit, where μ is the coefficient of friction.

Particles in DEM models are typically represented by spheres in three dimensional simulations [45]. Other shapes are possible as shown in the work of Cleary [46] with super-quadric particles that allow for angularity and varying principle aspect ratios. Three dimensional boundary objects can be created by extruding two dimensional line segments or using triangular finite-element surface meshes. Triangular finite-element surface meshes can be created using commercially available mesh generation software using dimensions imported from a CAD package.

Cohesive forces are often ignored in DEM simulations despite the strong effect they can have on many powders [47]. The relevant cohesive forces, van der Waals forces, electrostatic forces and liquid bridge forces, are reviewed in Zhu et al. [48]. Simple square well potential models for cohesive force in discrete element method models have been successfully implemented by Weber et al. [49], Ngai [50] and Alexander et al. [51]. In a square well potential model, the cohesive force goes to a fixed value whenever the distance between two particles drops below a threshold value. Alexander et al. [51] showed reasonable qualitative agreement between simulations and experiments for Avicel 102 in a rotated drum. Ngai [50] simulated blending in rotated drums for both lactose-caffeine and MCC-caffeine systems with cohesive forces measured using atomic force microscopy (AFM). Ngai's simulations were limited to a

single cohesive force. Domike [52] used a slightly more complex variation on the square well potential model allowing for a randomly sampled distribution of cohesive forces. Like Ngai, Domike also measured cohesive forces using AFM.

Domike [52] and Ngai [50] demonstrated the importance of cohesion in DEM simulation and the accuracy of DEM simulation of pharmaceutical powder flows using AFM measured cohesive forces. Domike's DEM simulations of angle of repose experiments demonstrated good agreement with experimental results for both glass beads (20° experimental and 21° simulation) and MCC (20° experimental and 23° simulation.). Further work by Domike varying the cohesive force for glass beads showed a linear increase in angle of repose with increasing cohesive force. Ngai's DEM simulations showed good qualitative agreement between the models and experimental results for blending in rotated drums. In Ngai's work, the blends with MCC particles had a longer time to homogeneity when compared to the less cohesive lactose particles. Based on Domike's and Ngai's work, the author will use AFM measured cohesive forces as the basis for the cohesion model in the DEM simulations of pharmaceutical powders in continuous blenders. In addition, cohesive force will be studied for its effects on homogeneity in continuous pharmaceutical powder blending.

The previously described contact force model and cohesive models are executed using a simple DEM algorithm consisting of three essential steps [53]:

1. A periodically updated search grid is used to maintain a near-neighbor interaction list for all particle pairs and particle boundary pairs that might participate in a collision in a given period.

2. At each time step, the near-neighbor list is used to identify all collisions that have occurred between particle pairs and particle boundary pairs. For particles that have collided, the forces are evaluated using a contact force model (most commonly, the spring and dashpot model).
3. The collisional forces calculated for each particle in step 2 are summed with cohesive interactions, other interactions and the force of gravity to give net forces. The resulting equations of motion for position (x) (Equation 13), velocity (u) (Equation 14), orientation (θ) (Equation 15) and spin (ω) (Equation 16) are then integrated to give the particle's new position, velocity, orientation and spin in the next time step.

$$\dot{x}_i = u_i$$

Equation 13: Position equation for spherical particle i.

$$\dot{u}_i = \frac{\sum_j F_{i,j} + F_{i,cohesion} + F_{i,other}}{m_i} + g$$

Equation 14: Velocity equation for spherical particle i.

$$\dot{\theta}_i = \omega_i$$

Equation 15: Orientation equation for spherical particle i.

$$\dot{\omega}_i = \frac{\sum_j M_{i,j}}{I_i}$$

Equation 16: Spin equation for spherical particle i with moment of inertia I.

Steps 2 and 3 are repeated sequentially moving the system state forward in time until the search information is no longer valid. Then a new search (step 1) is performed to update the interaction list.

DEM models are very CPU-intensive as shown by Bertrand et al. [45]. Bertrand et al. performed DEM simulations of 8 mm spheres in a tumbling mill rotating at 40 RPM on a single 700 MHz Xeon processor. One revolution of the mill required a CPU time of 3 hours for 10^3 particles, 1.25 days for 10^4 particles and 4 months for 10^6 particles. This makes DEM modeling time consuming for simulations having a large number of particles. For example, assuming a relative density of 0.625, a 1 L volume would have 10^9 100 μm diameter particles [40]. Given the linear scaling between time and particles shown by Bertrand et al., a simulation of this 1 L system would take 342 years. While current processors are four to six times as fast as those used by Bertrand et al., the issue of long computation times remains for many DEM simulations.

DEM has been successfully used to study a number of blending devices (Table 6).

Table 6: References for DEM simulations of various blenders

Blender	References
Bin blender	[56, 61]
V-blender	[55, 58, 59, 60, 65]
Drum blender	[57, 58, 61, 63, 65]
Ribbon blender	[45]
Paddle blender	[45, 54]
Plough share mixer	[46, 65]

Stewart et al. [54] have used DEM to model a high shear blade mixer and have shown good qualitative agreement with experimental measurements using positron emission particle tracking

(PEPT). Bertrand et al. [45] examined both ribbon and blade mixers using DEM models. Bertrand et al. verified their DEM models by comparing outflows of similar particles to the results expected from the Beverloo law in a simulated testing environment. Kuo et al. [55] examined V-blenders using DEM models and PEPT experiments. Arratia et al. [56] used DEM to study particle segregation for different fill fractions in a bin blender. Kwapinska et al. [57] and Finnie et al. [58] simulated drum blender models at different operating conditions using DEM.

One of the methods used to study mixing with DEM is granular temperature which has been used in simulations of rotating drums (Yamane [59]) and V-blenders (Lemieux et al. [60] and Lemieux et al. [61]). Granular temperature is conceptually similar to the thermodynamic temperature for gasses (Equation 17).

$$T = \frac{1}{3} \frac{m}{k_B} \overline{v^2}$$

Equation 17: Thermodynamic temperature (T) for gasses.

In the case of granular temperature, the thermal motion of molecules is replaced by collisions that randomize particle velocities. The sum of these velocity fluctuations is the granular temperature (Equation 18) [62].

$$T = \frac{1}{3} \left(\langle u_x'^2 \rangle + \langle u_y'^2 \rangle + \langle u_z'^2 \rangle \right)$$

Equation 18: Granular temperature (T) for particles.

As velocity fluctuations lead to greater axial and radial dispersion, higher granular temperature indicates an increase in the diffusion of particles [60]. Yamane [59] examined cross sections of granular temperature in DEM simulations of rotated drums. These granular temperature profiles showed a region of high granular temperature near the free surface that is roughly equivalent to the flowing region of the rolling regime. Sherritt et al. [10] demonstrated that powder mixing in rotated drums occurs almost entirely in this flowing region, thus one can use granular temperature to indicate spatially where mixing is occurring in a powder blender. Lemieux et al. [61] were able to relate increased granular temperature to greater homogeneity in DEM simulations of a V-blender operated at two different rotation rates mixing 6 mm and 3 mm spheres. Granular temperature can be useful for identifying the mechanisms of mixing in a blender by giving insight into where mixing is occurring and how this changes with different particle properties, blender designs and operating conditions. Granular temperature can also be used to improve blender design by highlighting the regions of a blender where little mixing is occurring.

Cleary et al. [63] demonstrated a method for tracking centroids as a measure of mixing with DEM models of rotating drums. This method was originally developed by Metcalfe et al. to experimentally measure mixing in a rotating drum [64]. The centroid method defines groups of particles by their initial position and then tracks the motion of these groups' centroids. Initially, all the particles belonging to a group lie in separate regions and the centroid locations are well separated. As the particles mix, the centroids of the different initial position groups move closer to the centroid of all of the particles (Figure 4).

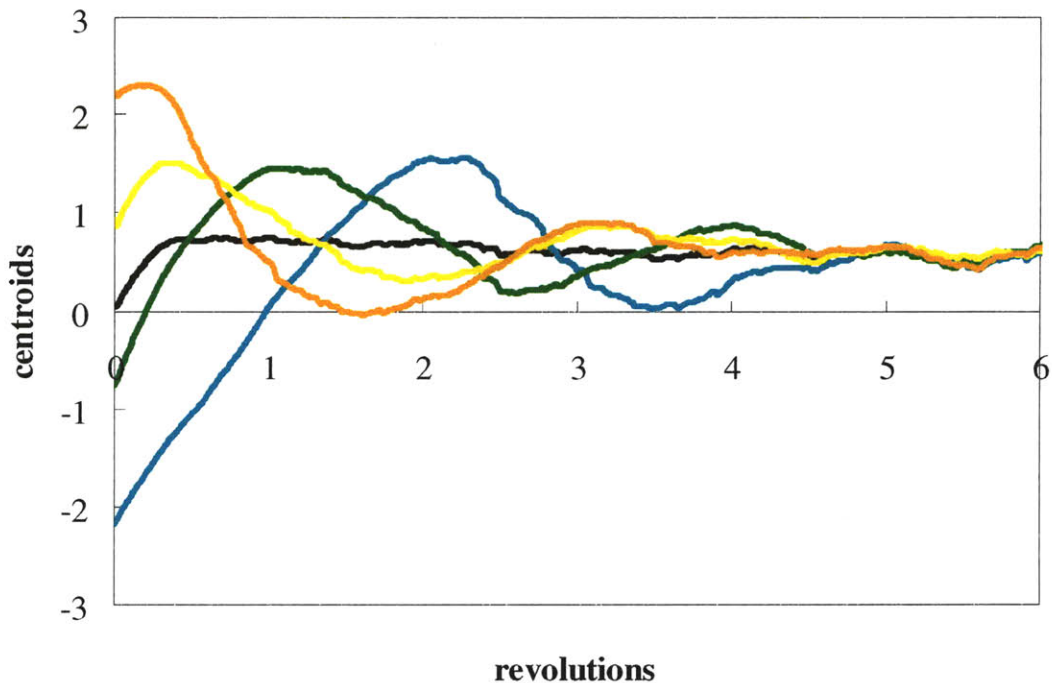


Figure 4: Initial position group centroids converging on the centroid of all of the particles (black line)

If the particles become completely mixed, then all the normalized centroid differences become zero. In rotated tumbling blenders, like the drum blenders used by Metcalfe et al. and Cleary et al., the position of the centroid is observed to be sinusoidal with respect to time with exponentially decaying amplitude. The rate of decay for the centroid can be used to define a rate of mixing or compare homogeneity between different materials, blender designs or operating conditions. Cleary and Sinnott [65] have used the centroid method to study the more complex plough share mixer to assess mixing at different rotation rates. In this plough share mixer, a single chevron shaped blade, the plough, is mounted on a shaft and rotated radially through a bed of particles. The centroid method was able to identify that radial mixing achieved an asymptotic limit depending on the rate of rotation.

Cleary et al. [63] also defined a quantitative mixing measure for use in their DEM simulations of rotating boxes. In this method, a three dimensional grid of cells is constructed over all the particles. Like the centroid method, particles are assigned to groups (designated by integers) based on their initial position. For all particles in a cell, a local average of the group designation is then calculated. These local averages form a probability distribution where the mean, standard deviation, and coefficient of variation (CV) can be calculated. In addition, the ideal limits are calculated for the CV of the fully segregated ($CV_{FullySegregated}$) and fully mixed states ($CV_{CompletelyMixed}$) of the system. The mixing measure is then calculated by Equation 19.

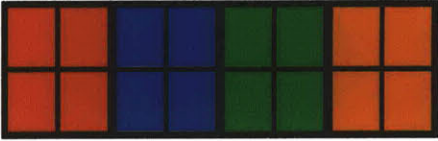
$$Mixing = 100 \times \frac{CV_{FullySegregated} - CV}{CV_{FullySegregated} - CV_{CompletelyMixed}}$$

Equation 19: Quantitative mixing measurement based on coefficient of variation, the fully segregated coefficient of variation and the perfectly mixed coefficient of variation


The mixing measure varies from 0% to 100% and provides a simple quantitative measure to track mixing over time. This can be illustrated for a simple system with 16 particles separated into four initial position groups and examined in four compartments (Figure 5).

Color	Value
Red	0
Blue	1
Green	2
Orange	3

Compartment	Red	Blue	Green	Orange
1	4			
2		4		
3			4	
4				4
Mean	Variance	CV	Mixing	
6	27	0.86	0%	



Compartment	Red	Blue	Green	Orange
1	3	1		
2	1	2	1	
3		1	2	1
4			1	3
Mean	Variance	CV	Mixing	
6	19	0.73	15%	



Compartment	Red	Blue	Green	Orange
1	1	1	1	1
2	1	1	1	1
3	1	1	1	1
4	1	1	1	1
Mean	Variance	CV	Mixing	
6	0	0.00	100%	




Figure 5: Quantitative mixing measure for 4 compartments with 16 particles in 4 initial position groups (red, blue, green, orange)

The quantitative mixing measure is similar to a normalized experimental RSD measurement, but with samples taken for every position within a blender.

Cleary and Sinnott [65] applied the quantitative mixing measure to a V-blender and a plough share mixer and found it useful for determining a rate of mixing. They were able to show that the rate of mixing for the V-blender declined progressively over time indicating that very

long times (greater than 120 revolutions) would be required to achieve a completely mixed state. The plough share mixer was examined at different rotation rates and demonstrated similar behavior, with a progressively declining mixing rate. The decline in mixing rate was also more significant at lower rotation rates.

2.5 Combined models of powder blending

A promising area of future research is the combination of the previously mentioned modeling techniques to create efficient multi-scale models. For example, recent research has seen the use of DEM models to analyze and create simpler correlative models [66].

Another use has been the combination of DEM with compartment models to decrease computational time. This has been demonstrated in the work of Portillo et al. [67] with a combined model of a horizontal drum with an impellor at one end. The blender was axially subdivided with the compartment near the impellor modeled with DEM and the other compartments defined by probabilistic fluxes. The model showed a promising near eight fold reduction in computation time with an average error in the number of particles in the compartments of 8% when compared to a full DEM model of the system.

Rhycroft et al. [68] have achieved some success in using a meso-scale “spot model” where the fundamental unit moves from a particle to a particle and its near neighbors (the so called spot). Kamrin and Bazant [69] developed this spot model into a stochastic flow rule where spots diffuse along slip lines. This theory has been shown to be a potential bridge between continuum models and discrete element method models and holds great potential for future use [70].

2.6 Process system models of downstream pharmaceutical manufacturing

The simulation of downstream manufacturing is essential for designing continuous process systems and quantifying the potential benefits of continuous manufacturing. To truly evaluate different process system designs for continuous downstream manufacturing requires a process model that can predict the quality of the final product. For process systems manufacturing oral solid dosage forms, the product qualities that need to be modeled are the mechanical and pharmacokinetic properties of the tablet and the homogeneity of the powder blend. However, if one makes the simplifying assumption that continuous unit operations can achieve the same product quality as existing batch unit operations, then simple mass and energy balances are sufficient to simulate the process system. Once a process simulation is in place, one can calculate the size and cost of the process equipment and make comparisons to other batch and continuous process designs.

SuperPro [71] is a general sequential process simulation package that has proven effective at simulating mass and energy balances for downstream pharmaceutical processes [72]. SuperPro was originally developed at the Biotechnology Process Engineering Center of the Massachusetts Institute of Technology and includes many of the downstream pharmaceutical manufacturing unit operations. SuperPro is not capable of predicting product quality for downstream process systems, but built in cost and economic models make SuperPro well suited for comparing the costs of different process systems [73].

The prediction of product qualities for fluid process systems is well supported using commercially available flow sheet simulation software, like aspenOne [74]. However, similar commercially available tools are unavailable for the powder processing seen in downstream pharmaceutical manufacturing [75]. Michaels [76] cites a lack of effort studying the meso-scale

properties of powders for this gap between the simulation of fluid process systems and powder process systems. Michaels believes the study of meso-scale properties will allow for the creation of governing mathematical models that connect micro-scale particle properties to macro-scale process behavior. Ng [77] also cites a need for a multiscale approach to simulation of powder process systems. Michaels's [76] and Ng's [77] theories are supported by the successful process simulation of powder unit operations where reasonable mathematical models do exist in the work of Kulikov et al. [78] and Gerstlauer et al. [79]. Kulikov et al. [78] simulated a process system consisting of a connected evaporation, crystallization and hydrocyclone separation system by using more flexible equation based process simulation software, like gProms [80] and Jacobian [81], for certain unit operations. Gerstlauer et al. [79] simulated a leaching and crystallization process using population balance models solved in PARSIVAL. Gerstlauer et al.'s simulation was able to capture the main features of the system's experimentally observed behaviors.

As robust models for predicting blend homogeneity in continuous pharmaceutical powder blending do not exist, the ability to predict product quality in process simulations of downstream pharmaceutical manufacturing are not currently possible. However, elements of the downstream pharmaceutical manufacturing processes have been simulated by Wibowo and Ng [82] and Fung and Ng [83]. Wibowo and Ng created a model tracking population balances of a potash granulation process and Fung and Ng created a model of a vitamin C tablet manufacturing process. Both models contained blending, milling, size classification and granulation steps. The fundamental models governing the unit operations were selected from various literature sources. Unfortunately, neither of these modeling efforts compared their results to experimental data and thus it is impossible to gauge their accuracy.

Given the weak and frequently untested models for many continuous downstream pharmaceutical unit operations, mass and energy balance process models based on process conditions derived from batch manufacturing are the best remaining options. However, these process simulations can still be useful for studying process equipment sizes, costs and basic process designs that allow for the quantification of potential benefits of continuous downstream pharmaceutical manufacturing.

3 THESIS OBJECTIVES

The primary goal of this thesis is to enhance the understanding of continuous pharmaceutical powder blending in pharmaceutical manufacturing. To place this work into the context of pharmaceutical manufacturing, process system models of continuous downstream pharmaceutical manufacturing are also developed.

3.1 Continuous pharmaceutical powder blending objectives

Pernenkil [4] and Portillo et al. [24] demonstrated promising experimental results for continuous pharmaceutical powder blending using a double helical ribbon blender and a paddle blender respectively. Both of these experimental efforts concentrated on macroscopic measurements of homogeneity, such as variance in active pharmaceutical ingredient (API) concentration. In addition, the particle flows were also examined using macroscopic parameters, such as fill weight or residence time distribution. Their experiments were able to correlate the effects of material properties, operating conditions and blender design with the measured homogeneity of pharmaceutical powder blends. However, these experimental efforts were not able to derive the mechanisms of mixing in their respective blenders nor has there been other prior work on the mechanisms of mixing for continuous blending of cohesive powders [25].

This work improves the understanding of mixing mechanisms for two blender designs through discrete element method (DEM) simulations. The DEM simulations create a refined spatial and temporal understanding of the flow behavior and mixing performance of continuous pharmaceutical powder blending. Velocity, granular temperature and volume fraction profiles are used to visualize the structure of particle flow and the mechanisms of mixing. The particle flows

are studied dynamically using mass flow rates measured at different points in the blender. The dynamics of homogeneity are assessed using the centroid method and the quantitative mixing measure defined by Cleary et al. [65].

The effects of material properties, operating conditions and blender design on blend homogeneity, particle flows and mechanisms of mixing are assessed using DEM simulations as illustrated in Figure 6.

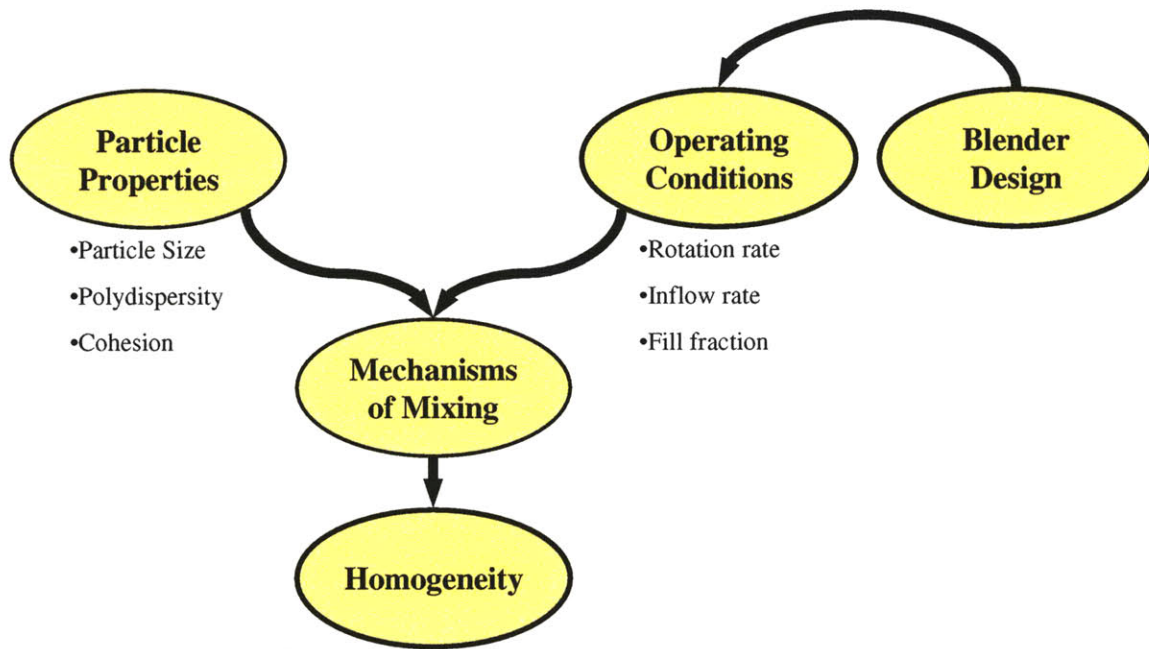


Figure 6: Factors affecting mechanisms of mixing and homogeneity

To study these effects, DEM simulations are performed for five particle sizes, four particle cohesion levels, three rotation rates, five initial fill fractions, three blender sizes and two blender designs to study their effects. These simulations are used to test existing scaling relationships and develop new correlative models for predicting blend homogeneity and flow rates.

3.1.1 Discrete element method simulation of a double helical ribbon blender

The first DEM simulation presented is the double helical ribbon blender described by Pernenkil [4]. This simulation used operating conditions and particles that are similar to those in Pernenkil’s experimental work (Table 7) and is the most accurate representation of the experimental system.

Table 7: Summary of model conditions for DEM simulation of the double helical ribbon blender.

Blender Scale	Shaft	Material	d_{particle} μm	Polydispersity	Cohesion	Ω RPM	Q_{inflow} mg/s	Fill Fraction frac
"1/8"	Ribbon	Lactose/Caffeine	100	Polydisperse	Standard	20	3.5	0.48

This simulation is compared to the experimental results as a means to verify the simulation. The flow behavior and the homogeneity are both qualitatively and quantitatively studied, and conclusions are drawn on the mechanisms of mixing in this blender. This analysis of mixing mechanisms serves as the foundation for the analysis of further simulations which explore the effects of changes in particle properties, blender design and operating conditions on flow behavior and blend homogeneity.

3.1.2 Particle property effects on simulated flow behavior and mixing performance

Particle size has been demonstrated to have an effect on both flow rate and the homogeneity of powder blends. Simulations with three different monodisperse particle sizes were performed (Table 8) to study particle size effects.

Table 8: Summary of model conditions for DEM simulations studying particle size effects.

Blender Scale	Shaft	Material	d_{particle} μm	Polydispersity	Cohesion	Ω <i>RPM</i>	Q_{inflow} <i>mg/s</i>	Fill Fraction <i>frac</i>
-	-	-	-	-	-	-	-	-
"1/8"	Ribbon	Lactose	100	Monodisperse	Standard	20	3.3	0.46
"1/8"	Ribbon	Lactose	200	Monodisperse	Standard	20	3.3	0.46
"1/8"	Ribbon	Lactose	300	Monodisperse	Standard	20	3.3	0.46

Polydispersity was not examined specifically in either Pernenkil’s [4] or Portillo et al.’s [24] previous experimental studies of continuous pharmaceutical powder blending. Two simulations were performed with the same mean particle size, one with monodisperse particles and one with polydisperse particles (Table 9).

Table 9: Summary of model conditions for DEM simulations studying polydispersity effects.

Blender Scale	Shaft	Material	d_{particle} μm	Polydispersity	Cohesion	Ω <i>RPM</i>	Q_{inflow} <i>mg/s</i>	Fill Fraction <i>frac</i>
-	-	-	-	-	-	-	-	-
"1/8"	Ribbon	Lactose	200	Monodisperse	Standard	20	3.3	0.46
"1/8"	Ribbon	Lactose	200	Polydisperse	Standard	20	3.3	0.46

Cohesive force is thought to have an effect on both mass flow rates and mixing performance. To study cohesion effects, four cohesive forces were examined ranging from no cohesive force to a cohesive force 50% greater than the experimentally measured cohesive force for lactose particles (Table 10).

Table 10: Summary of model conditions for DEM simulations studying particle cohesive force effects.

Blender Scale	Shaft	Material	d_{particle} μm	Polydispersity	Cohesion	Ω <i>RPM</i>	Q_{inflow} <i>mg/s</i>	Fill Fraction <i>frac</i>
-	-	-	-	-	-	<i>RPM</i>	<i>mg/s</i>	<i>frac</i>
"1/8"	Ribbon	Lactose	300	Monodisperse	None	20	3.5	0.48
"1/8"	Ribbon	Lactose	300	Monodisperse	Low	20	3.5	0.48
"1/8"	Ribbon	Lactose	300	Monodisperse	Standard	20	3.5	0.48
"1/8"	Ribbon	Lactose	300	Monodisperse	High	20	3.5	0.48

3.1.3 Blender design effects on simulated flow behavior and mixing performance

Blender size has been shown to increase axial dispersion and is an important parameter for the design and implementation of continuous powder blending systems. Three blender sizes were simulated. Each blender is a factor of two larger than the next smallest size (Table 11).

Table 11: Summary of model conditions for DEM simulations studying blender size effects.

Blender Scale	Shaft	Material	d_{particle} μm	Polydispersity	Cohesion	Ω <i>RPM</i>	Q_{inflow} <i>mg/s</i>	Fill Fraction <i>frac</i>
-	-	-	-	-	-	<i>RPM</i>	<i>mg/s</i>	<i>frac</i>
"1/16"	Ribbon	Lactose	200	Monodisperse	Standard	20	0.4	0.46
"1/8"	Ribbon	Lactose	200	Monodisperse	Standard	20	3.3	0.46
"1/4"	Ribbon	Lactose	200	Monodisperse	Standard	20	26.0	0.46

Pernenkil's [4] and Portillo et al.'s [24] experiments used two very different blender designs. The final set of DEM simulations will compare the dynamics of blend homogeneity between a ribbon blender and a paddle blender (Table 12).

Table 12: Summary of model conditions for DEM simulations studying shaft design effects.

Blender Scale	Shaft	Material	d_{particle} μm	Polydispersity	Cohesion	Ω RPM	Q_{inflow} mg/s	Fill Fraction frac
-	-	-	-	-	-	-	-	-
"1/8"	Ribbon	Lactose	300	Monodisperse	Standard	20	3.5	0.48
"1/8"	Paddle	Lactose	300	Monodisperse	Standard	40	3.5	0.48

3.1.4 Operating condition effects on simulated flow behavior and mixing performance

Rotation rate is an easily adjusted operating parameter and can have an effect on both flow rate and homogeneity. Three rotation rates were simulated (Table 13).

Table 13: Summary of model conditions for DEM simulations studying rotation rate effects.

Blender Scale	Shaft	Material	d_{particle} μm	Polydispersity	Cohesion	Ω RPM	Q_{inflow} mg/s	Fill Fraction frac
-	-	-	-	-	-	-	-	-
"1/8"	Ribbon	Lactose	300	Monodisperse	Standard	10	4.3	0.48
"1/8"	Ribbon	Lactose	300	Monodisperse	Standard	20	4.3	0.48
"1/8"	Ribbon	Lactose	300	Monodisperse	Standard	30	4.3	0.48

Fill fraction has been shown to be important to axial dispersion in tumbling blenders. Based on experimental results by Lin, five fill fractions and their corresponding rotation and inflow rates were simulated and examined for flow behavior and mixing performance (Table 14).

Table 14: Summary of model conditions for DEM simulations studying fill fraction effects.

Blender Scale	Shaft	Material	d_{particle} μm	Polydispersity	Cohesion	Ω <i>RPM</i>	Q_{inflow} <i>mg/s</i>	Fill Fraction <i>frac</i>
-	-	-	-	-	-	-	-	-
"1/8"	Ribbon	Lactose	300	Monodisperse	Standard	10	3.3	0.65
"1/8"	Ribbon	Lactose	300	Monodisperse	Standard	10	4.3	0.67
"1/8"	Ribbon	Lactose	300	Monodisperse	Standard	20	4.3	0.53
"1/8"	Ribbon	Lactose	300	Monodisperse	Standard	30	4.3	0.40
"1/8"	Ribbon	Lactose	300	Monodisperse	Standard	30	6.5	0.55

3.2 Continuous downstream pharmaceutical manufacturing process systems objectives

Process models were developed to study different process system designs and to quantify the potential benefits of continuous manufacturing. SuperPro was used to model wet granulation and direct compression processes for a hypothetical drug product for both batch and continuous systems. The batch and continuous process systems were compared based on process equipment sizes, operating costs (OPEX) and capital costs (CAPEX) over a range of process throughputs.

4 METHOD OF APPROACH FOR DISCRETE ELEMENT METHOD SIMULATION

4.1 Blenders

Two blenders were used in the DEM simulations: a double helical ribbon blender and a paddle blender. Both blenders utilized the same shell (Figure 7) designed and described by Pernenkil [4] for use in lab scale continuous blending experiments.

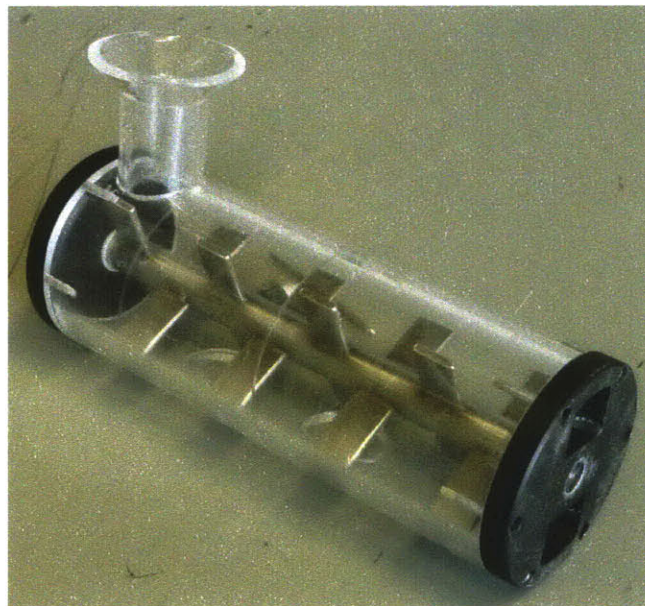


Figure 7: Blender shell.

The shell is a cylinder made from polycarbonate with an internal length of 6” and diameter of 2”. The dimensions of the shell were chosen by Pernenkil [4] to yield a 30 second mean residence time for a fill fraction of 0.50 using lactose particles fed at 5 kg/hr. The blender is fed on the

centerline from a top mounted feed port (Figure 8) and powder exits through two 20 mm by 15 mm exit ports positioned on the centerline above and below the central shaft.

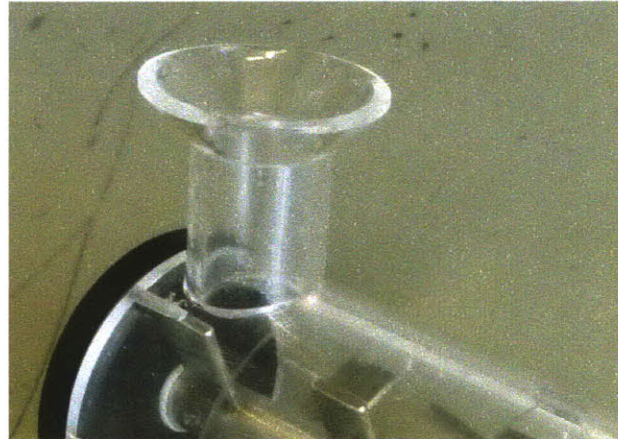


Figure 8: Blender feed port.

The original shaft design by Pernenkil [4] consists of two concentric helical ribbon elements made of a polycarbonate that are mounted on a central shaft (Figure 9).

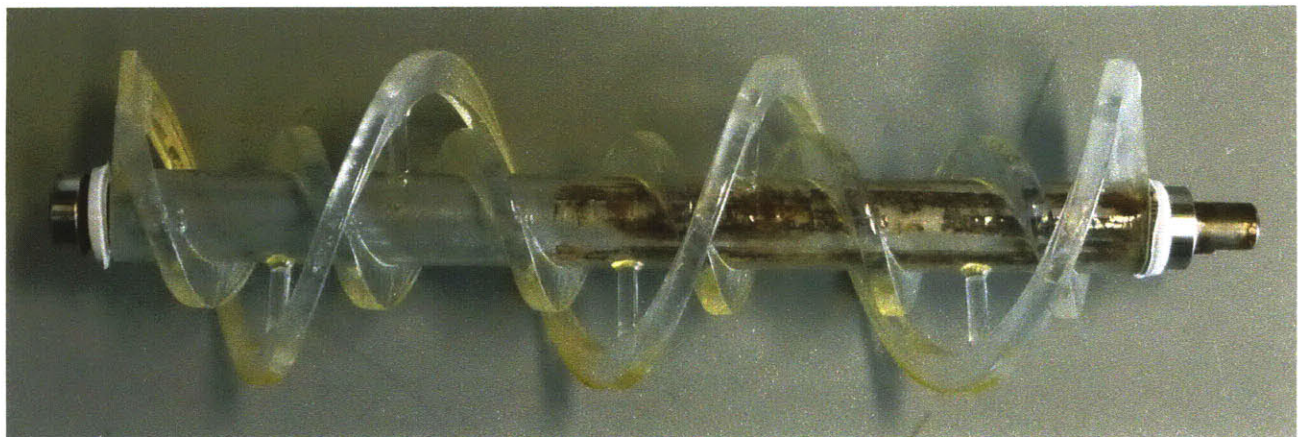


Figure 9: Double helical ribbon shaft.

The outer helix is pitched forward at 63° from horizontal to drive material from the inlet to the outlet and completes three turns over the length of the blender. The inner helix is pitched in the

opposite direction at 106° from horizontal to transport material from the outlet to the inlet and completes six turns over the length of the blender. There is a clearance of 0.5 mm between the outer ribbon and the blender shell and a 5mm clearance between the inner and outer ribbons. The ribbon shaft is designed to be rotated clockwise and has a practical operating range of 10 RPM to 40 RPM.

Paddle blenders have shown their potential for mixing pharmaceutical powders in both laboratory [24] and industrial [84] environments. To evaluate the performance of paddle blenders, the author and Benjamin Lin [85] designed a paddle type shaft to compare with Pernenkil's [4] double helical ribbon shaft. The paddle shaft was designed to use the existing blender shell to facilitate comparison with the double helical ribbon shaft and ensured compatibility with existing experimental feeding and measurement equipment.

The paddle shaft design consisted of choosing the number, shape, position and pitch of the paddles. After examining a paddle blender design by Hosokawa Micron B.V. [84], a configuration was decided on with two paddles offset by 180 degrees with these paddle pairs offset by 90 degrees down the length of the shaft. The paddles thus form a cross pattern when viewed on end (Figure 10).

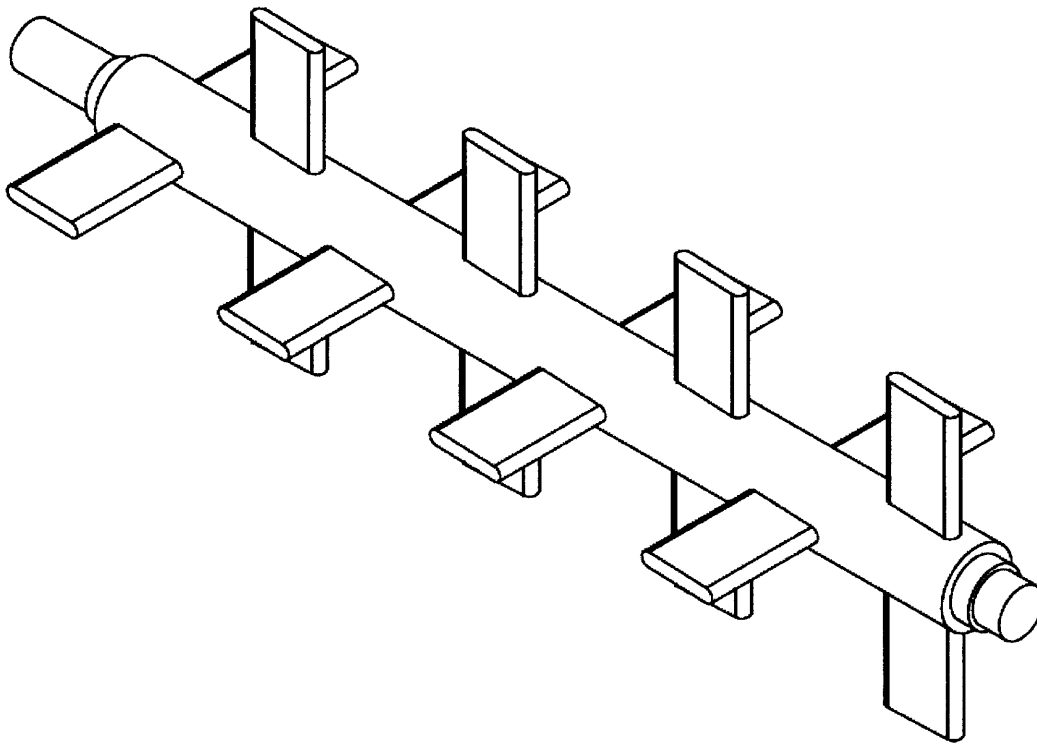


Figure 10: Isometric view of paddle shaft.

While the Hosokawa Micron B.V. design makes good use of reverse and neutrally pitched paddles, it was decided that this paddle blender would have all of its paddles pitched by a moderate 2.5° (Figure 11).

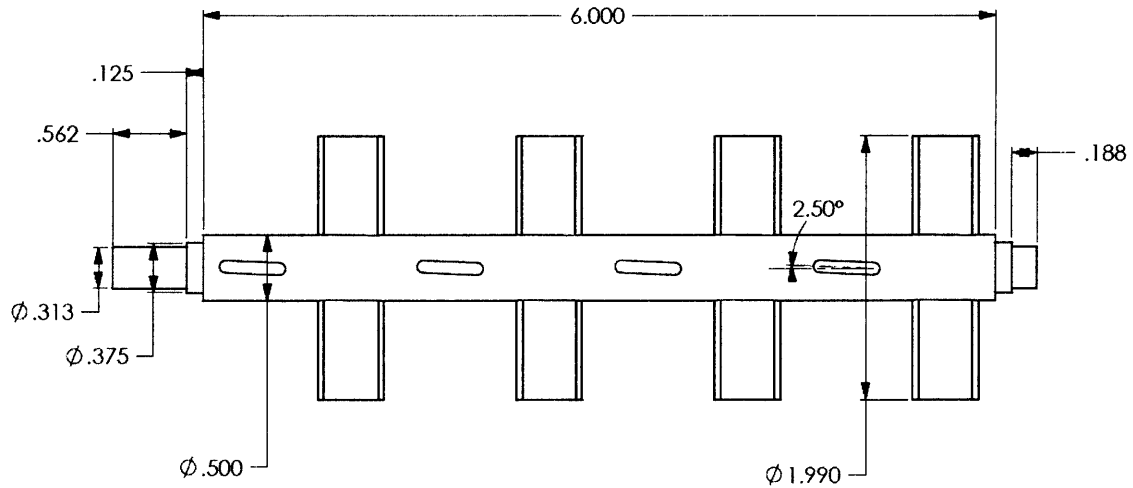


Figure 11: Plan view of paddle shaft with dimensions.

This allows the blender to be run with both forward and reverse pitched blades by simply changing the direction of rotation (clockwise for reverse pitched paddles and counterclockwise for forward pitched paddles). Finally, the paddles were chosen to have a rectangular shape with the same width from the shaft to the tip. This shape was chosen both for ease of manufacturing and for lack of evidence that trapezoidal designs or paddles with standoffs would provide more favorable results [86, 87].

An exit chute was placed below the lower outflow port to catch particles exiting the blender. The chute was angled downward to move particles away from the exit port and thus prevent material building up outside of the outflow ports.

4.2 Materials

To enable comparison to prior experimental work by Pernenkil [4] and ongoing experimental work by Lin [85], the materials used in the simulations were lactose as an excipient and caffeine as an active pharmaceutical ingredient.

4.2.1 Particle parameters

Five types of lactose particles and one type of caffeine particle were used in the DEM simulations (Table 15).

Table 15: Particle properties of simulated materials.

Material	Particle Diameter		Bulk Density
	<i>mean (μm)</i>	<i>standard deviation (μm)</i>	<i>kg/m³</i>
Lactose	100	50	610
Lactose	100	0	610
Lactose	200	29	610
Lactose	200	0	610
Lactose	300	0	610
Caffeine	196	100	530

Direct compressible lactose (DCL) particles based on DMV International's DCL 11 were chosen as the basis for the simulated particles. DCL 11 is a spray dried form of lactose that has relatively consistent spherical particles (Figure 12). The true size of DCL 11 has a mean particle size of 100 μm and is log normally distributed with a standard deviation of 50 μm . The three monodisperse lactose particles were chosen by the author to study the effects of particle size. The

polydisperse 200 μm lactose particles were chosen to study the effects of polydispersity. These particles are distributed uniformly between 150 μm and 250 μm .

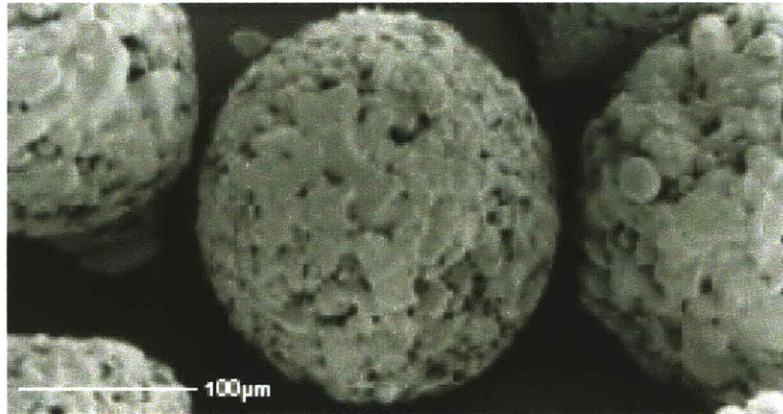


Figure 12: SEM Image of DCL 11 Lactose. [DMV International GmbH. Product group overview. Pharmatose® and DC lactose. Delhi, NY, 2006.]

The simulated caffeine particles were based on UPS grade caffeine obtained from Sigma Aldrich (Figure 13).

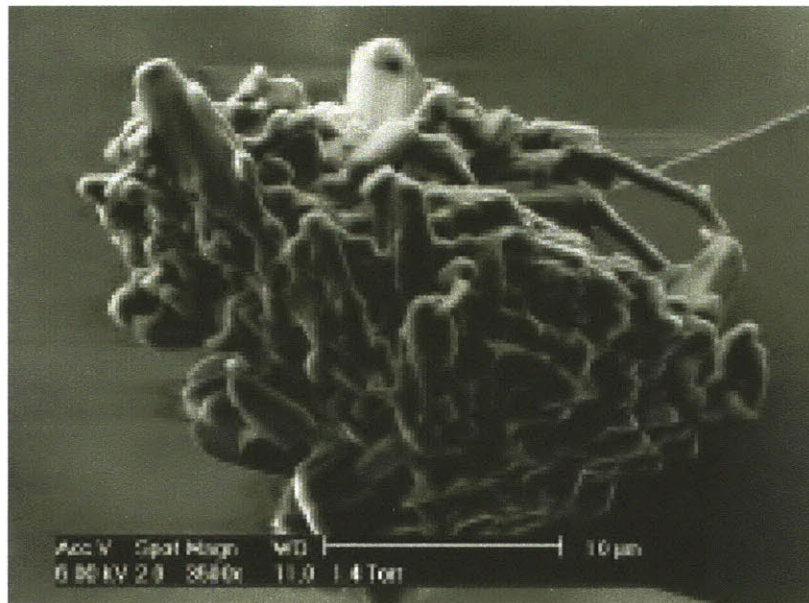


Figure 13: ESEM image of a caffeine particle [S.H. Ngai. Multiscale analysis and simulation of powder blending in pharmaceutical manufacturing. PhD dissertation, Massachusetts Institute of Technology, Department of Chemical Engineering. August 2005.].

The caffeine particles have a mean diameter of 196 μm and are log normally distributed with a standard deviation of 100 μm . All lactose and caffeine particles were modeled as spheres in the DEM simulations.

4.2.2 Particle interaction parameters

The spring constant (k) in the DEM simulation was tuned to yield a mean particle overlap of less than 1.0% and was modified for each particle system (Table 16). A mean particle overlap of less than 1.0% is commonly accepted in the literature [42] as sufficient for accurate DEM simulation.

Table 16: Spring constant (k) in N/m for simulation force law for each particle system.

Material	Particle Diameter		k N/m
	mean (μm)	standard deviation (μm)	
Lactose/Caffeine	100/196	50/100	1.5
Lactose	100	0	1.0
Lactose	200	29	1.5
Lactose	200	0	1.5
Lactose	300	0	2.0

The coefficient of restitution and a friction coefficient were taken from prior work by Domike [52]. Domike found that changing the coefficient of restitution between 0.5 and 0.9 had little effect on the physical behavior of similar particle systems. A coefficient of restitution (ε) of 0.8 was thus deemed appropriate for the author's simulations. Using AFM, Domike measured

a mean friction coefficient (μ) of 0.2 for lactose particles. This was the friction coefficient used in all of the author's simulations.

Cohesive forces were taken from experimental AFM measurements by Ngai [50]. These cohesive forces are unique to material pairs and were found to be dependant on particle size. Ngai normalized the cohesive forces with respect to a reduced radius (Equation 21) using the Johnson-Kendall-Roberts (JKR) contact model (Equation 20) [88] to yield a surface energy (γ [$=$] mJ / m^2).

$$F_{cohesion} = -\frac{3}{2} \gamma \cdot \pi \cdot R$$

Equation 20: JKR contact model relating cohesive force (F) to surface energy (γ) and reduced radius (R).

$$R = \frac{d_a \cdot d_b}{d_a + d_b}$$

Equation 21: Reduced radius (R) for two spheres a and b with diameter d.

The normalized surface energies reduce to a log normal distribution for each pair of materials and thus can be described by a mean surface energy (Table 17) and surface energy standard deviation (Table 18).

Table 17: Mean surface energy (γ) in mJ/m² for cohesive particle interactions [S.H. Ngai. Multiscale analysis and simulation of powder blending in pharmaceutical manufacturing. PhD dissertation, Massachusetts Institute of Technology, Department of Chemical Engineering. August 2005.].

	Caffeine	Lactose
Caffeine	0.43	-
Lactose	0.21	0.53
Polycarbonate	0.07	0.53

Table 18: Surface energy standard deviation (γ) in mJ/m² for cohesive particle interactions [S.H. Ngai. Multiscale analysis and simulation of powder blending in pharmaceutical manufacturing. PhD dissertation, Massachusetts Institute of Technology, Department of Chemical Engineering. August 2005.].

	Caffeine	Lactose
Caffeine	0.32	-
Lactose	0.20	0.41
Polycarbonate	0.06	0.20

When simulated particles get within a threshold distance from each other, a surface energy is sampled from the appropriate log normal distribution. This surface energy and the radii of the two particles are then used to calculate a maximum cohesive force that is applied to the particles in the DEM simulation. This cohesive force is linearly reduced based on the separation of the particles between the threshold distance and the point where the particles contact each other.

4.3 Simulations

4.3.1 Blender objects

Simulation objects (shell, shaft, exit chute) were created for the DEM simulations. These objects were three dimensional triangular meshes created from SolidWorks CAD files using Altair Hypermesh 9.

Simulating either the actual lab scale double helical ribbon or paddle blender used by Pernenkil [4] and Lin [85] in their experiments would require a DEM model with over 100 million particles (Table 19). As shown previously in the work of Bertrand et al. [45], this would require a simulation that would take several years to execute.

Table 19: Approximate particle numbers for linear size reductions in blender scale. Particles have 100 μm diameters with a packing fraction of 0.63.

Blender Size	Use	Blender Diameter (D)	Particle Diameter (d)	Fill Fraction	Particles
-	-	<i>m</i>	μm	<i>frac</i>	<i>number</i>
"Full"	Experiments	0.051	100	0.50	10^8
"1/4"	Simulation	0.013	100	0.50	10^6
"1/8"	Simulation	0.006	100	0.50	10^5
"1/16"	Simulation	0.003	100	0.50	10^4

To create simulations that could be executed and studied in a reasonable amount of time required reducing the number of particles. Reducing the number of particles can be accomplished by either reducing the scale of the blender or increasing the size of the particles. When particle size is increased, it changes the relative strength of cohesive forces to inertial and gravitational forces. Thus to maintain the correct inter-particle physics and decrease the number of particles in the

simulations, the scale of the blender was reduced. Blenders were simulated with “1/4”, “1/8” and “1/16” linear size reductions. The “1/8” size reduction offered the best balance between speed of execution and flexibility of particles that could be simulated.

4.3.2 Blender coordinate system

The simulations use a Cartesian coordinate system to define the position of particles and blender objects. The origin of the coordinates is at the point where the blender shell’s cylinder intersects the center of the inlet port’s cylinder (Figure 14, Figure 15, Figure 16).

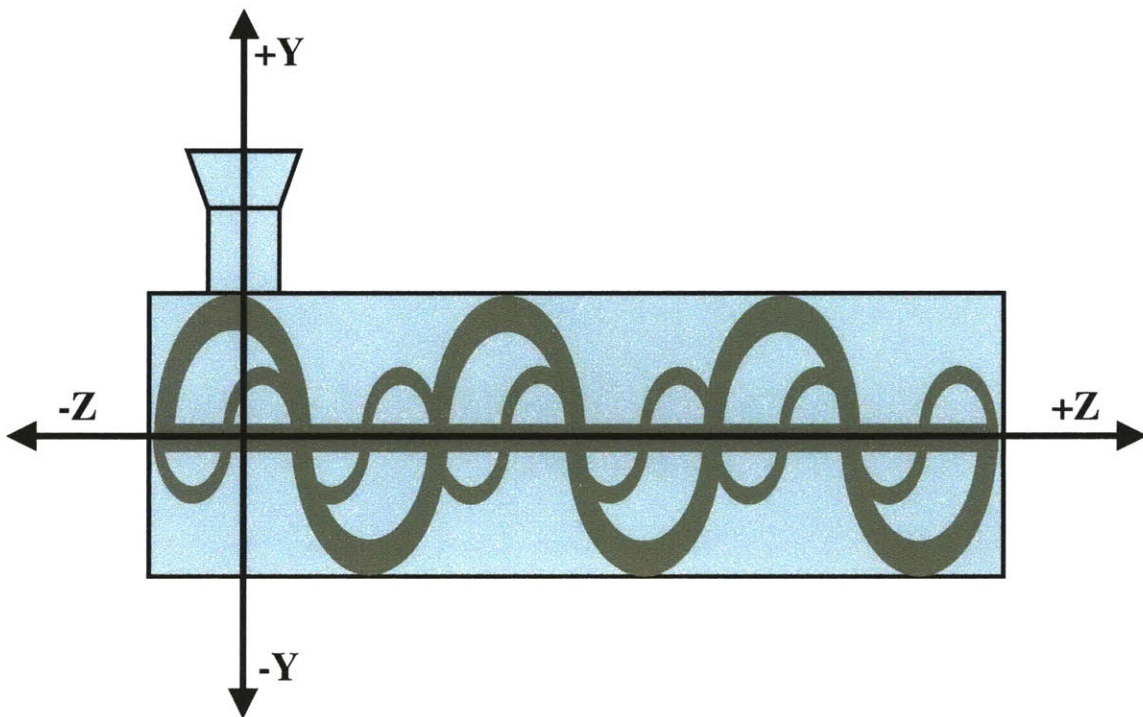


Figure 14: YZ coordinates for blender simulation.

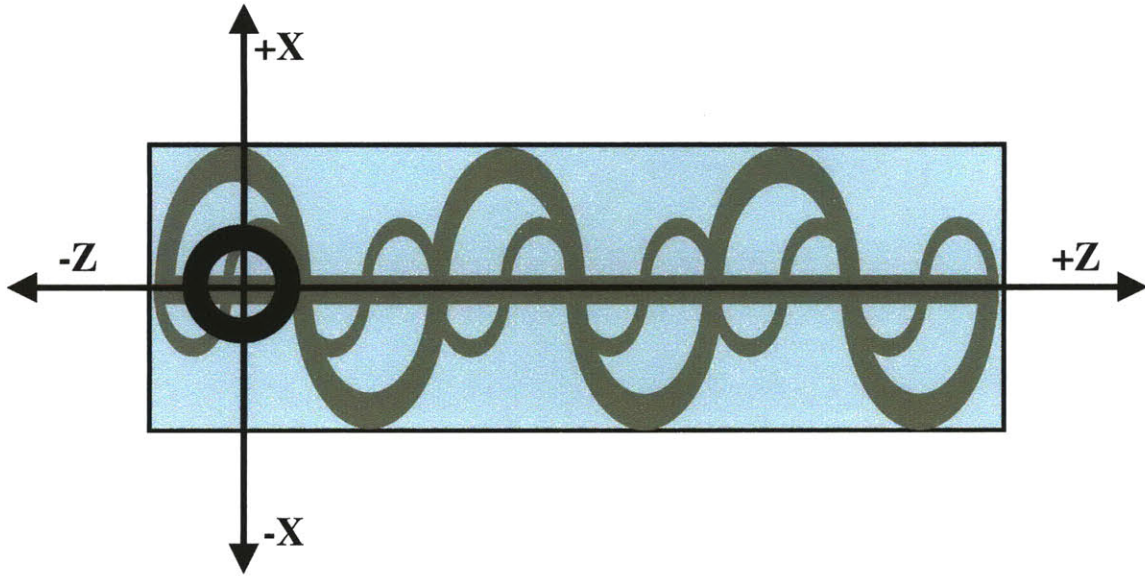


Figure 15: XZ coordinates for blender simulation.

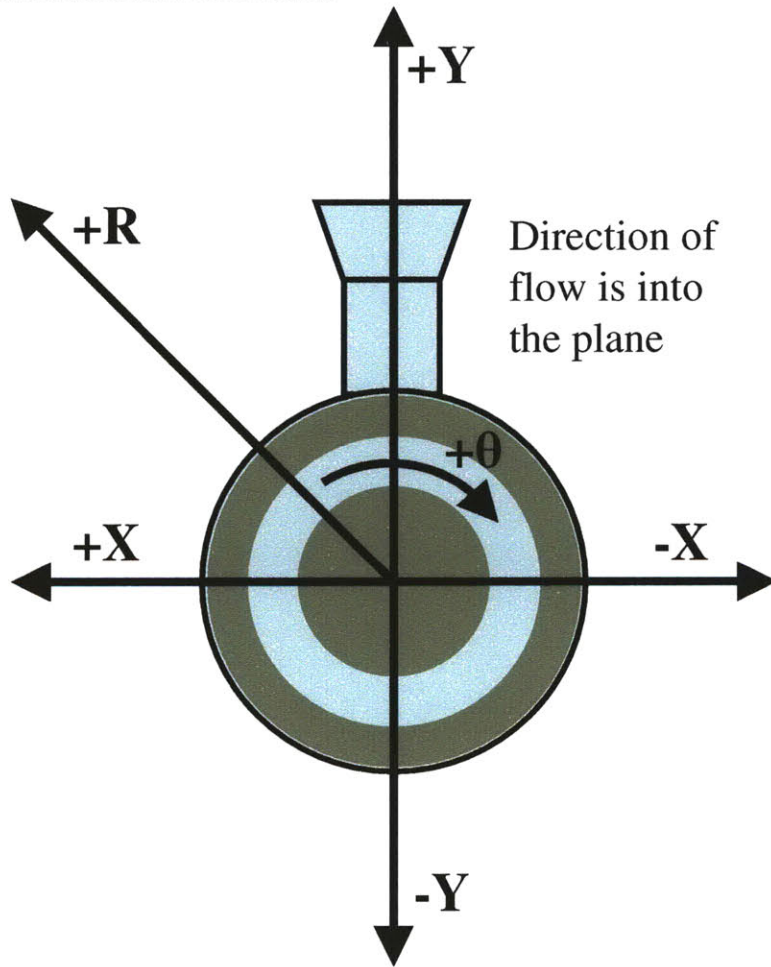


Figure 16: XY coordinates for blender simulation.

The X axis in this system defines the horizontal direction and has an origin at the center of the cylindrical portion of the blender shell. The X axis is normal to both the inflow and blender shaft. The positive X direction is to the left of the origin when the blender is viewed from the inlet to the outlet. The Y axis in this system defines the vertical direction and has an origin at the center of the cylindrical portion of the blender shell. The Y axis is parallel to the inflow and normal to the blender shaft. The positive Y direction is above the origin toward the inlet port when the blender is oriented correctly for operation. The Z axis in this system defines the axial direction and has an origin at the center of the cylinder of the inflow port. The Z axis is normal to the inflow and parallel to the blender shaft. The positive Z direction is the direction of flow from the inlet to the outlet.

4.3.3 Operating conditions

Rotation rates for the ribbon blender were 10, 20 and 30 RPM. The paddle blender used a rotation rate of 40 RPM. These rotation rates were based on ranges used in the experimental works of Pernenkil [4] and Lin [85].

Inflow rates also were based on values used in the experimental works of Pernenkil [4] and Lin [85] and ranged from 6 kg/hr to 12 kg/hr at the experimental/full scale. Simulation flow rates were volumetrically scaled down from the experimental flow rates to match their respective blender sizes.

The blenders were started with a specified mass of particles. This initial fill mass was determined by experimental measurements from Pernenkil [4] or Lin [85] or were chosen by the author to facilitate comparison (Table 20). These experimental or comparison fill masses were volumetrically scaled to match their respective blender sizes for the simulations.

Table 20: Initial fill conditions for blender size, inflow and rotation rate.

Blender Size	Shaft	Ω	Q_{inflow}	Fill Fraction	Fill Mass	Type	Reference
-	-	<i>RPM</i>	<i>mg/s</i>	<i>frac</i>	<i>g</i>	-	-
"1/16"	Ribbon	20	0.4	0.46	0.02	Experimental	Lin [85]
"1/8"	Ribbon	10	3.3	0.65	0.21	Experimental	Lin [85]
"1/8"	Ribbon	10	4.3	0.67	0.22	Experimental	Lin [85]
"1/8"	Ribbon	20	3.3	0.46	0.15	Experimental	Lin [85]
"1/8"	Ribbon	20	3.9	0.48	0.15	Experimental	Pernenkil [6]
"1/8"	Ribbon	20	4.3	0.53	0.18	Experimental	Lin [85]
"1/8"	Ribbon	30	4.3	0.40	0.13	Experimental	Lin [85]
"1/8"	Ribbon	30	6.5	0.55	0.18	Experimental	Lin [85]
"1/4"	Ribbon	20	26.0	0.46	1.16	Experimental	Lin [85]
"1/8"	Ribbon	10	4.3	0.48	0.15	Comparison	-
"1/8"	Ribbon	20	3.5	0.48	0.15	Comparison	-
"1/8"	Ribbon	20	4.3	0.48	0.15	Comparison	-
"1/8"	Ribbon	30	4.3	0.48	0.15	Comparison	-
"1/8"	Paddle	40	3.5	0.48	0.15	Comparison	-

4.3.4 Initialization

For the simulations, two dimensional circular regions were completely filled with randomly distributed particles of the appropriate material and size distribution. These two dimensional particle regions were replicated down the full length of the blender. Particles that intersected with the shaft were then removed. Finally, particles were removed from the top of the blender downwards until the specified fill mass was achieved.

4.3.5 Flow behavior measurements

Velocities, volume fractions and granular temperatures are measured using local spatial averages with a cylindrical grid with 20 cells in the radial direction, 64 cells in the theta direction and 100 cells in the axial direction. The properties are time averaged from the beginning of the simulation until the completion of two revolutions of the blender. Velocities are reported in their cylindrical components (r , θ , Z). Volume fractions are the ratio of volume taken up by particles in the cells to the volume of the cells. Time averaged volume fraction allows one to visualize the average position of particles in the blender. As the volume fraction increases, so does the likelihood that a particle will be in that region at any given time. These properties are presented as cross sections in the XY, XZ or YZ plane. The XY slice is taken at a point equidistant from the blender shell's end caps. The XZ slice was taken at a point equidistant from the top and bottom of the cylindrical portion of the blender shell. The YZ slice was taken at the centerline of the blender equidistant from the edges of the blender shell.

Mass flow rates are collected every 0.1 seconds using two sampling planes (middle and exit) normal to the Z axis (Figure 17). The mass flow rates are net flow rates where material moving forward through the sample plane is assigned a positive mass flow rate and material moving backwards towards the inlet is assigned a negative mass flow rate. Moving averages of the mass flow rates are calculated using an upwind moving average using a 1 blender revolution averaging period.

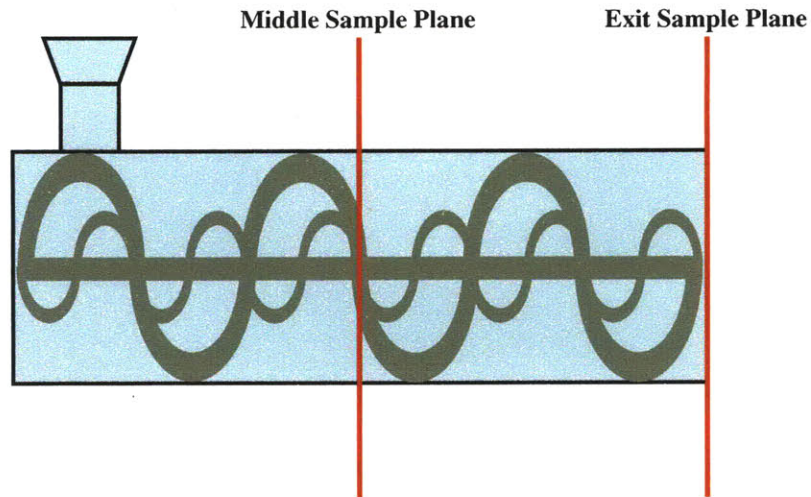


Figure 17: Mass flow rate sample plane positions.

4.3.6 Mixing measurements

Initial position groups for the centroid mixing measurement and the quantitative mixing measure were defined by their initial position in the X (Figure 18), Y (Figure 19), Z (Figure 20) and R (Figure 21) dimension. Every dimension has four groups of equal volume.

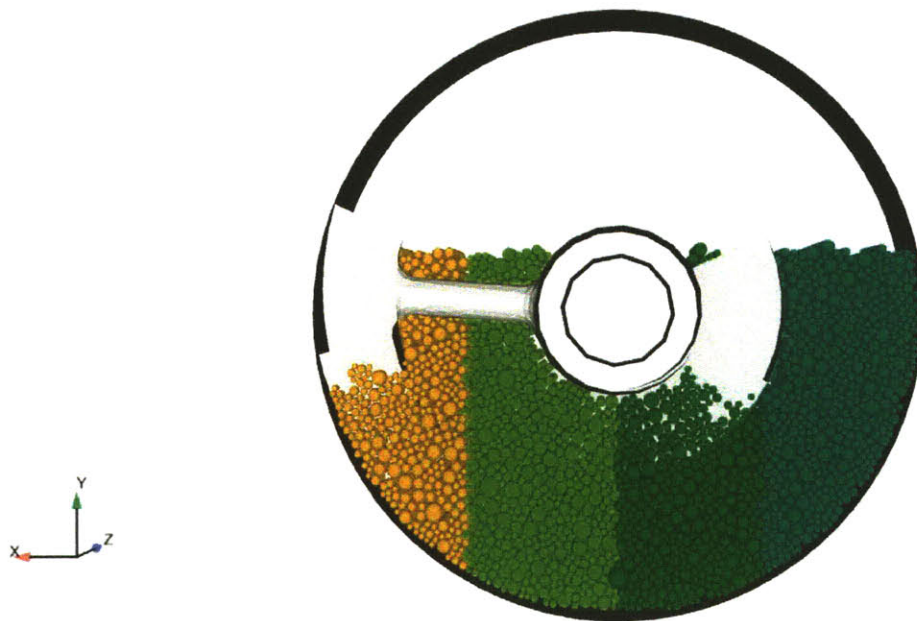


Figure 18: Initial position groups for measurement of mixing in the X direction.

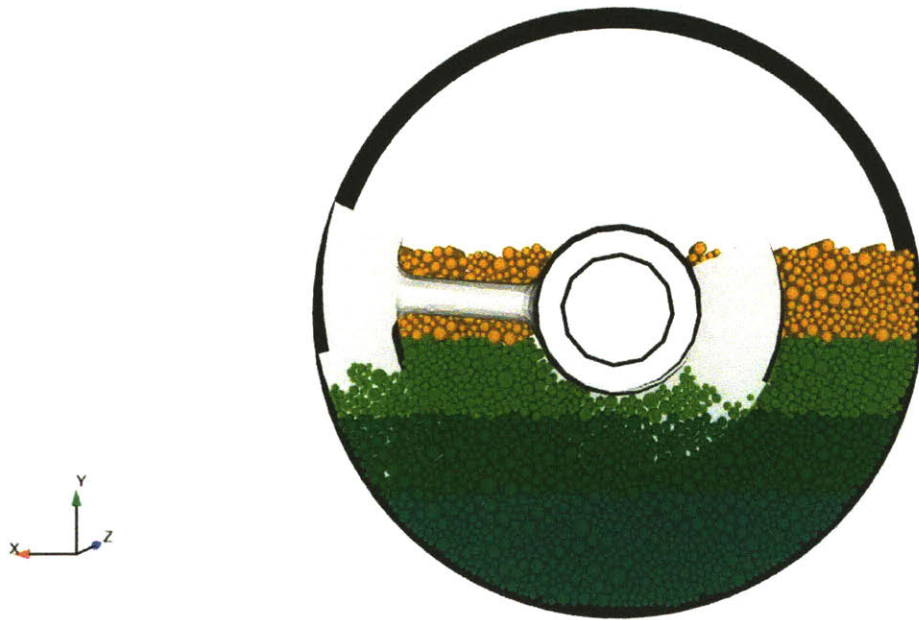


Figure 19: Initial position groups for measurement of mixing in the Y direction.

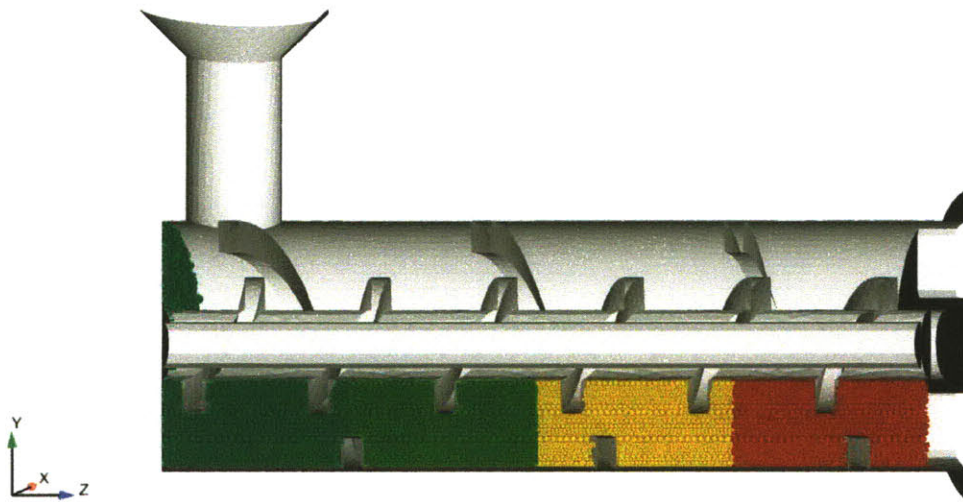


Figure 20: Initial position groups for measurement of mixing in the Z direction.



Figure 21: Initial position groups for measurement of mixing in the R direction.

The centroid mixing measure will be expressed in terms of the actual position of the centroid in the blender simulation's coordinate system. The magnitude of the deviation of the centroids' positions with respect to each other is an indication of the homogeneity of the particles (the lower the deviation, the more homogenous the blend).

For the quantitative mixing measure, the grid of cells for measurement was chosen to have a cell size of five times the mean particle diameter. Using a five particle diameter cell size gives a 95% confidence level that the true local mean is within 10% of the true mean [65]. This balances the need for local accuracy with the need to have sufficient points to create a distribution of local means.

The quantitative mixing measure is a direct measurement of the increase in homogeneity of the blend from its initial conditions. The change in homogeneity is calculated based on the current homogeneity minus the homogeneity at the beginning of the simulation. The quantitative

mixing measure calculates homogeneity as a percentage that indicates the state of homogeneity that the blender is in between the ideal limits of completely mixed and perfectly segregated. The value of the increase in homogeneity is reported as a mixing % and is subsequently referred to simply as homogeneity.

5 DISCRETE ELEMENT METHOD SIMULATION OF A CONTINUOUS DOUBLE HELICAL RIBBON BLENDER

The DEM simulation described in this chapter is used to characterize and better understand the mechanisms and dynamics of mixing in the double helical ribbon blender. This DEM simulation is the most accurate representation presented in this thesis of the continuous double helical ribbon blender studied by Pernenkil [4]. This simulation recreates the true particle properties (size distribution and cohesive forces) and operating conditions for a lactose and caffeine blend in the largest scale (eighth scale reduction of the experimental laboratory blender) feasible at the time of the work. At these operating conditions, the laboratory scale blender was experimentally measured to have variance reduction ratios (VRR) from 177 to 336 and output relative standard deviations (RSD) of 9% to 13% depending on the nature of the input feed variance.

The understanding of mixing mechanisms in the double helical ribbon blender from this simulation will provide the foundation for further simulations studying the effects of particle properties, blender design and operating conditions in subsequent chapters. The continuous double helical ribbon blender employs both convective and diffusive mixing to blend powders. The explicit design of the counter pitched ribbons provides convective mixing in the axial direction, and the tumbling nature of the blender provides diffusive mixing in all directions. The mechanisms of mixing will be studied using: volume fractions, velocity profiles, granular temperature, flow rates, centroid mixing measurements and the quantitative mixing measurement.

5.1 Simulation

The simulation uses a model of operating conditions used by Pernenkil [4] for lactose and caffeine blending and residence time distribution experiments (Table 21).

Table 21: Summary of model conditions for DEM simulation of the double helical ribbon blender.

Blender Scale	Shaft	Material	d_{particle} μm	Polydispersity	Cohesion	Ω RPM	Q_{inflow} mg/s	Fill Fraction frac
"1/8"	Ribbon	Lactose/Caffeine	100	Polydisperse	Standard	20	3.5	0.48

Using a rotation rate of 20 RPM and an inflow of 1.8 g/s, Pernenkil measured a mean residence time of 42 seconds and fill weight of 78 grams.

The simulated blender was linearly reduced in size by one eighth to decrease the scale of the model. This reduction in size yields a DEM simulation with approximately 400,000 particles. At this scale, each revolution of the blender took 7 weeks to compute on a single 3.0 GHz Pentium processor. The simulated inflow rate and fill mass were volumetrically reduced to 3.5 mg/s and 0.15 grams respectively. Rotation rate was maintained at 20 RPM in the simulation.

The particles in the simulation were 90% lactose and 10% caffeine by mass and 98% lactose and 2% caffeine by number of particles. The particle types were randomly distributed throughout the blender. Both the lactose and caffeine particles used their true size distributions in the simulations and had cohesive forces based on experimental measurements.

5.2 Verification

Unfortunately, it was not possible to replicate the homogeneity experiments of Pernenkil [4] using the DEM simulation due to the length of time required to simulate them. However, a viable technique for verifying DEM simulations, as shown in the work of Bertrand et al. [45], is

a comparison of flow rates to experimentally measured results. If the flow rates of the DEM simulation match the experimental results, then the particle flows in the DEM simulation are believed to be behaving in a similar way to the actual system.

Flow rates were not explicitly measured in Pernenkil's [4] experiments at these operating conditions. The experimental blender was operated at steady state and thus, its inflow must equal its outflow on average. As a result, the DEM simulation exit flow rate can be compared to the average volumetrically scaled inflow rate of the experimental blender (Figure 22).

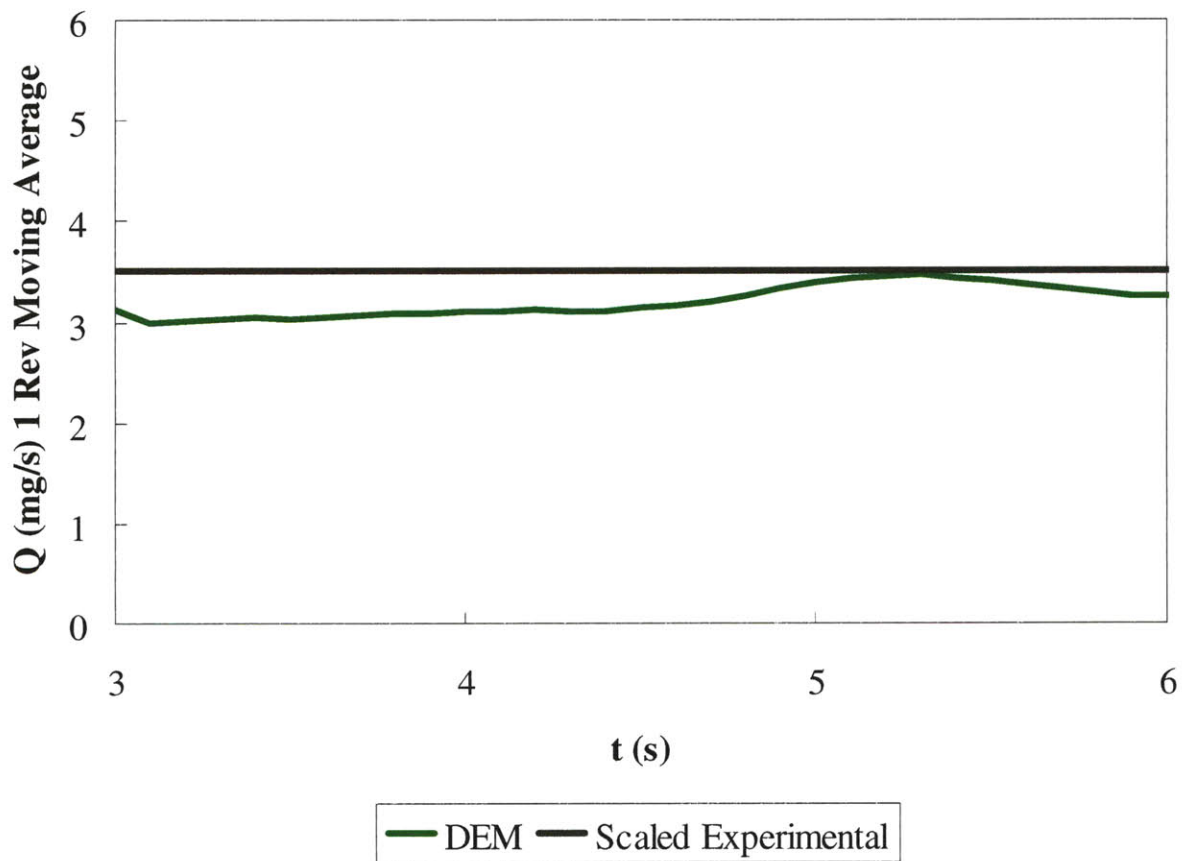


Figure 22: Comparison of 1 revolution moving average exit flow rates (mg/s) for the eighth scale DEM simulation (green) and scaled experiments (black) in the double helical ribbon blender operating at 20 RPM with 0.0035 g/s inflow mixing lactose and caffeine particles.

The DEM simulation slightly underestimated the expected flow rate, but generally demonstrated good agreement with the experimental results. This gives one confidence that the flow behavior results obtained for the eighth scale DEM simulation will be representative of the full scale blender.

5.3 Flow behavior results

Movies and images of the simulation show distinct blocks or wedges of particles fracturing from the main particle bed and sporadically falling over the central shaft of the blender (Figure 23). This indicates that the blender is operating in an avalanching flow regime.

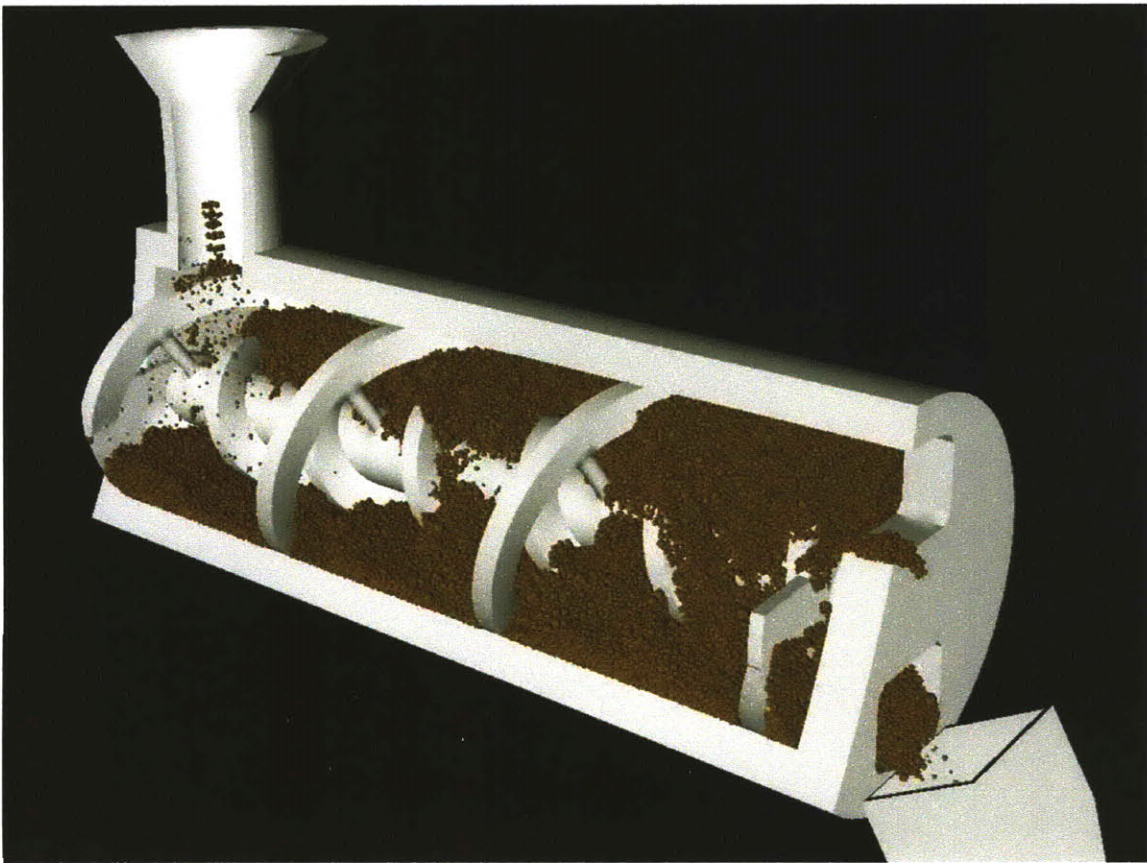


Figure 23: Eighth scale double helical ribbon blender operating at 20 RPM with 0.0035 g/s inflow mixing lactose and caffeine particles.

These wedges of particles are held together by the cohesive interaction between the particles. Unlike drum blenders where the avalanche wedge can fall unimpeded, the wedges in the double helical ribbon blender interact with the central shaft as they fall. This causes the particles to begin their avalanche higher in the blender as the particles have to travel over the shaft before they can fall. In addition, as the particles fall, they are guided by the inner helical ribbon elements which could limit their axial rearrangement. When the particle wedges fall and impact different parts of the blender they break apart and rearrange.

5.3.1 Volume fraction

The XY cross section of volume fraction bears some similarity to that of rotating drums. Like rotating drums, there is a dense particle bed that will be occupied at all times (red/yellow contours in Figure 24). Unlike the rotating drum, this dense particle bed occupies an annular region near the shell of the blender. The particle bed is broken up by the area occupied by the central shaft (black arrow in Figure 24) and a region of lower volume fraction surrounding it (magenta arrow in Figure 24). The volume occupied by the inner helical ribbon decreases the average volume fraction in this region. While the dense particle bed is discontinuous, the two sides of the free surface form a plane that is rotated approximately 30 degrees clockwise from horizontal.

Prior work on drum blenders [10] has shown that diffusive mixing primarily occurs when the particles are avalanching. The area where particles build up before an avalanche (solid black box in Figure 24) and where the particles land after an avalanche (dashed black box in Figure 24) are shown by green contours.

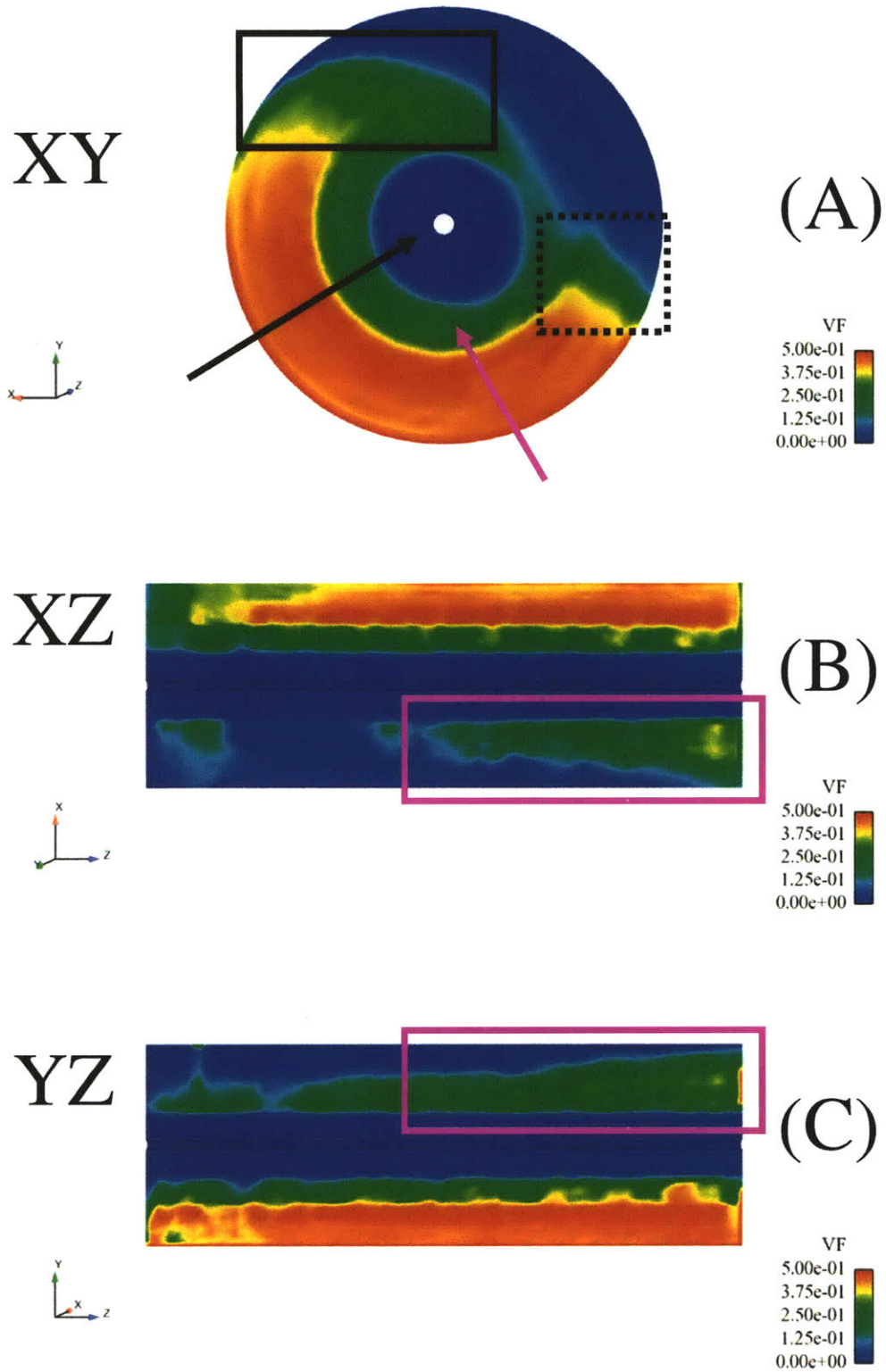


Figure 24: Cross sections showing volume fraction of grid cells of an eighth scale double helical ribbon blender with lactose and caffeine particles operating at 20 RPM with 0.0035 g/s inflow.

The XZ and YZ cross sections show a significant amount of material backing towards the exit of the blender. This is most notable in the positive X direction from the origin in the XZ cross section and in the YZ cross section above the origin (magenta boxes in Figure 24). This creates an uneven distribution of particles in the axial dimension. This will affect the diffusive mixing by significantly changing the length the wedges of particles will travel when they separate from the main particle bed and avalanche. Particles avalanching nearer the inlet will fall much further than particles near the exit and thus will have more time to rearrange. In addition, the particles near the inlet will be traveling at a greater velocity which could allow them to more easily break their cohesive bonds. There is also more material avalanching as one moves towards the exit of the blender as seen in the increasing height of the green contour above the shaft in the YZ cross section.

This accumulation of material towards the exit of the blender will also affect the convective mixing. As the fill fraction increases towards the exit of the blender, more particles will interact with the reverse pitched ribbon. These particles will be transported towards the inlet of the blender until the fill fraction decreases to the point where they can no longer interact with the reverse pitched ribbon and they rejoin the particles being transported toward the exit.

5.3.2 Particle velocities

The XY cross section displays three important regions related to formation and transport of avalanching wedges of particles. The first area (magenta box in Figure 25 A) is a region of negative radial velocity above the shaft. In this area, particles sit above the shaft and settle slightly before they begin their fall. The second region (black box in Figure 25 A) is the area where wedges of avalanching particles are actually falling. These particle wedges are expanding

outward with positive radial velocity. There is a distinct velocity gradient among the falling wedge of particles. This indicates that there will be radial mixing in this region. Finally, there is a small region (dashed black box in Figure 25 A) of negative radial velocity near the blender shell. This shows that some of the avalanching particles are bouncing off of the blender shell which should further enhance radial mixing.

The XZ cross section displays a region (black box in Figure 25 B) of positive radial velocity on the negative X side of the central shaft. Moving towards the inlet of the blender, the magnitude of this positive radial velocity increases. There is a distinct change in the velocity radial profile in from the inlet half to the outlet half of the blender. This change in the radial velocity profile coincides with an increase in volume fraction. In the outlet half of the blender, the fill fraction has increased to an extent that avalanching particles are significantly decelerating at the vertical center of the blender. Due to this decrease in the radial velocity seen in the XZ cross section, the particle wedges will be less likely to fully rearrange and diffusive mixing will be reduced.

The most distinct feature in the YZ cross section of radial velocity is the tendency for particles to compress and shift downwards above the central shaft (magenta box in Figure 25 C). Another interesting feature of the radial velocity is the lack of regions of positive radial velocity below the shaft. This indicates that there is very little material transferred between the forward and reverse flowing regions of the blender in the dense particle bed. Therefore transfer of material between these two regions, which is necessary for effective convective axial mixing, must occur in the avalanching region of the blender.

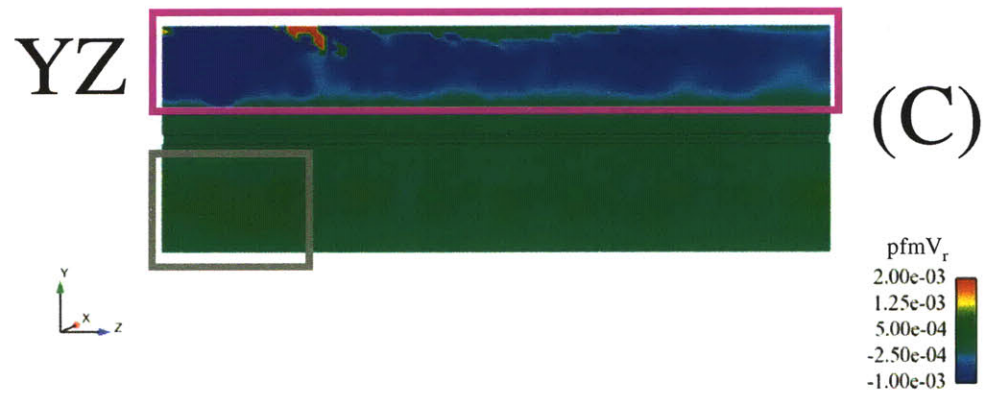
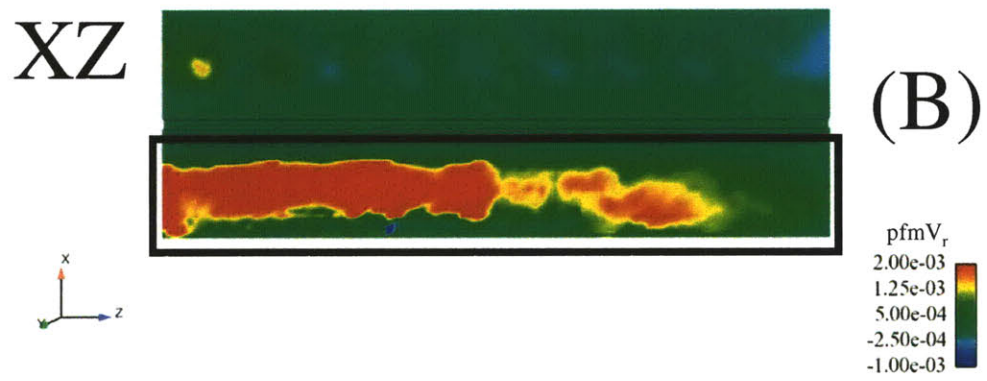
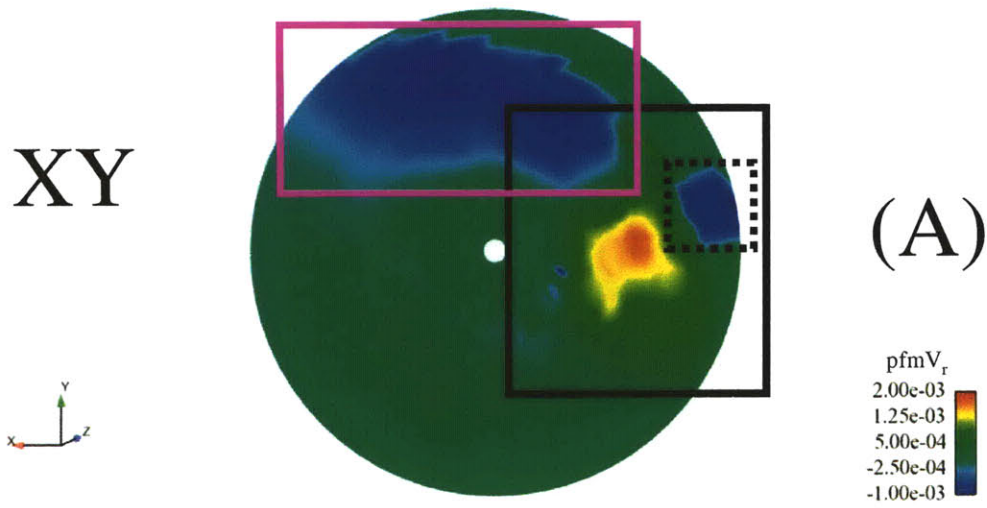


Figure 25: Cross sections of the r component of velocity in m/s for an eighth scale double helical ribbon blender operating at 20 RPM with a 0.0035 g/s inflow mixing lactose and caffeine particles.

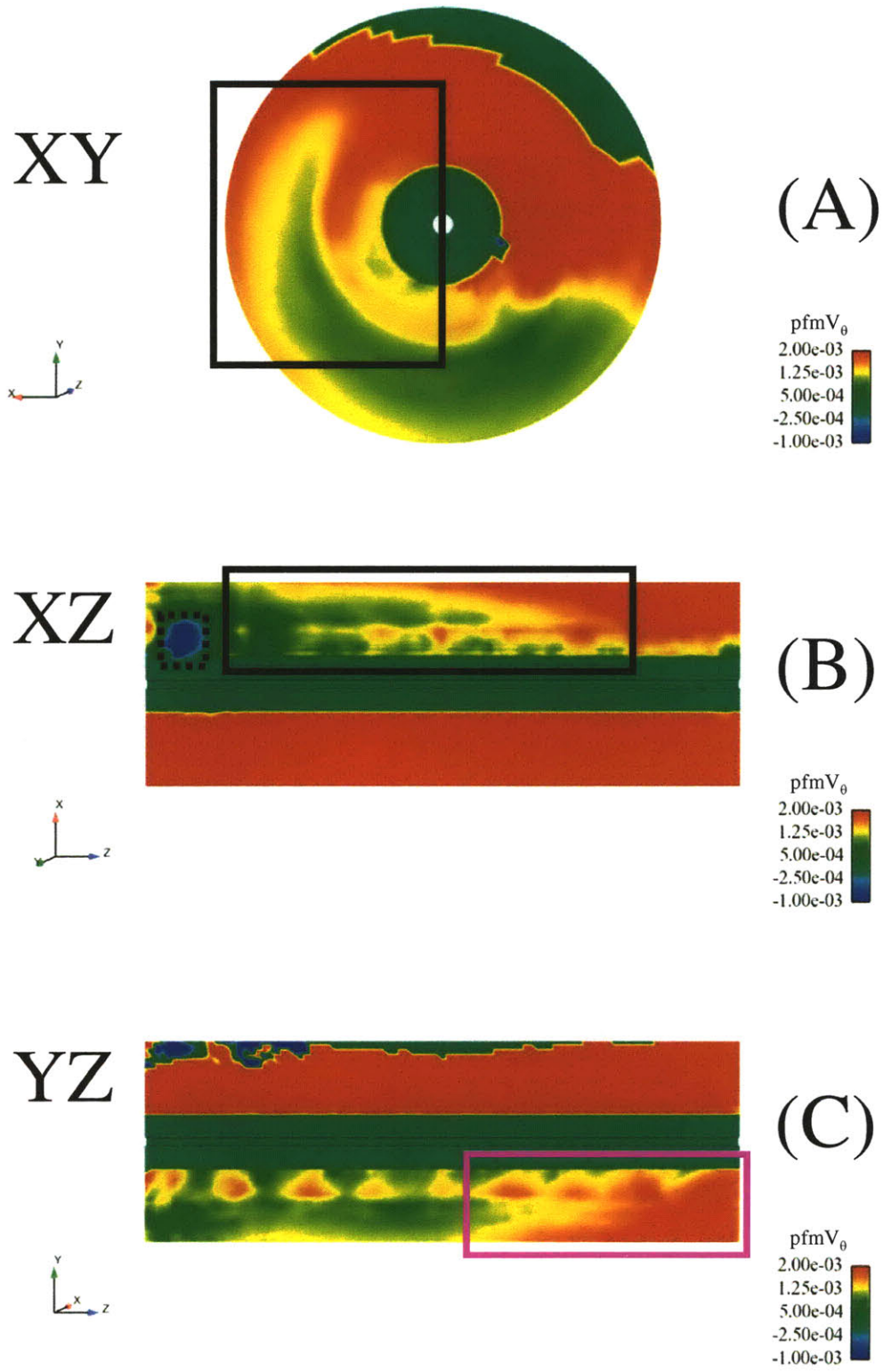


Figure 26: Cross sections showing the theta component of velocity in m/s for an eighth scale double helical ribbon blender operating at 20 RPM with 0.0035 g/s inflow mixing lactose and caffeine particles.

The avalanching particles are clearly visible in the red contour in the XY cross section of V_θ (the linear velocity in the theta direction) above and in the negative X direction from the central shaft (Figure 26 A). Like V_r , this avalanching region has the highest positive V_θ throughout the length of the blender. The most negative area of V_θ cross section is the region below the inlet port (dashed black box in Figure 26 B) where particles are falling into the blender.

The V_θ cross section also shows the interaction of the ribbon blades with the particles (black box in Figure 26 A and B). As both the inner and outer helical ribbons are rotating in the positive theta direction, both ribbons are contributing to regions of higher positive V_θ where they are contacting the particles. The particles between the ribbons form a finger of lower velocity. This lower velocity region between the ribbon blades decreases in width towards the exit of the blender as seen in the XZ cross section. In addition, a wedge of higher V_θ appears in the YZ cross section near the exit of the blender (magenta box in Figure 26 C). Both of these results are caused by the increasing fill fraction and density of materials near the exit of the blender. Unlike V_r , V_θ appears to be positively correlated to regions of higher particle density.

Regions of positive and negative V_z are the main contributors to convective axial mixing. The XY cross section clearly shows a forward flowing region of positive V_z (yellow contour in Figure 27 A) and a reverse flowing region of negative V_z (dark blue contour in Figure 27 A). These positive and negative V_z regions are driven by the outer helical ribbon and the inner helical ribbon respectively and are only present in the lower half of the blender (Figure 27 C). Axial transport is limited to the dense particle bed where random particle motion is limited. There is also a very clear transition region of essentially zero V_z between the two positive and negative velocity regions.

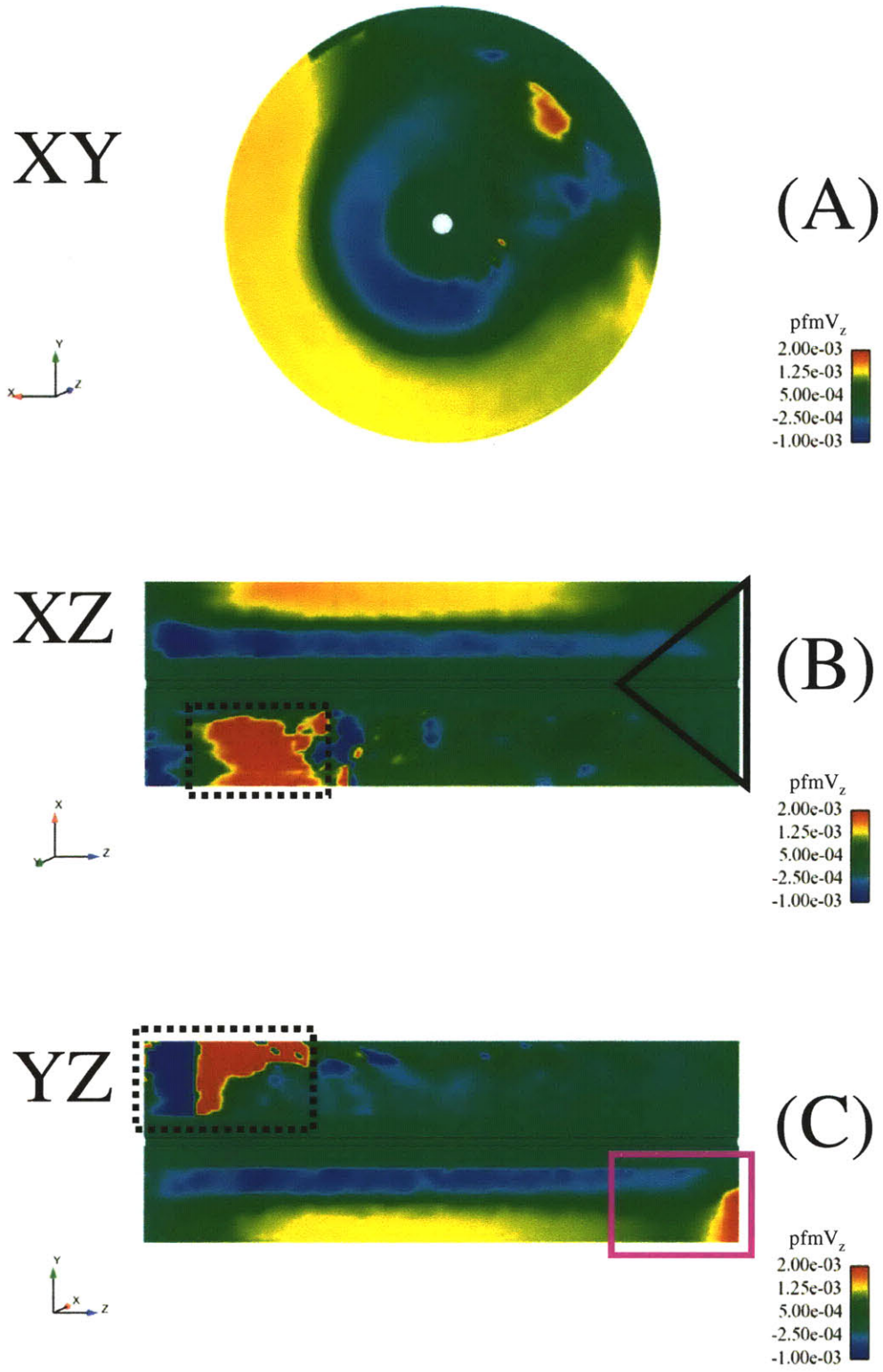


Figure 27: Cross sections showing the Z component of velocity in m/s for an eighth scale double helical ribbon blender operating at 20 RPM with 0.0035 g/s inflow mixing lactose and caffeine particles.

The magnitude and area of the negative velocity regions are not constant along the length of the blender. In the XZ cross section there is a decrease in velocity magnitude for the reverse flowing region on the positive X side of the central shaft moving towards the exit of the blender. The cross sections of V_θ indicate that the denser particle regions near the outlet improve transport by the ribbon blades in the theta direction. One would expect the opposite V_z profile for the reverse flowing region near the shaft as material would move from the denser exit region to the less dense inlet region. Despite material building up on the negative X side of the central shaft near the exit of the blender, there is no indication in the XZ cross section of V_z that any of the material is being transported backwards in the blender. This indicates that the reverse pitched inner ribbon blade is only effective at transporting particles in the dense particle bed.

The XZ cross section shows a conically shaped region (black triangle in Figure 27 B) near the exit of the blender with near zero average V_z . This low velocity region is caused by particles being forced up against the flat end plate and not having room to travel further axially. While one might expect to see particles circulating inwards towards the shaft and the reverse flowing region, the V_r cross section (Figure 25 B and C) indicates that this does not happen. Instead, animations of the flow show the outer ribbon rotating and sweeping across the end plate. When the last sixth of the angled outer ribbon sweeps across the end plate, it collects groups of particles and forces them out of the exit ports. This wiping effect moves the particles in the theta direction to the exit port (Figure 26 B and C) and prevents material from stagnating in this outflow region.

The YZ cross section shows that particles in the forward flowing region at the bottom of the blender move at a relatively constant velocity for much of the length of the blender, however, this changes near the exit of the blender (magenta box in Figure 27 C). Particles begin to slow in

the last 10% of the blender before reaccelerating in the last 5% as they exit the blender. When the particles are slowing in the axial direction, they are moving more in the theta direction. Finally, in the last 5% of the length of the blender there is a region of high, positive V_z caused by the exit port. This high velocity region near the outlet also seems to pinch out the reverse flowing region driven by the inner helical ribbon.

5.3.3 Granular temperature

The regions of high granular temperature should indicate where diffusive mixing is occurring in the blender. In the XY cross section (black box in Figure 28 A), the region of highest granular temperature coincides with the region where the particles are avalanching. This area also coincides with the area of peak radial velocity and includes a hot spot where the avalanching particles are bouncing off of the shell of the blender. These impacts are important to creating diffusive mixing in the blender as the cohesive particle wedges need to be broken apart for diffusive mixing to occur. In the XZ cross section, the region of highest granular temperature is in the negative X half of the blender and in the first half axially (magenta box in Figure 28 B) and corresponds to the avalanching region. In the avalanching region, particles are transported over the central shaft and fall down towards the bottom of the blender. There is also a region of no granular temperature at the center of the blender in the XZ cross section (Figure 28 B) that corresponds to the central shaft where no particles exist.

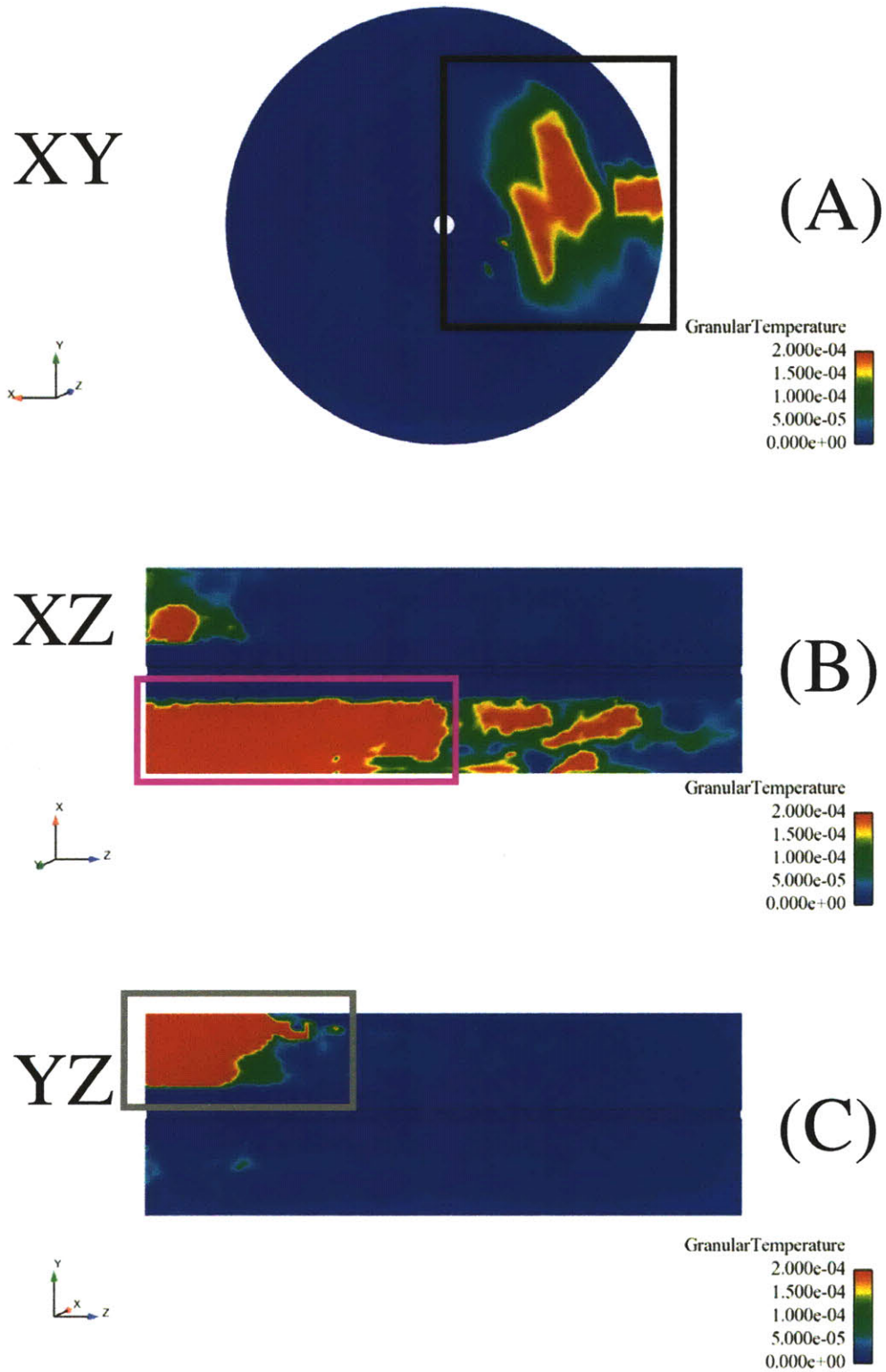


Figure 28: Cross sections showing granular temperature for an eighth scale double helical ribbon blender operating at 20 RPM with 0.0035 g/s inflow mixing lactose and caffeine particles.

When compared to the XZ cross section of volume fraction (Figure 24 B), the regions of highest granular temperature correspond to the regions of lowest volume fraction. As the volume fraction increases towards the outlet of the blender, the mobility of the particles is reduced leading to decreasing and more erratic granular temperature. This also implies that maintaining a more consistent fill fraction along the length of the blender would better utilize its volume for diffusive mixing.

The YZ cross section also shows a region of high granular temperature where the particles from the inlet are falling into the blender (grey box in Figure 28 C). It is noteworthy that this region is neither symmetrical nor perfectly coincident with the high velocity region as the high granular temperature is maintained up to the inflow side end cap. This is most likely caused by particles that are falling down the inlet bouncing off the end cap, the helical ribbons and the central shaft which impart more random motion.

Another interesting area in the YZ cross section (Figure 28 C) is a set of faint light blue granular temperature contours below the centerline. The edge of the inner ribbon blade is impacting particles and causing some diffusive mixing. However, the diffusive mixing in this region is not nearly as significant as within the avalanching region.

5.3.4 Flow rate

The flow rates reported here are for the net flux of particles passing through a plane at either the middle axial point or at the exit of the blender. The flow rate at both the middle and exit of the blender is periodic (Figure 29) with the expected 3 second period that corresponds to the 20 RPM shaft rotation rate. The flow in the middle of the blender is sinusoidal in shape.

Initially there is a roughly symmetric rise and decline with amplitude of 1.6 mg/s, but this ultimately declines after two revolutions of the blender as material migrates towards the exit.

The flow at the exit decreases to almost zero at times and exhibits a different shape than the flow in the middle with a gradual rise and then a rapid decline. The flow at the exit also has greater amplitude of 3 mg/s. Movies of the outflow show that the outer helical ribbon wiping across the end plate drives almost all of the flow of material out of the blender.

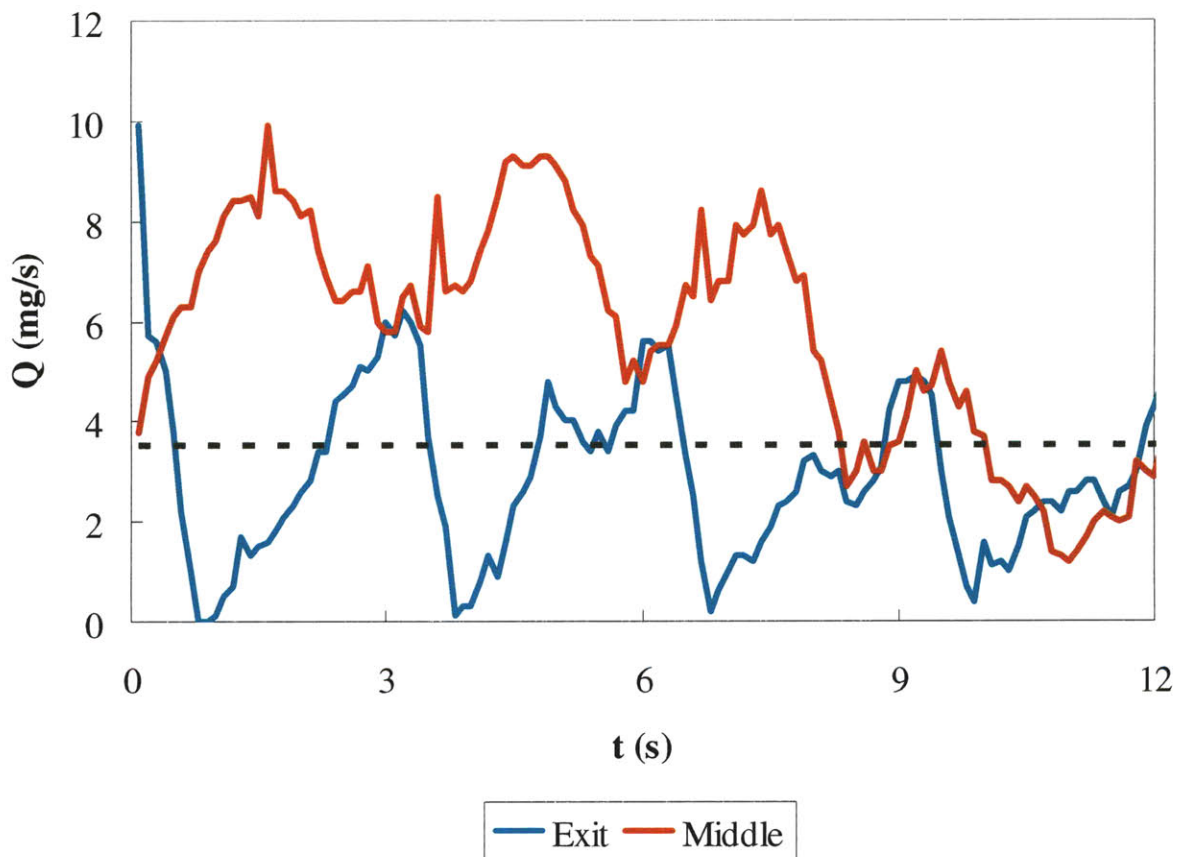


Figure 29: Instantaneous flow rate in the direction of flow for the middle and exit of an eighth scale double helical ribbon blender with lactose and caffeine particles operating at 20 RPM with 0.0035 g/s inflow.

Taking a 1 revolution (3 second) moving average of the flow rates (Figure 30) removes the periodic nature of the flow and gives a better indication of the average throughput at various

points in the blender. Initially, the exit flow rate is relatively constant, but after 2.5 revolutions a slight decline is observed. This may be caused by an increase in mean bond strength between the particles (Figure 31). The mean bond strength is the average cohesive force currently acting on a particle in the DEM simulation. As the simulation progresses, there is a pronounced rise in the mean bond strength indicating that more particles are participating in multiple cohesive interactions and increasing the effective cohesive force.

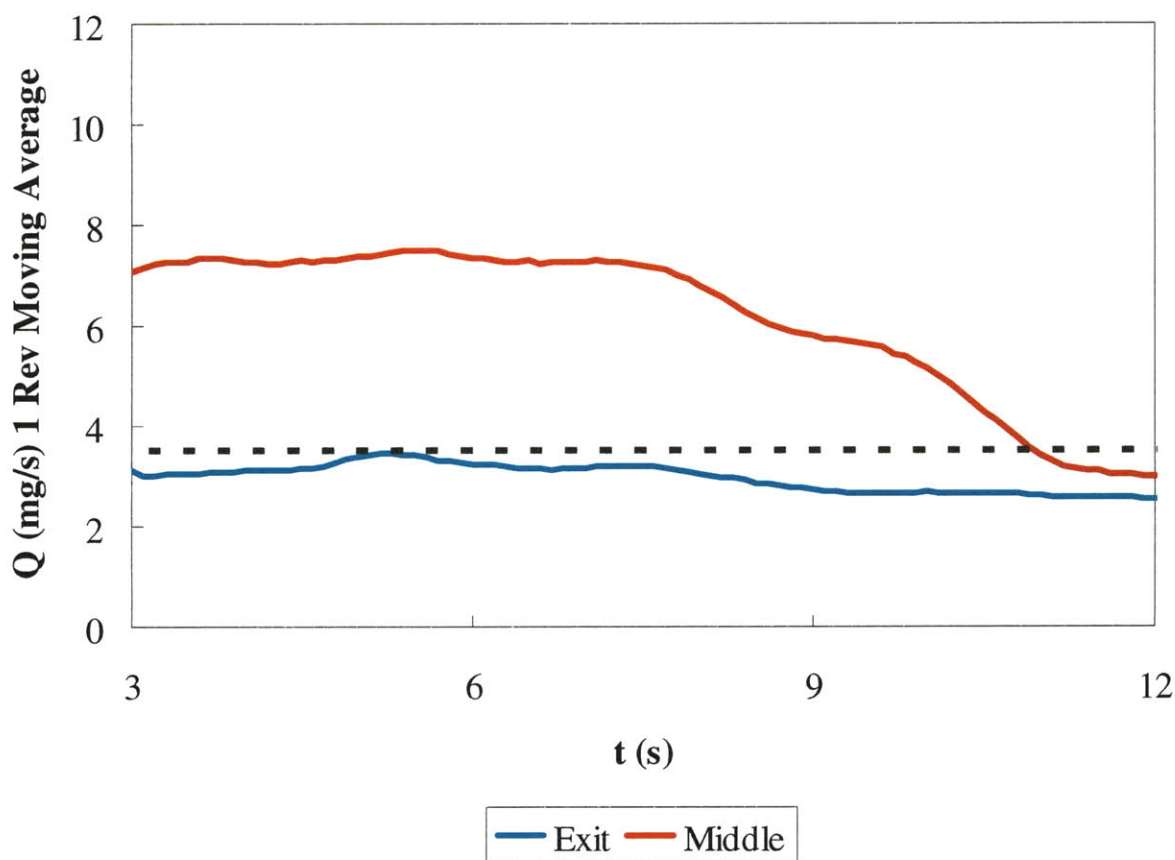


Figure 30: 1 revolution moving average flow rate in the direction of flow for the middle and exit of an eighth scale double helical ribbon blender with lactose and caffeine particles operating at 20 RPM with 0.0035 g/s inflow.

The flow rate in the middle of the blender is initially significantly greater than the flow rate at the exit, but ultimately is equal to the exit flow rate after three revolutions. This is a result

of the particles' initial position in the blender as they are evenly distributed in the axial direction when the simulation starts with a flat free surface. The true steady state free surface is much more complex and the material in the middle of the blender must migrate towards the exit.

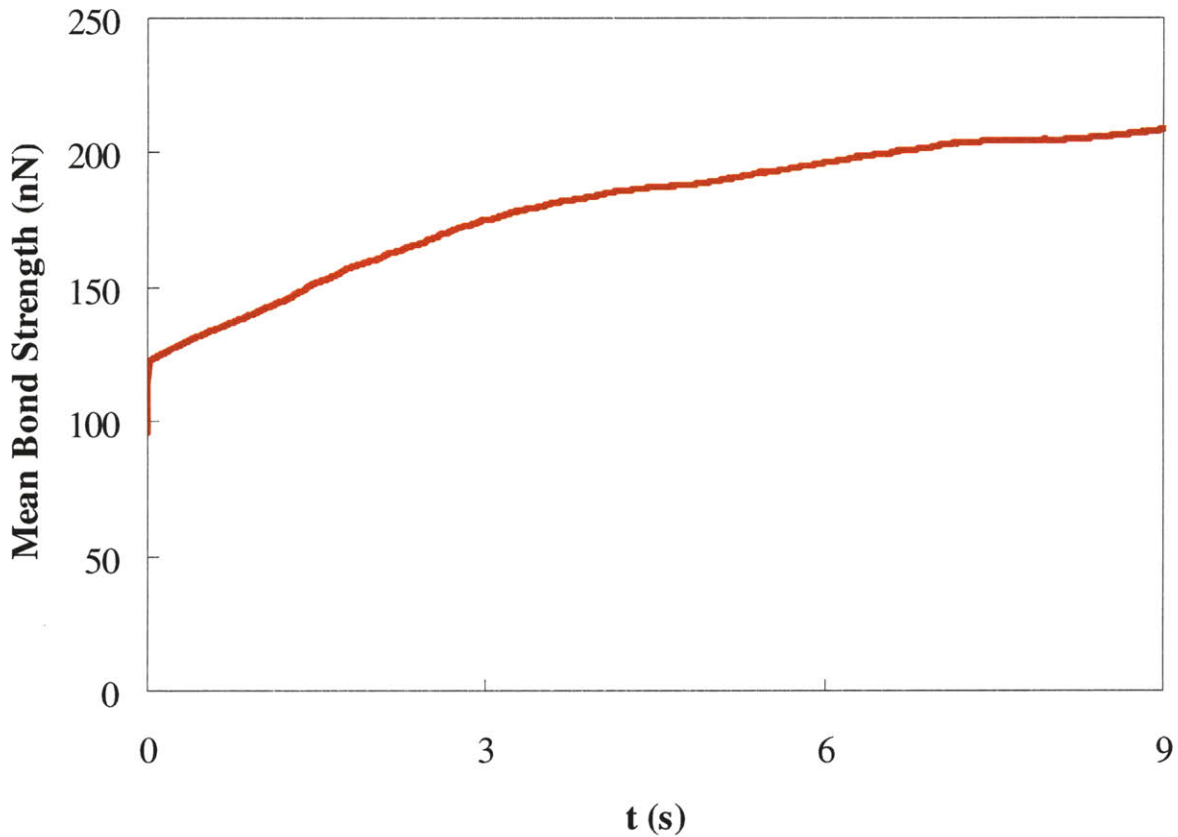


Figure 31: Mean particle to particle or particle to object bond strength in nN for an eighth scale double helical ribbon blender with lactose and caffeine particles operating at 20 RPM with 0.0035 g/s inflow.

5.4 Mixing results

5.4.1 Centroid

To visualize the movement of particles, it is useful to assign them to groups based on their initial position and then follow them as they are mixed. This can be accomplished both

quantitatively and qualitatively. Quantitatively, the movements of the initial position groups' centroids are presented with respect to their most relevant dimension (X for X initial position groups, Y for Y initial position groups, Z for Z initial position groups and R for R initial position groups). If the particles are mixing, the centroid positions of the different groups should ultimately converge to a single position. Qualitatively, the initial position groups will be distinctly colored and cutaway images of the particles' positions will be presented at the start of the simulation and then after 1 and 2 revolutions. Initially, all four groups will be presented simultaneously and then subsequently as an image of each individual initial position group. The images of individual groups are useful as it often becomes difficult to identify the extent of motion of individual groups after even a small amount of mixing. For images of either all of the groups or individual groups, mixing will be demonstrated by the particles becoming more homogeneously spread throughout the blender.

The amplitude of the centroids' oscillation for the X groups (Figure 32) is decaying over time. This decay in the periodic oscillation of the centroid indicates that mixing is occurring in the X direction. The centroids of the X groups converge for the first 3 revolutions of the blender and then do not converge further. After these 3 revolutions, the blender is not completely mixed. This indicates that most of the mixing is accomplished in the first 3 revolutions and the subsequent 14 revolutions that the average particle will spend in the blender adds little to the blend's homogeneity.

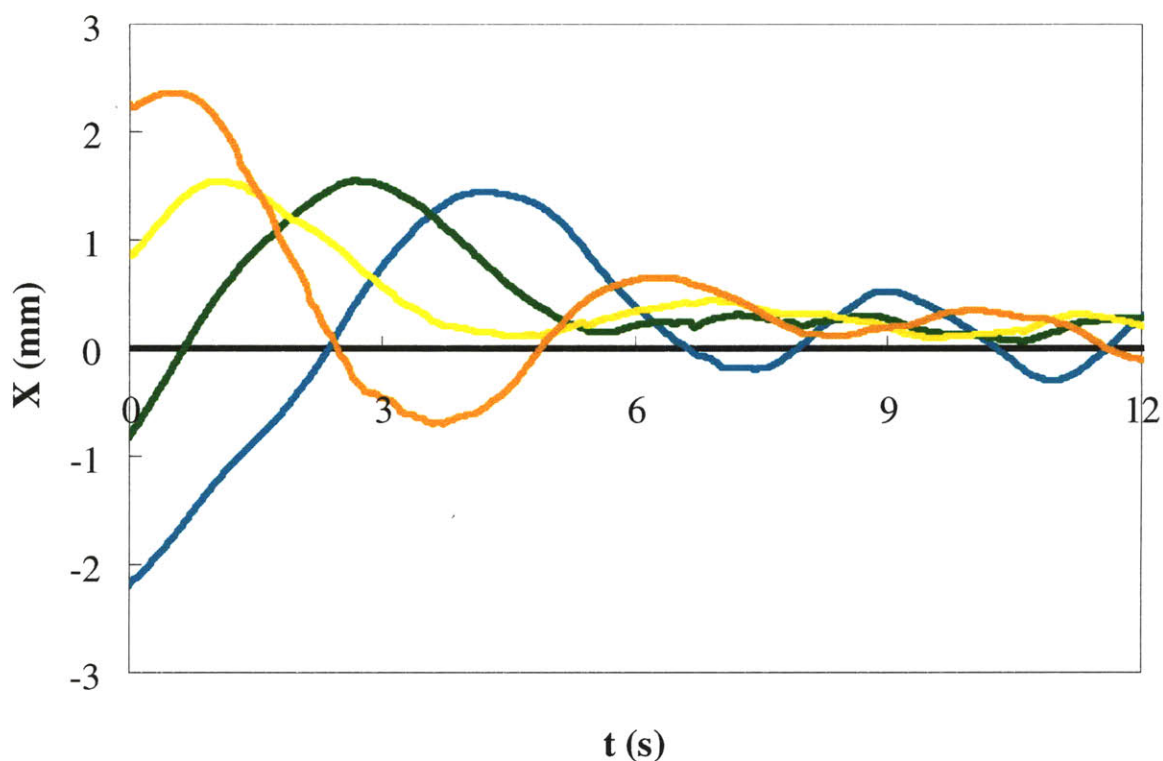


Figure 32: Centroids of X dimension initial positions (blue = 1, green = 2, yellow = 3, orange = 4) in the X direction in an eighth scale double helical ribbon blender with lactose and caffeine particles operating at 20 RPM with 0.0035 g/s inflow.

The period of the particle motions decreases in duration as the simulation progresses. Many of the groups' centroids' movements demonstrate an initial period of 6 seconds. This is readily apparent in the path of Group 1's centroid (blue line in Figure 32). It takes Group 1 over 6 seconds to complete its initial periodic path through the blender, but subsequent periods take only 3 seconds. This indicates that it takes 1 to 2 revolutions for the rotational particle flows to develop a consistent pattern.

One can also see the X particle groups mixing in the XY cutaways over the first two revolutions of the blender (Figure 33). After the first revolution of the blender, the initial position groups still form very distinct and separate regions albeit with less uniform borders than in their

initial positions. This is particularly evident for Group 1 and 2 (black boxes in Figure 34 and Figure 35). However, some of the particle groups that have begun to avalanche at the first revolution (Group 3 and Group 4) are showing signs of mixing between themselves (magenta boxes in Figure 36 and Figure 37).

When 2 full revolutions of the blender are completed, there is strong visual evidence of mixing for some of the initial position groups. Group 3's particles (Figure 36 Rev 2) are becoming widely dispersed in the X dimension. The shape of Group 3's particle group bears little resemblance to their initial shape. Group 2 (Figure 35 Rev 2) and Group 4 (Figure 37 Rev 2) are not as widely dispersed after 2 revolutions with particles in their respective groups predominantly still in close proximity. Despite this, Group 2 and Group 4 are wider than they were initially and are beginning to overlap with neighboring groups. Finally, the particles in Group 1 (dashed black box in Figure 34) have remained in much of the same arrangement after 2 revolutions of the blender.

These observations reinforce the earlier conclusion that much of the particle mixing is happening when the particles are avalanching. Group 3 and 4 are the first groups to avalanche, whereas Group 1 is the last. At both 1 and 2 revolutions, Groups 3 and 4 are more homogeneously dispersed than Group 1 in both the radial and theta direction. Material initially closer to the central shaft (Group 3) also appears to be mixing more rapidly than material closer to the blender shell (Group 4).

Groups 1 to 4



Figure 33: XY cutaway with X dimension initial positions (blue = 1, green = 2, yellow = 3, orange = 4) in an eighth scale double helical ribbon blender with lactose and caffeine particles operating at 20 RPM with 0.0035 g/s inflow.

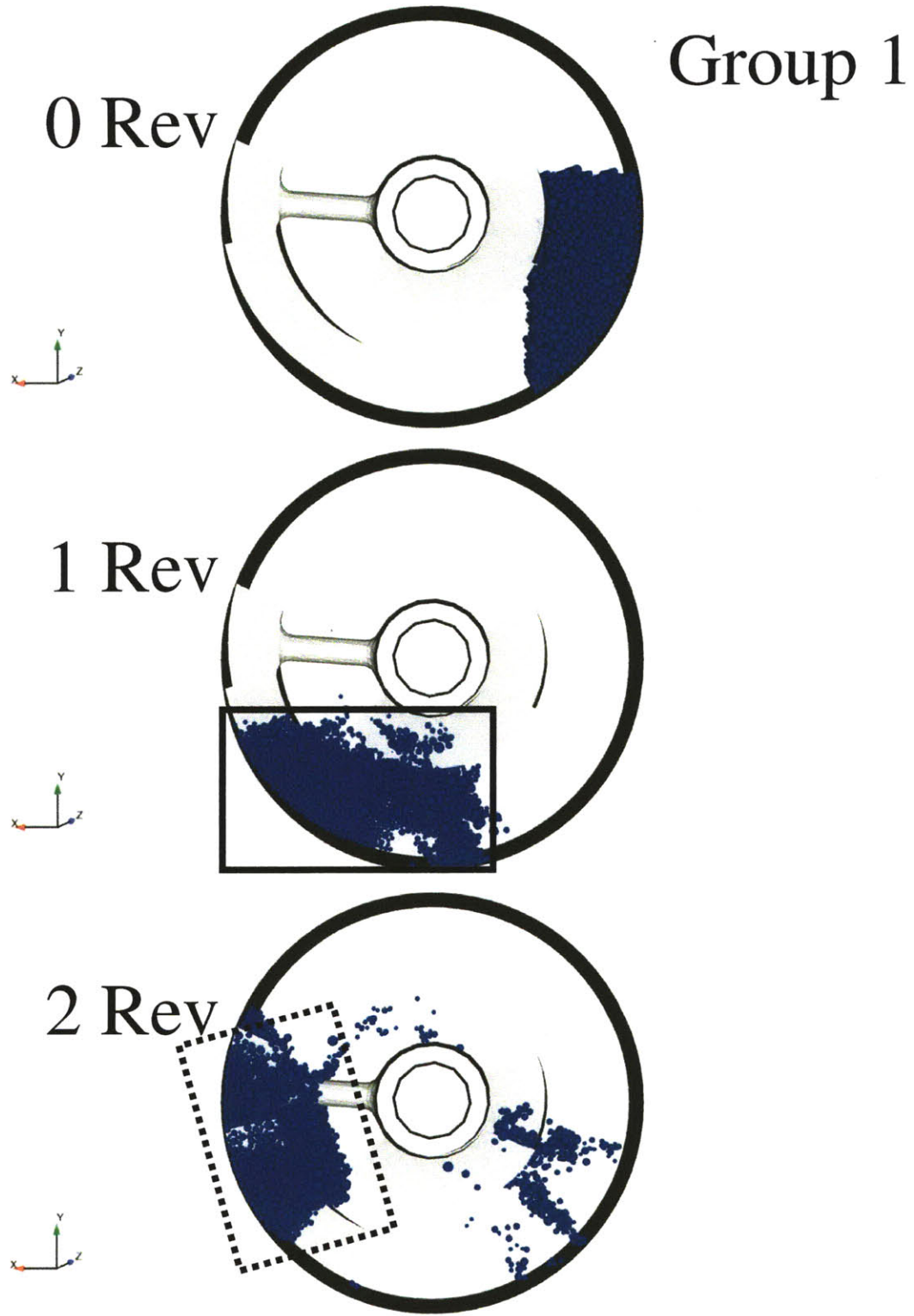


Figure 34: XY cutaway of X initial position Group 1 (blue) in an eighth scale double helical ribbon blender with lactose and caffeine particles operating at 20 RPM with 0.0035 g/s inflow.

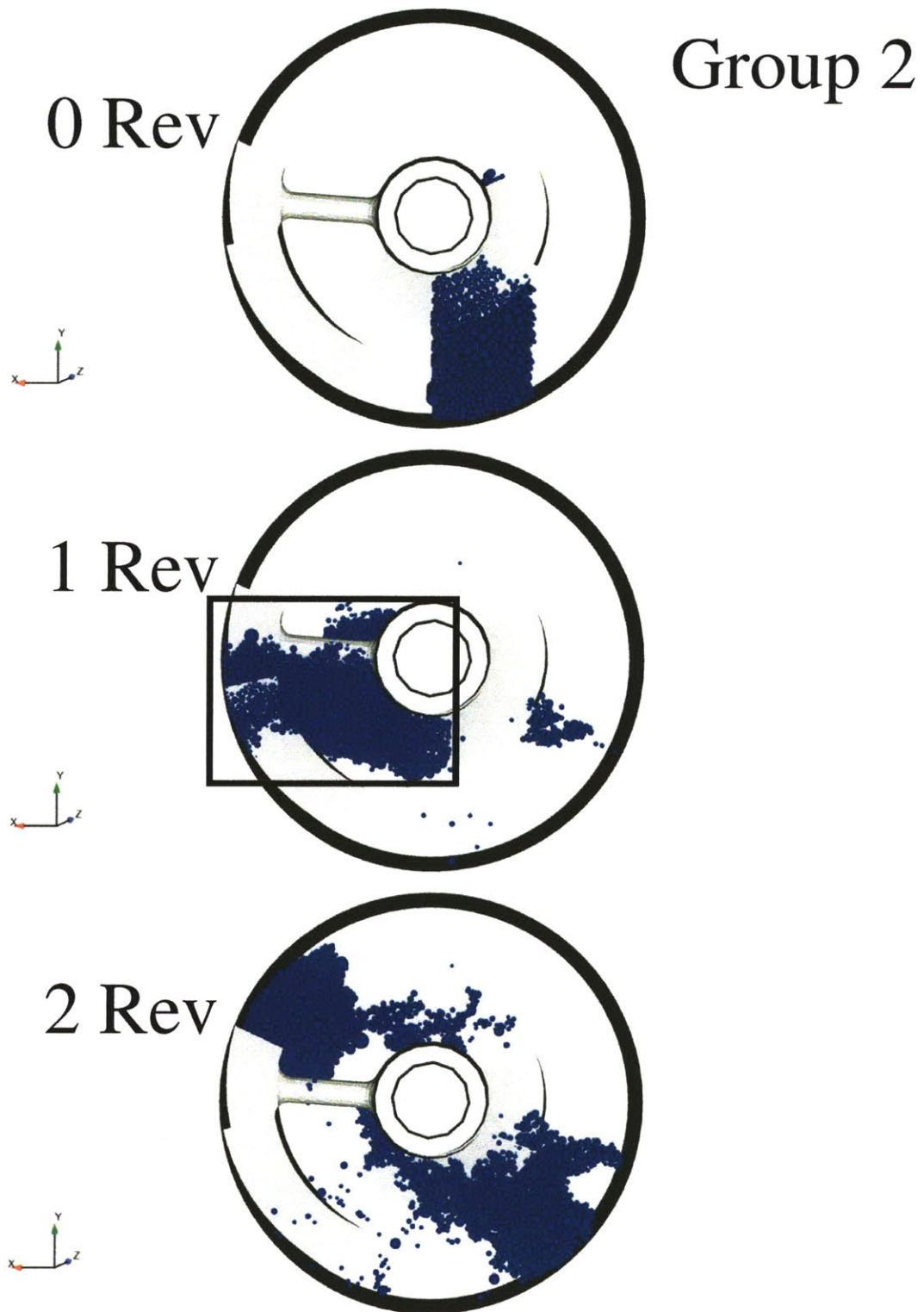


Figure 35: XY cutaway of X initial position Group 2 (green) in an eighth scale double helical ribbon blender with lactose and caffeine particles operating at 20 RPM with 0.0035 g/s inflow.

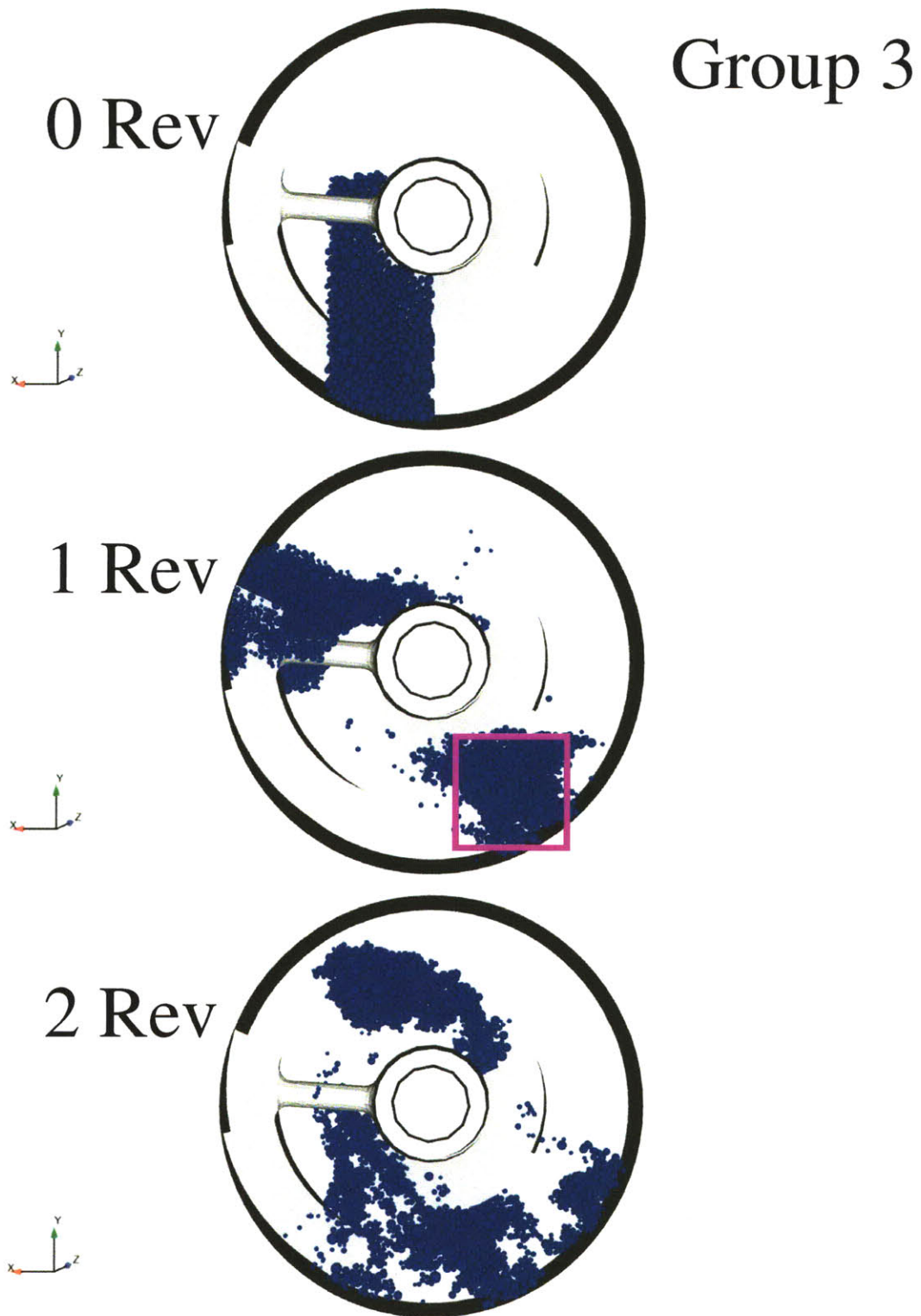


Figure 36: XY cutaway of X initial position Group 3 (yellow) in an eighth scale double helical ribbon blender with lactose and caffeine particles operating at 20 RPM with 0.0035 g/s inflow.

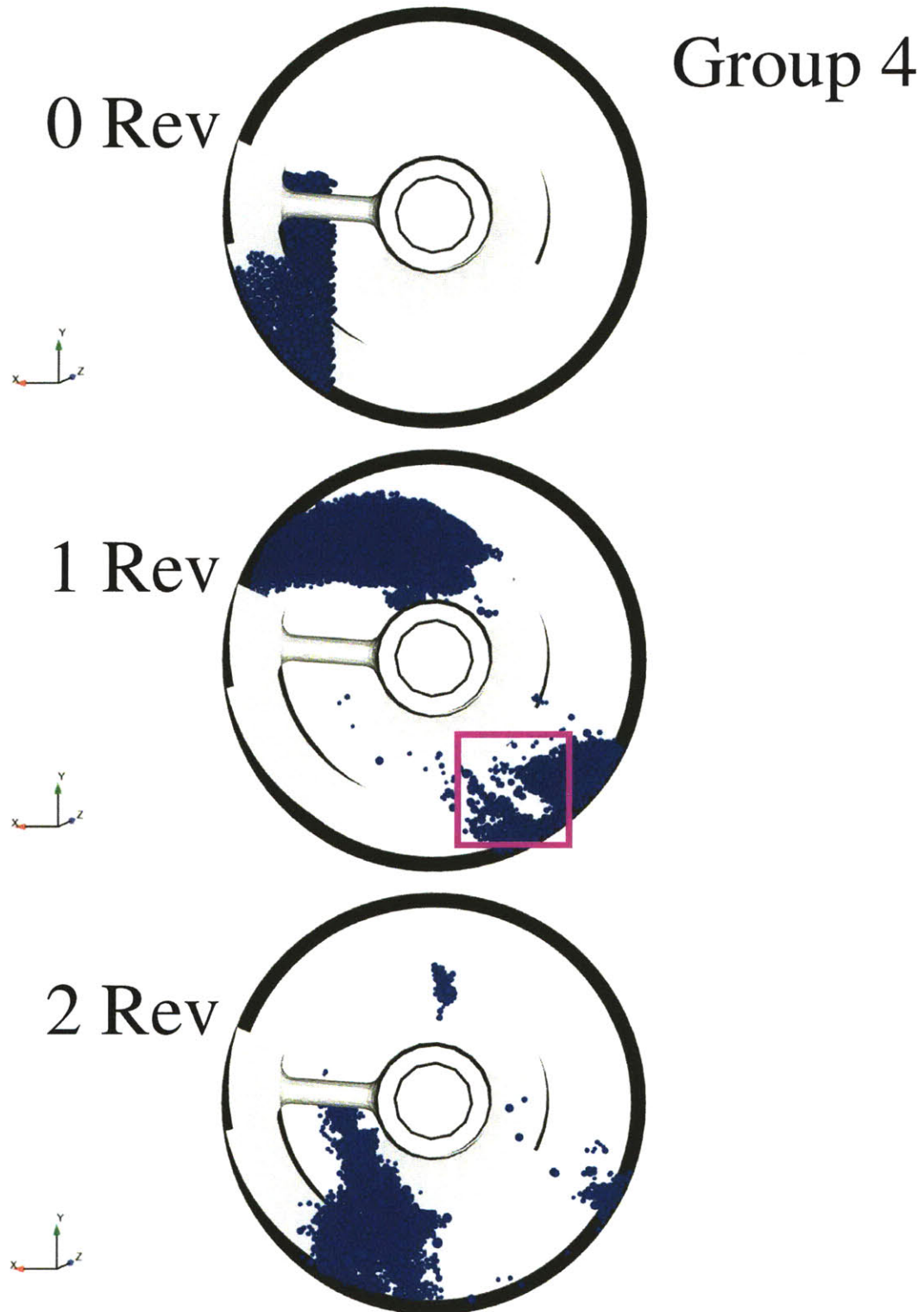


Figure 37: XY cutaway of X initial position Group 4 (orange) in an eighth scale double helical ribbon blender with lactose and caffeine particles operating at 20 RPM with 0.0035 g/s inflow.

The Y groups (Figure 38) demonstrate similar mixing behavior to the X groups. Again, the groups have mixed and the centroids have converged after 3 revolutions of the blender with little additional convergence after that.

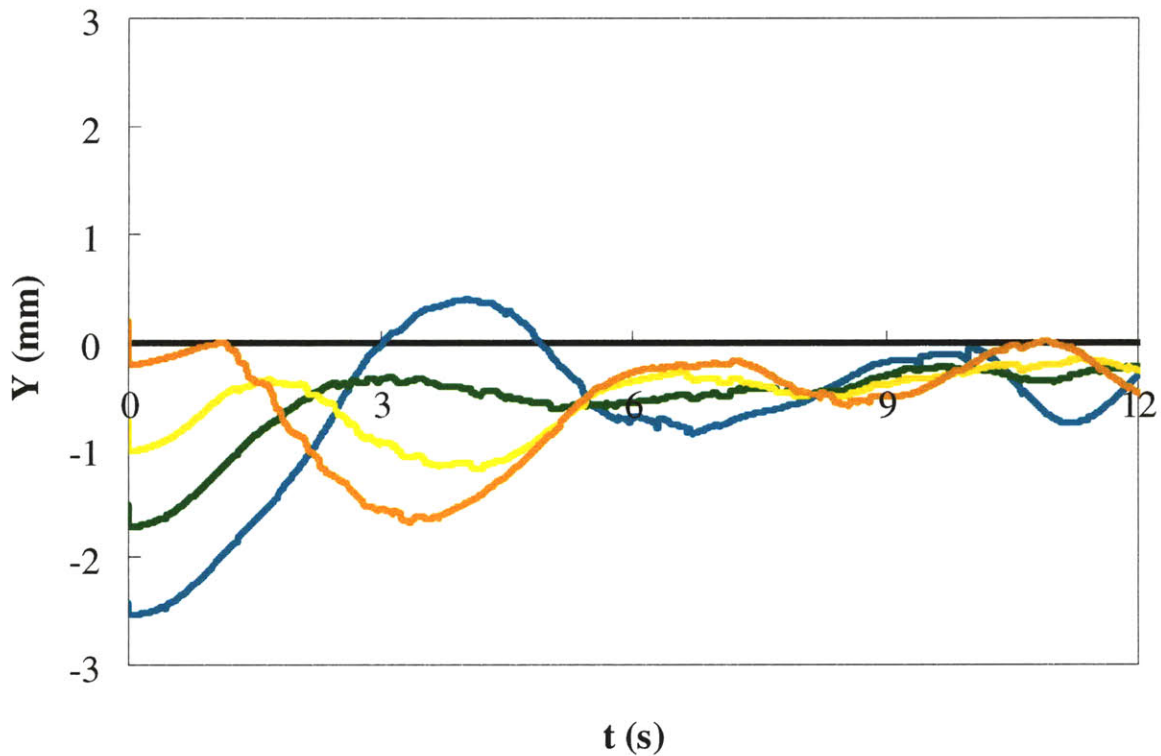


Figure 38: Centroids of Y position colors (blue = 1, green = 2, yellow = 3, orange = 4) in the Y direction in an eighth scale double helical ribbon blender with lactose and caffeine particles operating at 20 RPM with 0.0035 g/s inflow.

Visualizing the Y groups, one can still distinctly discern the individual groups after 1 revolution, but this structure mostly disappears after the second revolution (Figure 39). The one group that is still maintaining its initial structure after 2 revolutions is Group 1 (Figure 40). Group 1 is the bottom layer and sits next to the blender shell. Much like was seen for X groups, particles nearer to the blender shell seem to mix slower than particles closer to the center of the blender. The V_{θ} profile (Figure 26) indicates that particles in this region near the blender shell

are being moved at the same speed as particles closer to the central shaft, so it does not seem to be a transport issue. The V_r profile (Figure 25) provides a reasonable explanation for this phenomenon. On the negative X side of the blender where the avalanching particles are falling, there is generally a positive radial velocity moving particles away from the central shaft. Therefore regions with particles that initially occupy this central region, like Group 2 (Figure 41), Group 3 (Figure 42) and Group 4 (Figure 43), have to spread across the radial dimension when they avalanche. Particles near the shell, however, have a much smaller area in which to rearrange. The granular temperature profile (Figure 28) demonstrates that there is mixing in this region, but that mixing is primarily internal to the group and over much shorter distances.

Groups 1 to 4

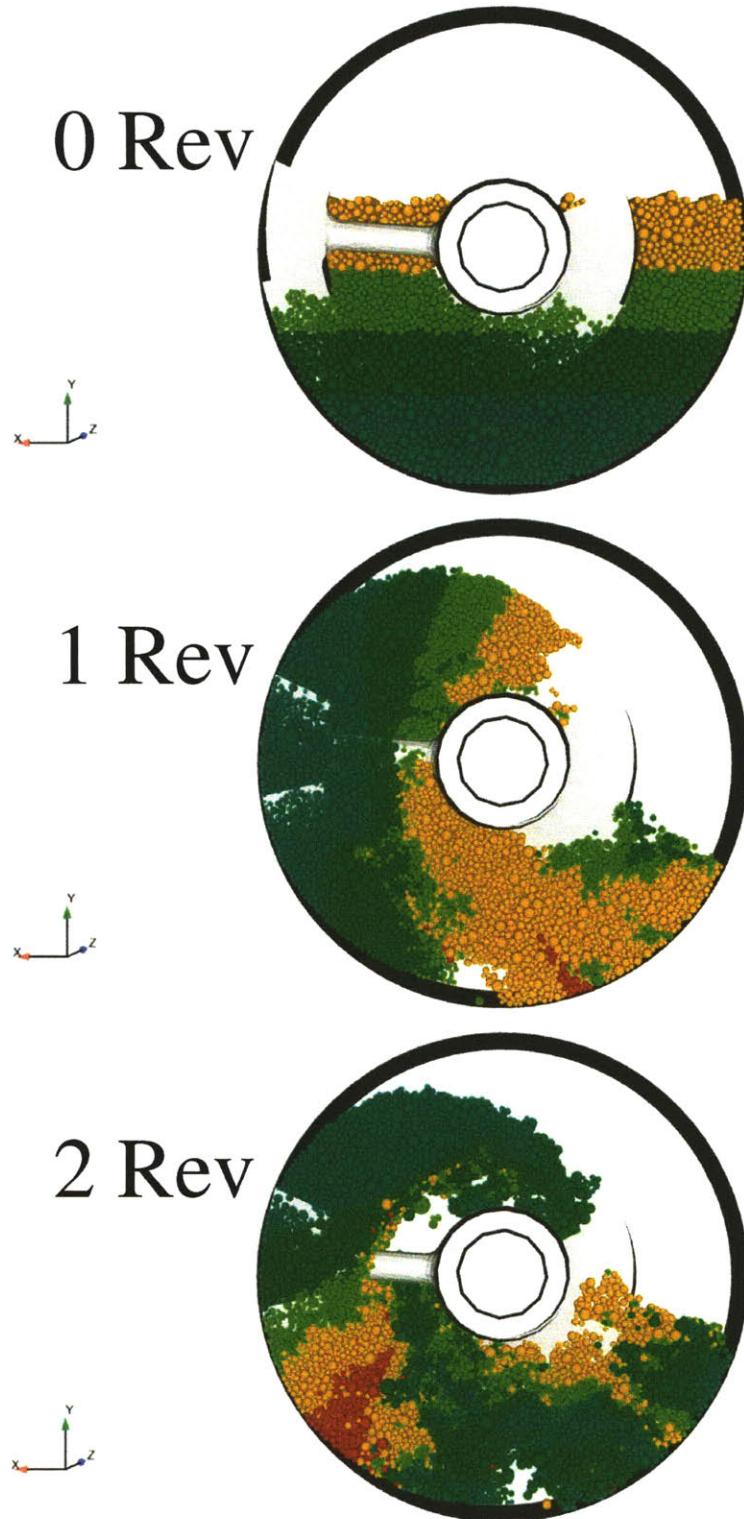


Figure 39: XY cutaway with coloration by Y initial position Group (blue = 1, green = 2, yellow = 3, orange = 4) in an eighth scale double helical ribbon blender with lactose and caffeine particles operating at 20 RPM with 0.0035 g/s inflow.

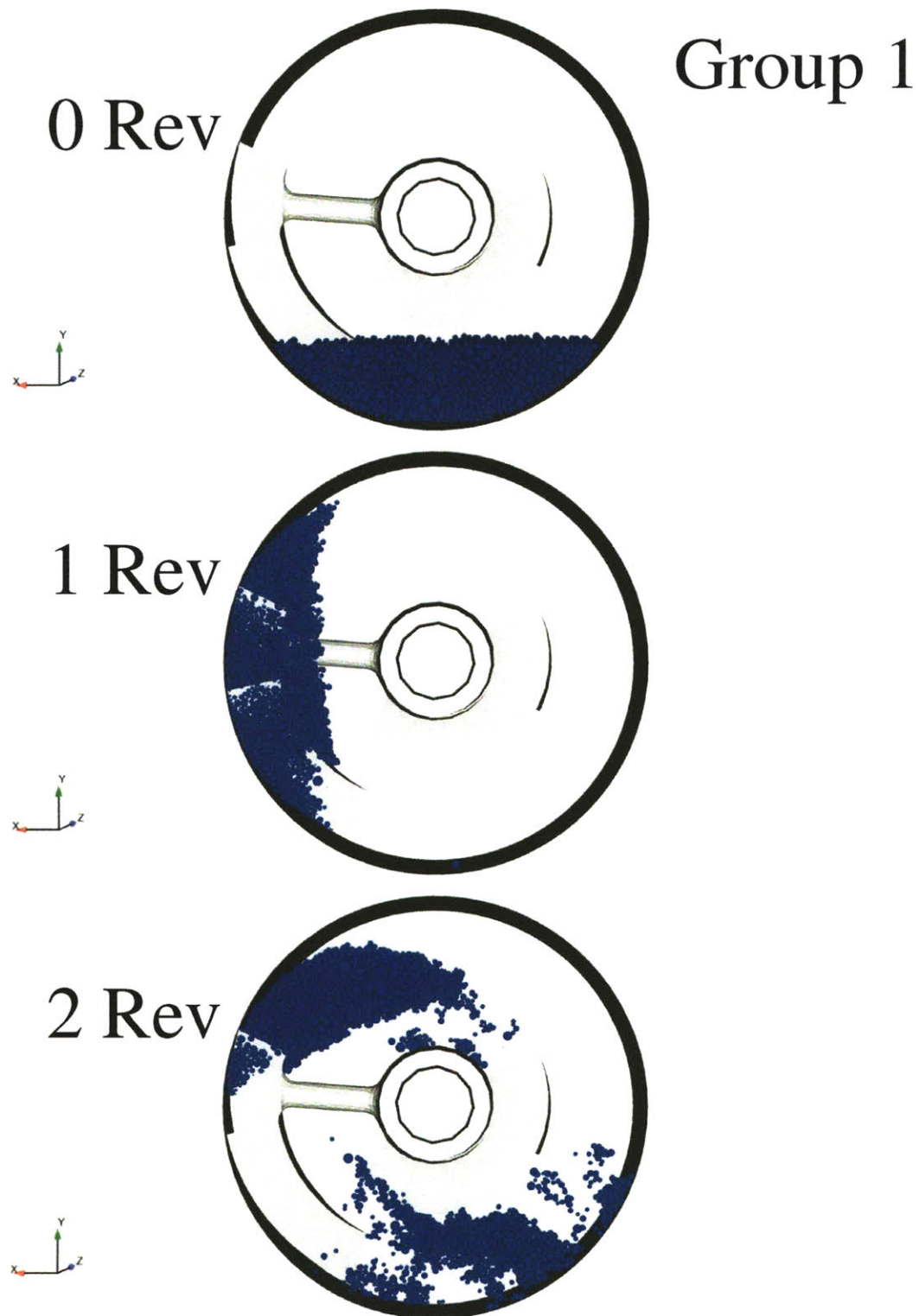
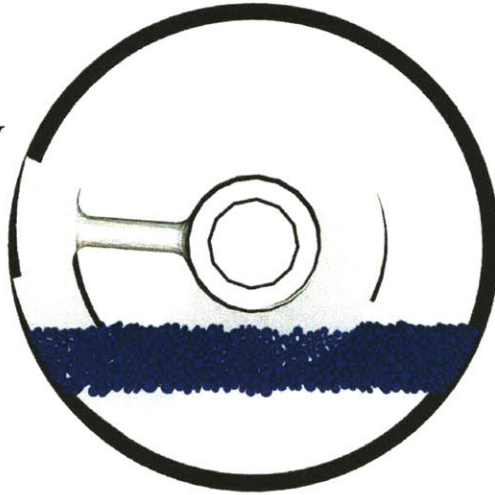


Figure 40: XY cutaway of Y initial position Group 1 (blue) in an eighth scale double helical ribbon blender with lactose and caffeine particles operating at 20 RPM with 0.0035 g/s inflow.

Group 2

0 Rev



1 Rev



2 Rev

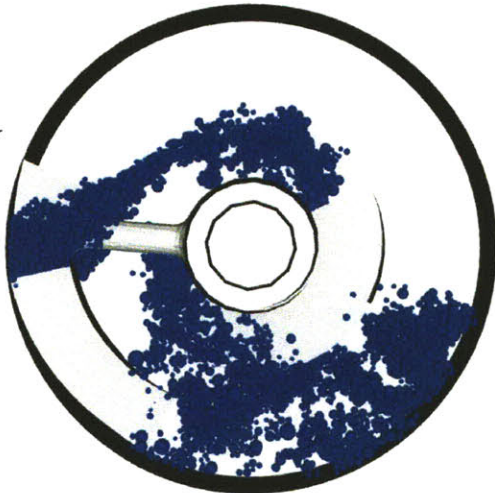


Figure 41: XY cutaway of Y initial position Group 2 (green) in an eighth scale double helical ribbon blender with lactose and caffeine particles operating at 20 RPM with 0.0035 g/s inflow.

Group 3

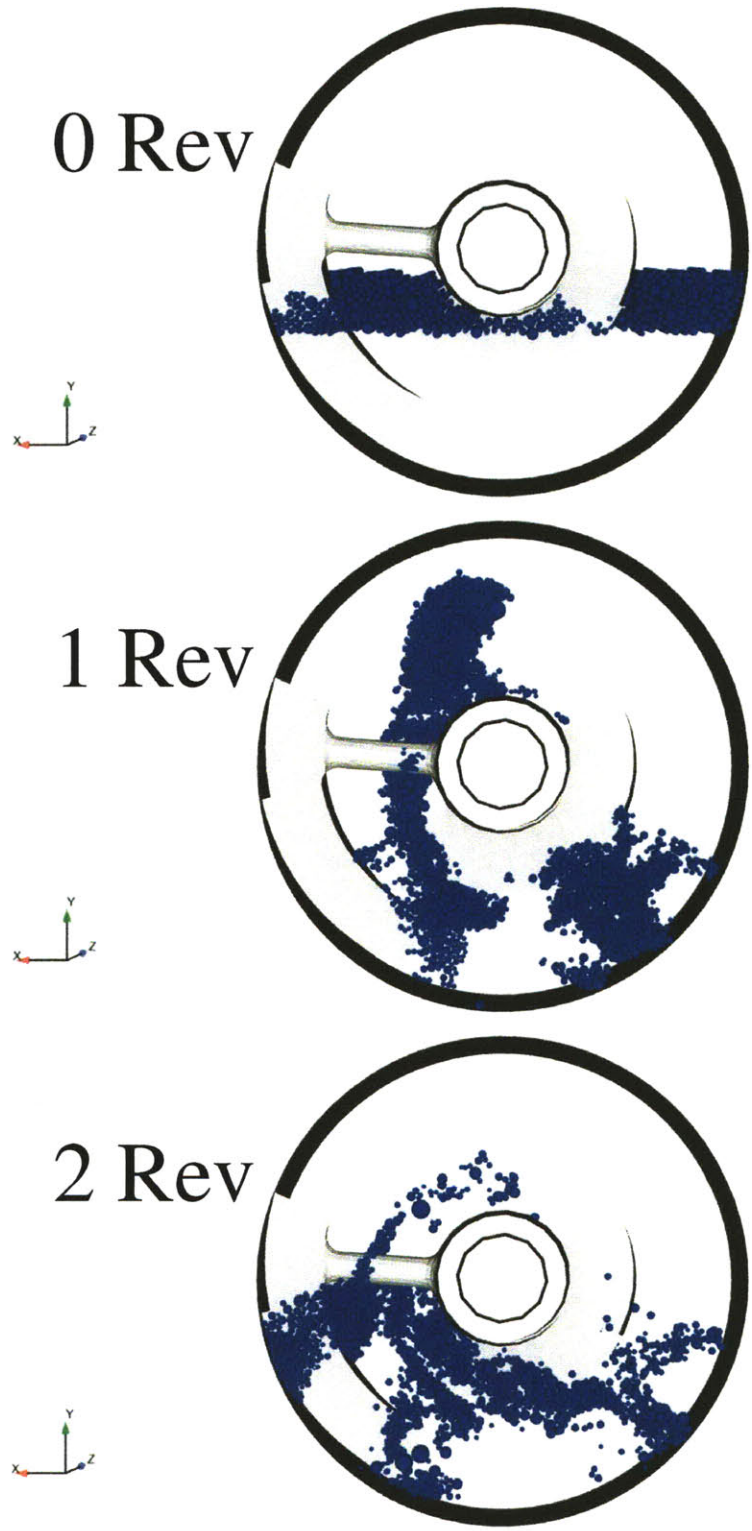


Figure 42: XY cutaway of Y initial position Group 3 (yellow) in an eighth scale double helical ribbon blender with lactose and caffeine particles operating at 20 RPM with 0.0035 g/s inflow.



Figure 43: XY cutaway of Y initial position Group 4 (orange) in an eighth scale double helical ribbon blender with lactose and caffeine particles operating at 20 RPM with 0.0035 g/s inflow.

The Z groups generally show a forward axial transport of particles towards the exit of the blender (Figure 44 and Figure 45). Although the Z centroids are converging to some extent, the blender does not achieve axial homogeneity over the first four revolutions. This is not surprising given the much larger distances over which the Z groups are initially spread in the axial direction compared to the X and Y groups in the horizontal and vertical dimensions respectively.

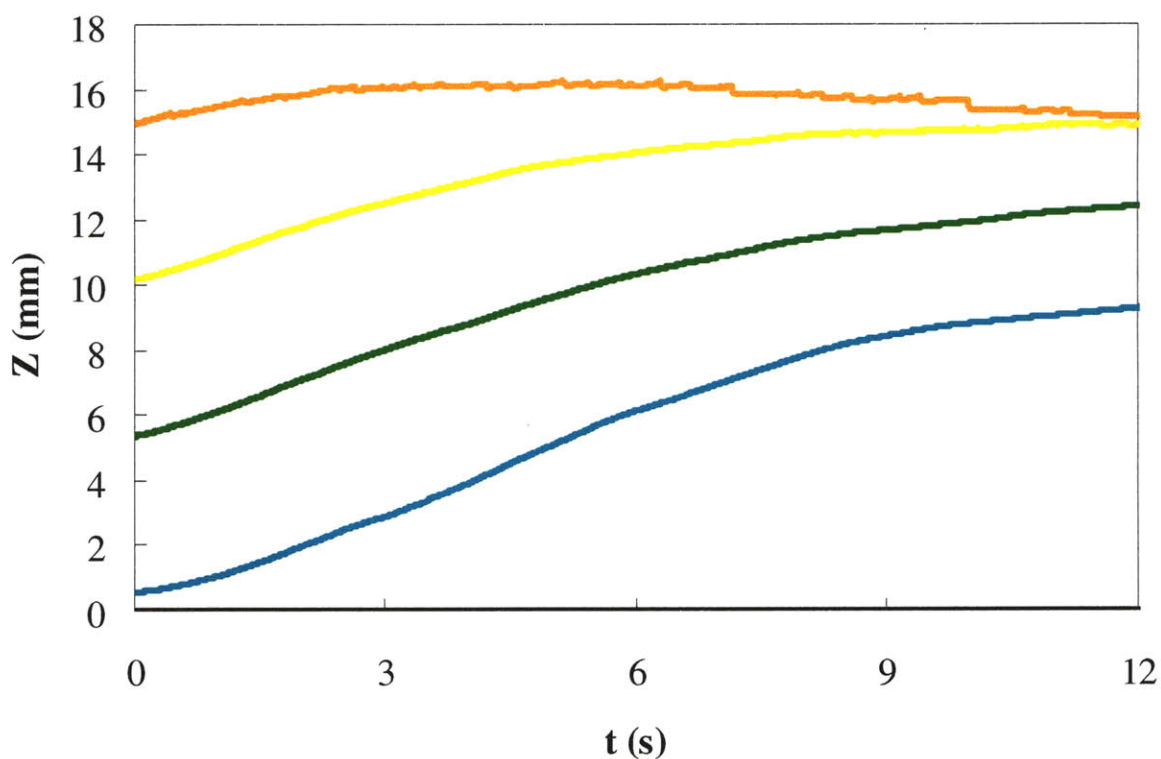


Figure 44: Centroids of Z initial position Groups (blue = 1, green = 2, yellow = 3, orange = 4) in the Z direction in an eighth scale double helical ribbon blender with lactose and caffeine particles operating at 20 RPM with 0.0035 g/s inflow.

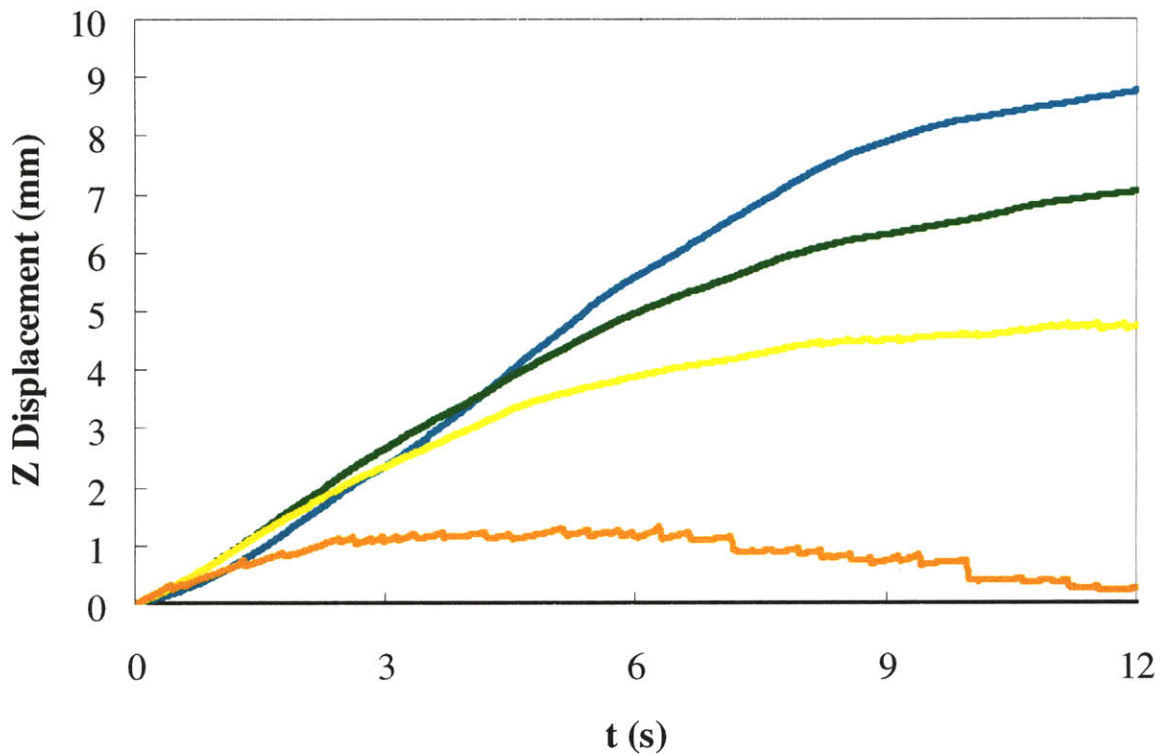


Figure 45: Displacement of centroids of Z initial position Groups (blue = 1, green = 2, yellow = 3, orange = 4) in the Z direction in an eighth scale double helical ribbon blender with lactose and caffeine particles operating at 20 RPM with 0.0035 g/s inflow.

As expected from the V_z profiles (Figure 27), the rate of displacement of the Z groups' centroid decreases as it approaches the exit of the blender (Figure 45). This trend continues until material begins to exit the blender and further displacement of the centroid in the Z direction stops. This is visible in Group 4's (Figure 57) Z displacement where, after the first revolution of the blender, its centroid actually moves backwards.

The mixing of particles in the axial direction is accomplished by both the convective action of the double helical ribbons and the avalanching of particles. While it is difficult to quantitatively separate the effects of these two mechanisms of mixing, the visualization of the Z groups gives some qualitative indications. Looking at all of the groups together (Figure 46), the most obvious feature is the dilation of the groups due to the forward and reverse conveying

regions. While the groups are beginning to overlap in the axial direction as early as the end of the first revolution (black box in Figure 54 and Figure 55 and magenta box in Figure 55 and Figure 56), the groups themselves are still highly contiguous bodies. Even after the second revolution, the four original regions still are distinctly visible with relatively clear boundaries. Looking at Group 1 (Figure 54 Rev 2), Group 2 (Figure 55 Rev 2) and Group 3 (Figure 56 Rev 2), one can see more clearly that the particles are being spread axially by the convective and the diffusive mechanisms of mixing.

There is a clear trend that the groups initially closer to the exit of the blender, like Group 3, have a narrower axial distribution of particles than groups closer to the inlet, like Group 1. This can be seen in how far the particles have travelled axially in Group 1 (dashed black arrow in Figure 54) and in Group 3 (dashed black arrow in Figure 56). This again indicates that the regions closer to the exit of the blender are less efficient at diffusive mixing than the regions closer to the inlet due to their higher volume fraction. When compared to the granular temperature profiles (Figure 28), one sees the clear decline in granular temperature in the XZ cross section in the exit axial half of the blender. Declining diffusive mixing from avalanching particles thus seems to drive the decreased axial mixing seen in the images of Group 1 (Figure 54), Group 2 (Figure 55) and Group 3 (Figure 56). Additionally, this trend indicates that diffusive mixing from the avalanching of particles is a more significant mechanism of mixing in the axial direction than the convective mixing from the double helical ribbons.

Groups 1 to 4

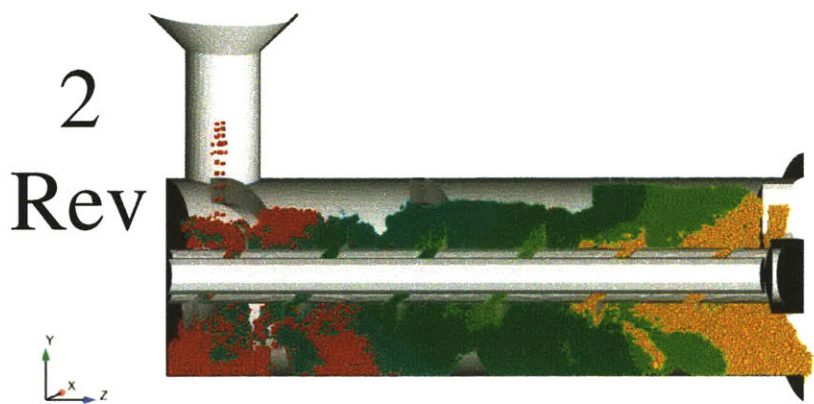
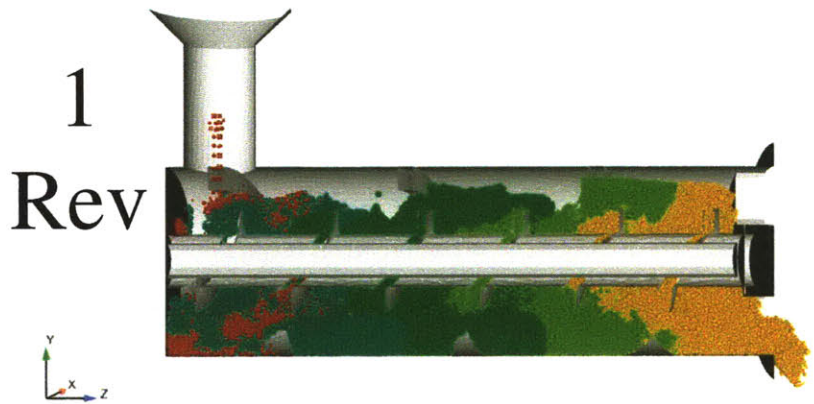
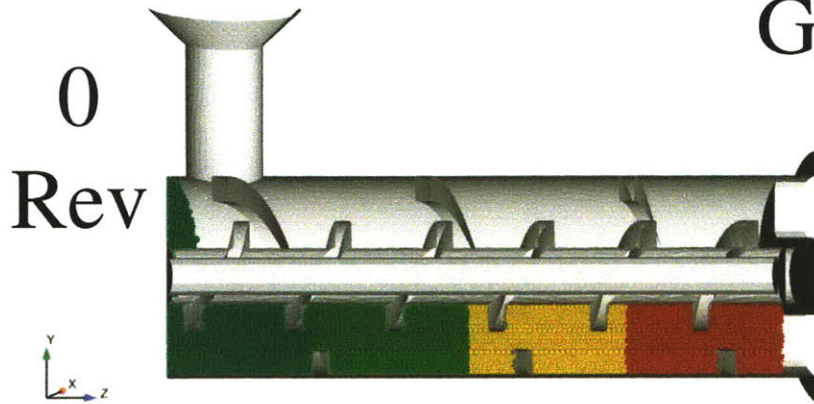


Figure 46: YZ cutaway with coloration by Z initial position Group (blue = 1, green = 2, yellow = 3, orange/red = 4) in an eighth scale double helical ribbon blender with lactose and caffeine particles operating at 20 RPM with 0.0035 g/s inflow.

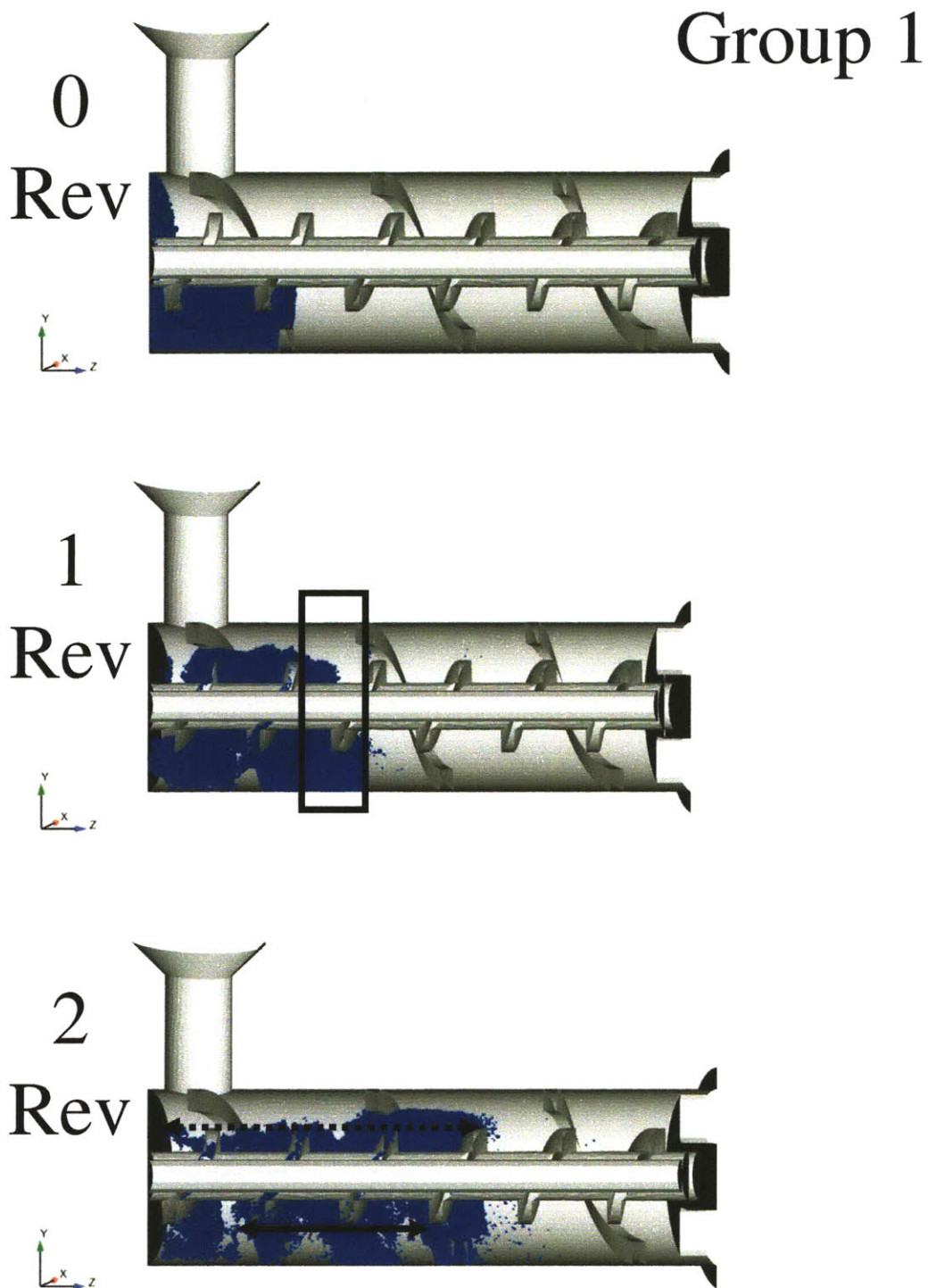


Figure 47: YZ cutaway of Z initial position Group 1 (blue) in an eighth scale double helical ribbon blender with lactose and caffeine particles operating at 20 RPM with 0.0035 g/s inflow.

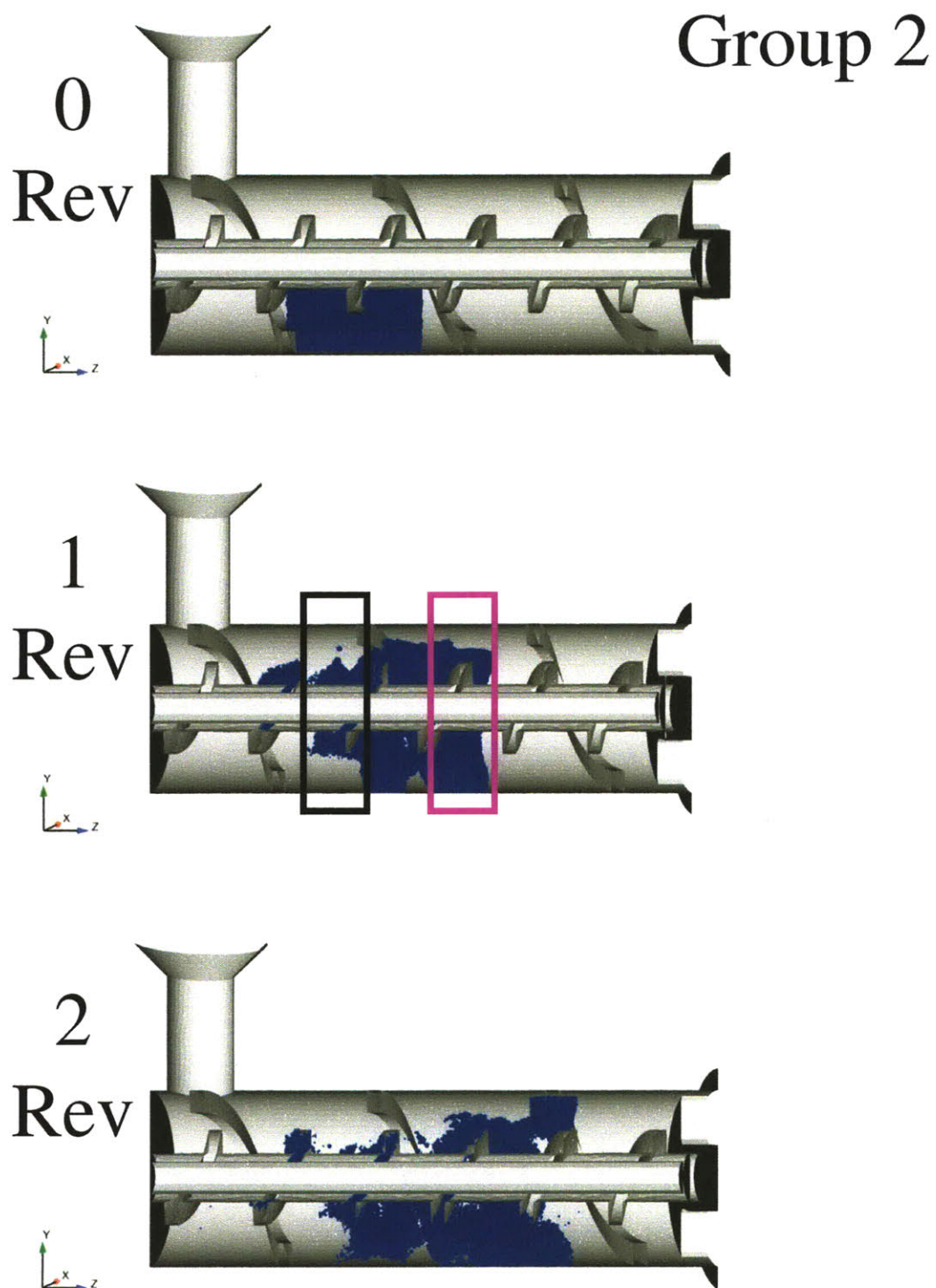


Figure 48: YZ cutaway of Z initial position Group 2 (green) in an eighth scale double helical ribbon blender with lactose and caffeine particles operating at 20 RPM with 0.0035 g/s inflow.

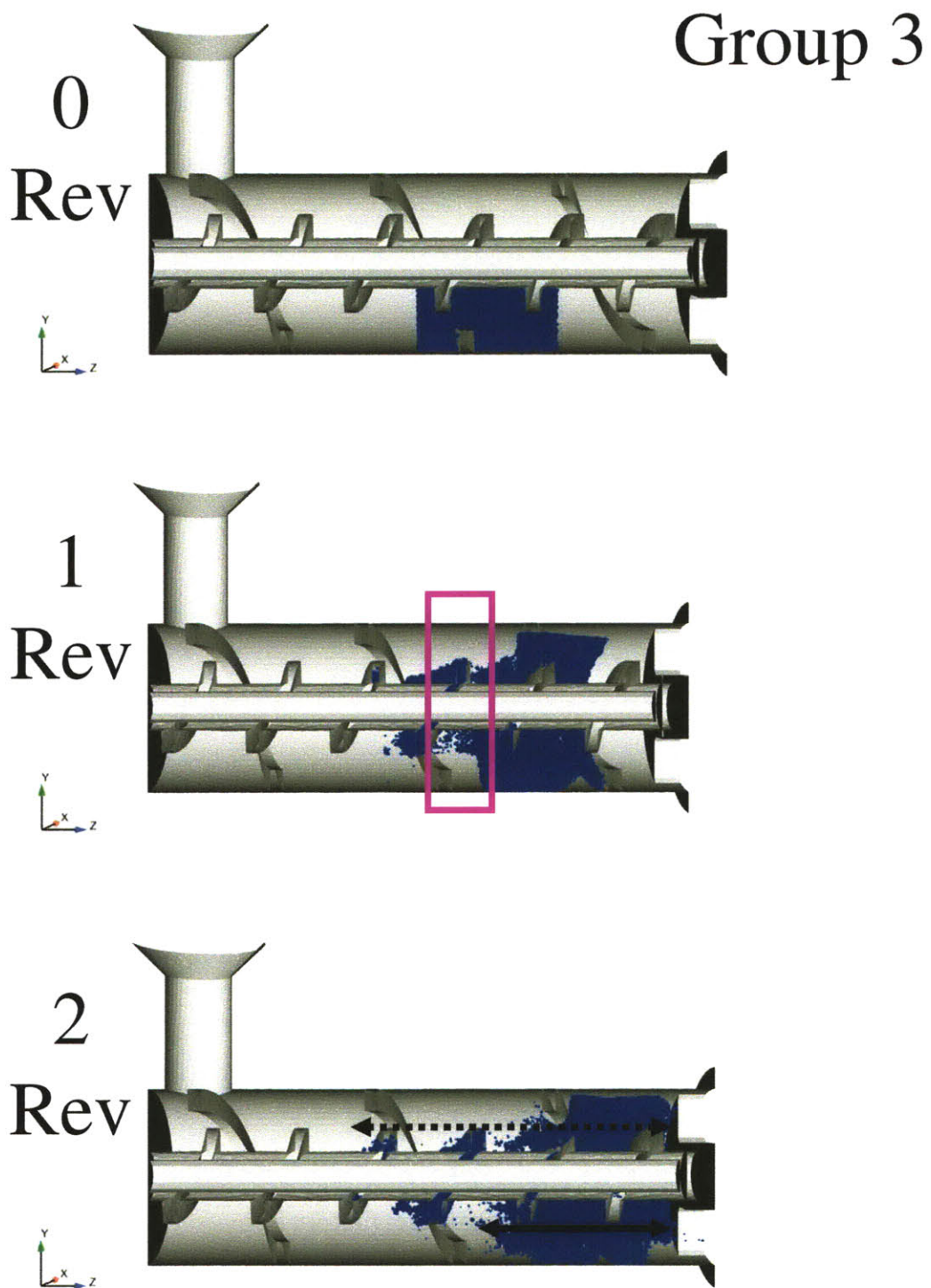


Figure 49: YZ cutaway of Z initial position Group 3 (yellow) in an eighth scale double helical ribbon blender with lactose and caffeine particles operating at 20 RPM with 0.0035 g/s inflow.

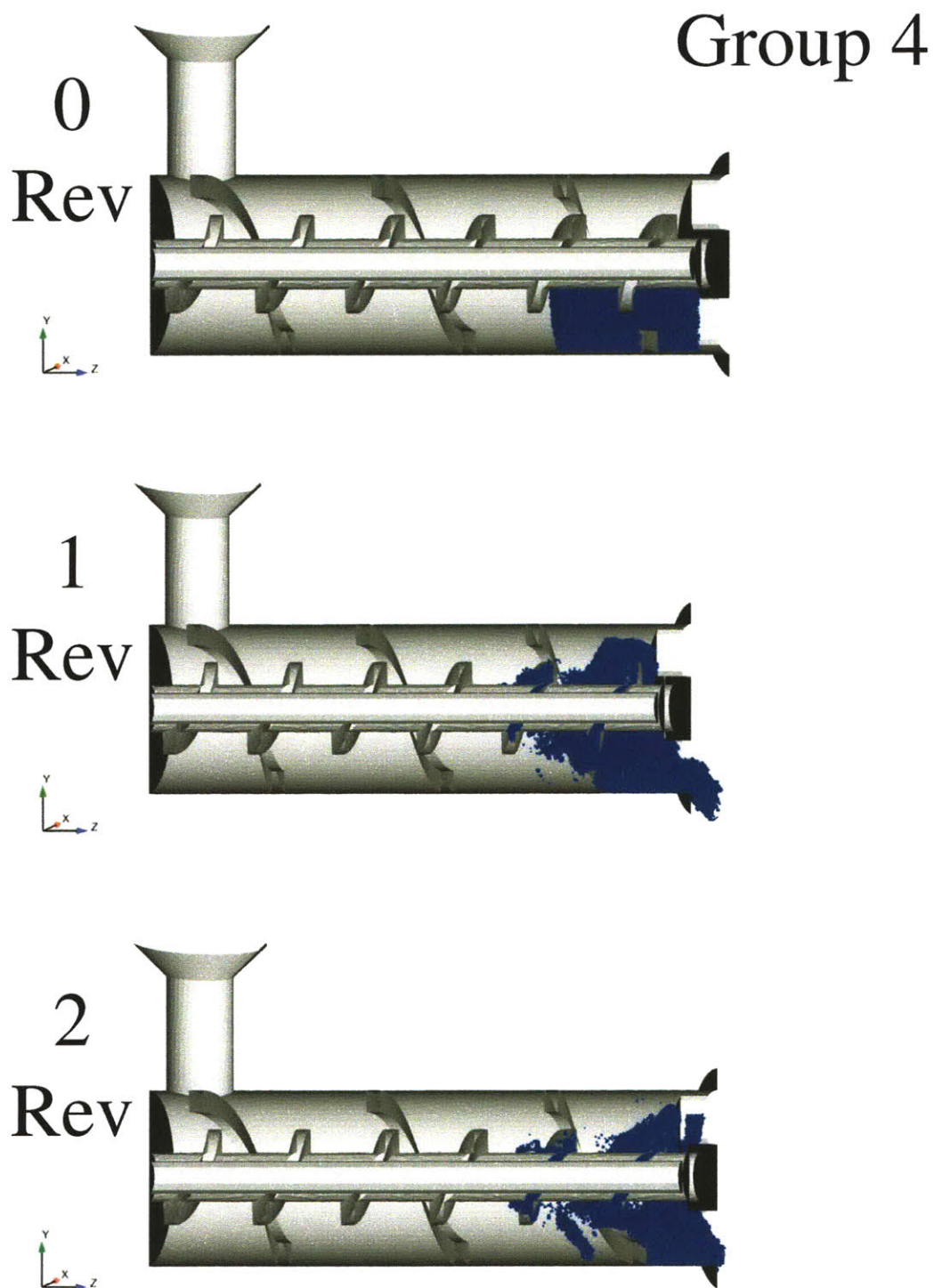


Figure 50: YZ cutaway of Z initial position Group 4 (orange/red) in an eighth scale double helical ribbon blender with lactose and caffeine particles operating at 20 RPM with 0.0035 g/s inflow.

The primacy of the diffusive mixing mechanism is an important consideration for the design of continuous blenders. Blender designs that are able to create more diffusive mixing will create more homogenous blends and more consistent drug products. More diffusive mixing can be created either through improved particle transport to the avalanching region or through elements that serve to randomize the particle flow.

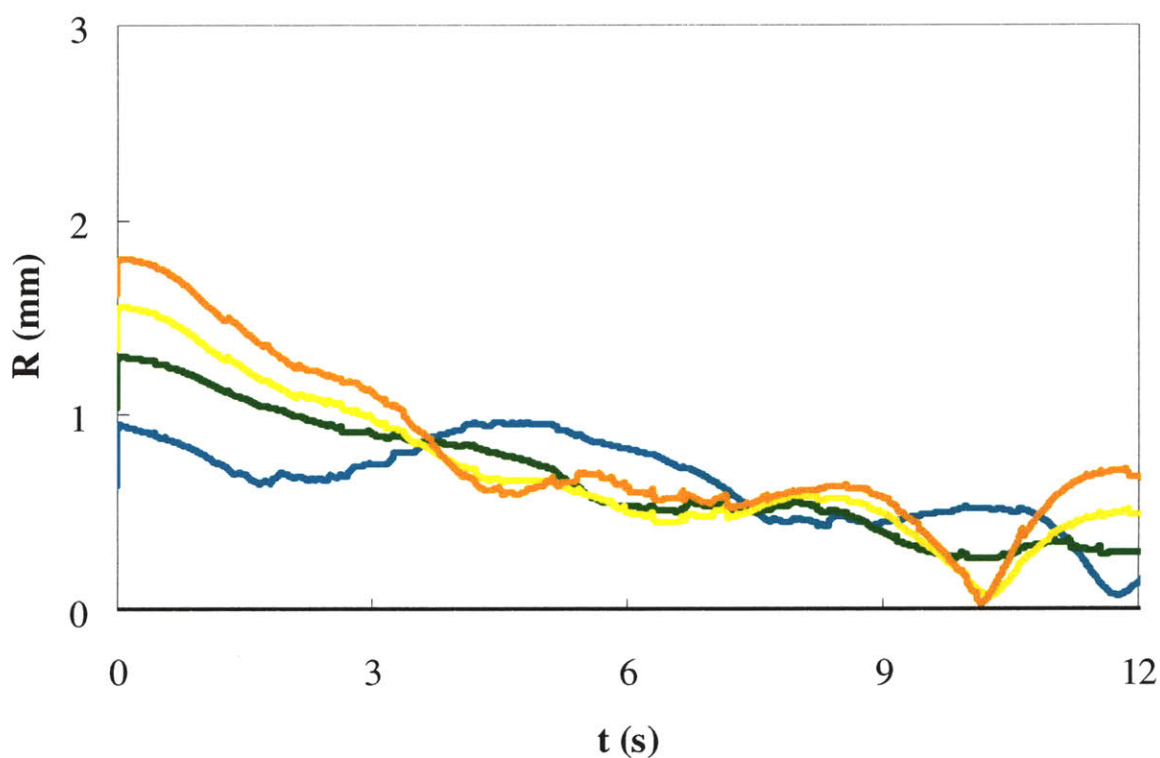


Figure 51: Centroids of R initial position groups (blue = 1, green = 2, yellow = 3, orange = 4) in the R direction in an eighth scale double helical ribbon blender with lactose and caffeine particles operating at 20 RPM with 0.0035 g/s inflow.

The centroid movement of the radial initial position groups (Figure 51) shows very similar behavior to the X and Y groups, but with a slightly faster convergence. In the radial direction, the centroids appear to have converged after 2.5 revolutions of the blender rather than

the 3 revolutions seen in the X and Y directions. It is important to note the movement of the radial initial position groups' centroids in the axial direction (Figure 52). Group 1 (Figure 54) overlaps the area of the inner helical ribbon (Figure 53); Group 2 (Figure 55) overlaps the region between the ribbons; Group 3 (Figure 56) and Group 4 (Figure 57) overlap the outer ribbon. Groups 2, 3 and 4 begin immediately moving forward at the start of the simulation at relatively similar rates. This is not surprising for Groups 3 and 4 which are being pushed by the forward pitched outer ribbon. However, this is surprising for Group 2, as one might expect the reverse flowing region would retard Group 2's forward motion to some extent.

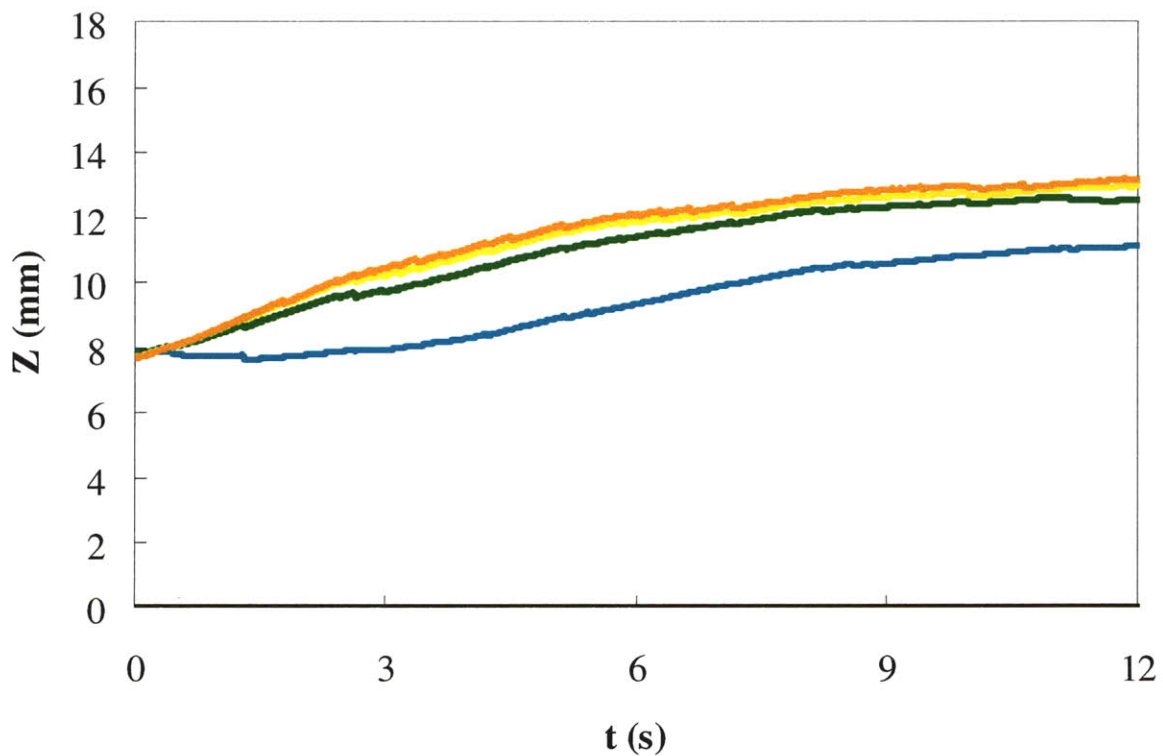


Figure 52: Centroids of R initial position groups (blue = 1, green = 2, yellow = 3, orange = 4) in the Z direction in an eighth scale double helical ribbon blender with lactose and caffeine particles operating at 20 RPM with 0.0035 g/s inflow.

Group 1 is the only group to travel backwards and this only occurs during the first revolution of the blender. After the first revolution, the particles in Group 1 begin traveling forward at the same rate as the particles in Groups 2, 3 and 4. This indicates that the particles that begin in Group 1 (the center radial region) are transported out of this region after 1 revolution of the blender. Generally, one can expect that particles will have a median residence time in the reverse conveying region of approximately 1 revolution.

Examining the initial position groups visually in the cutaway images shows that little mixing has occurred after the first revolution (Figure 53 1 Rev), but after 2 revolutions there is significant mixing for the material that has avalanched a second time (the lower half of Figure 53 2 Rev). Like the images of the X and Y groups, the radial groups show a pronounced trend of less efficient mixing for groups initially closer to the shell of the blender. This is clearly visible in the images of Group 4 (Figure 57) which is at the edge of the blender shell at both 1 and 2 revolutions. The lack of the radial mixing in Group 4 at 2 revolutions stands in stark contrast to the significant radial mixing seen in Group 1 (Figure 54) and Group 2 (Figure 55).

Groups 1 to 4

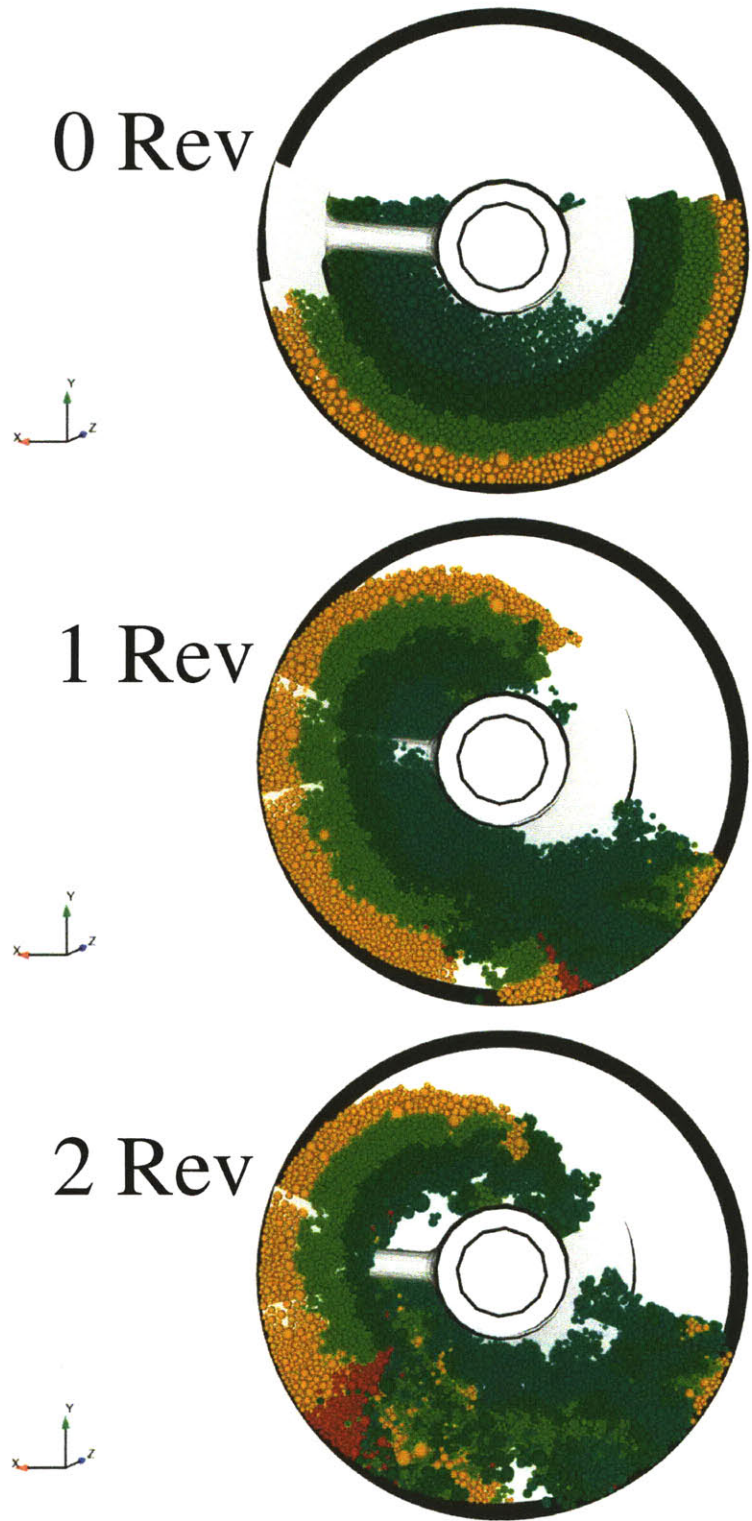


Figure 53: XY cutaway with coloration by radial (R) initial position group (blue = 1, green = 2, yellow = 3, orange = 4) in an eighth scale double helical ribbon blender with lactose and caffeine particles operating at 20 RPM with 0.0035 g/s inflow.

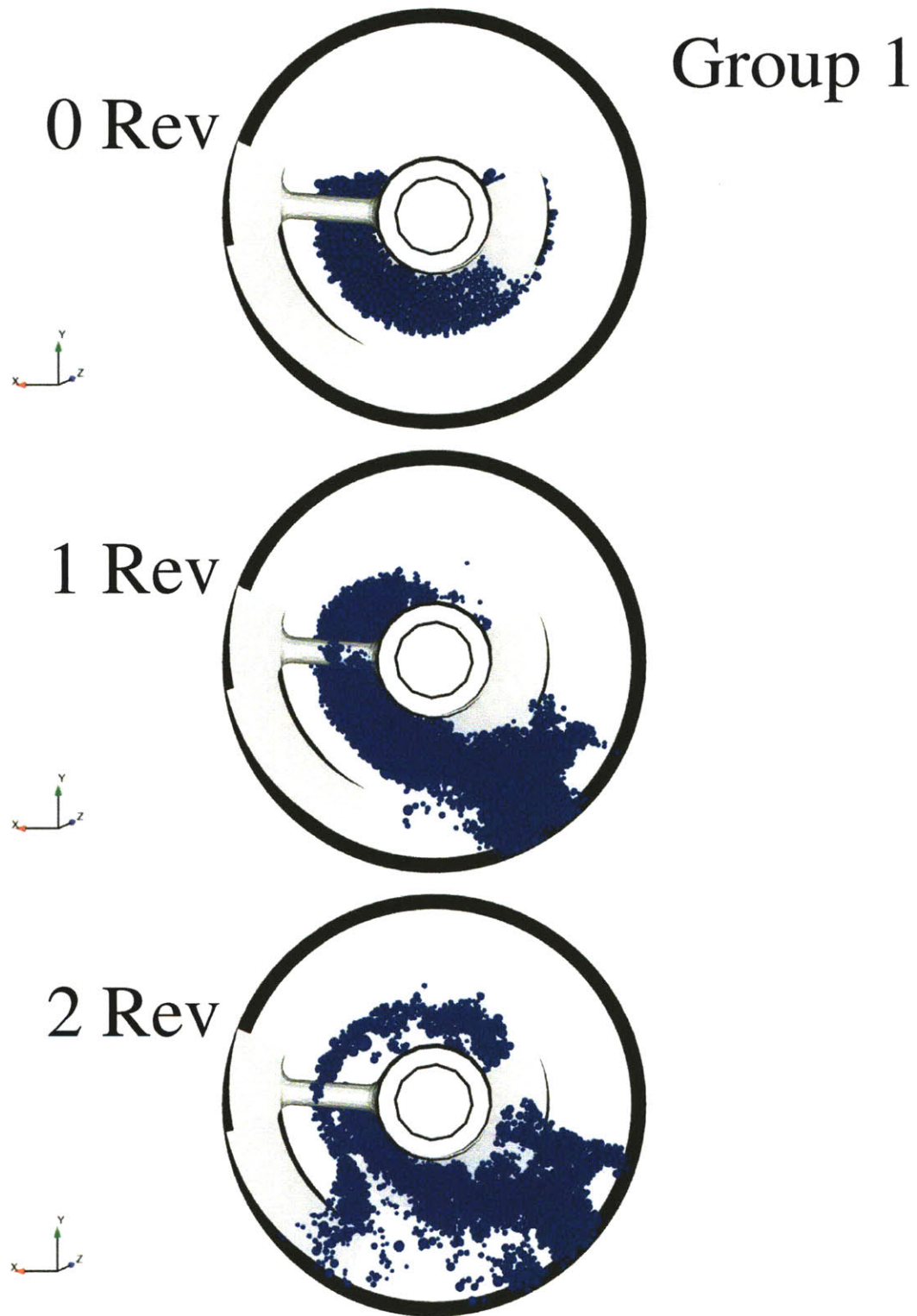


Figure 54: XY cutaway of R initial position Group 1 (blue) in an eighth scale double helical ribbon blender with lactose and caffeine particles operating at 20 RPM with 0.0035 g/s inflow.

Group 2

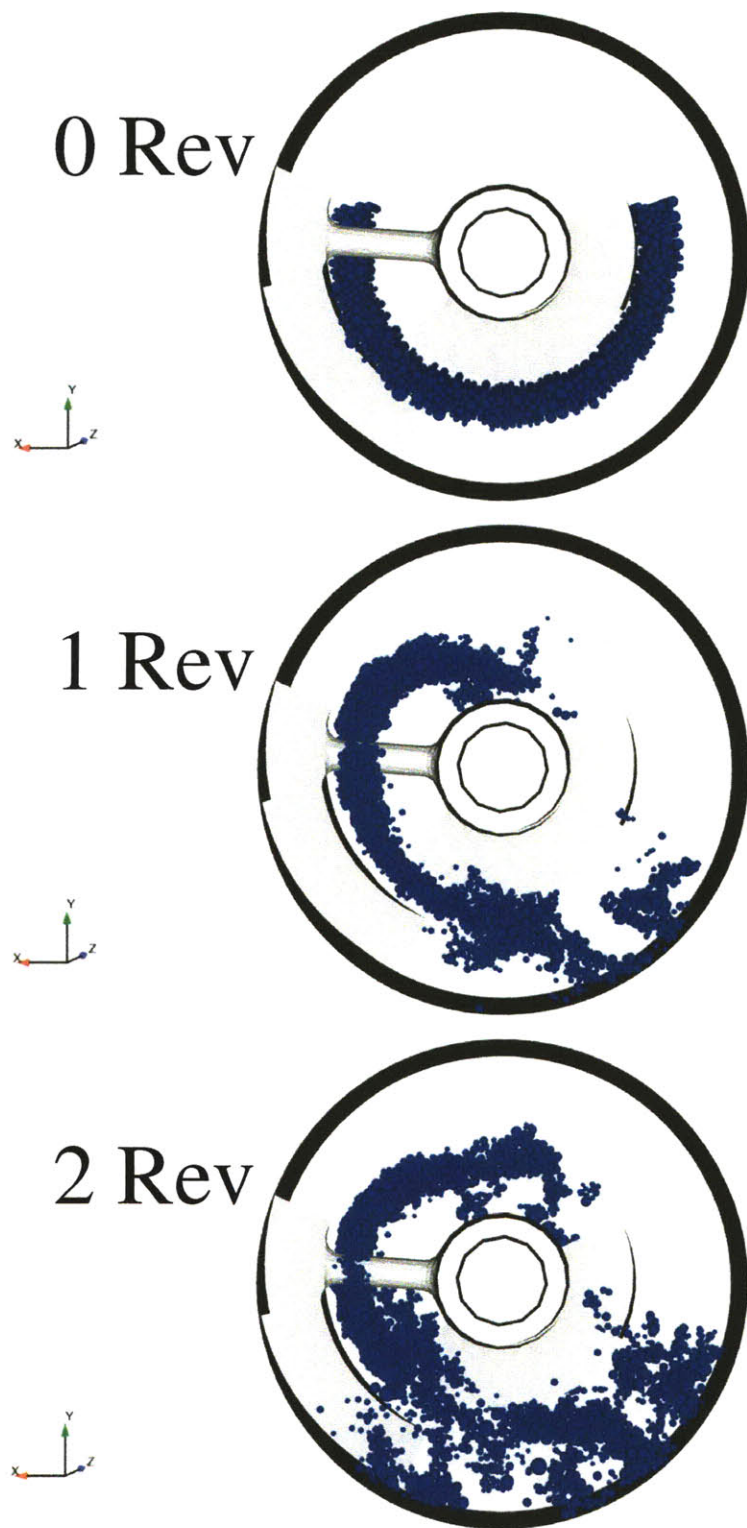
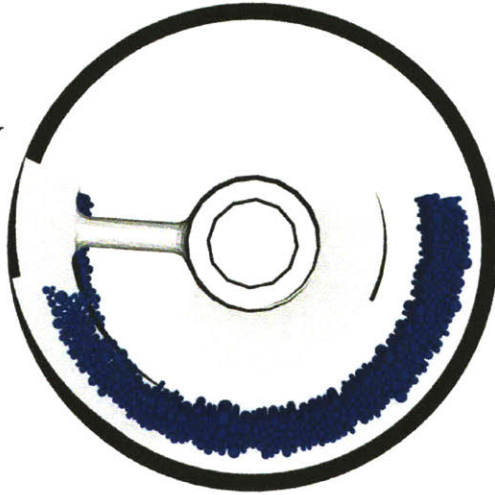


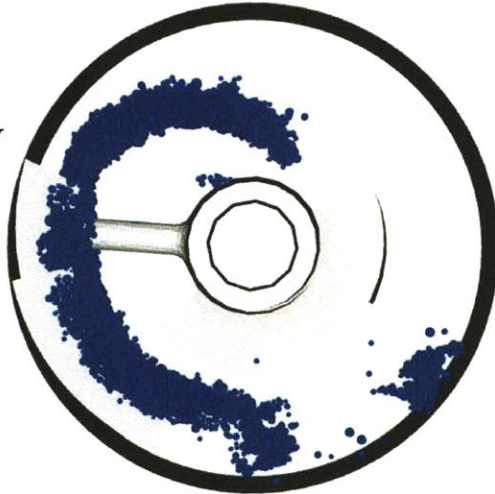
Figure 55: XY cutaway of R initial position Group 2 (green) in an eighth scale double helical ribbon blender with lactose and caffeine particles operating at 20 RPM with 0.0035 g/s inflow.

Group 3

0 Rev



1 Rev



2 Rev



Figure 56: XY cutaway of R initial position Group 3 (yellow) in an eighth scale double helical ribbon blender with lactose and caffeine particles operating at 20 RPM with 0.0035 g/s inflow.

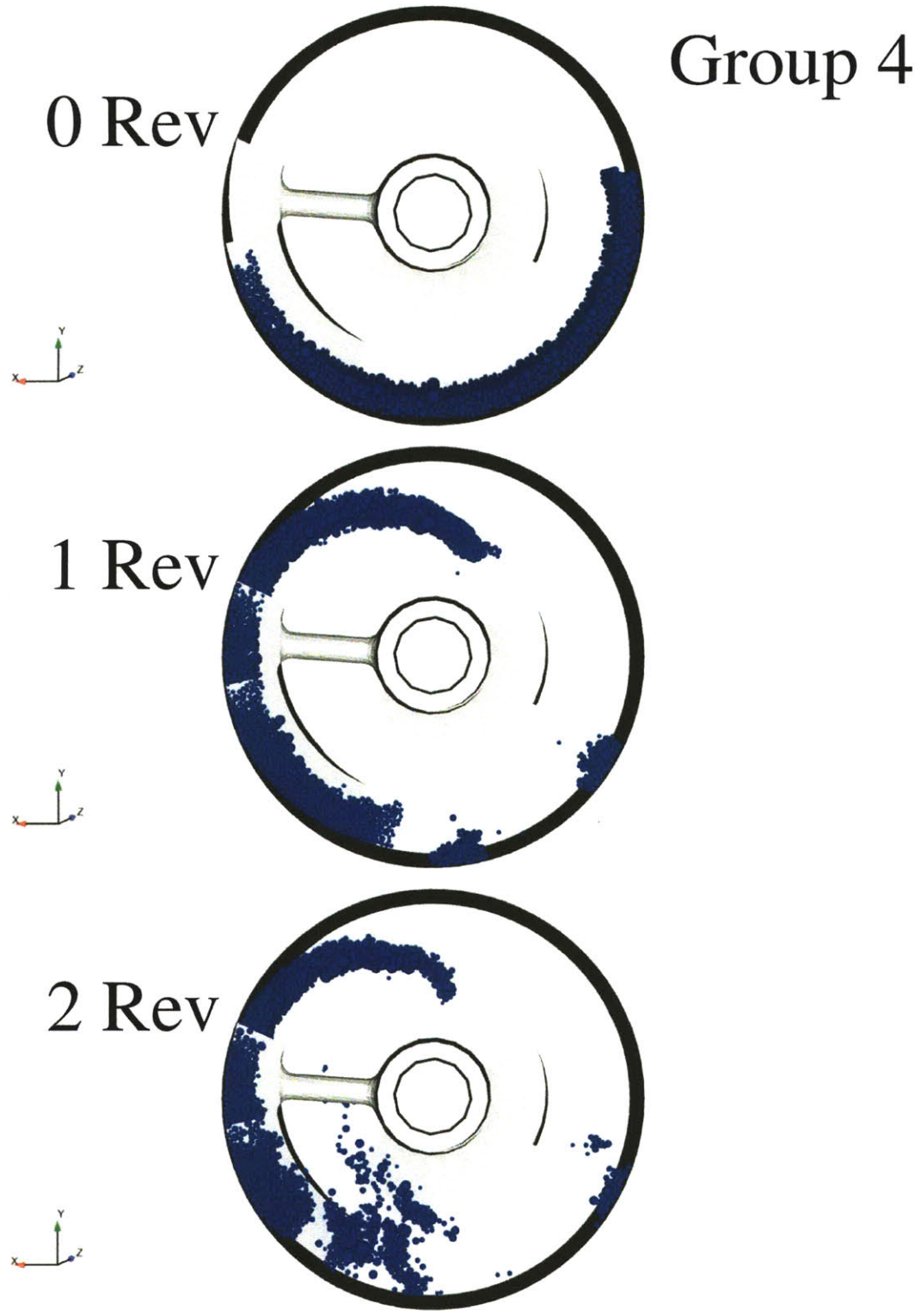


Figure 57: XY cutaway of R initial position Group 4 (orange) in an eighth scale double helical ribbon blender with lactose and caffeine particles operating at 20 RPM with 0.0035 g/s inflow.

5.4.2 Quantitative mixing measure

The quantitative mixing measure [63] uses initial position groups of equal volume in the X, Y, Z and R directions (see Figure 33, Figure 39, Figure 46 and Figure 53 for views of the X, Y, Z and R initial position groups respectively). The inflow is a separate group and is considered as well in the mixing measure calculations. The inflow makes a comparison of the X, Y and R homogeneity to the Z homogeneity difficult as the Z homogeneity is more strongly affected by the inflow than the other dimensions.

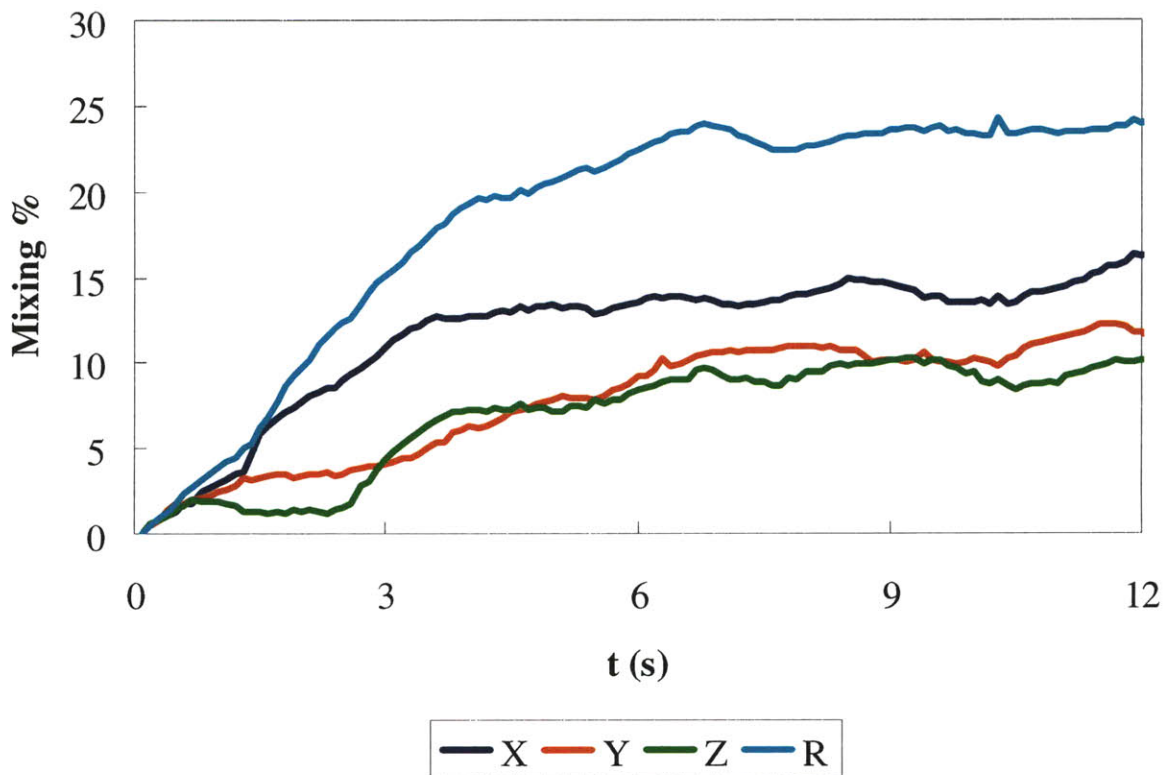


Figure 58: Mixing % for X, Y, Z and R initial position coloring for an eighth scale double helical ribbon blender with lactose and caffeine particles operating at 20 RPM with 0.0035 g/s inflow.

The homogeneity of the blend (mixing %) for the various initial position groups (Figure 58) displays a number of different phases as the mixing progresses. There is an initial setup period for half a revolution (1.5 seconds) as the particles are lifted and ultimately begin to avalanche

over the shaft. The homogeneity in the X, Y and R direction shows the expected behavior that as the particles begin to avalanche, they begin to mix. The rate of X and R mixing demonstrate an inflection near 1.5 revolutions (4.5 seconds) (Figure 59) where the rate of mixing decreases. A similar inflection occurs in the rate of Y mixing near 2 revolutions (6 seconds). It is interesting to note that much of the mixing in the X and R direction is actually accomplished in the first revolution of the blender and subsequent mixing is much less rapid. This might appear to be counter to what was observed in the cutaway images of the initial position groups, where the particle had not significantly changed shape at 1 revolution. However, the change in homogeneity in the quantitative mixing measure demonstrates the importance that small overlaps between neighboring particle groups can have on overall homogeneity.

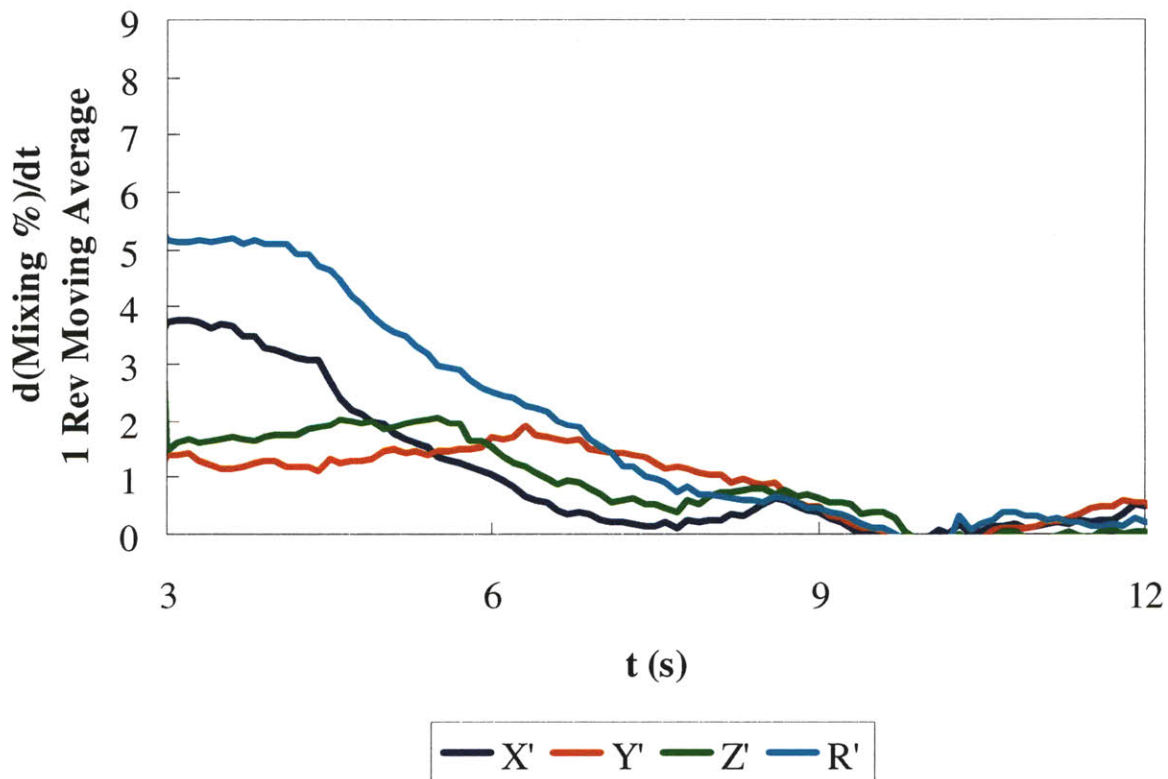


Figure 59: Rate of mixing for X, Y, Z and R initial position coloring for an eighth scale double helical ribbon blender with lactose and caffeine particles operating at 20 RPM with 0.0035 g/s inflow.

Like the movement of centroids, the rate of mixing decreases progressively in all directions over the first 3 revolutions (9 seconds) of the blender (Figure 59). At 4 revolutions (12 seconds), none of the initial position groups has mixed to more than 25% of homogeneity, and the challenging axial mixing is only at 10%.

While the average particle will ultimately spend another 10 revolutions in the blender, it seems unlikely that the blend will achieve full homogeneity in the DEM simulation given that there is little quantitative indication that the initial position groups are mixing much past 3 revolutions of the blender. This does not contradict the fact that Pernenkil [4] was able to experimentally measure VRRs in the hundreds for the lab scale blender at the same operating conditions. The VRR measurement used by Pernenkil was examining changes in variance for a tracer material at the output of the blender, whereas the quantitative mixing measure is examining homogeneity for the entire blender. In addition, even with VRRs in the hundreds, the output of Pernenkil's experiments still showed discernable periodic variation at the exit of the blender for his pulse inputs indicating that his blends also did not achieve complete homogeneity.

5.5 Summary of results

The DEM simulation of the double helical ribbon blender has provided new insight into the mechanisms of mixing and the dynamics of the blending process. Visualizing the blender and measuring the homogeneity of the particles has produced a number of notable results:

1. The double helical ribbon blender produces complex particle flows that blend using both diffusive mixing in a tumbling avalanche and convective mixing driven by its oppositely

pitched helical ribbons. The diffusive mixing from the avalanching particles is the dominant mechanism of mixing in the radial direction. In the axial direction, both mechanisms contribute to mixing, but again diffusive mixing of the avalanching particles appears to be the more significant mechanism. This implies that efficient lifting of particles by the mixing element is essential for rapid mixing as more particles will move to a positions where they can avalanche. Unfortunately, the shape of the helical ribbon elements and the V_θ (Figure 26) profile do not suggest that the helical ribbon design is well optimized for lifting particles.

2. The shaft itself proves to be an active participant in the blending process by increasing the height necessary for particles to reach their avalanche point. In addition, the inner helical ribbon guides particles downward as they avalanche and limits their axial dispersion.
3. Particles are positionally biased towards the exit region. This creates a situation where the fill fraction of the blender is much higher near the exit than it is near the inlet. This is shown to adversely affect diffusive mixing which is visible in the granular temperature profiles (Figure 28). The higher fill fraction regions decrease the distance the avalanching particles fall as well as their velocity. Ultimately, this leads to significantly less mixing for the exit half of the blender and an inefficient use of the blender volume. Modifying the size or quantity of outflow ports could improve the homogeneity of particle blends by creating a more even fill fraction throughout the blender.
4. Particles initially positioned near the blender shell mix slower than particles positioned near the central shaft. This is due to the generally outward radial velocity of the avalanching particles. Due to the positioning of the exit ports, this also creates the possibility of particles short circuiting through the blender along a path near the shell.

5. The rate of mixing decreases significantly over the first 3 revolutions of the blender and subsequent revolutions do little to increase the homogeneity of the blend. Based on the quantitative mixing measure, this implies that the initial position groups will not achieve much more than 25% homogeneity in the radial direction and 10% homogeneity in the axial direction. However, this level of homogeneity may be sufficient for actual operations.
6. Using a one eighth scale reduction of the blender appears to be a reasonable compromise between model accuracy and computation time. The simulation proves to be reasonably accurate in modeling the exit flow rates when verified against the expected scaled experimental values. To reasonably assess the blender's performance requires at least 2 revolutions and 3 months of computation time. This makes the reduced scale DEM models useful for both blender design work and long-term process development projects. Ultimately, a truly effective parallel computing solution should allow for larger scale simulations for similar computation times.

6 EFFECTS OF PARTICLE PROPERTIES

This chapter examines the effects of particle properties on the flow behavior and homogeneity of particles in the double helical ribbon blender. Three aspects of the particle's properties were explored: particle size, polydispersity and cohesive force.

6.1 Particle size simulations

To explore the effects of particle size on powder flow and blending performance, three simulations were conducted. The simulation operating conditions are modeled on those used by Lin [85] for residence time distribution experiments (Table 22).

Table 22: Summary of model conditions for DEM simulations comparing the effects of particle size.

Blender Scale	Shaft	Material	d_{particle} μm	Polydispersity	Cohesion	Ω <i>RPM</i>	Q_{inflow} <i>mg/s</i>	Fill Fraction <i>frac</i>
"1/8"	Ribbon	Lactose	100	Monodisperse	Standard	20	3.3	0.46
"1/8"	Ribbon	Lactose	200	Monodisperse	Standard	20	3.3	0.46
"1/8"	Ribbon	Lactose	300	Monodisperse	Standard	20	3.3	0.46

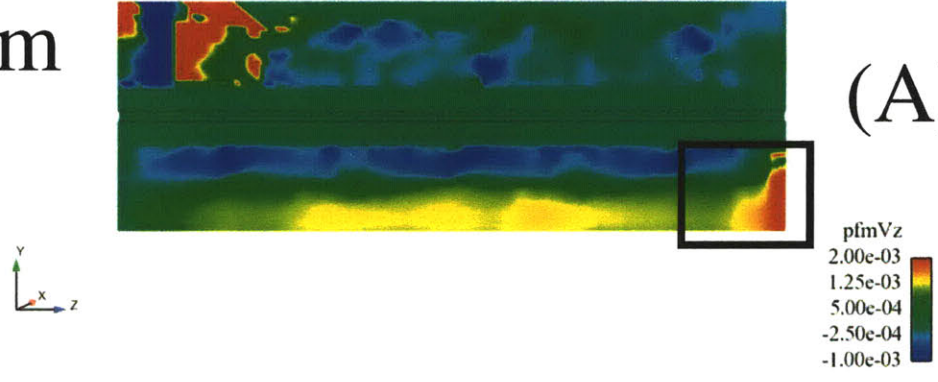
The DCL 11 grade lactose used in many of Pernenkil's [4] and Lin's [85] experiments has a mean particle size of 100 microns and was chosen as the lower size for the particle size simulations. Two larger particle sizes were chosen for comparison, 200 microns and 300 microns.

6.2 Comparison of powder flows for particle size

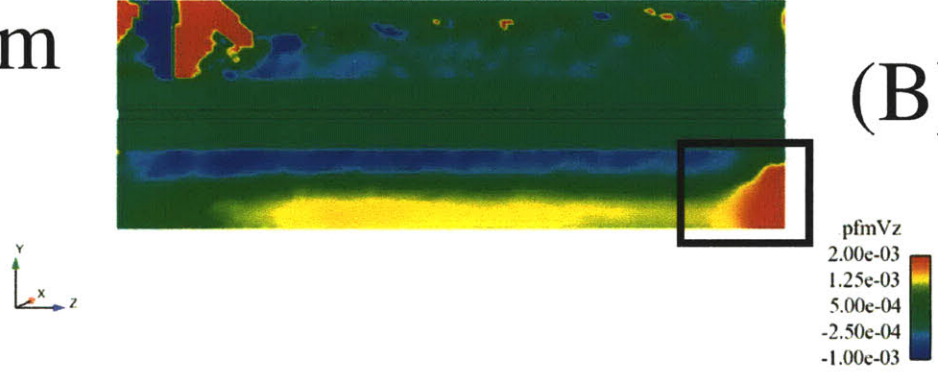
6.2.1 Particle velocities

The YZ cross sections of V_z are similar along the Z axis for the various particle sizes (Figure 60 A, B, C). The primary differences occur near the exit where the larger particle sizes generally have a larger contour of high velocity (black boxes in Figure 60 A, B, C). The larger contour of higher velocity for the 300 micron particles (Figure 60 C) indicates that these particles are more easily driven by the outer helical ribbon of the blender which should result in higher flow rates at the exit of the blender.

100 μm (A)



200 μm (B)



300 μm (C)

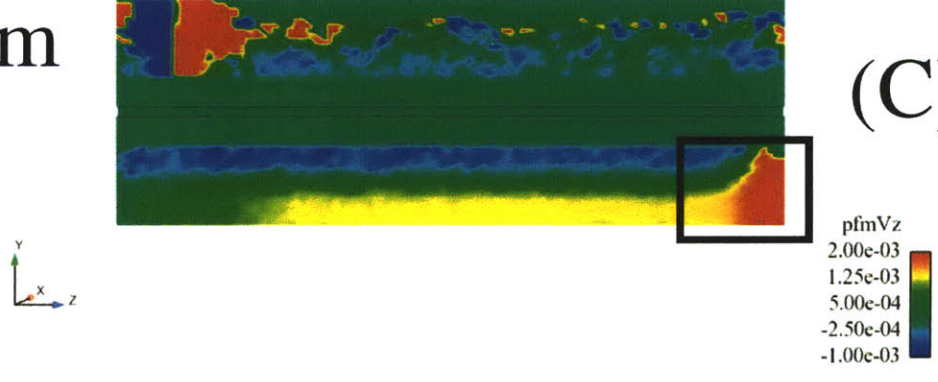
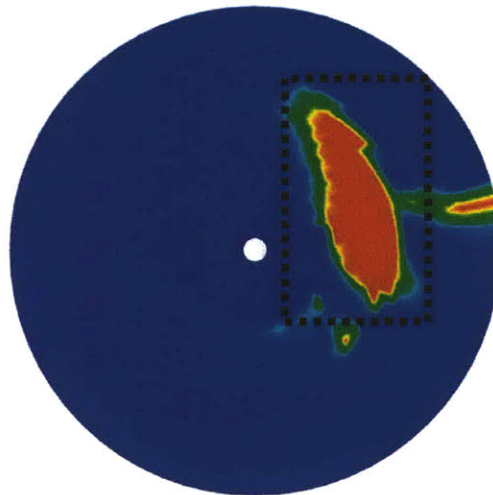


Figure 60: YZ cross section showing Z component of velocity in m/s for an eighth scale double helical ribbon blender with 100, 200 and 300 micron lactose particles operating at 20 RPM and a 0.0033 g/s inflow.

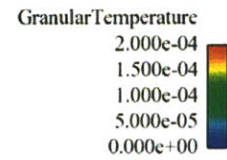
6.2.2 Granular temperature

The highest granular temperature contour in the XY cross section (Figure 61 A, B, C) demonstrates a consistent trend of larger areas for larger particle sizes. Spatially, the avalanche region where granular temperature is the highest extends further towards the blender shell as one increases particle size. The 300 micron particle simulation's high granular temperature contour (black box in Figure 61 C) extends all the way from the central shaft to the blender shell. In contrast, the 100 micron particle simulation's high granular temperature contour (dashed black box in Figure 61 A) only extends to the radial end point of the inner helical ribbon. This indicates that the larger particles will homogenize faster in the radial direction than the smaller particles. In the dense particle bed at the bottom the blender, there is also an indication that the larger particles are able to achieve more diffusive mixing between the ribbon blades further enhancing their ability to create more homogenous blends.

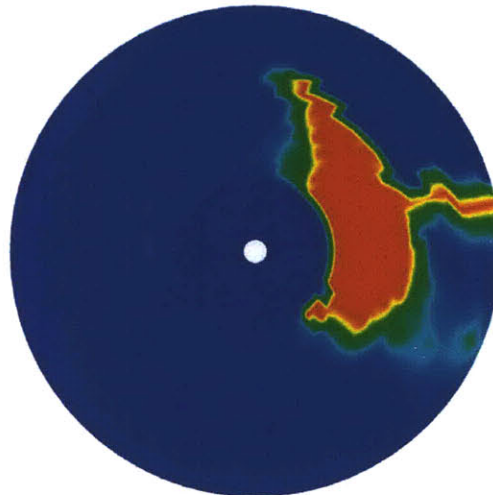
100 μm



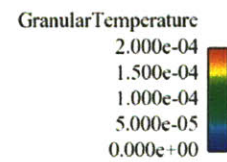
(A)



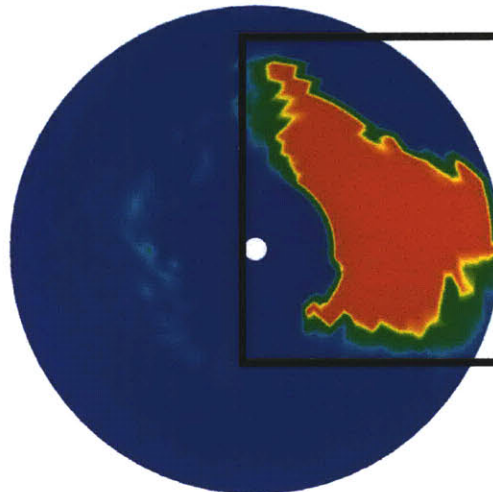
200 μm



(B)



300 μm



(C)

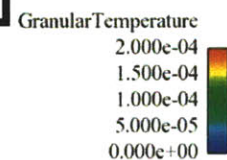
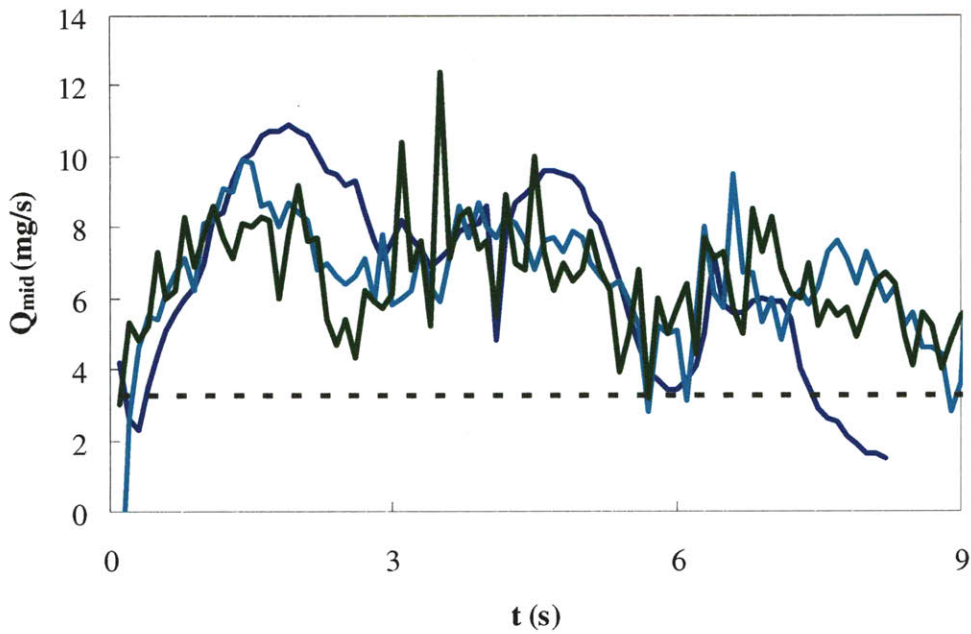


Figure 61: XY cross section showing granular temperature for an eighth scale double helical ribbon blender with 100, 200 and 300 micron lactose particles operating at 20 RPM and a 0.0033 g/s inflow.

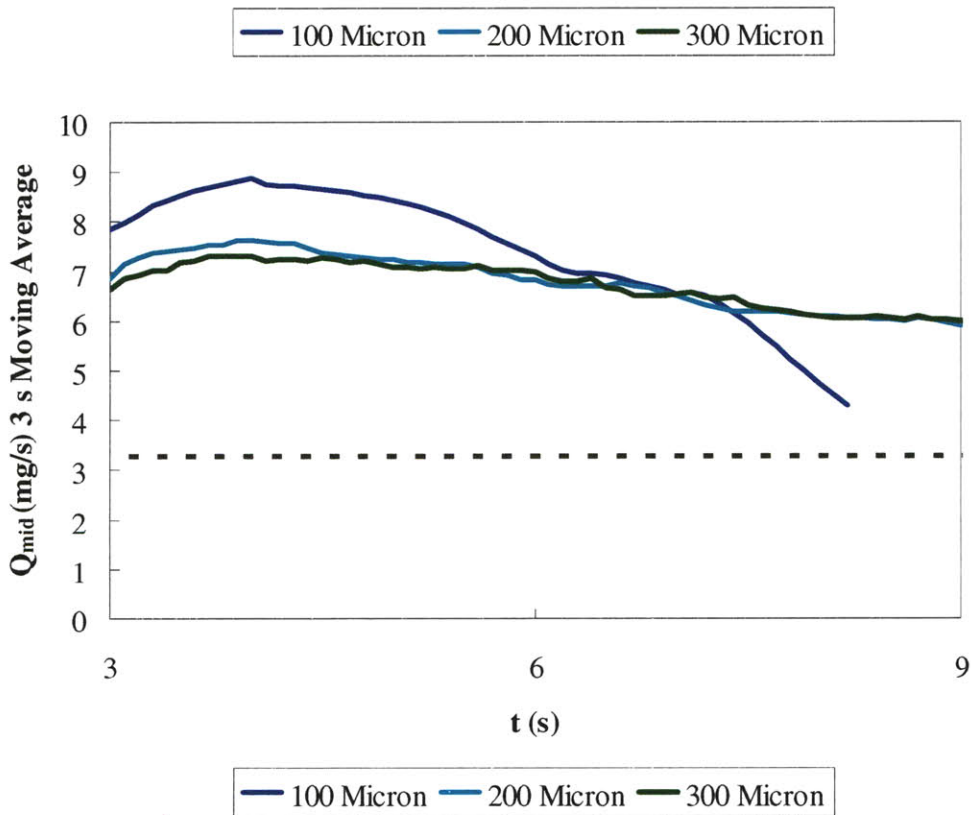
6.2.3 Flow rate

The flow rate in the middle of the blender (Figure 62 A, B) is generally higher for the 100 micron particles and is comparable for the 200 and 300 micron particles. As one increases the particle size, the flow rate becomes less consistent with significant spikes and lulls. The flow rates in the middle of the blender are significantly greater than the inflow rate for all of the particle sizes as particles are transported towards the exit.

The flow rate at the exit of the blender (Figure 63 A, B) has the opposite trend from the flow rate in the middle of the blender with the particle size being positively correlated to flow rate. However, the variance of the flow rate is still positively correlated to particle size. Taking away the differences in amplitude and sporadic spikes in outflow, the shape of the flow rate at the exit is consistent between the three particle sizes as well. It is also notable that the 100 micron particle flow rate at the exit is near the expected inflow rate and thus is close to modeling the flow rate of the experimentally measured blender.



(A)



(B)

Figure 62: Flow rate in mg/s at the middle of an eighth scale double helical ribbon blender with 100, 200 and 300 micron lactose particles operating at 20 RPM and a 0.0033 g/s inflow.

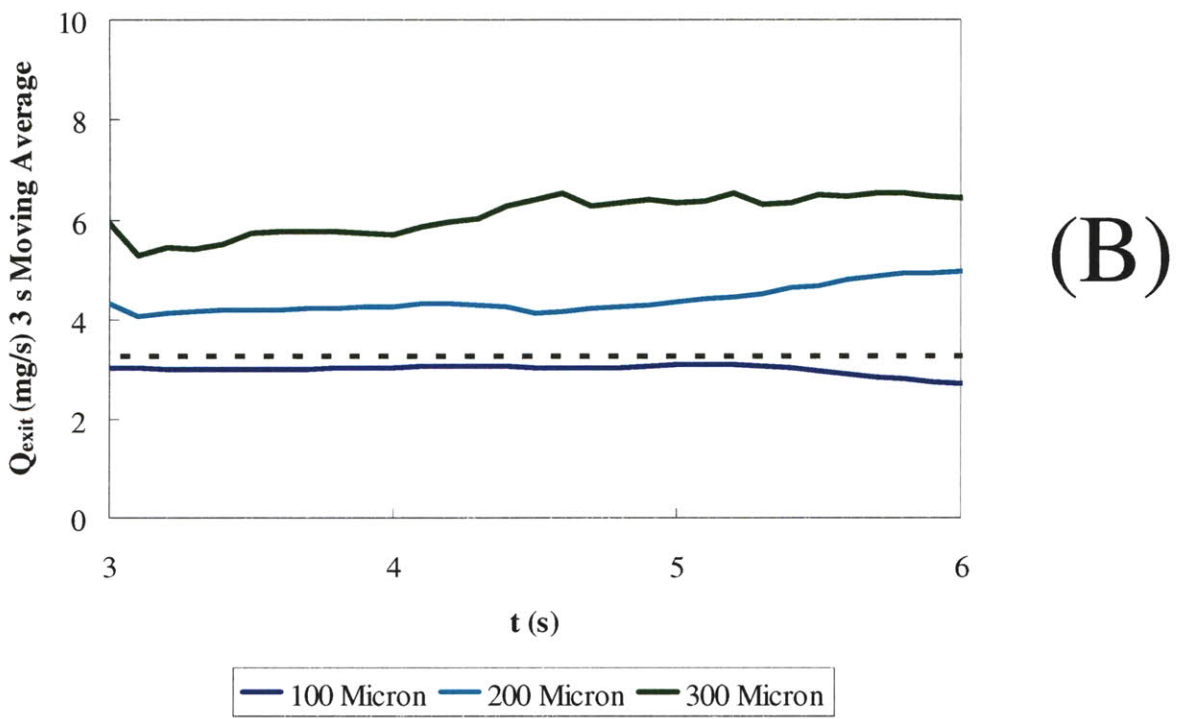
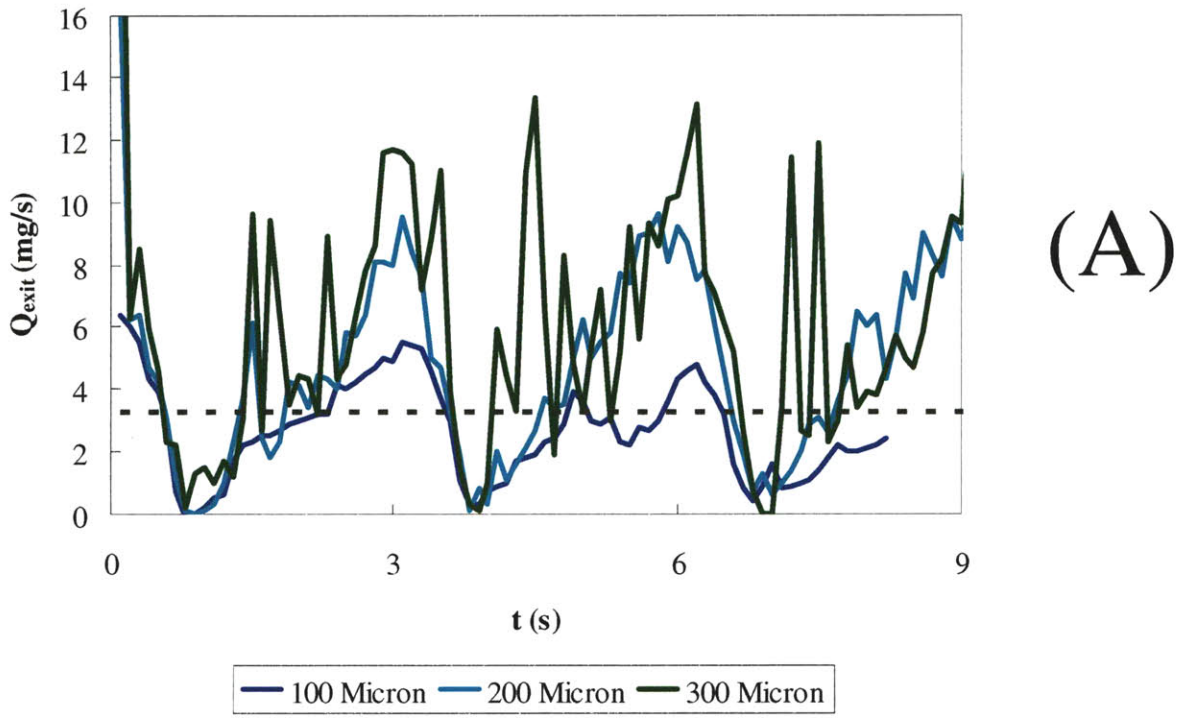


Figure 63: Flow rate in mg/s at the exit of an eighth scale double helical ribbon blender with 100, 200 and 300 micron lactose particles operating at 20 RPM and a 0.0033 g/s inflow

6.3 Mixing results for particle size simulations

6.3.1 Quantitative mixing measure

The homogeneity (mixing %) of the X and Y initial position groups (Figure 64 A, B) corroborates what one would expect from the granular temperature data with mixing favoring the larger particles once material begins avalanching over the shaft (~1.5 seconds from the start of the simulation). However, after the first avalanche of material, the mixing rates of the 200 and 300 micron particles are quite similar. The 100 micron particles lag significantly behind the 200 and 300 micron particles with a 60% lower mixing % at 1 revolution (3 seconds). The homogeneity (mixing %) of the Z and R initial position groups (Figure 65 A, B) also shows little difference between the 200 and 300 micron particles. Again, the 100 micron particle initial position groups are not nearly as homogenous as the 200 and 300 micron particle initial position groups.

The mechanism of mixing appears to be similar for all of the particle sizes with diffusive mixing of avalanching particles the dominant contributor. Granular temperature profiles indicate that the 100 micron particles have a much narrower area where particles randomize and mix. This results in lower blend homogeneity and is clearly shown by this quantitative mixing measure.

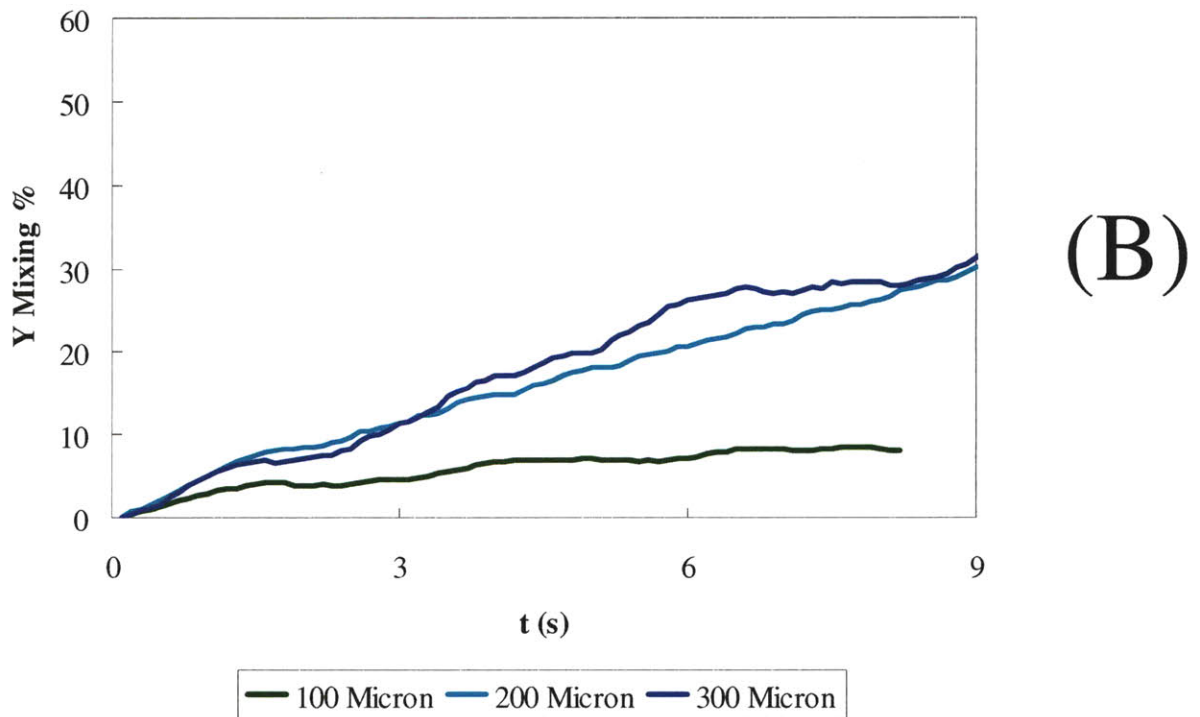
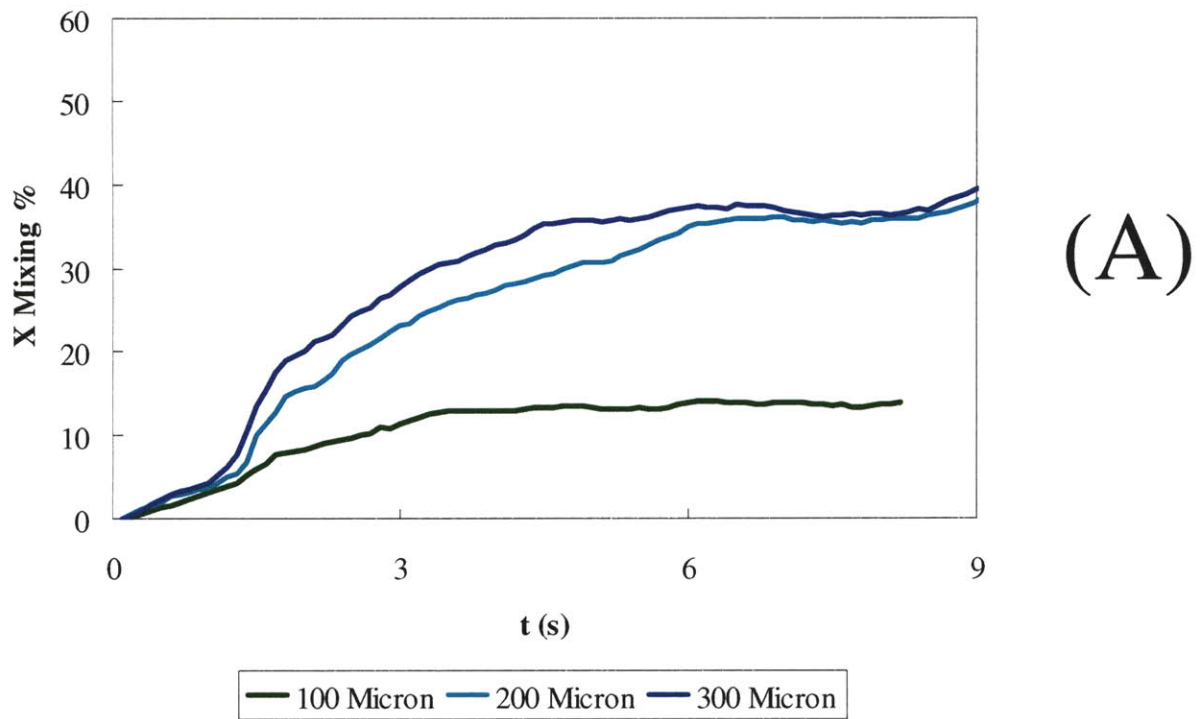
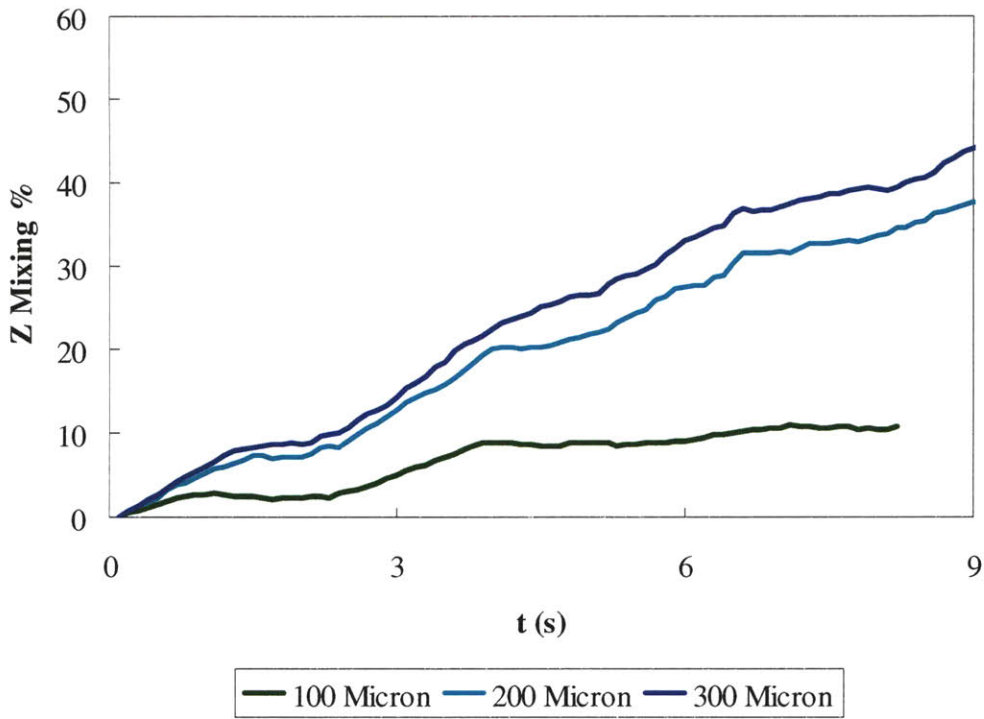
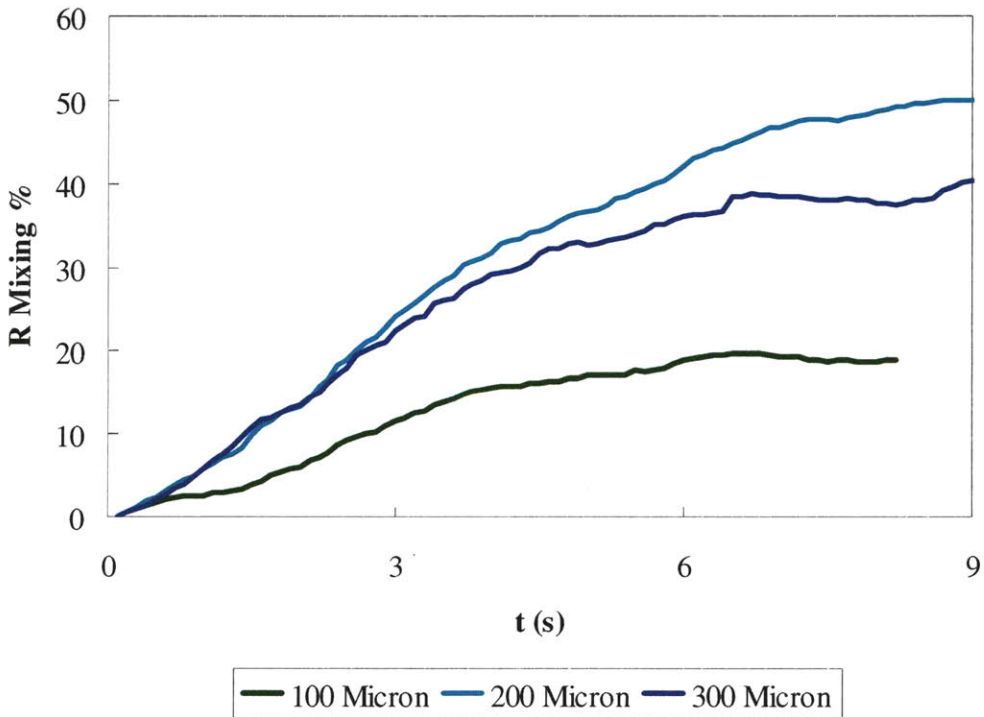


Figure 64: Homogeneity (mixing %) for X and Y initial position groups in an eighth scale double helical ribbon blender with 100, 200 and 300 micron lactose particles operating at 20 RPM and a 0.0033 g/s inflow.



(A)



(B)

Figure 65: Homogeneity (mixing %) for Z and R initial position groups in an eighth scale double helical ribbon blender with 100, 200 and 300 micron lactose particles operating at 20 RPM and a 0.0033 g/s inflow.

6.4 Polydispersity simulations

To explore the effects of polydispersity on powder flow and blending performance two simulations were conducted. The simulation operating conditions are modeled on those used by Lin [85] for residence time distribution experiments (Table 23).

Table 23: Summary of model conditions for DEM simulations comparing the effects of polydispersity.

Blender Scale	Shaft	Material	d_{particle} μm	Polydispersity	Cohesion	Ω <i>RPM</i>	Q_{inflow} <i>mg/s</i>	Fill Fraction <i>frac</i>
"1/8"	Ribbon	Lactose	200	Monodisperse	Standard	20	3.3	0.46
"1/8"	Ribbon	Lactose	200	Polydisperse	Standard	20	3.3	0.46

Both simulations started with an initial fill mass of monodisperse lactose particles with a mean particle size of 200 microns. The monodisperse simulation's inflow used monodisperse 200 micron lactose particles. The polydisperse simulation had an inflow with lactose particles evenly distributed in size between 150 and 250 microns.

6.5 Flow behavior results for polydispersity simulations

6.5.1 Flow rate

The periodic nature of the flow rate in the middle blender (Figure 66) is the same whether there is a polydisperse inflow or a monodisperse inflow. The flow rates for the two polydispersities are also relatively similar in magnitude. This indicates that polydispersity does not significantly affect the flow rates.

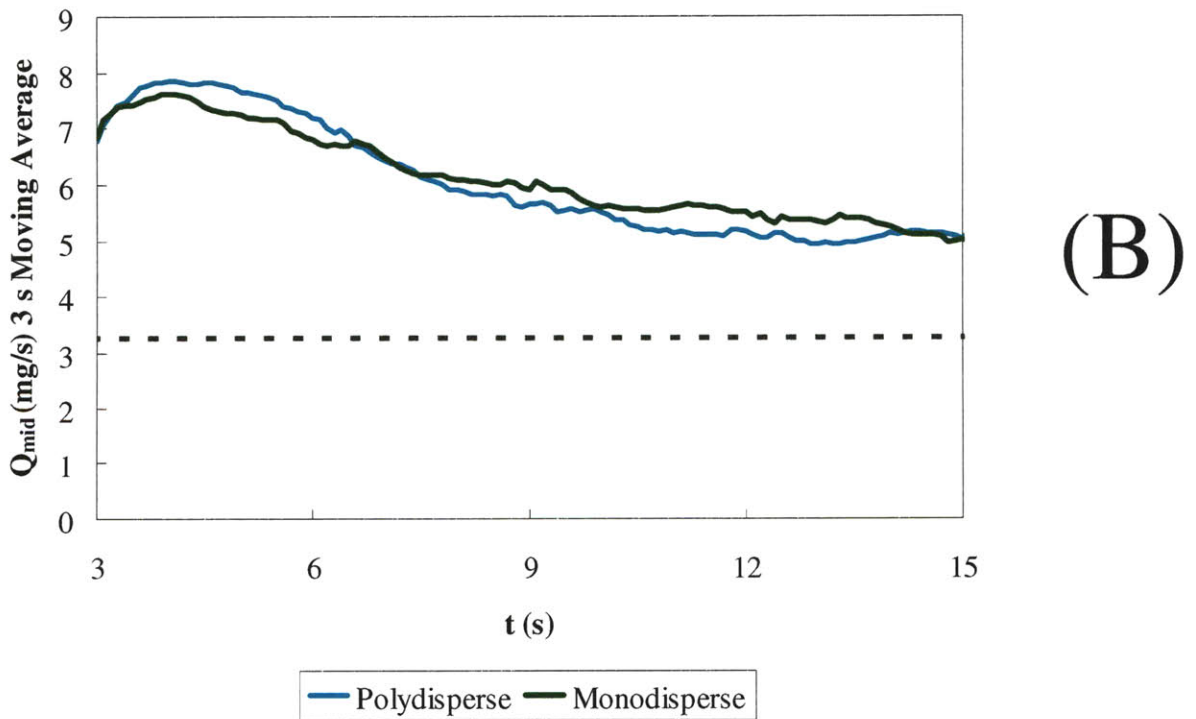
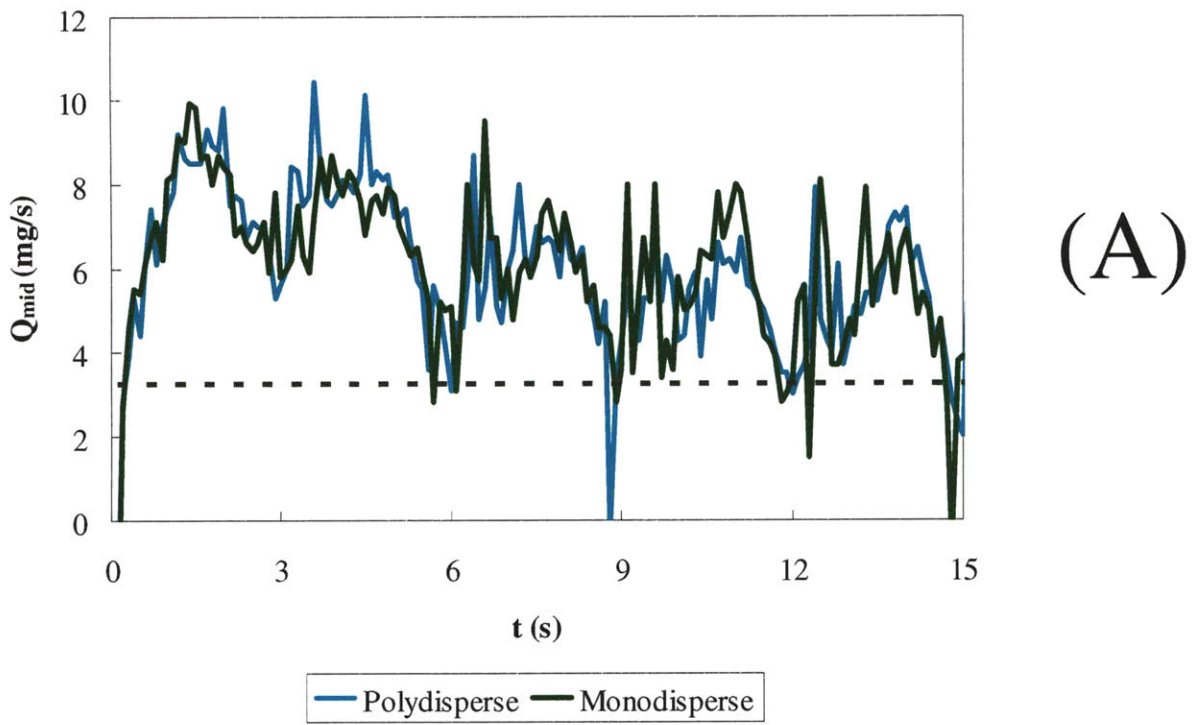


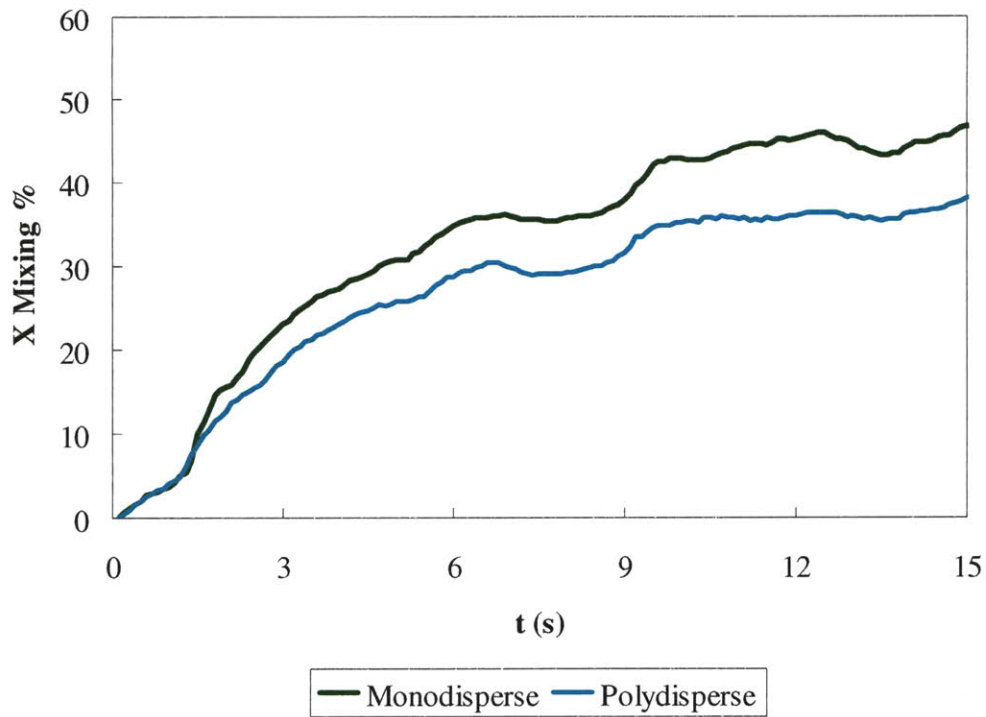
Figure 66: Flow rate in mg/s at the middle of an eighth scale double helical ribbon blender with 200 micron monodisperse and 200 micron polydisperse lactose particles operating at 20 RPM and a 0.0033 g/s inflow.

6.6 Mixing results for polydispersity simulations

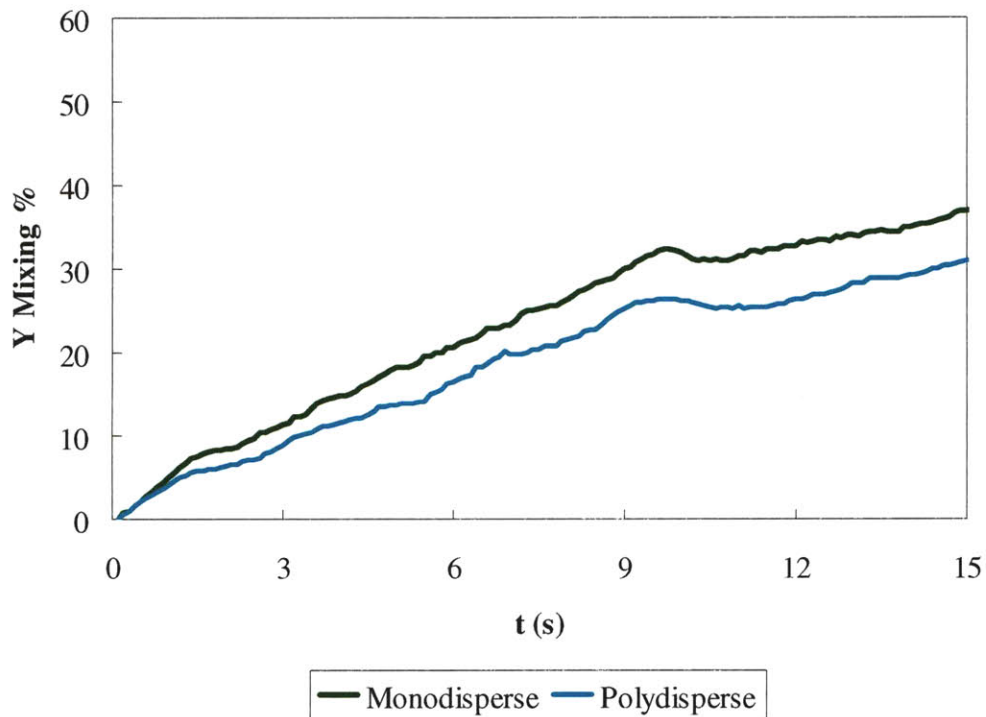
6.6.1 Quantitative mixing measure

The homogeneity for the X and Y initial position groups (Figure 67 A, B) is slightly greater for the monodisperse particles than for the polydisperse particles. The greater homogeneity of the Y initial position groups for the monodisperse particles is due to their periodically higher mixing rate. The period of the mixing rate is 1 revolution and is tied to the particles avalanching. The homogeneity of the Z and R initial position groups (Figure 68 A, B) is initially similar between the two polydispersities, but begins to favor the monodisperse particles after the first revolution and second revolution respectively. The mixing rate for the Z initial position groups (Figure 68 A) is periodic with similar amplitude for both the monodisperse and polydisperse particles. However, the shoulders of the peak are wider for the monodisperse material and this is where it achieves a higher homogeneity.

Generally, the monodisperse particles have periods of greater mixing rate interspersed with periods of similar mixing rate to the polydisperse particles. This behavior indicates that increasing polydispersity is affecting the particles as they are avalanching and is reducing the diffusive mixing.



(A)



(B)

Figure 67: Homogeneity (mixing %) for X and Y initial position groups in an eighth scale double helical ribbon blender with 200 micron monodisperse and 200 micron polydisperse lactose particles operating at 20 RPM and a 0.0033 g/s inflow.

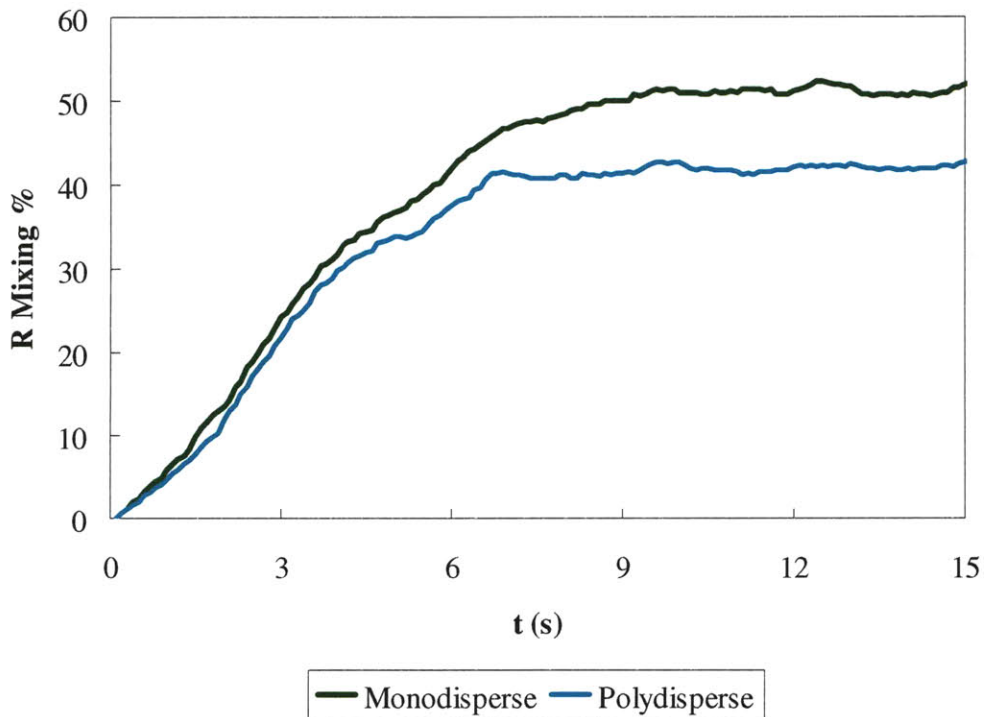
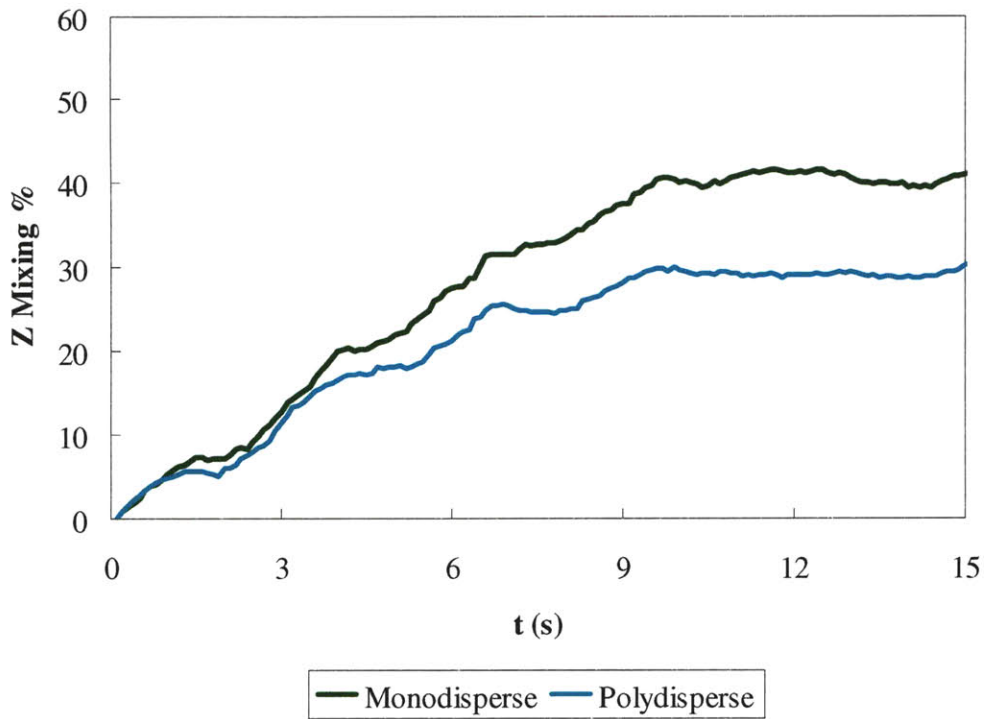


Figure 68: Homogeneity (mixing %) for Z and R initial position groups in eighth scale double helical ribbon blender with 200 micron monodisperse and 200 micron polydisperse lactose particles operating at 20 RPM and a 0.0033 g/s inflow.

6.7 Cohesive force simulations

To explore the effects of cohesive forces on powder flow and blending performance, four simulations were conducted. The simulation operating conditions are modeled on those used by Pernenkil [4] for blending and residence time distribution experiments (Table 24).

Table 24: Summary of model conditions for DEM simulations comparing the effects of cohesive forces.

Blender Scale	Shaft	Material	d_{particle} μm	Polydispersity	Cohesion	Ω RPM	Q_{inflow} mg/s	Fill Fraction frac
"1/8"	Ribbon	Lactose	300	Monodisperse	None	20	3.5	0.48
"1/8"	Ribbon	Lactose	300	Monodisperse	Low	20	3.5	0.48
"1/8"	Ribbon	Lactose	300	Monodisperse	Standard	20	3.5	0.48
"1/8"	Ribbon	Lactose	300	Monodisperse	High	20	3.5	0.48

The particles, however, have been modified for this simulation with larger 300 micron monodisperse lactose particles with varying cohesive force. Four cohesive forces were used for these simulations: “None” has no (0%) cohesive forces; “Low Cohesion” has cohesive forces equivalent to 50% of the experimental measured lactose cohesive force; “Standard Cohesion” has the standard (100%) experimentally measured cohesive force; “High Cohesion” has cohesive forces equivalent to 150% of the experimental measured lactose cohesive force.

6.8 Flow behavior results for cohesive force simulations

6.8.1 Volume fraction

As the cohesive forces between the particles increases, more particles are lifted over the central shaft and more particles are retained in the blender (Figure 69).

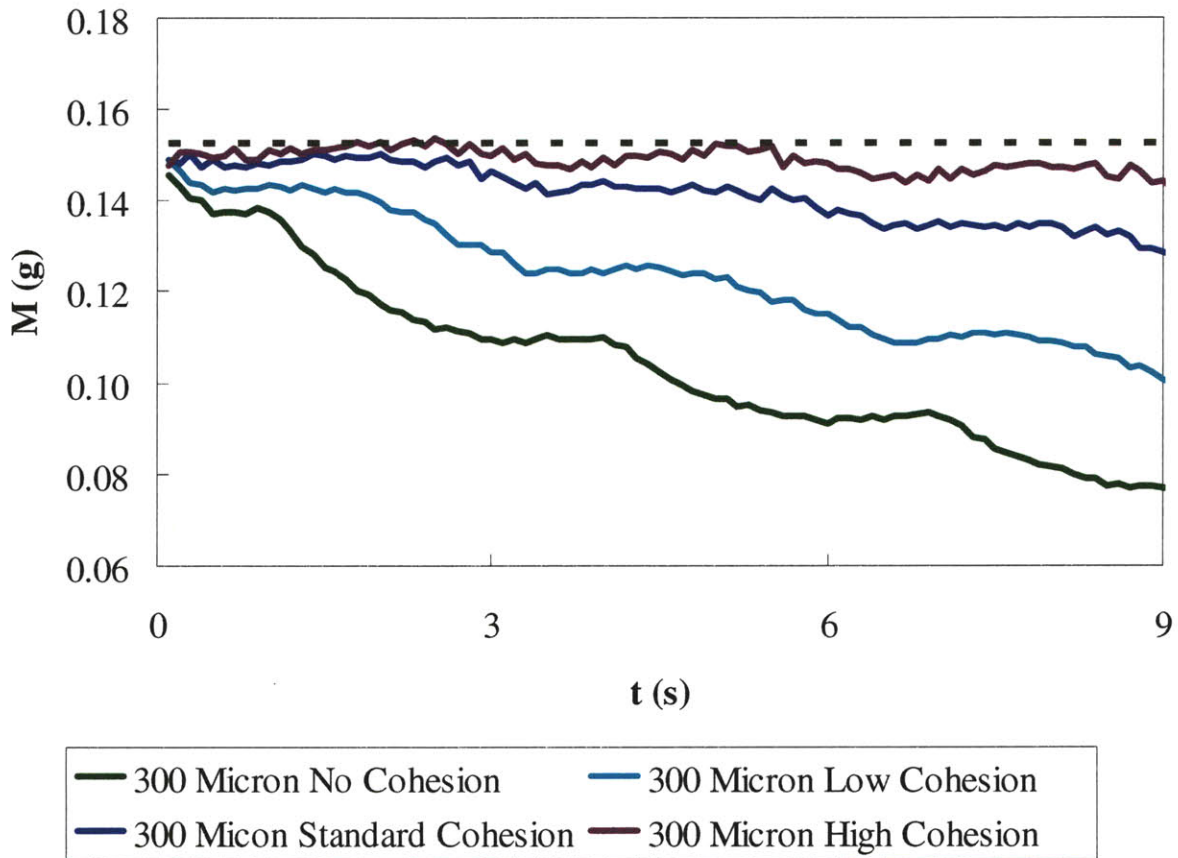
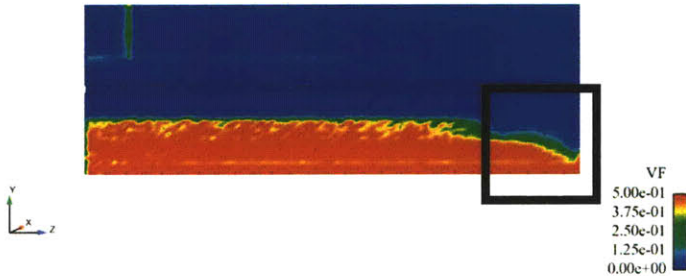


Figure 69: Fill weight in g of an eighth scale double helical ribbon blender with 300 micron lactose particles with 0%, 50%, 100% and 150% of the standard experimentally measured cohesion operating at 20 RPM and a 0.0035 g/s inflow.

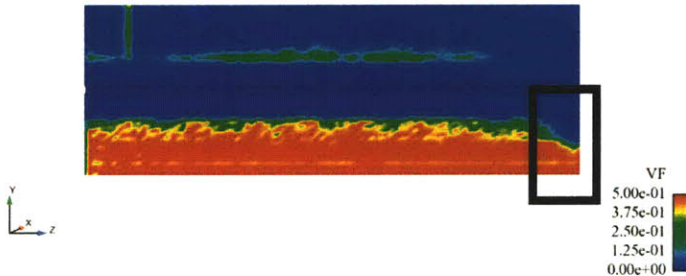
The standard cohesion (Figure 70 C) and high cohesion (Figure 70 D) demonstrate similar YZ volume cross sections to the previous simulation with smaller particles. With these cohesive forces, particles are positionally biased towards the exit side of the blender with higher volume fractions in the exit region (black arrows in Figure 70 C, D).

None



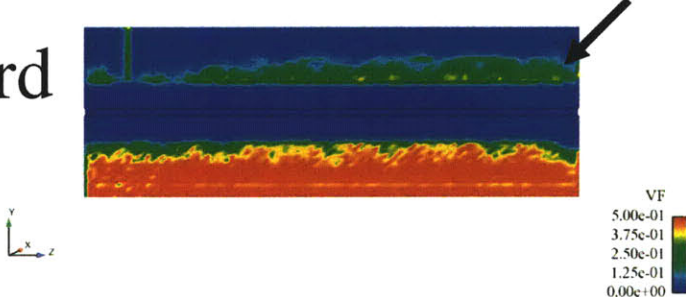
(A)

Low



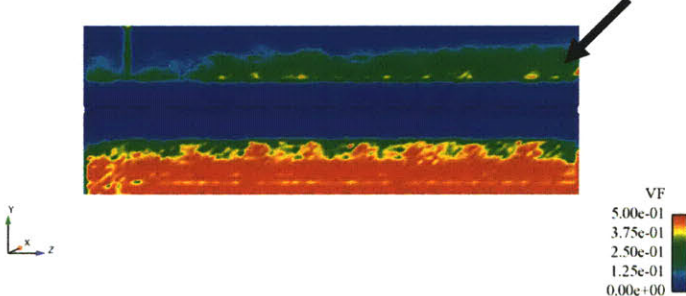
(B)

Standard



(C)

High



(D)

Figure 70: YZ cross section showing volume fraction for an eighth scale double helical ribbon blender with 300 micron lactose particles operating at 20 RPM and a 0.0035 g/s inflow.

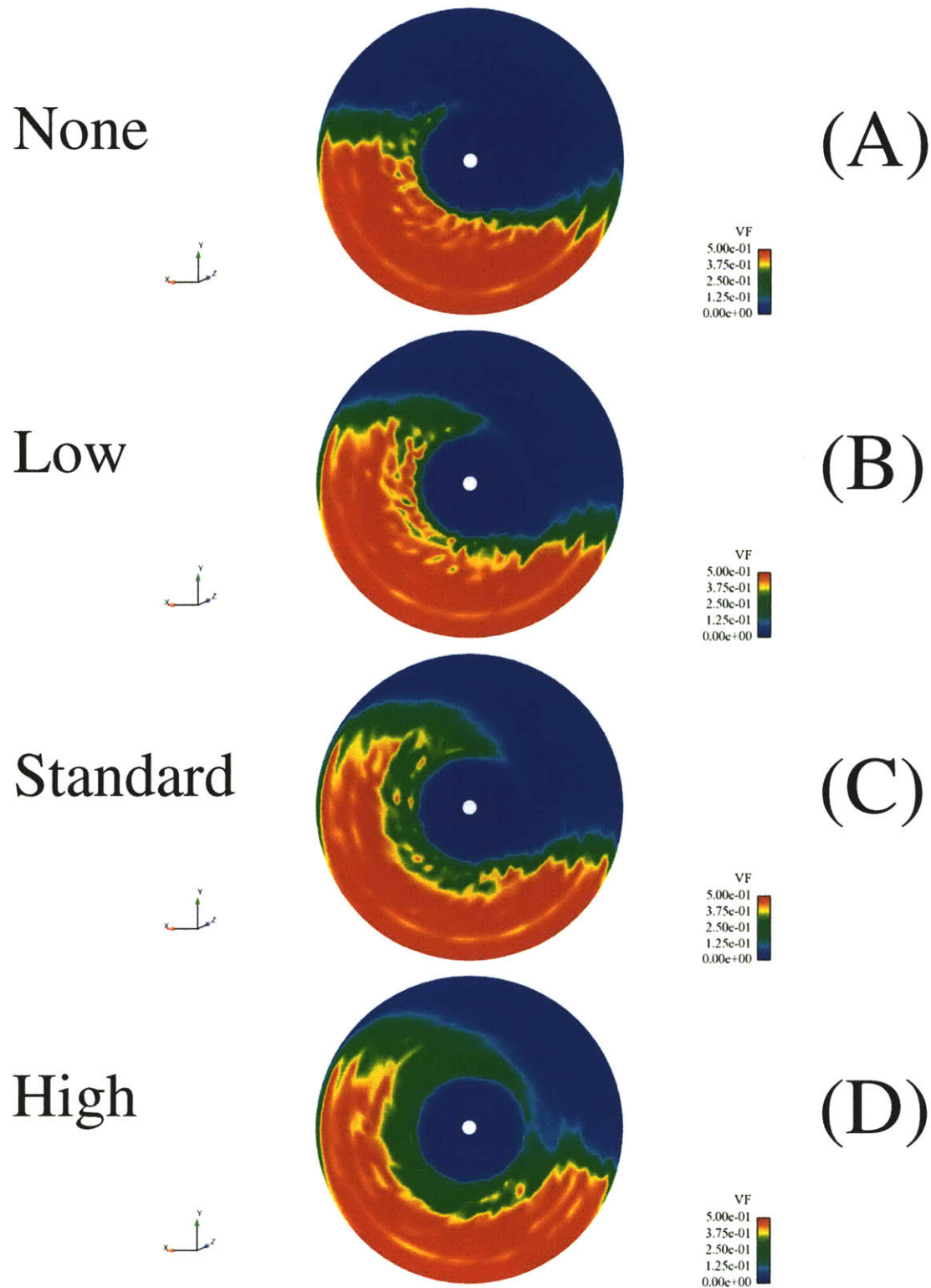


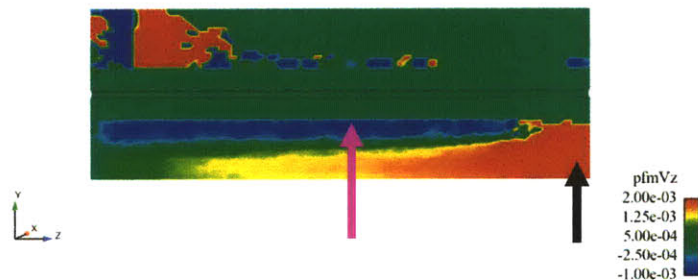
Figure 71: XY cross section showing volume fraction for an eighth scale double helical ribbon blender with 300 micron lactose particles operating at 20 RPM and a 0.0035 g/s inflow.

The no cohesion (Figure 70 A) and low cohesion (Figure 70 B) simulations show the opposite effect with particles biased towards the inlet side of the blender. In the no cohesion simulation (Figure 71 A), very few particles are travelling over the shaft and avalanching into the particle bed. This is caused by fewer particles being in the blender due to its higher exit flow rate and lower fill mass (Figure 69), as well as the particles not being lifted as easily by the ribbons. This can be seen in the XY cross section of volume fraction where the dense particle bed of the no cohesion simulation (Figure 71 A) has a much lower surface angle than the simulations with cohesive forces (Figure 71 B, C, D). The more freely flowing particles without cohesive forces will fall back between the ribbons rather than being lifted over the shaft.

6.8.2 Velocity

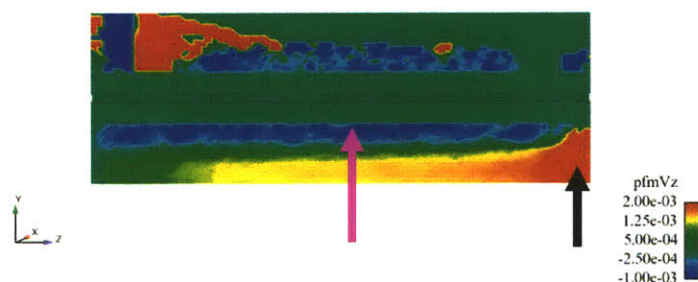
In the YZ volume fraction profile, one sees the height of the powder bed dipping towards the exit ports in the no cohesion (black box in Figure 70 A) and low cohesion simulations (black box in Figure 70 B). This appears to be the result of a considerable acceleration in Z velocity as particles near the exits (Figure 72 A, B). For all of the different cohesive forces, there is a high velocity contour near the exit (black arrows in Figure 72 A, B, C, D), but in the no cohesion and low cohesion case this contour reaches back to near the axial middle of the blender. Importantly for convective mixing, the no cohesion and low cohesion simulations also have a higher negative V_z in the reverse conveying region of the blender near the central shaft (magenta arrows in Figure 72 A, B).

None



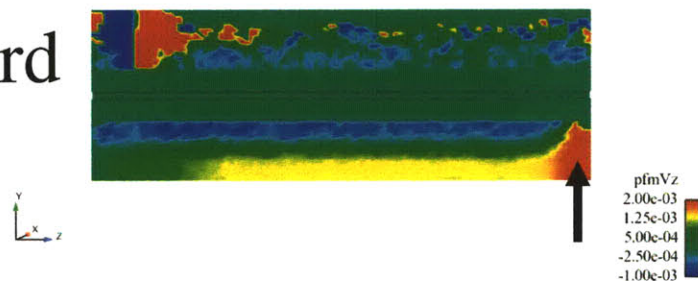
(A)

Low



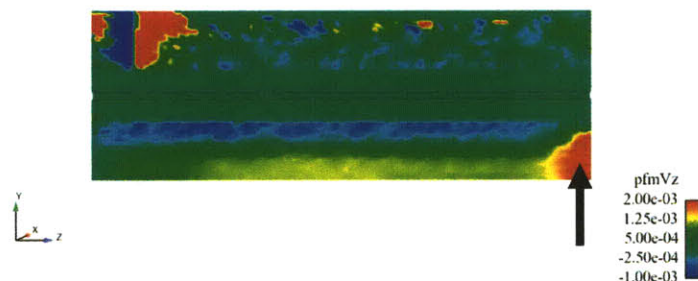
(B)

Standard



(C)

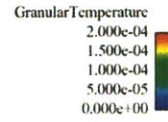
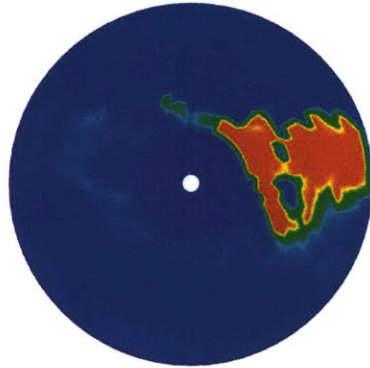
High



(D)

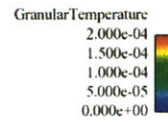
Figure 72: YZ cross section showing Z velocity for an eighth scale double helical ribbon blender with 300 micron lactose particles operating at 20 RPM and a 0.0035 g/s inflow.

None



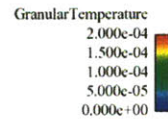
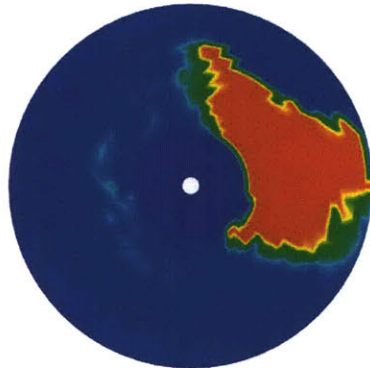
(A)

Low



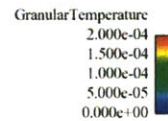
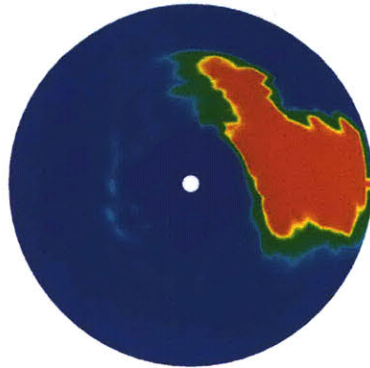
(B)

Standard



(C)

High



(D)

Figure 73: XY cross section showing granular temperature for an eighth scale double helical ribbon blender with 300 micron lactose particles operating at 20 RPM and a 0.0035 g/s inflow.

6.8.3 Granular temperature

The XY granular temperature cross sections look relatively similar for the different cohesive forces (Figure 73 A, B, C, D). There is a slight trend that increasing the cohesion force enlarges the area of the high granular contour, but this is simply the product of a greater volume of particles moving over the shaft for the higher cohesion materials.

6.8.4 Flow rate

Regardless of the cohesive force between the particles, all of the simulations exhibited significant periodic fluctuations in flow rate at both the middle (Figure 74 A, B) and exit of the blender (Figure 75 A, B). The flow rates in the middle of the blender exhibit a roughly sinusoidal oscillation in flow rate as the outer ribbon moves into and out of the particle bed. Flow rate is generally inversely proportional to cohesive force at the middle of the blender.

At the exit of the blender (Figure 75 A), the amplitude and the shape of the periodic outflows is highly dependant on the cohesive force. The particles without cohesion have a very steep rise in flow rate followed by a slow decline, while the standard and high cohesion materials have the opposite shape of a slow rise in flow rate followed by a steep decline. The low cohesion simulation seems to be somewhere in between these two extremes with a moderate rise and decline. The general trend in flow rates at the exit of the blender is that higher cohesive force leads to lower flow rates. It is interesting to see that the high cohesion simulation has very similar exit flow behavior to the lactose and caffeine particles with the standard cohesion and true size distribution seen in the previous chapter. Thus from a flow rate perspective, increasing cohesion by 50% has a similar effect as decreasing the mean particle size by a factor of 3 and increasing polydispersity.

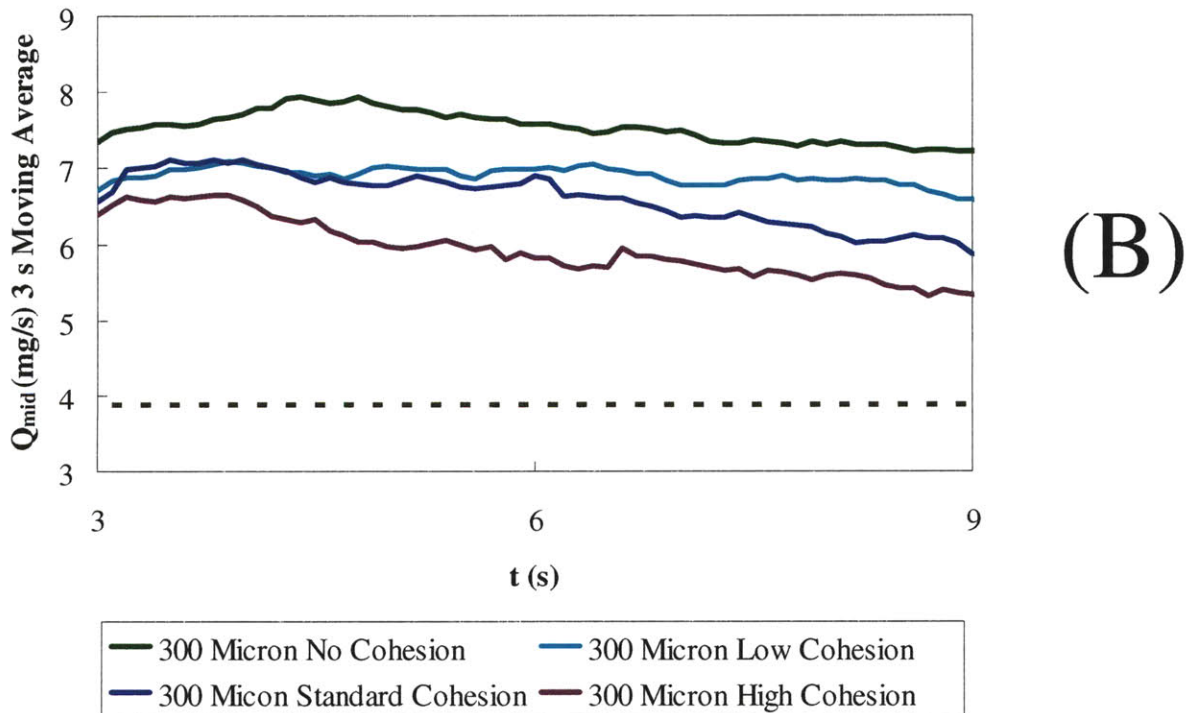
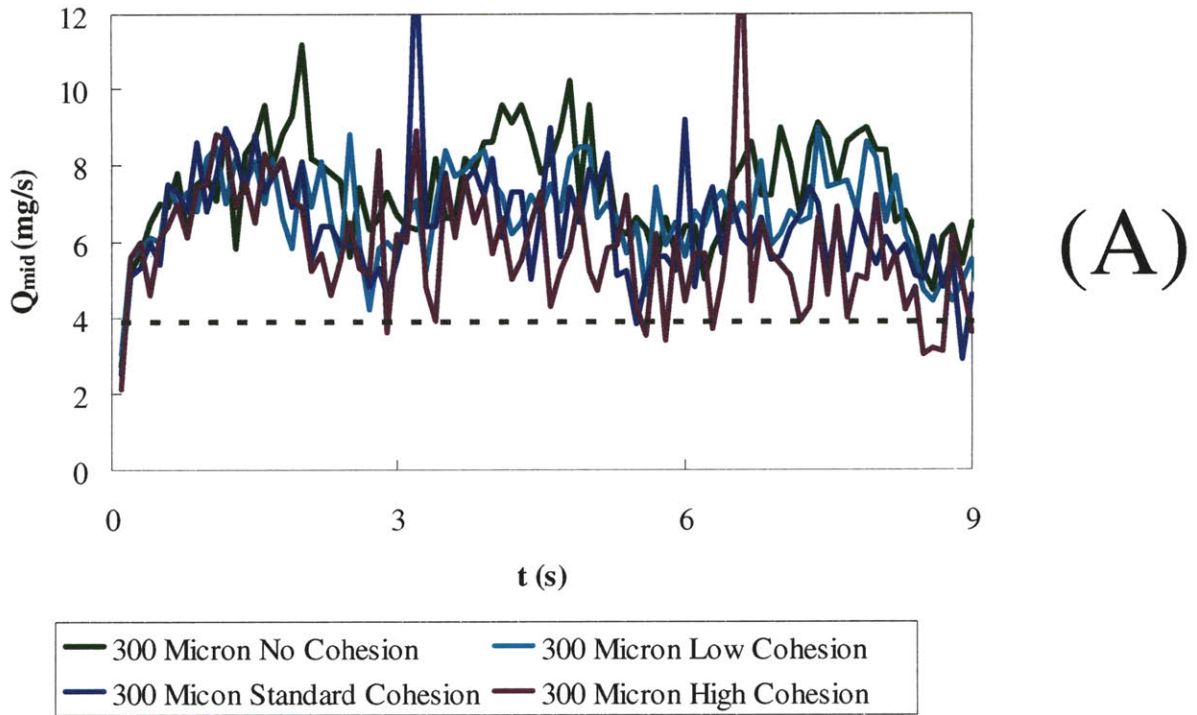
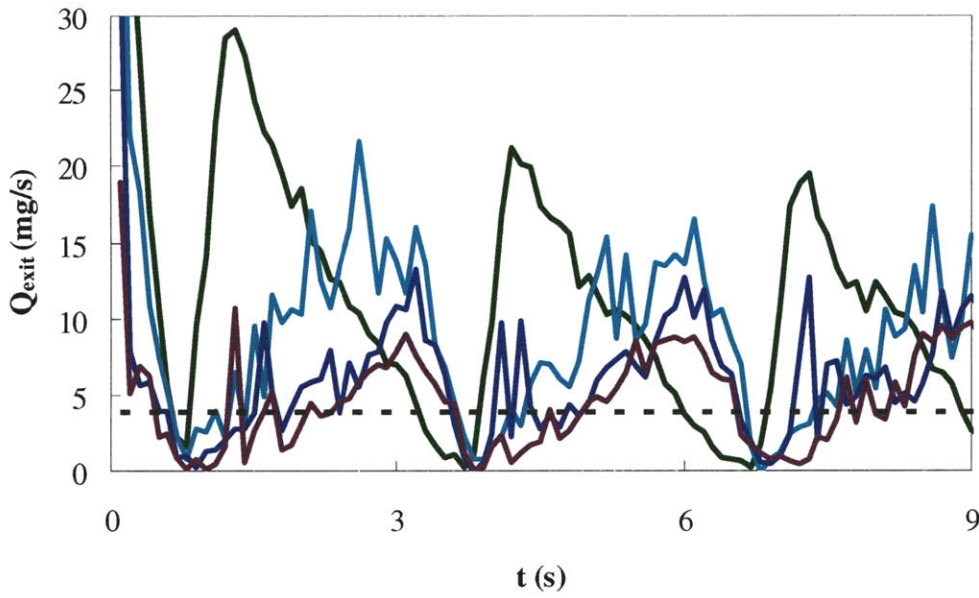
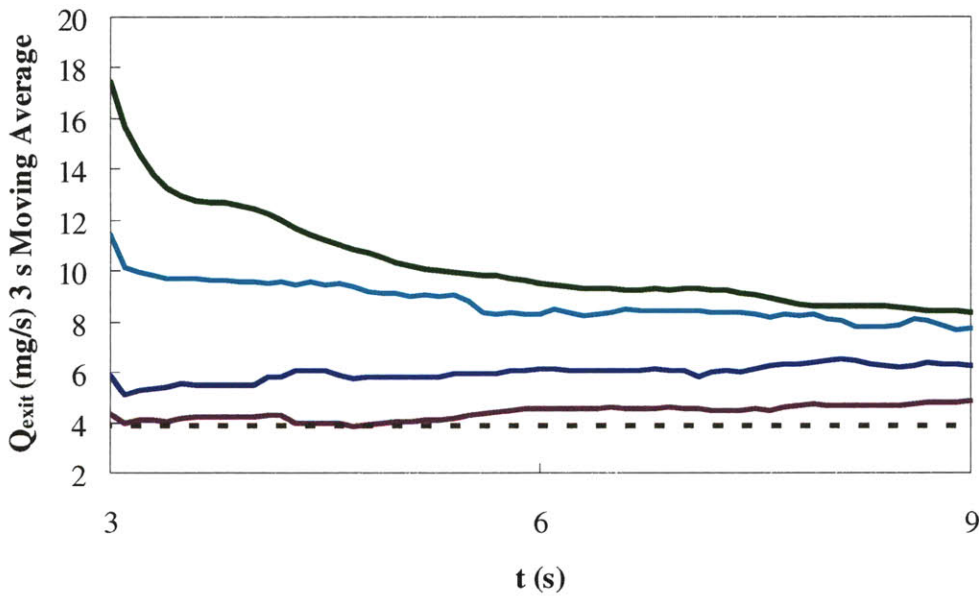


Figure 74: Flow rates in mg/s at the middle of an eighth scale double helical ribbon blender with 300 micron lactose particles with 0%, 50%, 100% and 150% of the standard experimentally measured cohesion operating at 20 RPM and a 0.0035 g/s inflow.



(A)



(B)



Figure 75: Flow rate in mg/s at the exit of an eighth scale double helical ribbon blender with 300 micron lactose particles with 0%, 50%, 100% and 150% of the standard experimentally measured cohesion operating at 20 RPM and a 0.0035 g/s inflow.

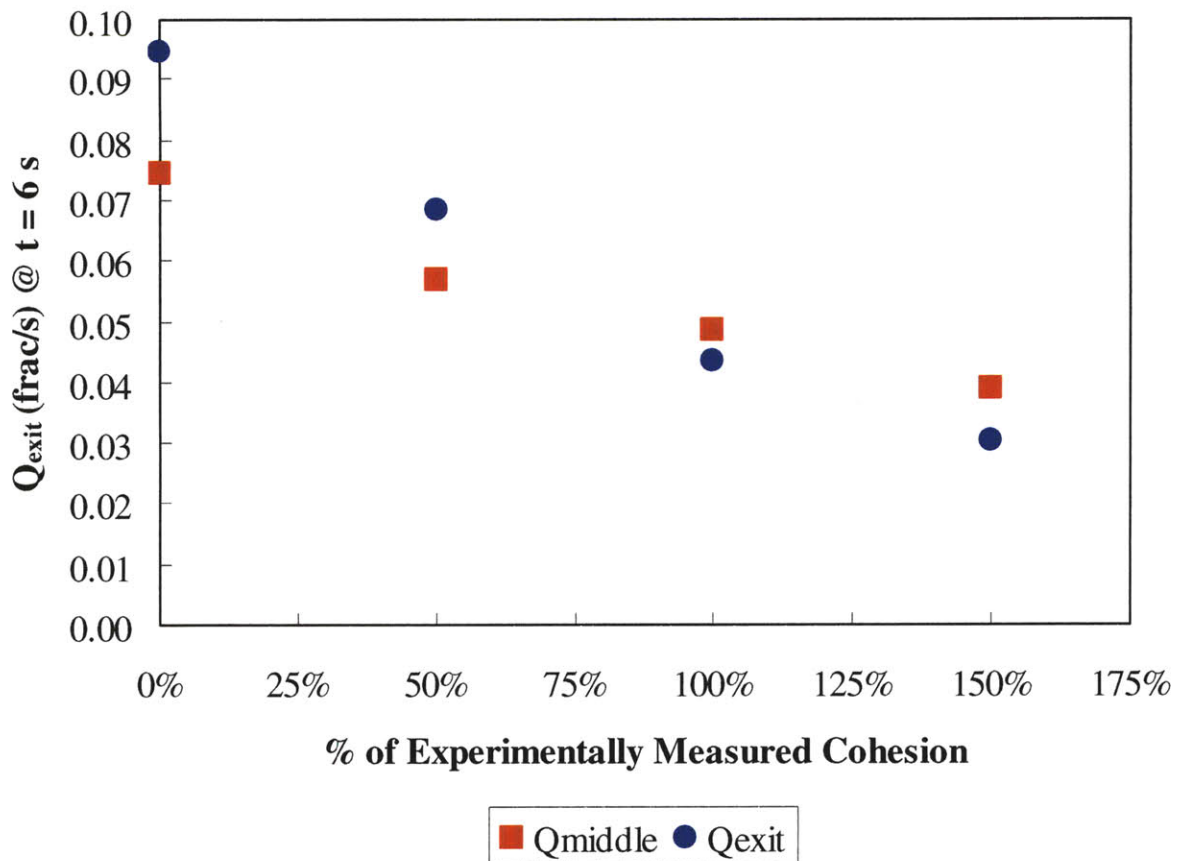


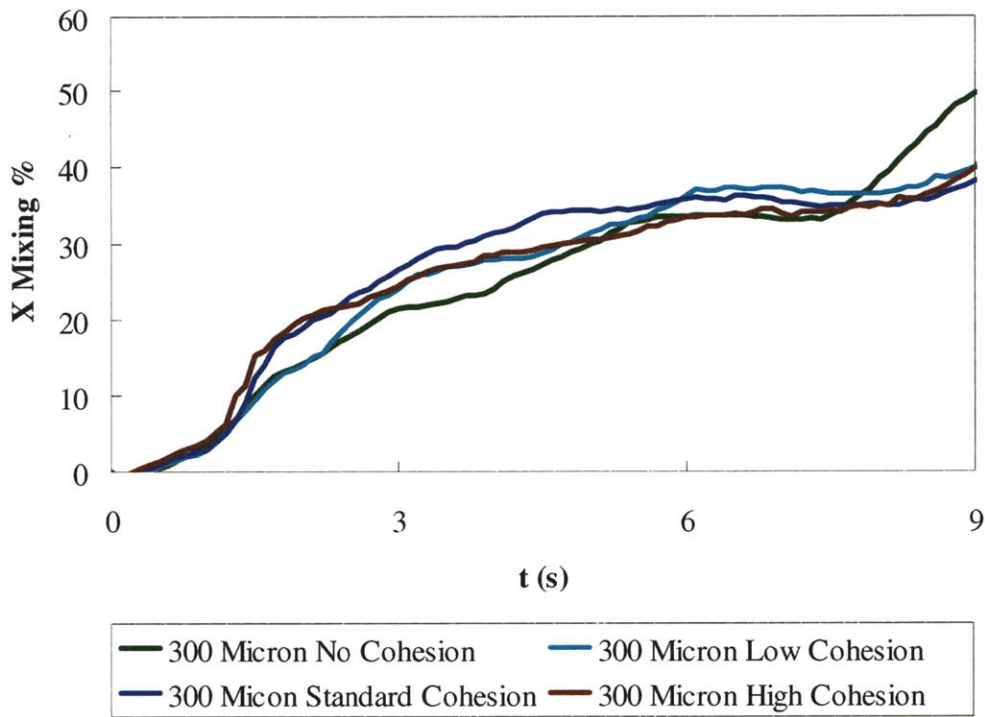
Figure 76: Flow rate normalized by the fill weight at t = 6 seconds versus % of the standard experimentally measured cohesion for exit of the double helical ribbon blender with 200 micron lactose particles operating at 20 RPM and a 0.0035 g/s inflow.

Removing the effect of the blender emptying by normalizing the flow rates to the fill weight gives a relatively consistent flow rate over the range of 3 to 9 seconds. This makes it possible to effectively plot the flow rates versus their cohesive forces (Figure 76). Both the middle and exit flow rates follow the same general trend of flow rate being inversely proportional to cohesive force, but the exit flow rate is significantly more affected.

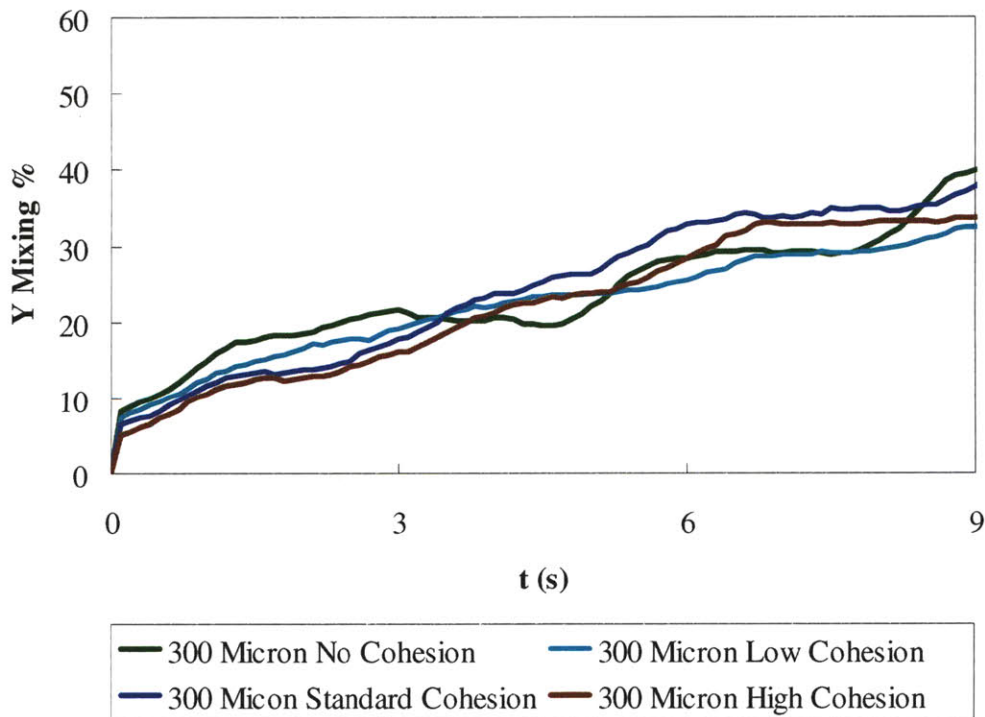
6.9 Mixing results for cohesive force simulations

6.9.1 Quantitative mixing measure

There is very little difference between the homogeneity of the X and Y initial position groups (Figure 77 A, B) at a given time for any of the cohesive forces simulated. Even more than the X and Y mixing, the R mixing (Figure 78 B) shows how little the differences in cohesive force affect homogeneity in the double helical ribbon blender. These results are in stark contrast to the flow behavior, which leads to the conclusion that flow behavior is most likely a poor indicator of mixing performance. It seems that there are two competing effects resulting in the similar blend homogeneities. The more cohesive particles are more efficient at transporting material into a position where it can avalanche so diffusive mixing can occur. The less cohesive particles will move more freely when they avalanche and accomplish more mixing per avalanche, but fewer particles will be transported to the avalanche region. It is unclear whether these competing effects are balanced only for this double helical ribbon blender or whether they are a more general trend of tumbling blenders with cohesive powders.



(A)



(B)

Figure 77: Homogeneity (mixing %) for X and Y initial position groups in an eighth scale double helical ribbon blender with 300 micron lactose particles with 0%, 50%, 100% and 150% of the standard experimentally measured cohesion operating at 20 RPM and a 0.0035 g/s inflow.

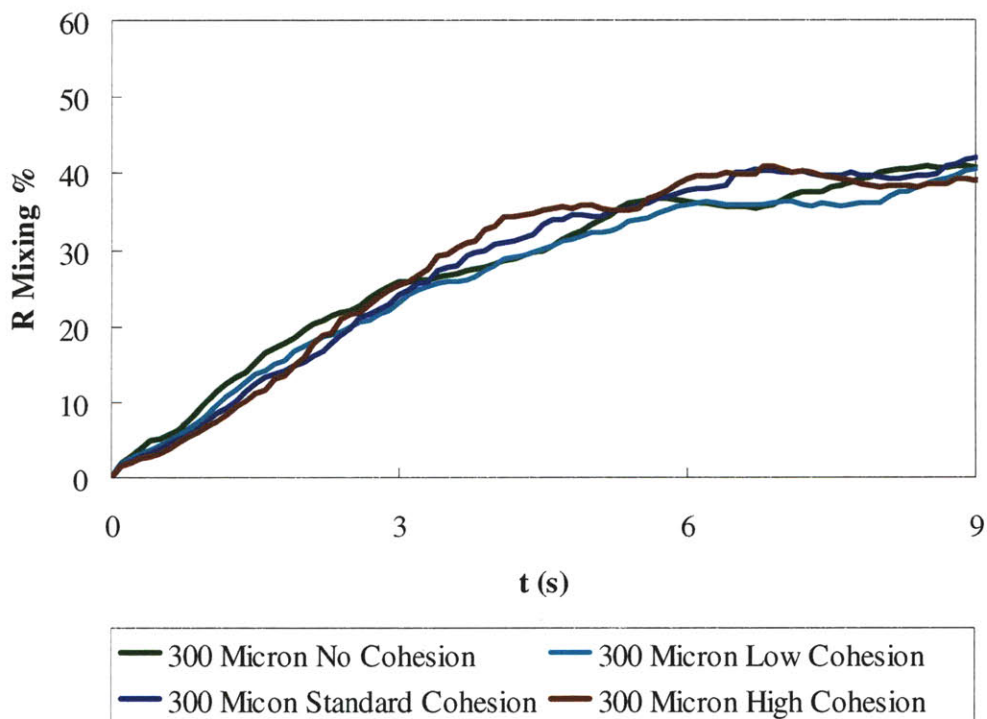
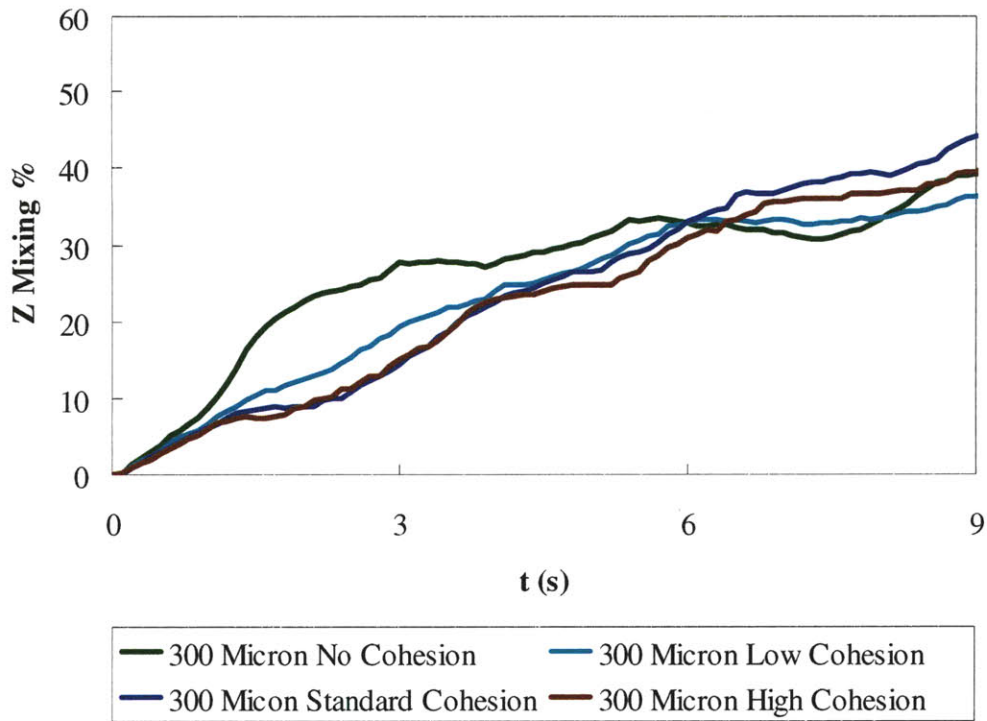


Figure 78: Homogeneity (mixing %) for Z and R initial position groups in an eighth scale double helical ribbon blender with 300 micron lactose particles with 0%, 50%, 100% and 150% of the standard experimentally measured cohesion operating at 20 RPM and a 0.0035 g/s inflow.

The Z mixing (Figure 78 A) shows a very similar mixing rate for the low, standard and high cohesion, but the no cohesion particles have at times a very different mixing rate. Looking at V_z profiles for the no cohesion particles shows a higher negative V_z in the reverse region with the inner helical ribbon. Since the material does not get pulled over the shaft, it sits along the reverse helical shaft and is driven backwards very effectively, which accounts for the initially higher Z mixing rate. The ultimately lower Z mixing rate for the no cohesion particles is the effect of the blender defilling and the particles not being high enough in the blender to effectively interact with the reverse helical ribbon.

6.10 Summary of results

1. There is a complex relationship between particle size and flow rate. The 100 micron particles have a higher flow rate than either 200 or 300 micron particles in the middle blender and 200 and 300 micron particles have a relatively similar flow rate. However, at the exit of the blender there is a consistent trend of larger particles having higher flow rates due to the cohesive forces having a less significant effect on the larger particles.
2. The quantitative mixing measure shows that the initial position groups in the 100 micron particle simulation were substantially less homogeneous than the groups in the 200 micron particle simulations. A similar trend was observed by Pernenkil [4] in mixing experiments with lactose particles of the same mean particles sizes. Comparing the homogeneity of the initial position groups in the 200 and 300 micron particle simulations is less consistent with the homogeneity in the X dimension showing a clear advantage for the 300 micron particles, but relatively similar homogeneity for the other dimensions. It appears there is a critical size

between 100 and 200 microns where the increasing mass of the particle is able to overcome the cohesive forces and diffusively mix at a greater rate.

3. There is little difference in flow rate between the simulation with the polydisperse inflow and the simulation with the monodisperse inflow.
4. There is a small, but seemingly consistent decrease in homogeneity for the simulation with the polydisperse inflow.
5. Cohesive force has a strong effect on particle flows. This is manifested in significantly different volume fraction and velocity profiles as well as flow rates. Throughout the blender the flow rates increase as the cohesive forces decrease. This effect, however, is far more pronounced at the exit of the blender as the material has to pass through the exit ports.
6. There is little substantial difference between the homogeneity of blends for particles with different cohesive forces in the double helical ribbon blender. It is possible that there are competing effects between the transport of particles and microscale particle interactions that balance each other out for mixing in the double helical ribbon blender.
7. Over the entire set of particle property simulations, flow rate appears a poor predictor of homogeneity.

7 EFFECTS OF BLENDER DESIGN

7.1 Blender size simulations

Three simulations were run to explore the effects of blender size on particle flows and blend homogeneity. The simulation operating conditions are modeled on those used by Lin [85] for residence time distribution experiments (Table 25).

Table 25: Summary of model conditions for DEM simulations comparing the size of double helical ribbon blenders.

Blender Scale	Shaft	Material	d_{particle} μm	Polydispersity	Cohesion	Ω <i>RPM</i>	Q_{inflow} <i>mg/s</i>	Fill Fraction <i>frac</i>
-	-	-	-	-	-	<i>RPM</i>	<i>mg/s</i>	<i>frac</i>
"1/16"	Ribbon	Lactose	200	Monodisperse	Standard	20	0.4	0.46
"1/8"	Ribbon	Lactose	200	Monodisperse	Standard	20	3.3	0.46
"1/4"	Ribbon	Lactose	200	Monodisperse	Standard	20	26.0	0.46

The three blender sizes examined are a sixteenth, an eighth and a quarter scale linear reduction of the double helical ribbon blender. The sixteenth scale reduction is the smallest size possible to achieve a steady feed of particles in the DEM simulations. The eighth scale reduction is the size most commonly used by the author for DEM simulations of the double helical ribbon blender in this thesis. The quarter scale reduction completes the analysis by providing a larger size for observing trends across blender sizes.

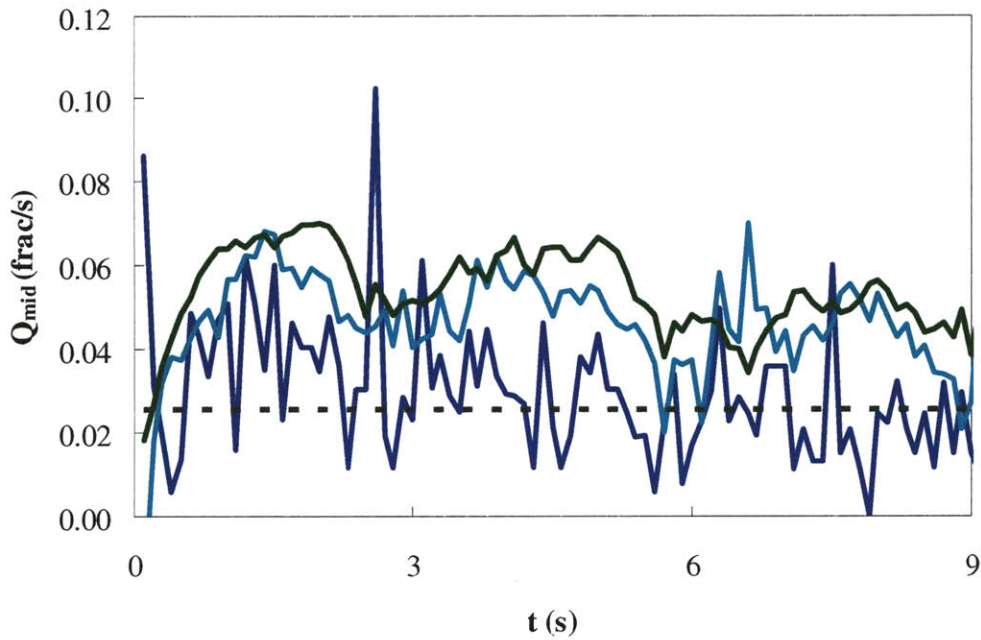
7.2 Flow behavior results for blender size simulations

7.2.1 Flow rate

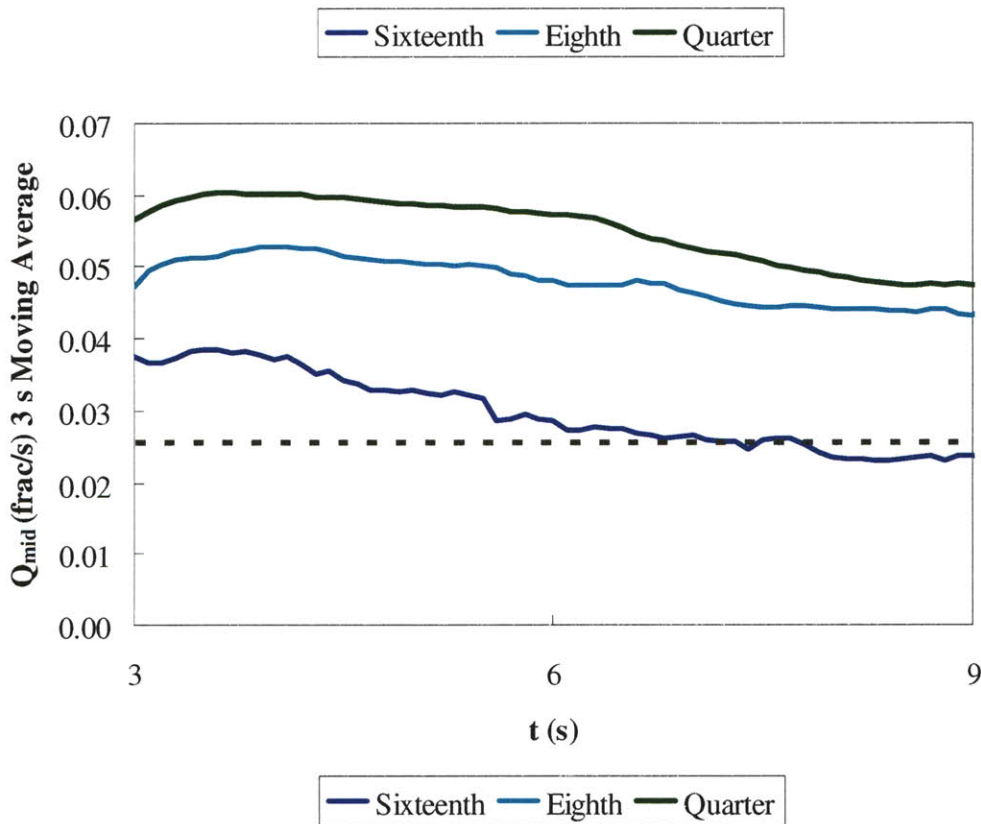
The blender size simulations show a general trend of lower normalized flow rates as the blender size decreases (Figure 79 A, B). The periodicity of the flow rate is similar for the quarter

and eighth scale simulations in the middle of the blender with both having a consistent rise and fall in flow rate timed with the motion of the ribbons. The sixteenth scale simulation does not have an obvious periodic aspect to its flow rate. This is surprising given that consistent periodic flow rate fluctuations are a common trait of all of the eighth and quarter scale simulations. This periodic flow is caused by the outer ribbon moving into and out of the particle bed and thus removing the forward driving force on the particles. The lack of periodic flow in the sixteenth scale blender is possibly caused by the small size of the blender and the cohesiveness of the particles. The particles are forming cohesive blocks that span the distance between turns in the outer ribbon and move the particles forward. It is also worth noting that the eighth scale simulation achieves brief peak flow rates in the middle of the blender that are as high as the quarter scale blender.

The flow rate at the exit of the blender exhibits the same trend of lower normalized flow as the size of the blender decreases (Figure 80 A, B). The peaks of the eighth scale blender are significantly lower than the peaks of the quarter scale blender at the exit which is unlike the peak flow rates seen in the middle of the blender. Unlike the middle of the blender, all of the blender sizes display consistent periodic fluctuations in flow rate at the exit of the blender. All of the blender sizes have the slow rise and steep decay caused by the outer helical blade wiping across the exit ports and driving material out of the blender.

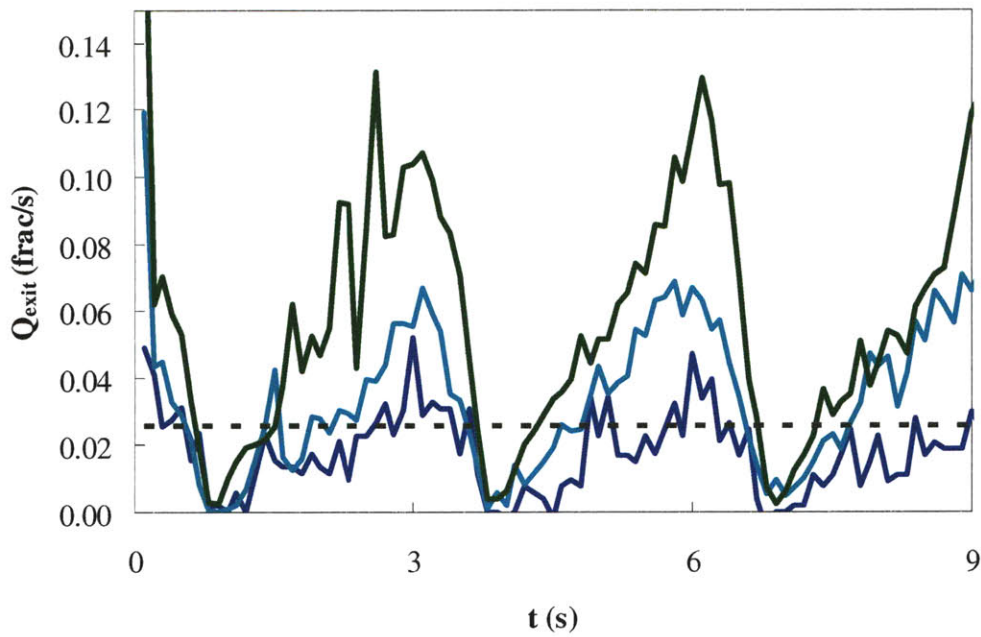


(A)

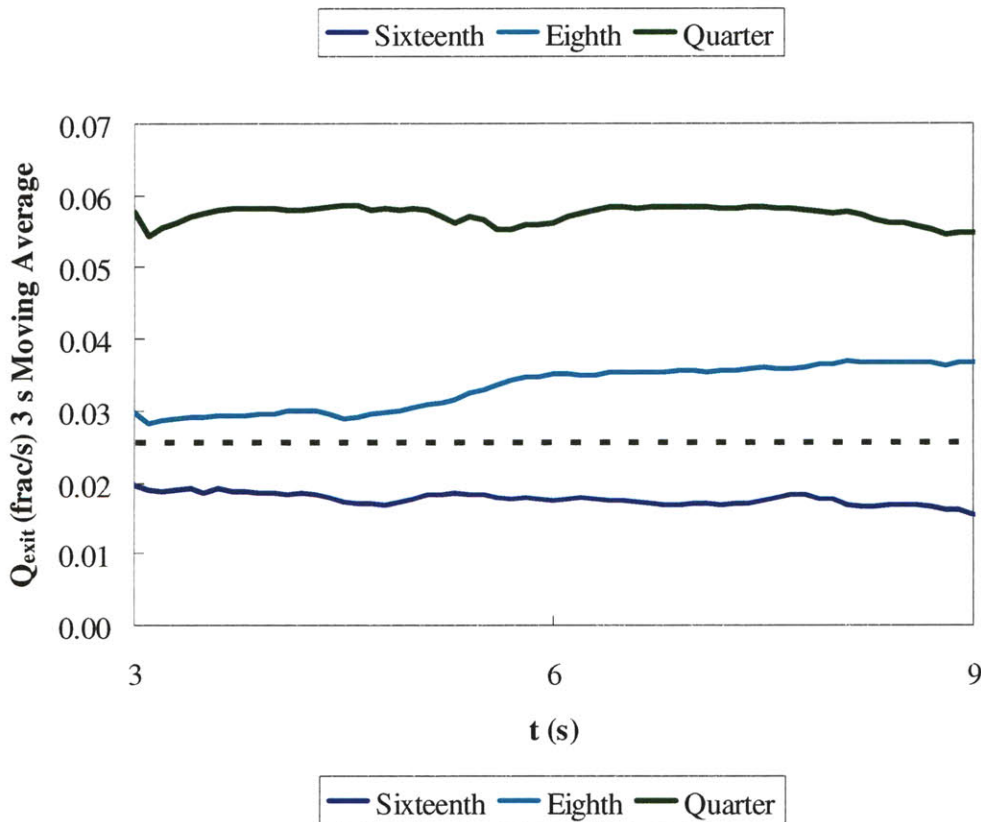


(B)

Figure 79: Flow rate normalized by the fill weight for the middle of the double helical ribbon blender with 200 micron lactose particles operating at 20 RPM at a sixteenth scale with 0.0004 g/s inflow, an eighth scale with 0.0033 g/s inflow and a quarter scale with 0.0260 g/s inflow.

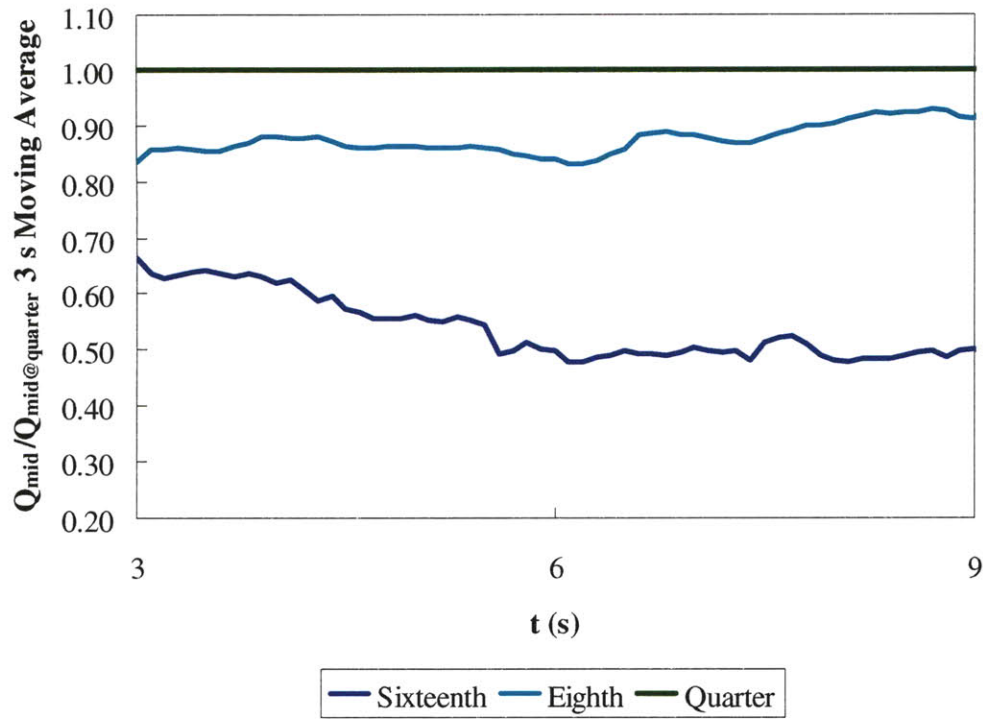


(A)

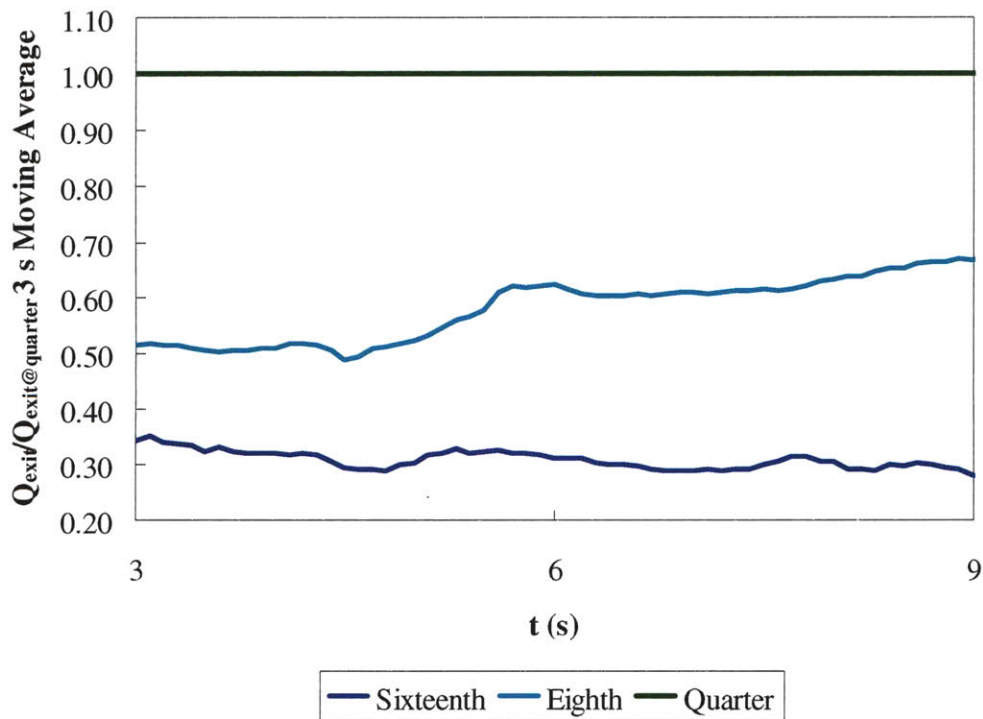


(B)

Figure 80: Flow rate normalized by the fill weight for exit of the double helical ribbon blender with 200 micron lactose particles operating at 20 RPM at a sixteenth scale with 0.0004 g/s inflow, an eighth scale with 0.0033 g/s inflow and a quarter scale with 0.0260 g/s inflow.



(A)



(B)

Figure 81: Flow rates normalized by the fill weight and scaled to the quarter scale normalized flow rate of the double helical ribbon blender with 200 micron lactose particles operating at 20 RPM at a sixteenth scale with 0.0004 g/s inflow, an eighth scale with 0.0033 g/s inflow and a quarter scale with 0.0260 g/s inflow.

Dividing the normalized flow rates of the various blender sizes by the normalized flow rate of the quarter scale blender (Figure 81 A, B) demonstrates that there is a proportionally much greater decrease in flow rate at the sixteenth scale (50% of the quarter scale at 6 seconds) than the eighth scale (84% of the quarter scale at 6 seconds) in the middle of the blender. This trend is even more pronounced at the exit of the blender with the ratio of both the sixteenth (31% of the quarter scale at 6 seconds) and the eighth scale (63% of the quarter scale at 6 seconds) flow rate. Comparing the middle and exit flow rates, the eighth scale flow rate ratio is 25% less at the exit than the middle and the sixteenth scale flow rate ratio is 38% less at the exit than the middle.

$$Q \propto C_{middle / exit} \times (D_{middle / exit})^a$$

Equation 22: Proportionality between blender diameter or exit port diameter and flow rate.

These flow rate results are obviously not following the scaling predicted by the Beverloo law, where “a” in Equation 22 is 2.5, or a volumetric scaling, where “a” in Equation 22 is 3.0.

Table 26: Observed (t = 6 seconds) and calculated flow rates ratio normalized to the quarter scale blender.

	Observed (middle)	Observed (exit)	Beverloo (a = 2.5)	Volumetric (a = 3.0)	Hagen–Poiseuille (a = 4.0)
Quarter	1.00	1.00	1.00	1.00	1.00
Eighth	0.84	0.63	1.41	1.00	0.50
Sixteenth	0.50	0.31	2.00	1.00	0.25

The Beverloo law would predict that the normalized flow rates for the sixteenth and eighth scale blenders would be greater than the quarter scale blender; the volumetric scaling would predict that they would be even (Table 26). One gets closer to the observed behavior when using an “a” value of 4.0 as one does in the Hagen-Poiseuille law for pressure driven flow of liquids [89].

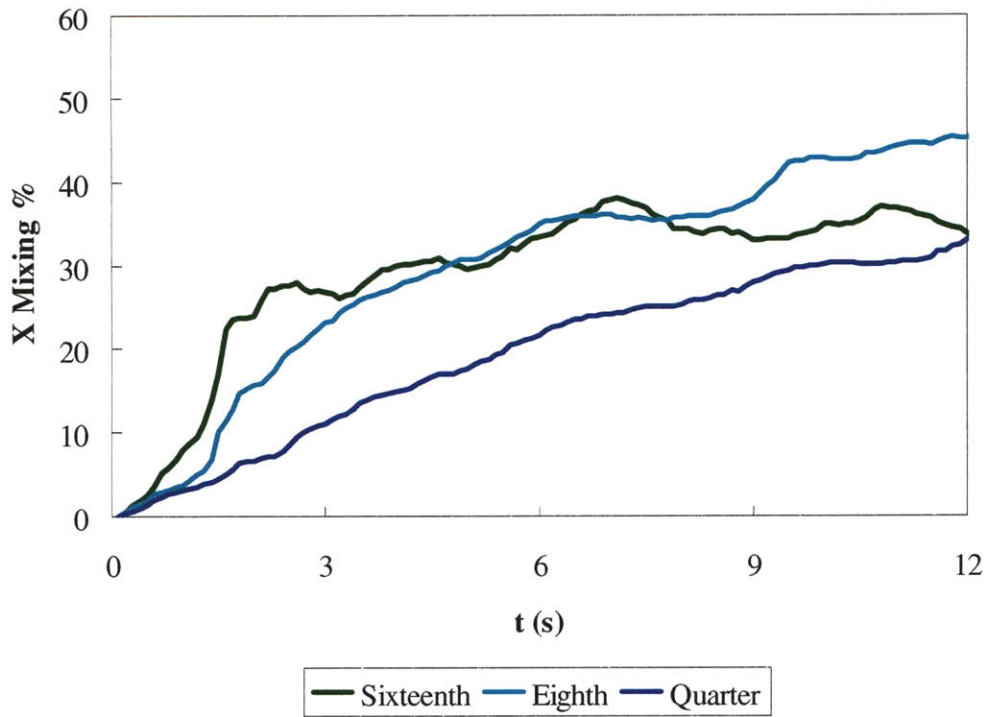
Fitting “a” for the middle and exit of the blender yields values of 3.4 and 3.8 respectively. Given

the orifice diameter at the middle of the blender (blender shell diameter) and the exit of the blender (exit port diameter) are different might indicate that “a” is a function of the orifice diameter.

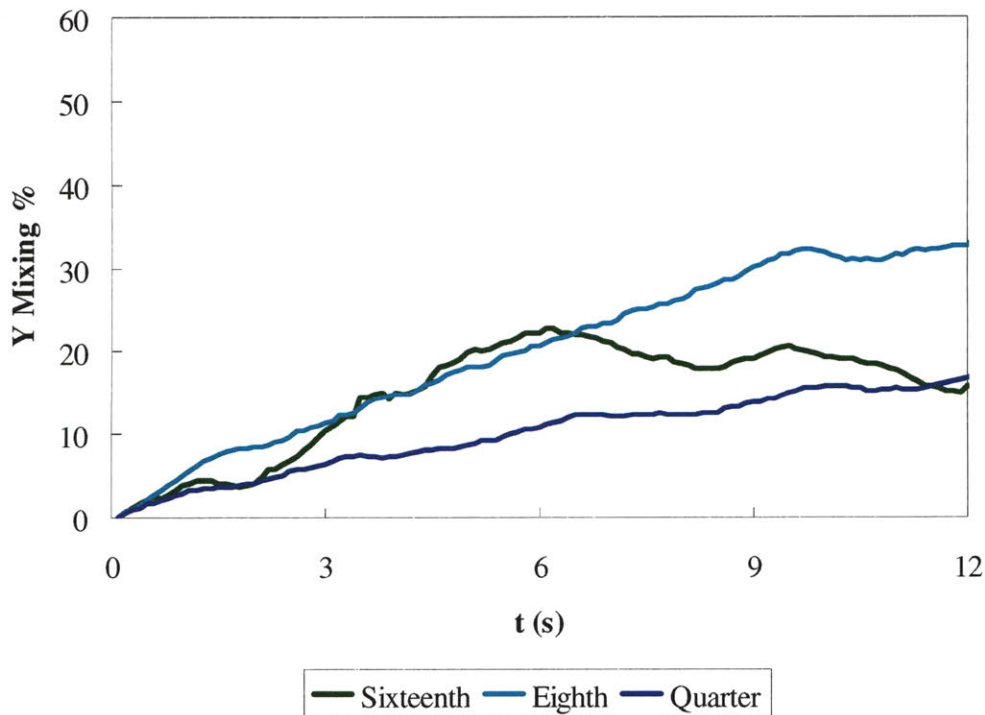
7.3 Mixing results for blender size simulations

7.3.1 Quantitative mixing measure

All of the blender sizes have the characteristics of a system where the primary mechanism of mixing is the diffusion of avalanching particles for the homogeneity (mixing %) of the X initial position groups (Figure 82 A). This can be seen in the increase of mixing rate at half a revolution (1.5 seconds) where the first avalanches begin to occur. The amount of mixing accomplished in these initial avalanches favors smaller blenders with the sixteenth scale blender having the most homogenous blend at the end of the first revolution (3 seconds) followed by the eighth and then the quarter scale blender. However, at 2 revolutions (6 seconds), the sixteenth scale blender has the same homogeneity as the eighth scale blender. Subsequent revolutions of the blender do not further increase the homogeneity of the blend in the sixteenth scale blender.

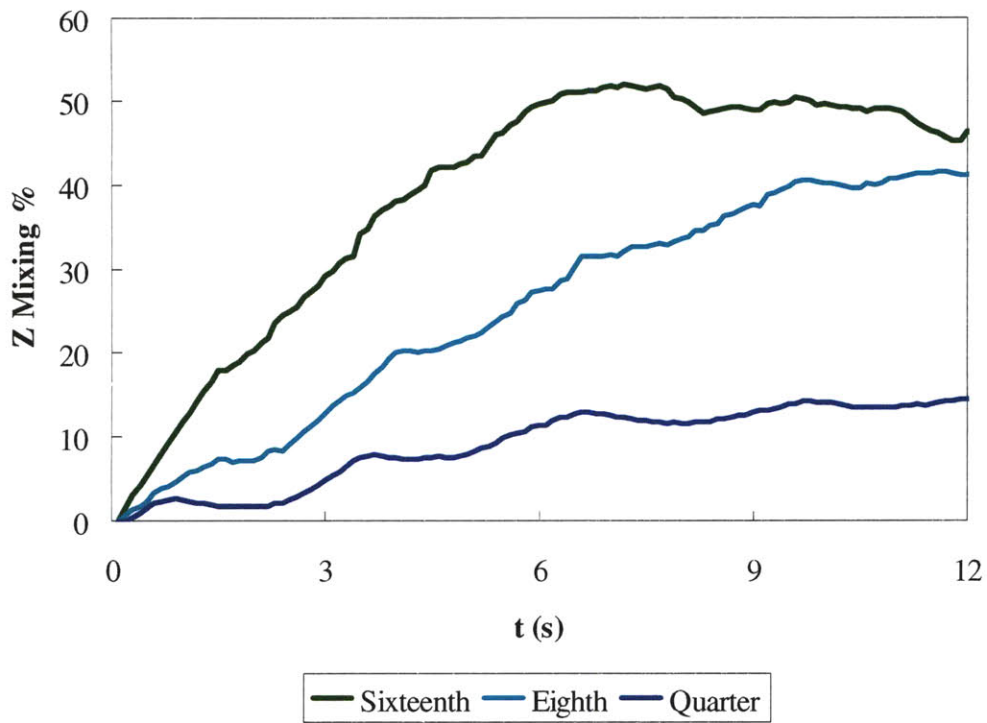


(A)

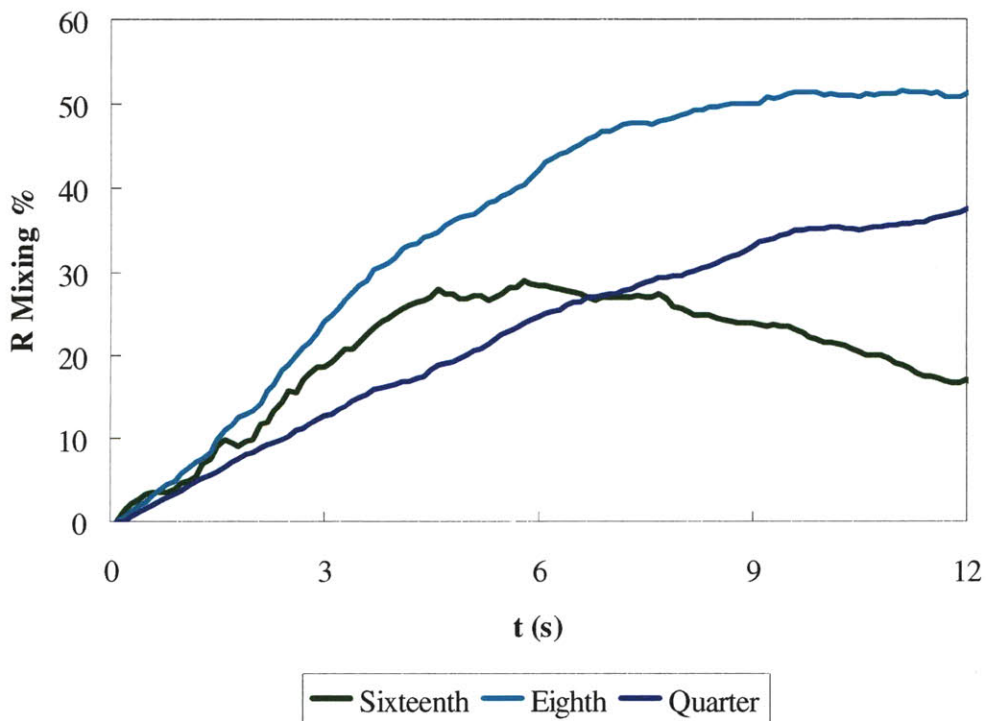


(B)

Figure 82: Homogeneity (mixing %) for X and Y initial position groups in the double helical ribbon blender with 200 micron lactose particles operating at 20 RPM at a sixteenth scale with 0.0004 g/s inflow, an eighth scale with 0.0033 g/s inflow and a quarter scale with 0.0260 g/s inflow.



(A)



(B)

Figure 83: Homogeneity (mixing %) for Z and R initial position groups in the double helical ribbon blender with 200 micron lactose particles operating at 20 RPM at a sixteenth scale with 0.0004 g/s inflow, an eighth scale with 0.0033 g/s inflow and a quarter scale with 0.0260 g/s inflow.

The homogeneity of the Y initial position groups (Figure 82 B) shows a similar homogeneity behavior with the eighth scale and sixteenth scale blenders even at 2 revolutions. The Y initial position group's homogeneity also demonstrates a pronounced decrease in mixing rate for the eighth scale simulation after 3 revolutions (9 seconds). This trend was also observed in the eighth scale simulation with smaller polydisperse lactose and caffeine particles. This decrease in mixing rate for the eighth scale simulation is not observed in the quarter scale simulation on the time scale simulated.

The homogeneity of the Z initial position groups demonstrates a clear trend of greater homogeneity for smaller blender size (Figure 83 A). However, the trend of a decrease in mixing rate at 2 revolutions for the sixteenth scale blender and at 3 revolutions for the eighth scale blender still exists. The trend of lower homogeneity for the quarter scale blender compared to the eighth scale blender is also apparent in the homogeneity of the R initial position groups (Figure 83 B). However, it is possible that mixing will continue for longer in the quarter scale blender and that the ultimate homogeneity for the quarter scale blender will be higher than for the smaller scale blenders.

The most likely mechanism of mixing is still diffusive regardless of the blender scale. Thus one can explain the differences in homogeneity between the blender scales in the context of their ability to promote diffusive mixing through avalanching particles. The eighth scale blender can potentially transport a greater percentage of its particles to a position where it can avalanche than the quarter scale blender. This is due to particles being swept by the ribbon dragging neighboring particles (a quasi boundary layer) out of the particle bed. As the depth of this boundary layer does not scale linearly with blender scale, the eighth scale blender becomes a more effective blender than quarter scale blender and produces a more homogenous blend. The inconsistent

homogeneity trends for the sixteenth scale blender are most likely due to an inability of the blender to rearrange particles in the radial dimension. This is due to the small scale of the blender which leaves less than 4 particle diameters between the central shaft and the blender shell.

7.4 Shaft design simulations

There are countless options for agitating elements in continuous blenders. Helical ribbon designs and paddle designs have proved to be capable of producing sufficiently homogenous blends for use in pharmaceutical manufacturing during continuous laboratory blending experiments [4,24]. However, questions remain as to which design will produce the more homogenous blend for pharmaceutical powders. These simulations compare Pernekil’s double helical ribbon blender and a paddle blender designed by the author and Lin [85]. The simulation operating conditions are modeled on those used by Pernekil [4] for blending and residence time distribution experiments (Table 27).

Table 27: Summary of model conditions for DEM simulations comparing the effects of shaft design.

Blender Scale	Shaft	Material	d_{particle} μm	Polydispersity	Cohesion	Ω RPM	Q_{inflow} mg/s	Fill Fraction frac
"1/8"	Ribbon	Lactose	300	Monodisperse	Standard	20	3.5	0.48
"1/8"	Paddle	Lactose	300	Monodisperse	Standard	40	3.5	0.48

To remove the effects of varying fill fraction, the blenders were operated at different rotation rates. Lin found that operating the paddle blender at 40 RPM in the forward direction achieved a similar steady state fill fraction to the ribbon blender operated at 20 RPM. Additionally, the paddle blender was operated at 40 RPM with a reverse rotation rate for comparison. Results are presented with time in revolutions to better compare the two blenders given these different rotation rates.

7.5 Flow behavior results for shaft design simulations

7.5.1 Volume fraction

The ribbon blender (Figure 84 A), the forward paddle blender (Figure 84 B) and the reverse paddle blender (Figure 84 C) have very different volume fraction profiles when looking at the YZ slice. As seen previously, the ribbon blender tends to have less material near the inlet of the blender with material building up near the exits (dashed black box in Figure 84 A). The paddle blenders are the exact opposite with more material both above and below the central shaft as one gets closer to the inlet of the blender (black boxes in Figure 84 A, B, C). This biasing of material towards the inlet region of the blender is slightly more pronounced in the reverse paddle blender than the forward paddle blender. In addition, the paddle blenders move more material above the shaft. The particles transported above the central shaft are not as evenly distributed axially for the paddle blenders as they are in the ribbon blender. In the paddle blenders, there are distinct hot spots that align with the paddles (black arrows in Figure 84 B, C) indicating that only particles in the path of the paddle are lifted over the shaft and avalanche.

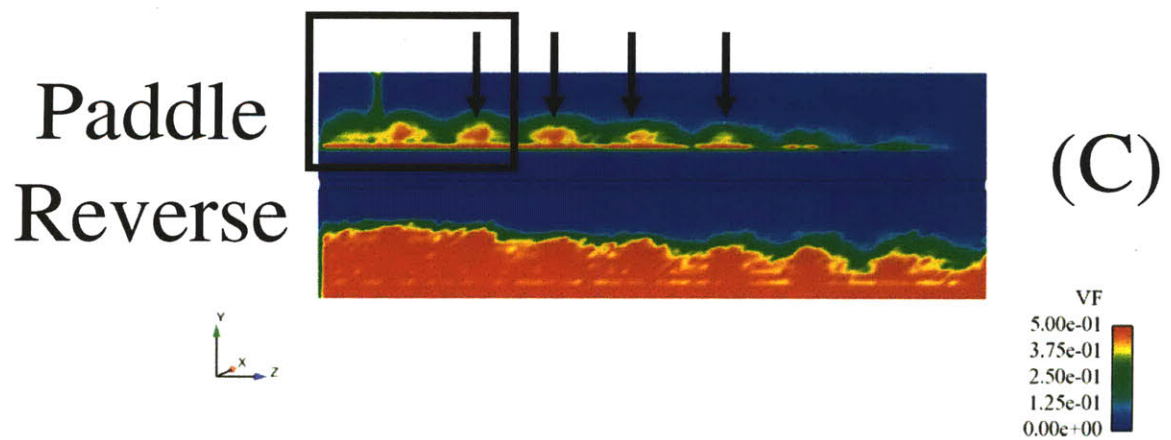
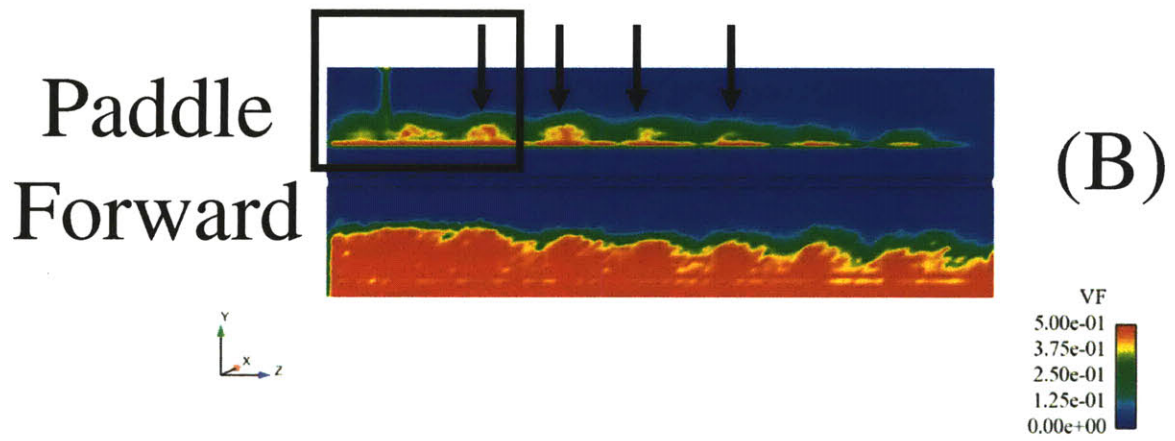
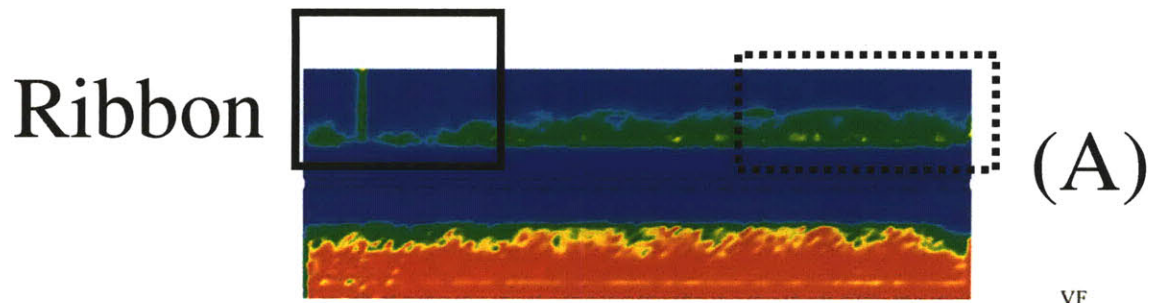


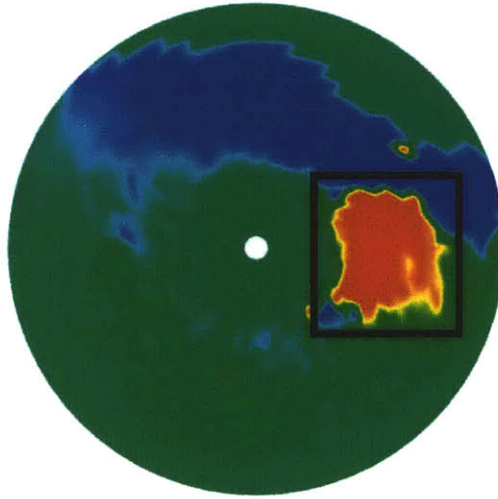
Figure 84: YZ cross section showing volume fraction for an eighth scale blender with 300 micron lactose particles and a 0.0035 g/s inflow.

7.5.2 Particle velocities

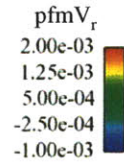
The XY cross section of V_r for the paddle blenders (black boxes in Figure 85 B, C) demonstrates significantly greater outward radial velocity as particles are avalanching than was found for the ribbon blender (black box in Figure 85 A). There is very little difference in the radial velocity profile between the forward and reverse paddle blender. In addition, there is a distinct negative radial velocity contour in the paddle blenders that begins in the middle vertical point in the blender. This is caused when the paddle moves past horizontal and particles can slide down it and migrate towards the center of the blender (dashed black boxes in Figure 85 B, C). This indicates that the particles begin their avalanche much earlier in the rotational cycle than for the ribbon blender, and also that the avalanche will travel a greater distance as it migrates almost the full diameter of the blender.

The XY cross section of V_θ indicates that the particles in the paddle blender (black arrows in Figure 86 B, C) are travelling significantly faster on average in the theta direction than for the ribbon blender (black arrow in Figure 86 A). This is most evident in the dense particle bed at the bottom of the blender where the flat blades of the paddle blender can push whole portions of the particle bed. The ribbons in the ribbon blender have considerably less area to push particles in the theta direction and thus much of the particle bed has a lower V_θ .

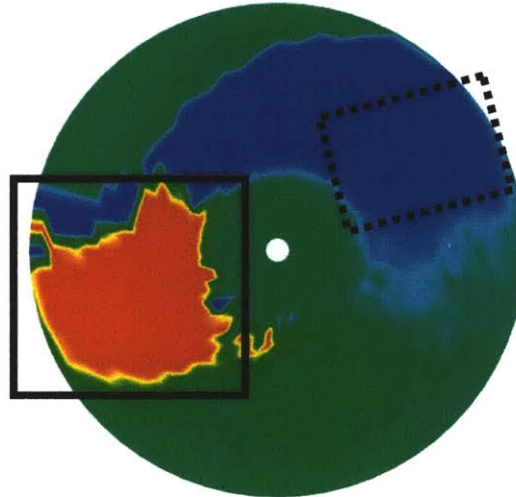
Ribbon



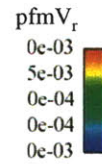
(A)



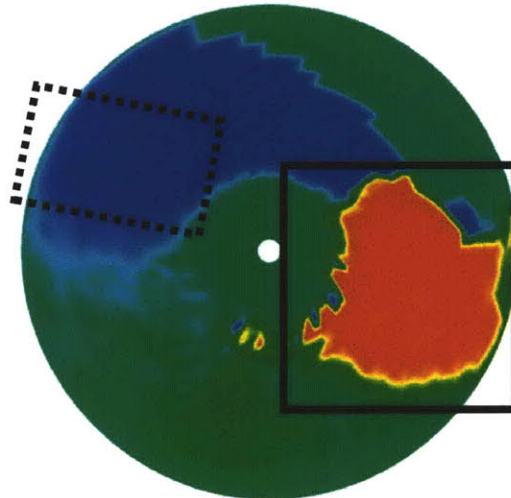
Paddle
Forward



(B)



Paddle
Reverse



(C)

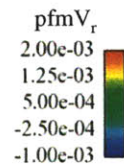
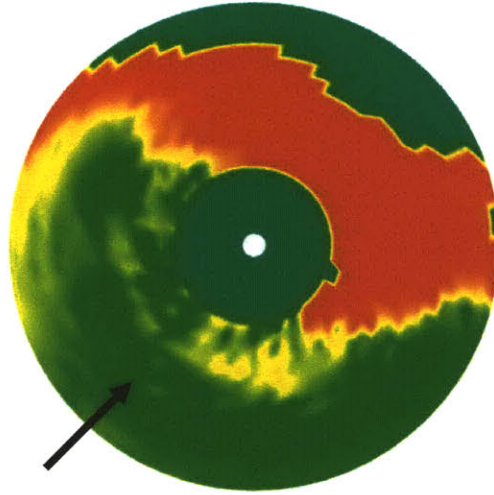
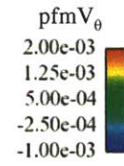


Figure 85: XY cross section showing r component of velocity in m/s for an eighth scale blender with 300 micron lactose particles and a 0.0035 g/s inflow.

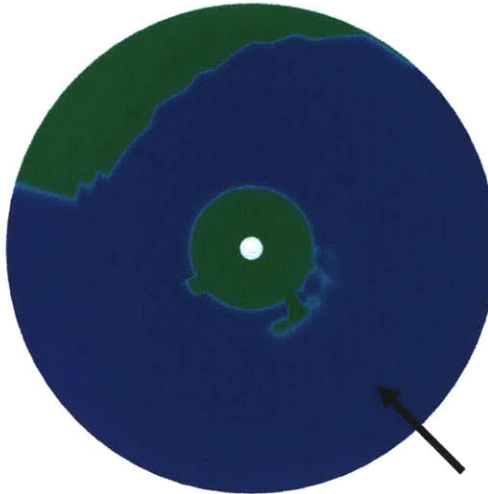
Ribbon



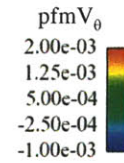
(A)



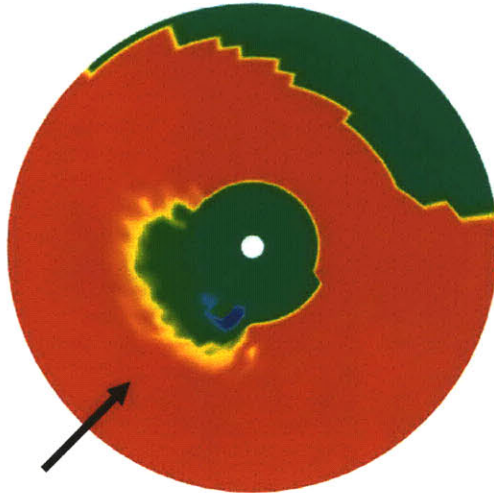
Paddle Forward



(B)



Paddle Reverse



(C)

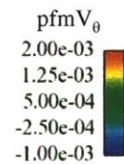
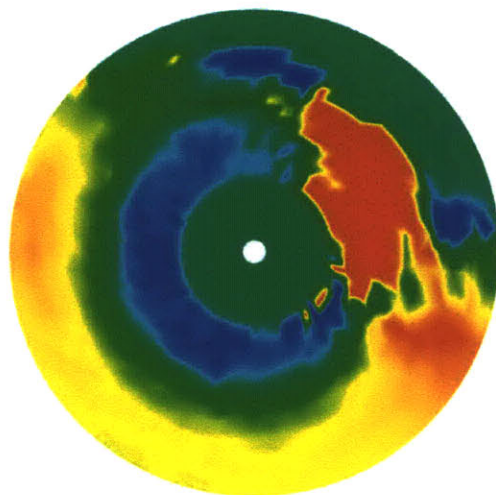
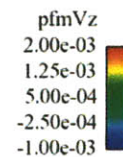


Figure 86: XY cross section showing the theta component of velocity in m/s for an eighth scale blender 300 micron lactose particles and a 0.0035 g/s inflow.

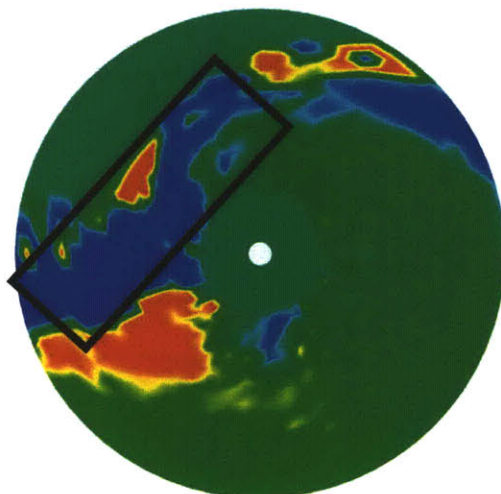
Ribbon



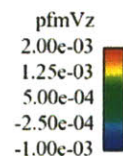
(A)



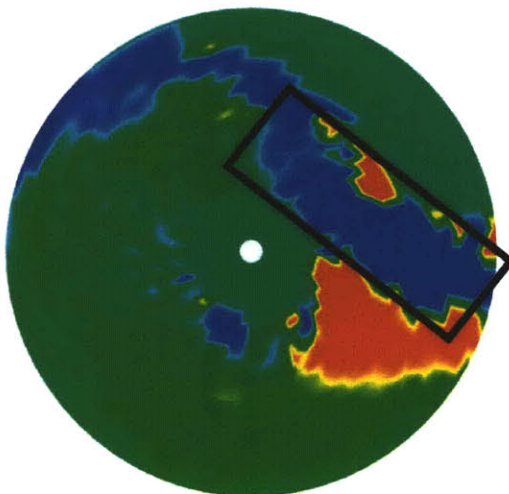
Paddle
Forward



(B)



Paddle
Reverse



(C)

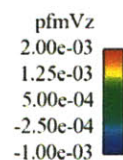
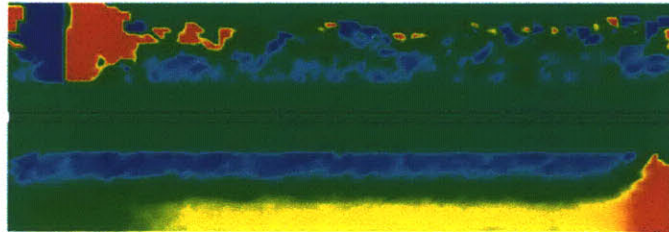
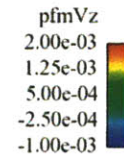


Figure 87: XY cross section showing the Z component of velocity in m/s for an eighth scale blender with 300 micron lactose particles and a 0.0035 g/s inflow.

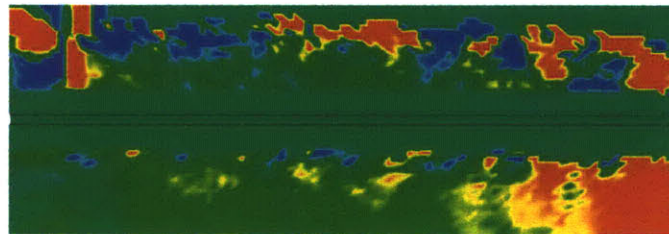
Ribbon



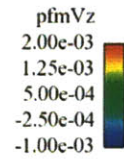
(A)



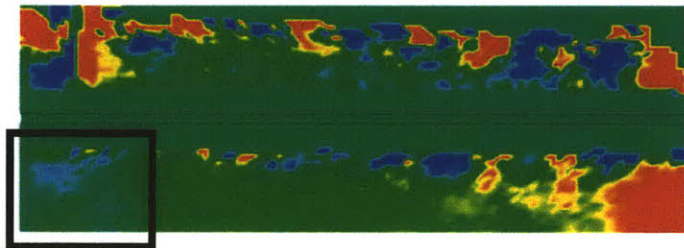
Paddle
Forward



(B)



Paddle
Reverse



(C)

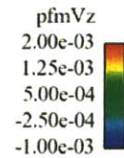


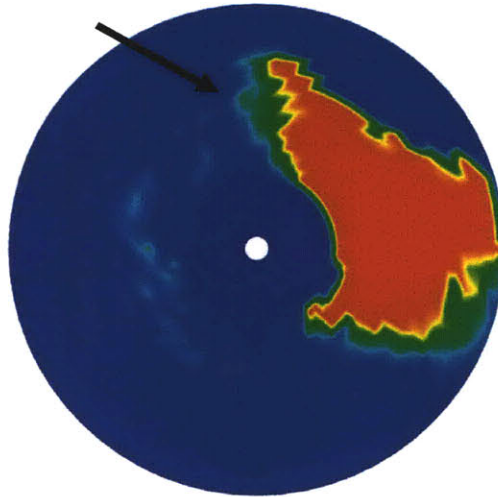
Figure 88: YZ cross section showing the Z component of velocity in m/s for an eighth scale blender with 300 micron lactose particles and a 0.0035 g/s inflow.

The V_z profiles in the XY (Figure 87 A) and YZ (Figure 88 A) cross sections for the ribbon blender show the usual trend of a well defined forward positive velocity region near the blender shell and a negative velocity region near the central shaft. The V_z profile for the forward paddle blender (Figure 87 B and Figure 88 B) and the reverse paddle blender (Figure 87 C and Figure 88 C) is generally positive for most of the particle bed, but has a lower positive velocity than the forward conveying region of the ribbon blender. As this XY cross section intersects the paddle blender at a point between paddles, there is also a streak of negative V_z (black box in Figure 87 B, C) that indicates material is either bouncing off or being pushed backwards by the sweep of the paddle in front. The paddle blender has some pockets of negative V_z and shows a relatively random velocity profile above the shaft which is most likely good for mixing. The primary negative aspect of the reverse paddle blender from a Z velocity perspective is there is a stagnation region near the inflow side end cap (black box in Figure 88 B).

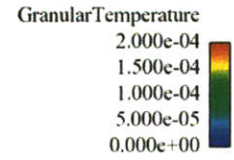
7.5.3 Granular temperature

The paddle blenders have a larger area of the highest granular temperature contour (black arrows in Figure 89 B, C) in the XY cross section compared to the ribbon blender (black arrow in Figure 89 A). In addition, the paddle blenders have a higher granular temperature in the dense particle bed (magenta arrows in Figure 89 B, C) indicating that paddle shafts are actually producing diffusive blending in this region.

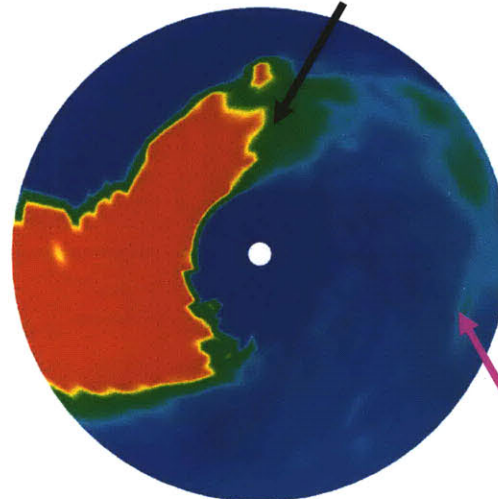
Ribbon



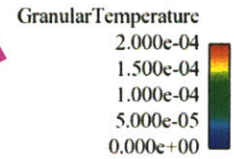
(A)



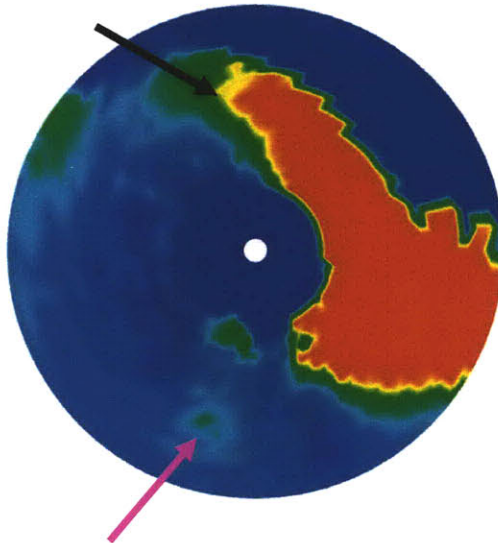
Paddle
Forward



(B)



Paddle
Reverse



(C)

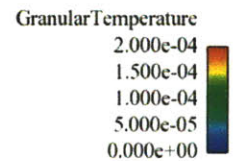
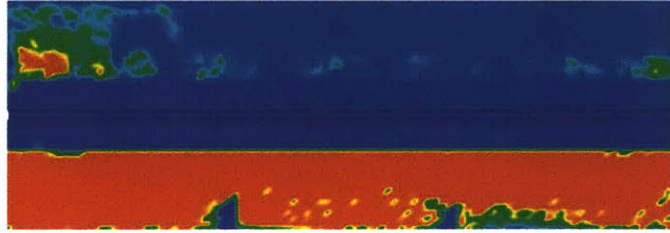
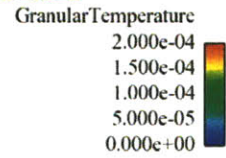


Figure 89: XY cross section showing granular temperature for an eighth scale blender with 300 micron lactose particles and a 0.0035 g/s inflow.

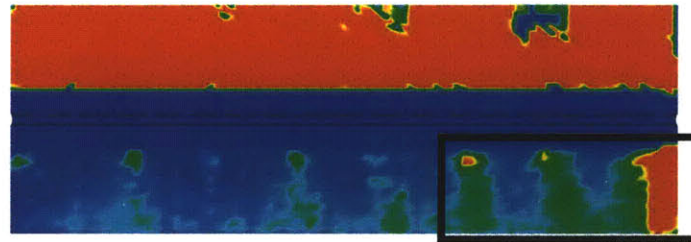
Ribbon



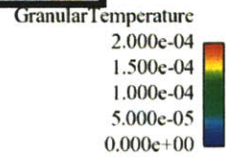
(A)



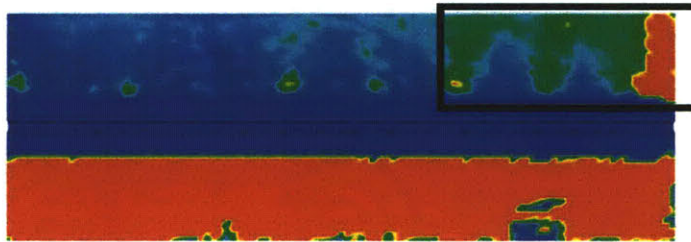
Paddle
Forward



(B)



Paddle
Reverse



(C)

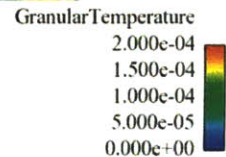
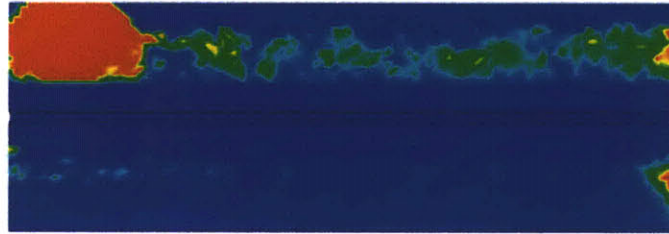
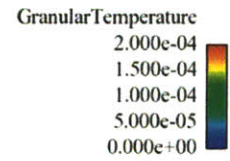


Figure 90: XZ cross section showing granular temperature for an eighth scale blender with 300 micron lactose particles and a 0.0035 g/s inflow.

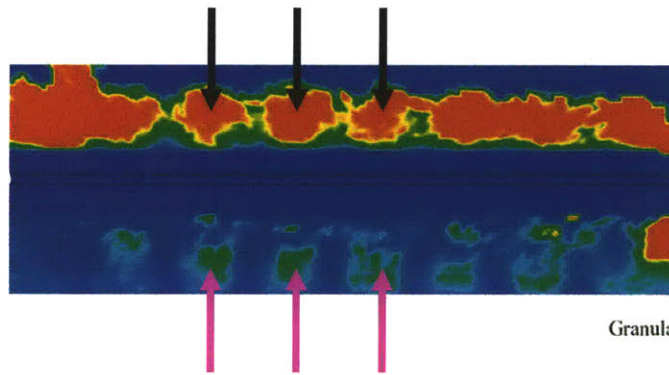
Ribbon



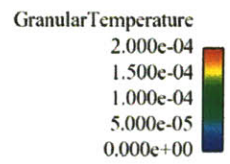
(A)



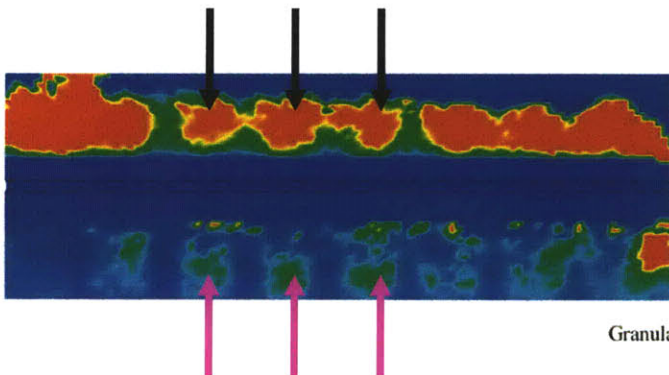
Paddle
Forward



(B)



Paddle
Reverse



(C)

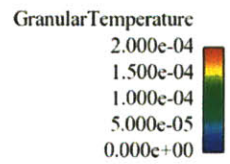


Figure 91: YZ cross section showing granular temperature for an eighth scale blender with 300 micron lactose particles and a 0.0035 g/s inflow.

The XZ cross section also shows higher granular temperature in the dense particle bed for the paddle blenders (Figure 90 A, B, C). The granular temperature is also not constant axially in the XZ cross section for the paddle blender with greater granular temperature observed near the exit of the blender for the both the forward paddle blender (black box in Figure 90 B) and the reverse paddle blender (black box in Figure 90 C). This is most likely due to the lower fill fraction in this region that allows more space for particles to move freely.

The YZ cross section of granular temperature shows that there is diffusive mixing occurring between the paddles both in the free flowing region above the shaft (black arrows in Figure 91 B, C) and in the dense particle bed (magenta arrows in Figure 91 B, C). This effect is visible in animations of the blender as particles spill off of neighboring blades and collide with each other. In general, the granular temperature results indicate strongly that the paddle shaft operating at 40 RPM is likely to create more diffusive mixing than the more slowly rotating ribbon shaft and should create a more homogenous blend.

7.5.4 Flow rate

The flow rate in the middle of the blenders (Figure 92 A, B) is very different between the ribbon blender and the paddle blenders. The ribbon blender has a sinusoidal flow rate pattern with a period of one revolution. However, there appears to be approximately four flow rate peaks per revolution in the paddle blender which is logical given that four blades will sweep through the particle bed and push material through a sample plane on a revolution. The 1 revolution moving average (Figure 92 B) of the flow rates indicates that the ribbon blender is capable of much higher flow rates in the relatively open space of the middle of the blender and reinforces that the ribbon blender is superior to the paddle blender in the axial transport of particles.

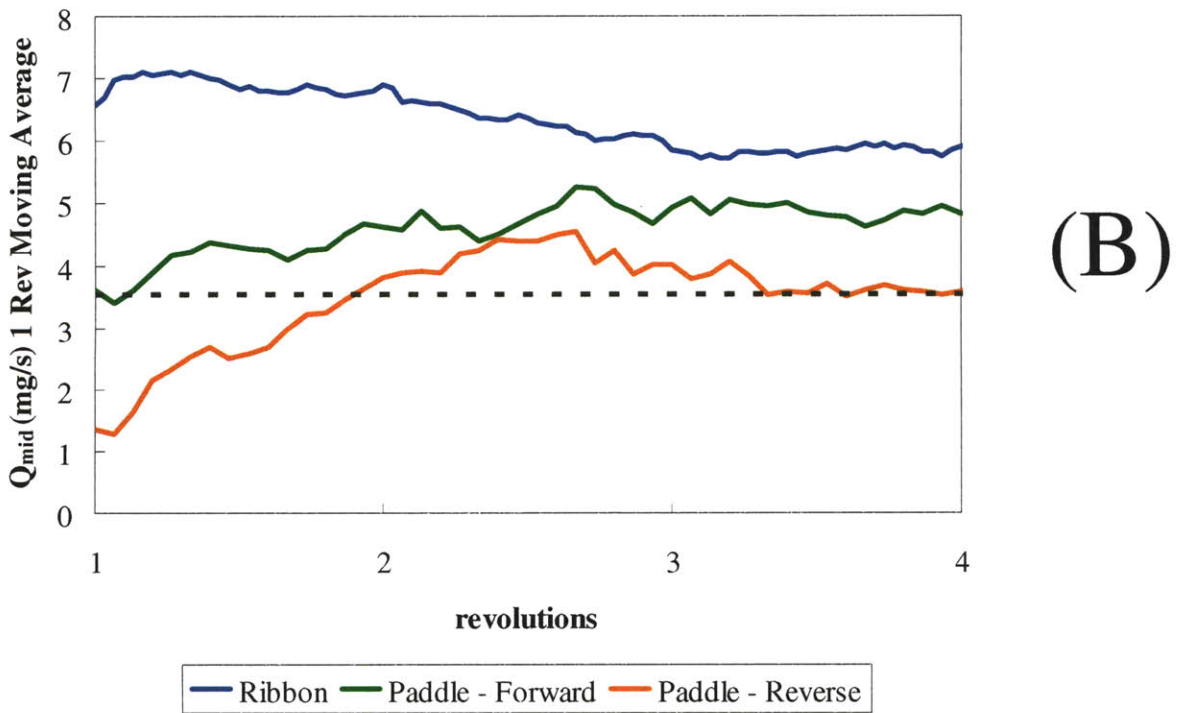
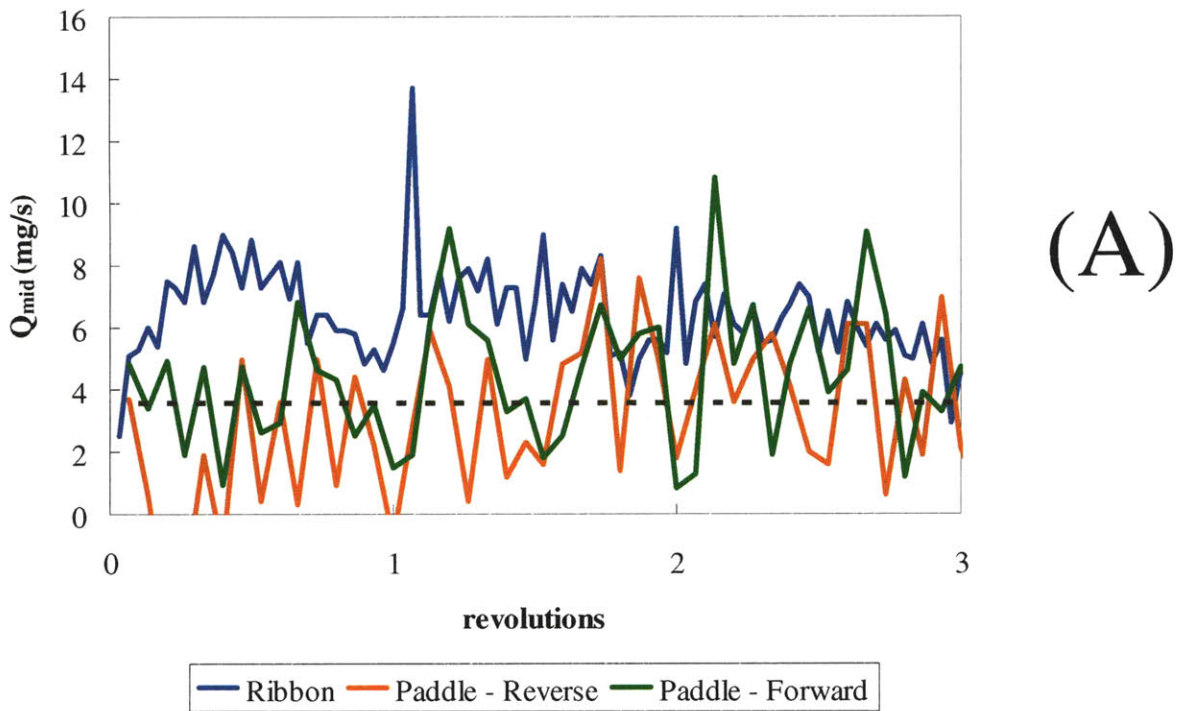


Figure 92: Flow rate in mg/s at the middle of an eighth scale double helical ribbon blender operating at 20 RPM or a paddle blender operating at 40 RPM with 300 micron lactose particles and a 0.0035 g/s inflow.

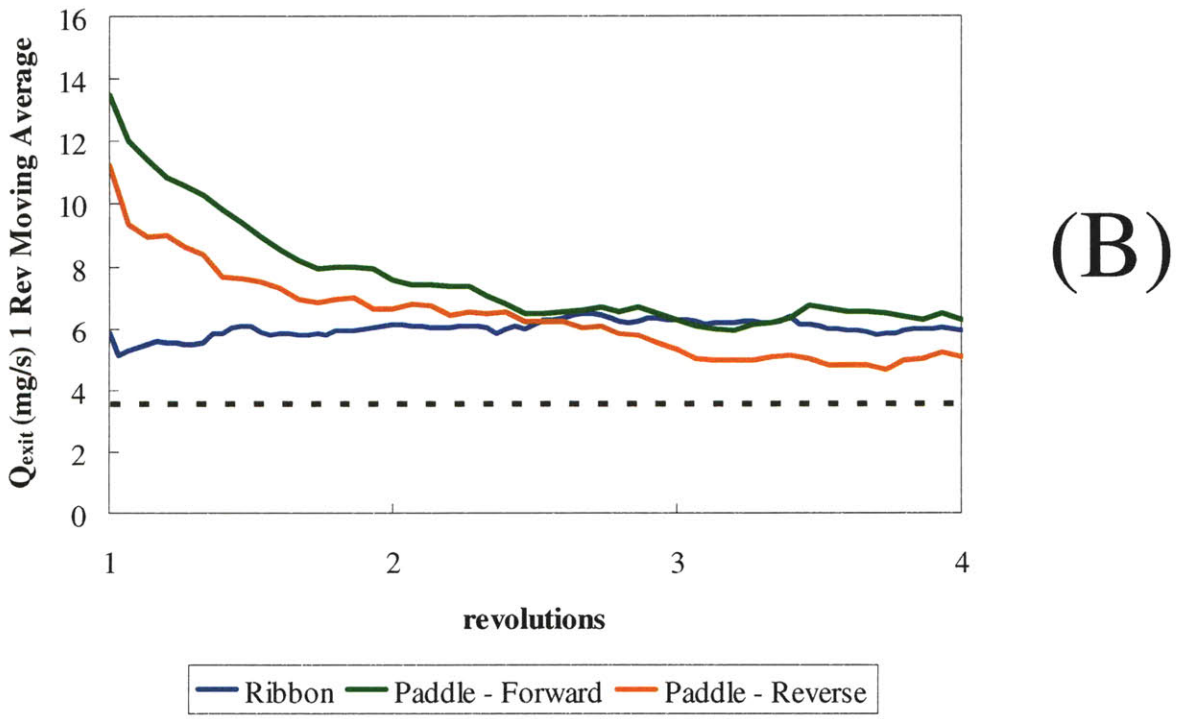
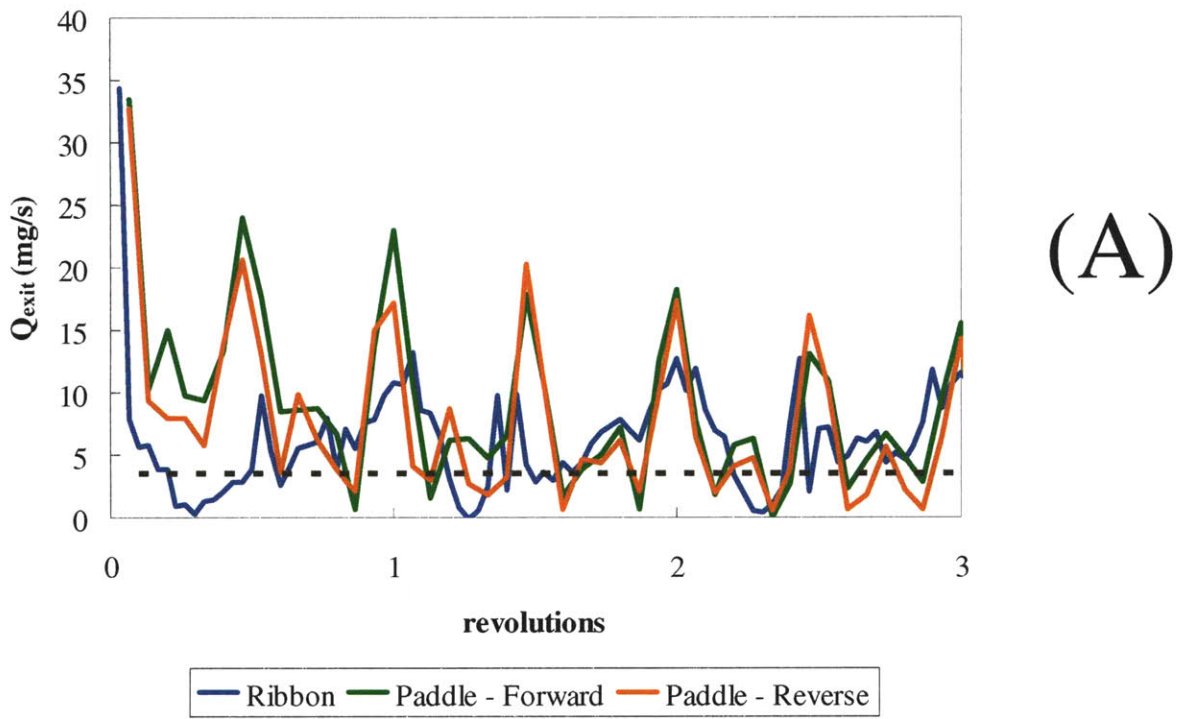


Figure 93: Flow rate in mg/s at the exit of an eighth scale double helical ribbon blender operating at 20 RPM or a paddle blender operating at 40 RPM with 300 micron lactose particles and a 0.0035 g/s inflow.

At the exit (Figure 93 A), the paddle blenders have two flow rate peaks per revolution. Initially, the peak flow rate is greater in magnitude for the paddle blender than for the ribbon blender. These peaks also have a very quick rise and decline unlike the gentle rise for the ribbon blender. This creates an even more pulsatile flow for the paddle blender and could be problematic from a process system design perspective. The 1 revolution moving average (Figure 93 B) of the exit flow rate shows that while the paddle blenders are initially flowing at a greater rate than the ribbon blender, they decline rapidly and are ultimately equal (forward paddle blender) or slightly less (reverse paddle blender) than the ribbon blender exit flow rate. This result mirrors the experimental measurements of Lin [85] who found that the forward rotating paddle blender at 40 RPM had a similar exit flow rate as the ribbon blender operating at 20 RPM.

7.6 Mixing results for shaft design

7.6.1 Color centroids

The movement of the X initial position groups' centroids for the paddle blenders (Figure 94 A, B) shows fairly rapid convergence after 2.5 revolutions to a steady position. The centroids of initial position Group 1 (Figure 96 A) converge to a steady position much faster on a per revolution basis (2.5 revolutions) than the ribbon blender (5 revolutions). This is a notable result as the paddle shaft passes twice through the material per revolution at four points while the ribbon shaft passes once through the material per revolution. In both cases, this indicates that when particles avalanche, diffusion is the primary method of mixing.

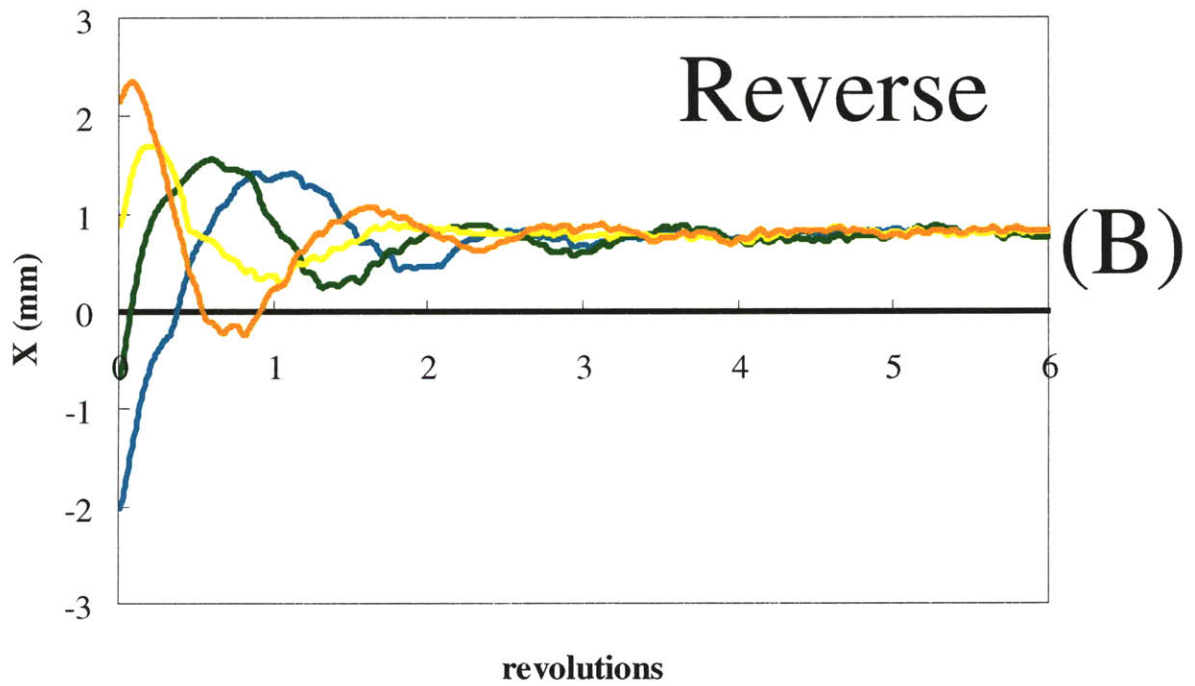
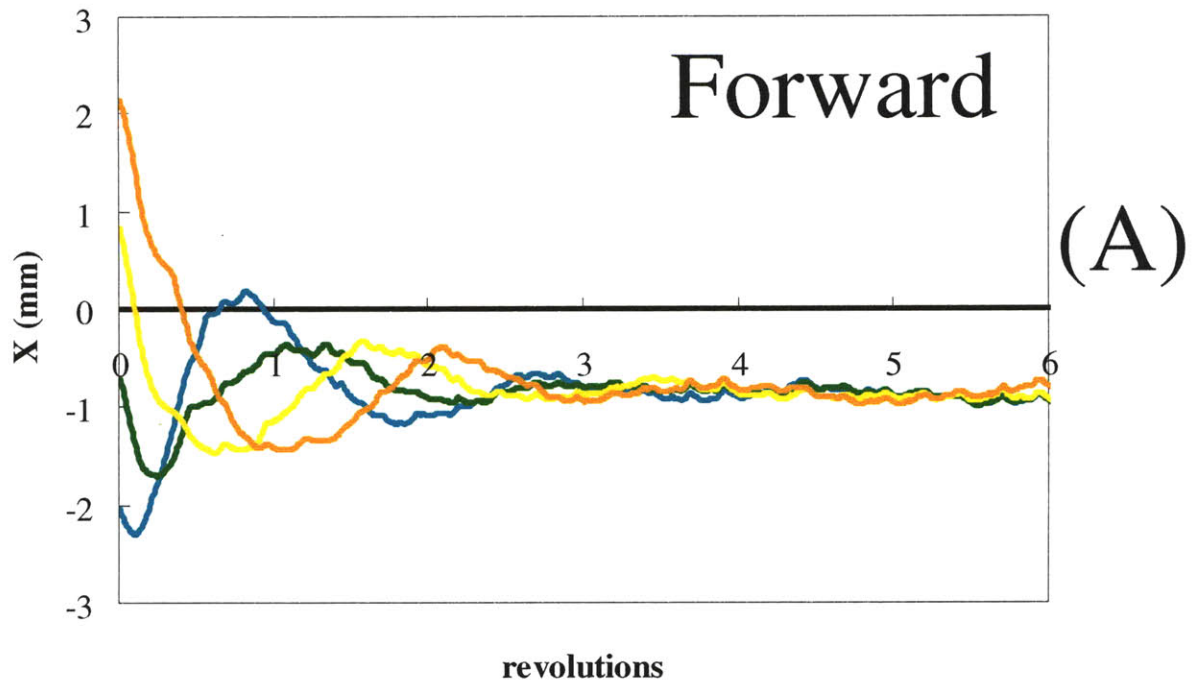


Figure 94: Centroids of X initial position groups (blue = 1, green = 2, yellow = 3, orange = 4) in the X direction for an eighth scale paddle blender operating at 40 RPM with 300 micron lactose particles and a 0.0035 g/s inflow.

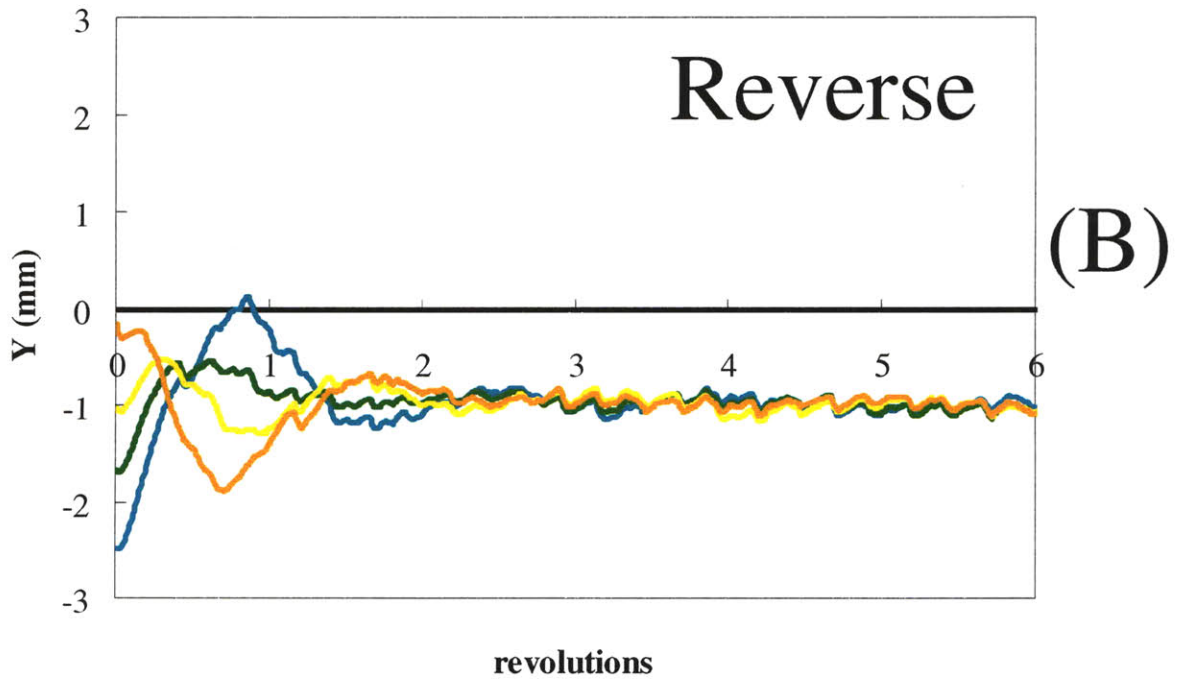
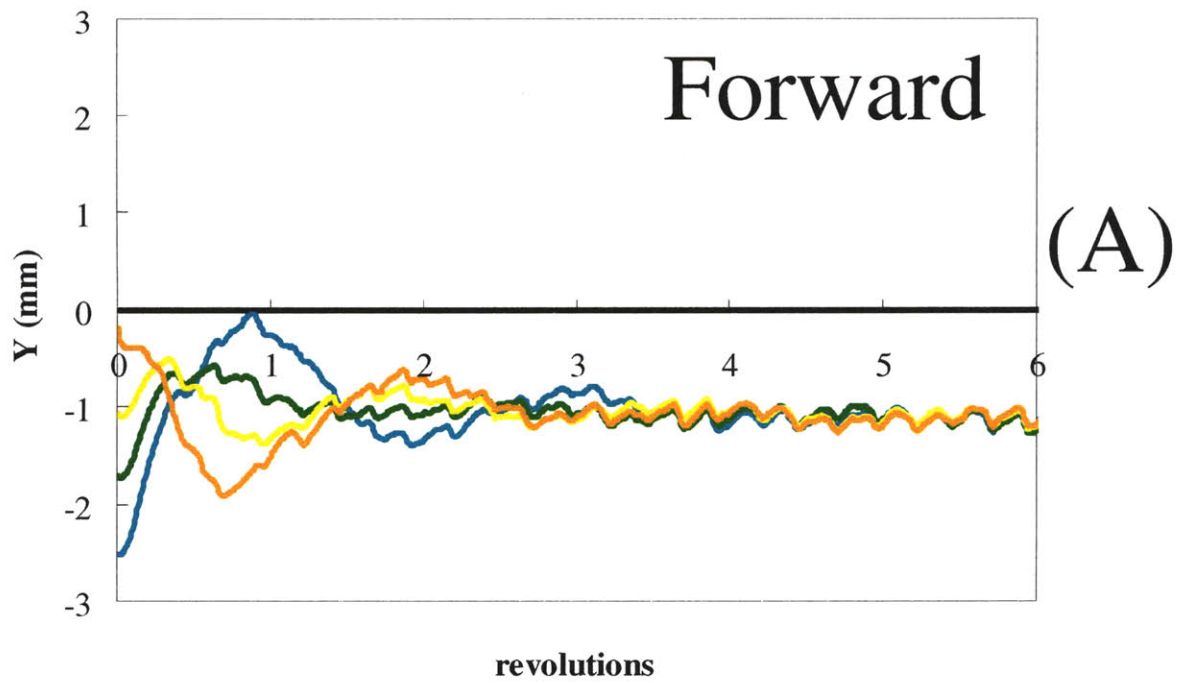
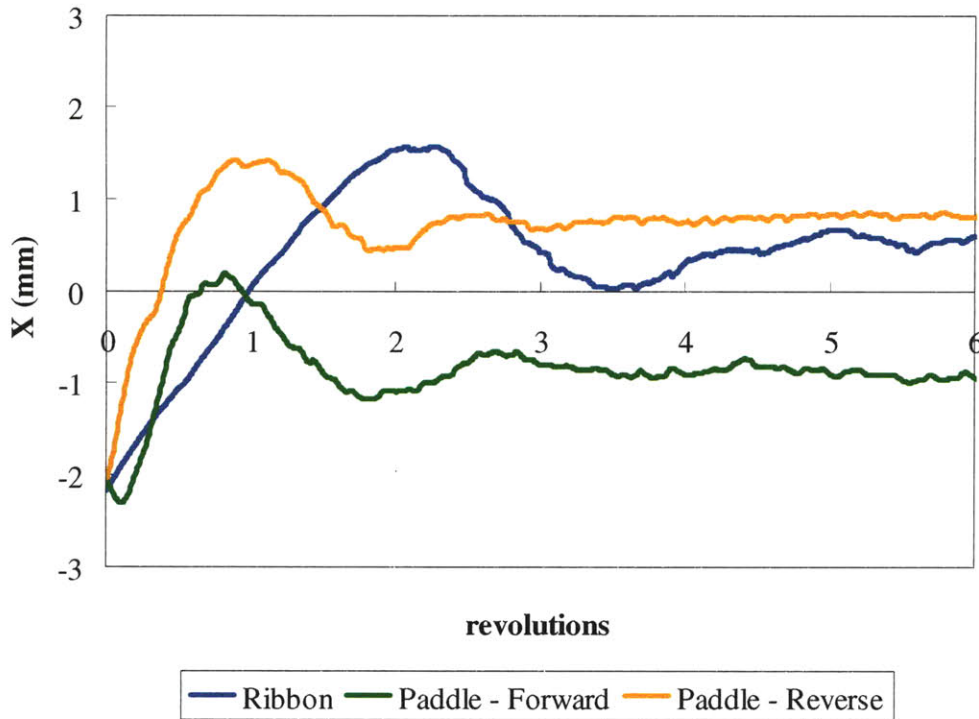
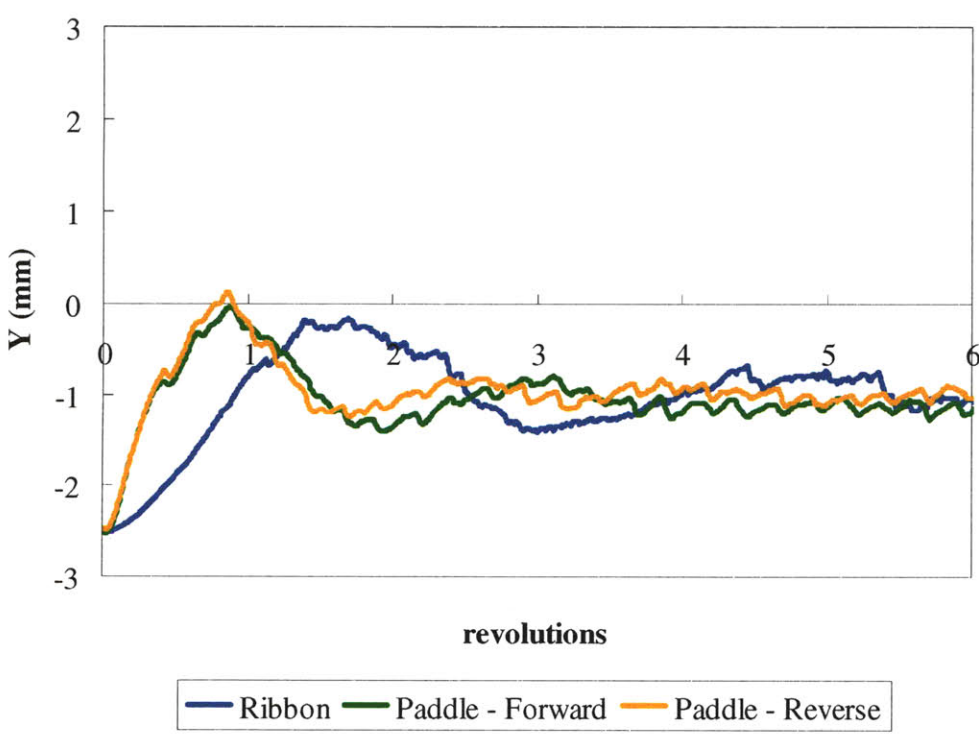


Figure 95: Centroids of Y initial position groups (blue = 1, green = 2, yellow = 3, orange = 4) in the Y direction for an eighth scale paddle blender operating at 40 RPM with 300 micron lactose particles and a 0.0035 g/s inflow.



(A)



(B)

Figure 96: Centroids of X and Y initial position Group 1 (blue) in the Y direction for an eighth scale double helical ribbon blender operating at 20 RPM or a paddle blender operating at 40 RPM with 300 micron lactose particles and a 0.0035 g/s inflow.

The Y initial position groups' centroids (Figure 95 A, B) behave similarly to the X groups with convergence for the paddle blenders occurring at approximately 2.5 revolutions and the ribbon blender at 5 revolutions. Y initial position Group 1 (Figure 96 B) converges to the same steady state position for both the paddle blenders and the ribbon. This is a surprising result given the different rotation rates between the two types of blenders.

The Z initial position groups' centroids (Figure 97 A, B) accelerate over the first half of the blender. This can be seen in the Group 2 centroid as it increases its axial velocity over the time period examined. The initial position Group 2 centroid (Figure 99 A) moves much faster in the axial direction in the ribbon blender than in either of the paddle blenders. It is also not surprising that the Group 2 moves slightly faster axially for the forward turning paddle blender than in the reverse turning paddle blender.

The R initial position groups' centroids (Figure 98 A, B) rapidly converge to a common position within the first two revolutions for both paddle blenders. The R initial position group centroids of the ribbon blender never truly converge to same extent, as can be seen when comparing the Group 1 centroids (Figure 99 B).

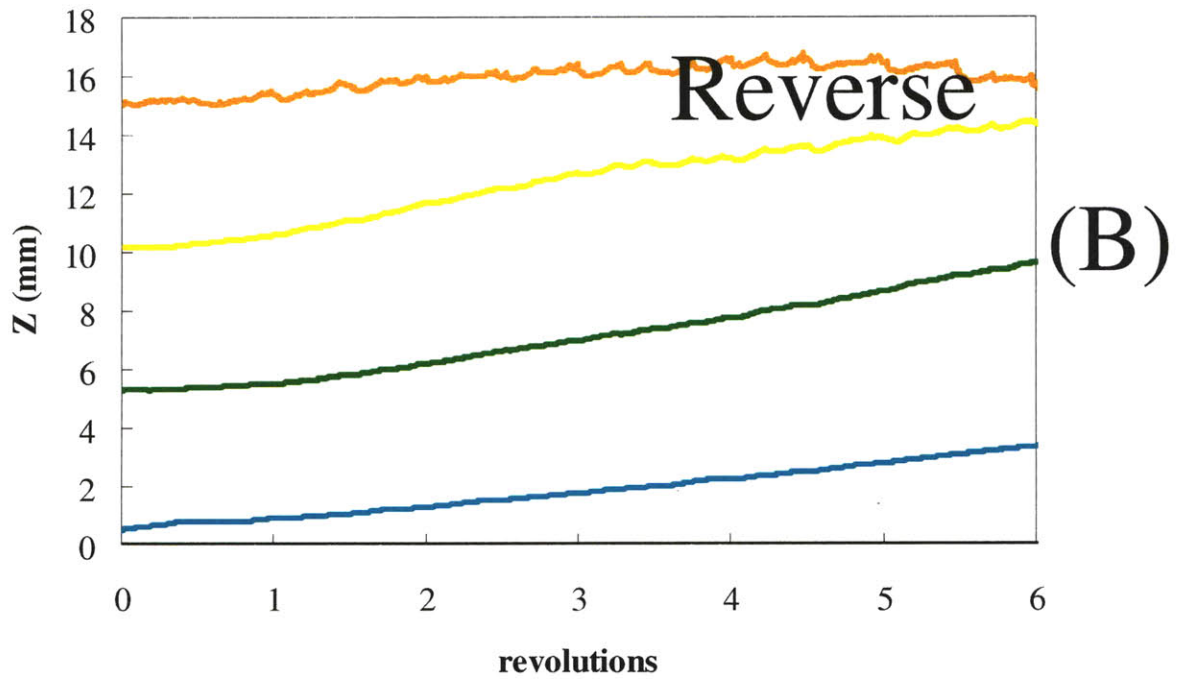
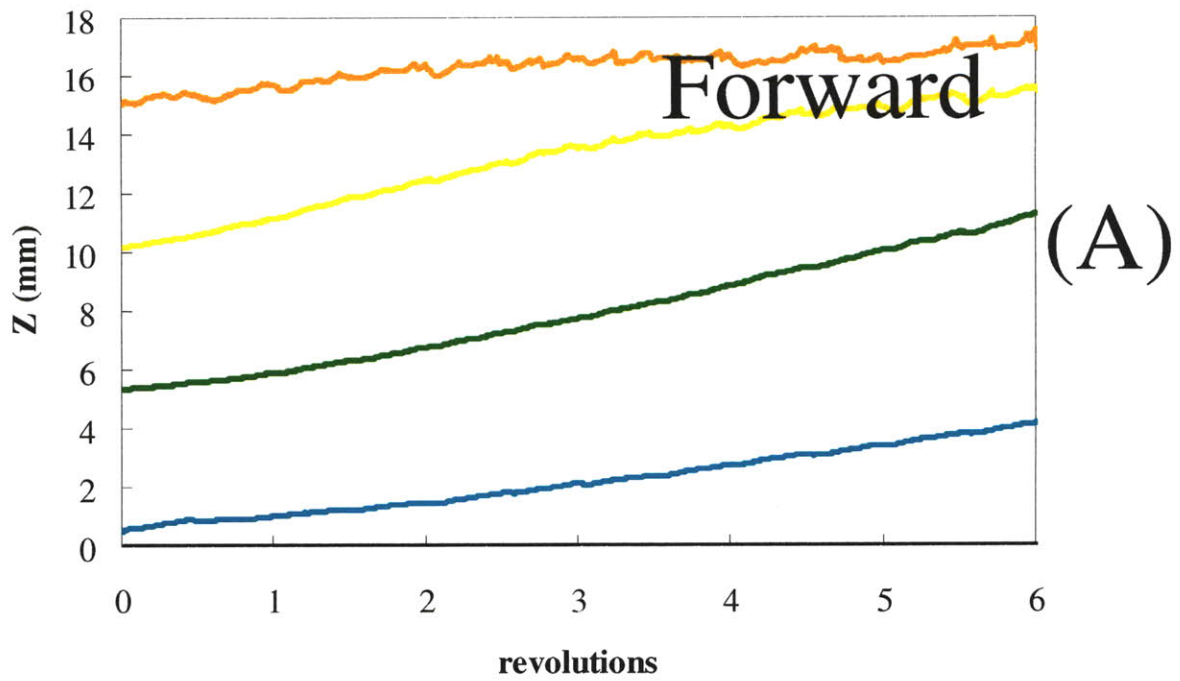


Figure 97: Centroids of Z initial position groups (blue = 1, green = 2, yellow = 3, orange = 4) in the Z direction for an eighth scale paddle blender operating at 40 RPM with 300 micron lactose particles and a 0.0035 g/s inflow.

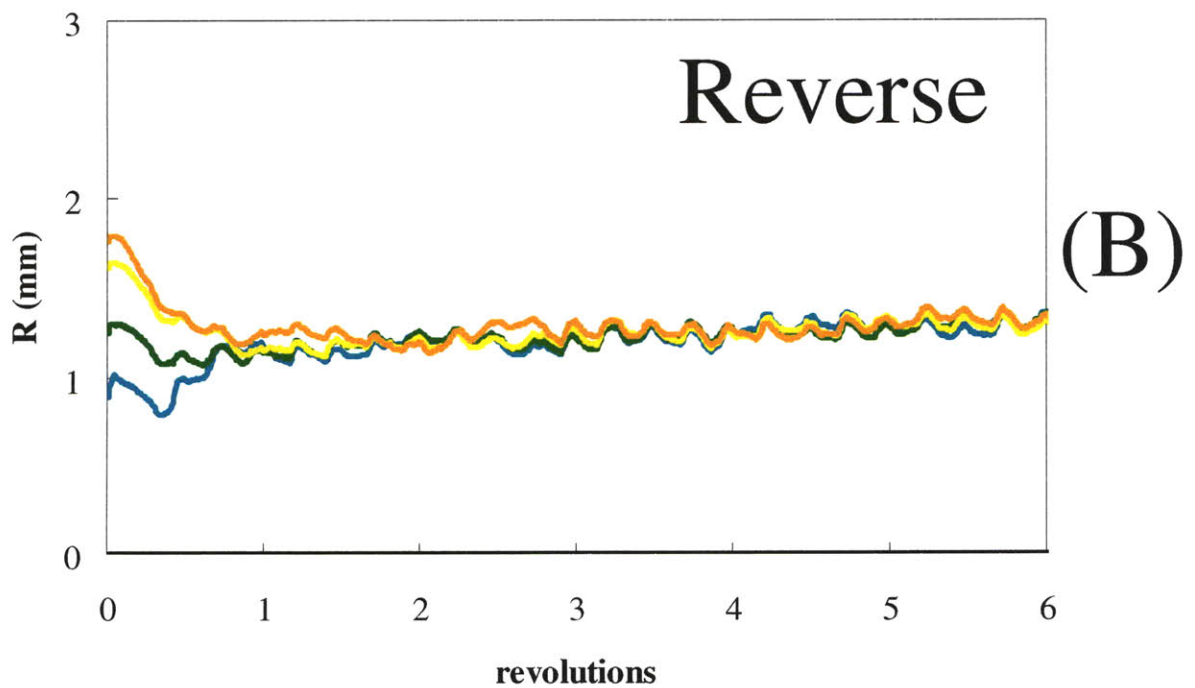
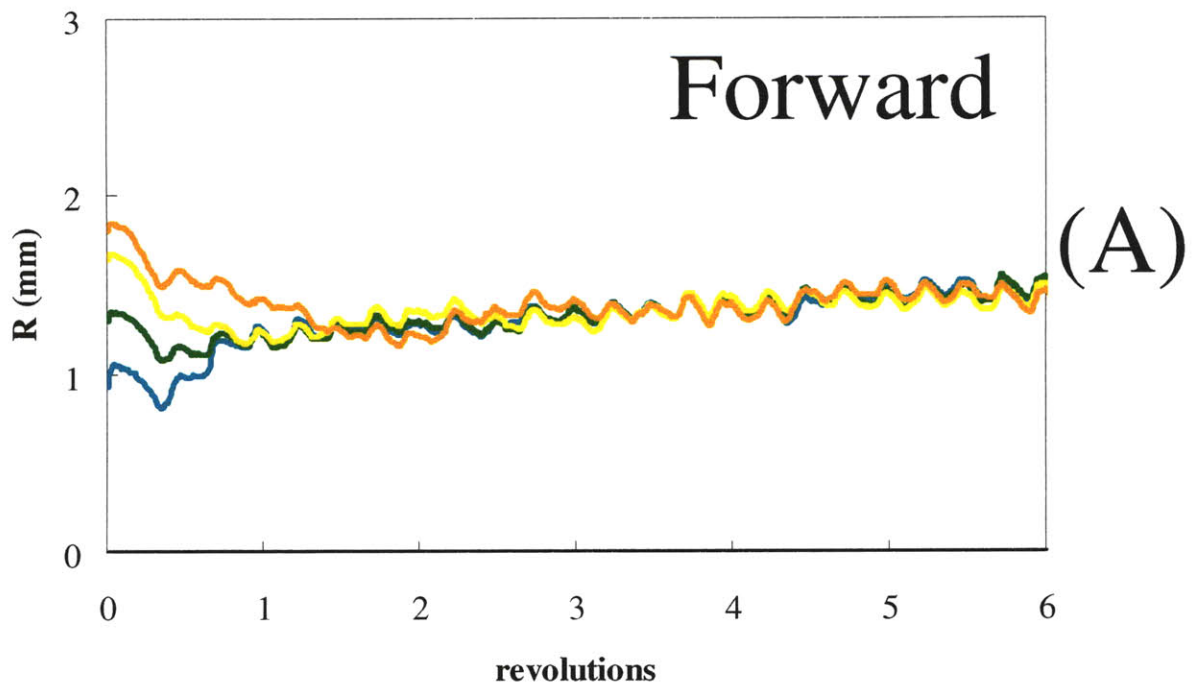
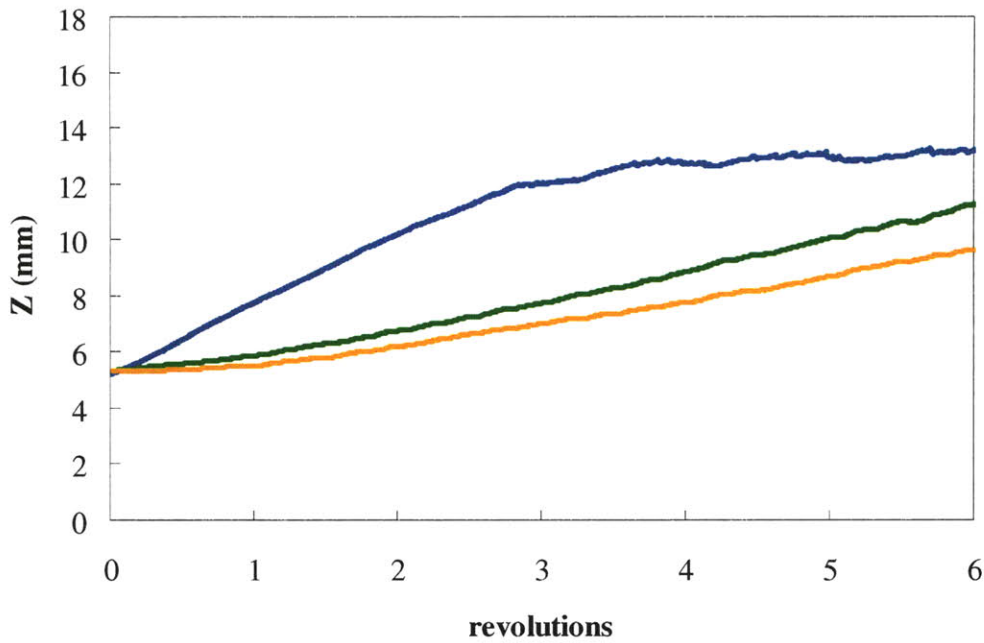
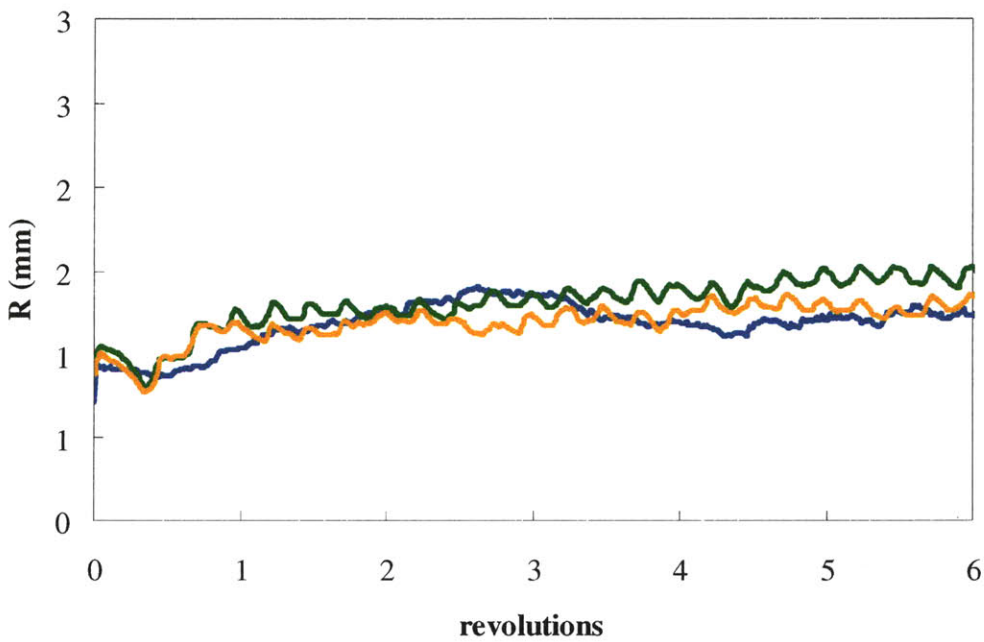


Figure 98: Centroids of R initial position groups (blue = 1, green = 2, yellow = 3, orange = 4) in the R direction for an eighth scale paddle blender operating at 40 RPM with 300 micron lactose particles and a 0.0035 g/s inflow.



(A)



(B)

Figure 99: Centroids of Z initial position Group 2 (green) and R initial position Group 1 (blue) in the R direction for an eighth scale double helical ribbon blender operating at 20 RPM or a paddle blender operating at 40 RPM with 300 micron lactose particles and a 0.0035 g/s inflow.

7.6.2 *Quantitative mixing measure*

The paddle blenders have a linear increase in the homogeneity of the X initial position groups (Figure 100 A) for the first 2 revolutions. There is little difference in homogeneity whether the paddle blender is run forwards or backwards. In addition, both paddle blenders increase their X initial position group homogeneity at a much greater rate than the ribbon blender on a per revolution basis. The homogeneity of the Y initial position groups (Figure 100 B) in the paddle blenders has an initial linear increase in mixing state for the first revolution and then decreases to a slower linear increase in mixing state for the next 2 revolutions. For the Y initial position groups, the paddle blenders increase their homogeneity significantly faster than the ribbon blender after the first half revolution.

The homogeneity of the Z initial position groups (Figure 101 A) is fundamentally the same for both the ribbon blenders and the paddle blender over the first three revolutions. Notably, the paddle blenders continue mixing past these first 3 revolutions to produce a more homogenous blend than the ribbon blender. This result highlights the importance of diffusive mixing in avalanching particles for effective mixing in the axial direction. Finally, the homogeneity for the R initial position groups (Figure 101 B) is significantly higher for the paddle blenders than the ribbon blender. It is also worth noting that due to the higher rotation rate (40 RPM) of the paddle blenders, they are actually mixing at an even greater rate than the ribbon blender.

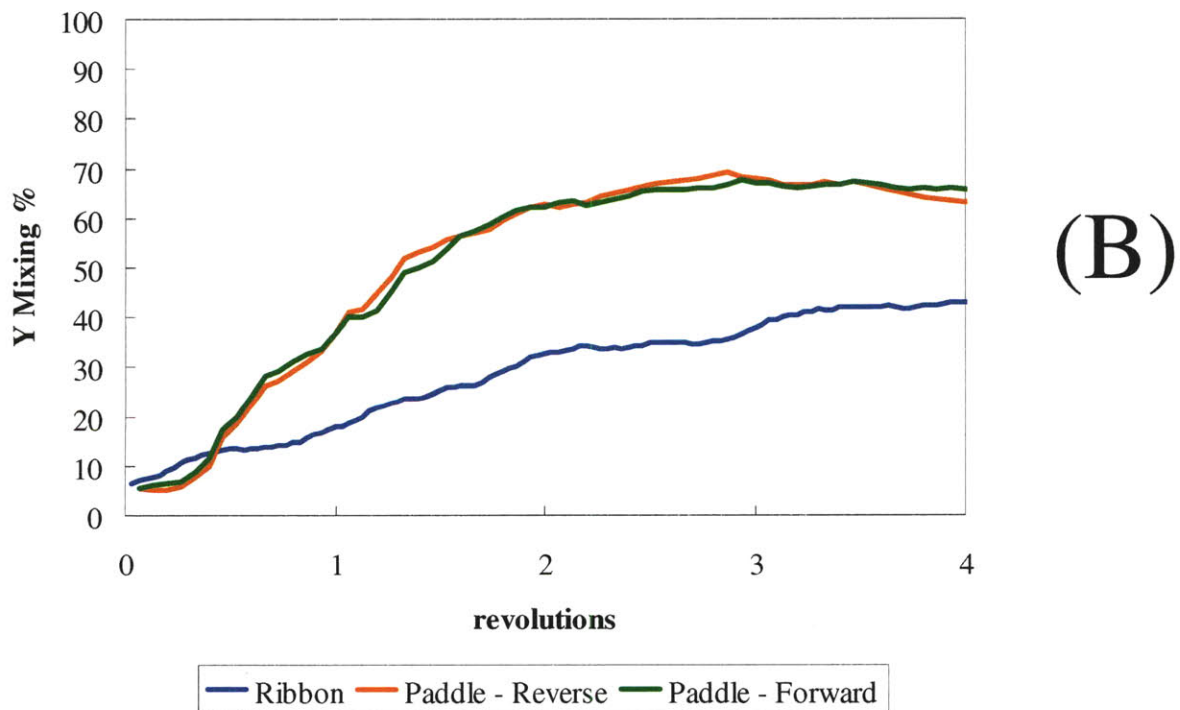
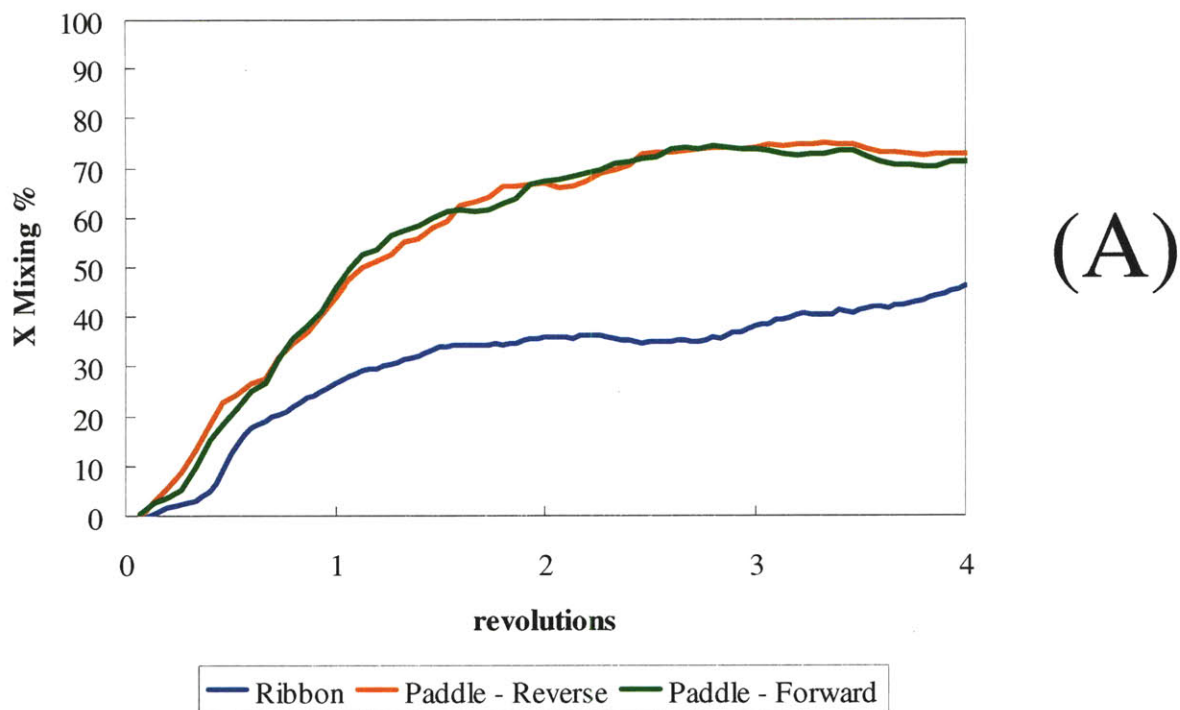


Figure 100: Homogeneity (mixing %) for X and Y initial position groups in eighth scale blenders with 300 micron lactose particles and a 0.0035 g/s inflow.

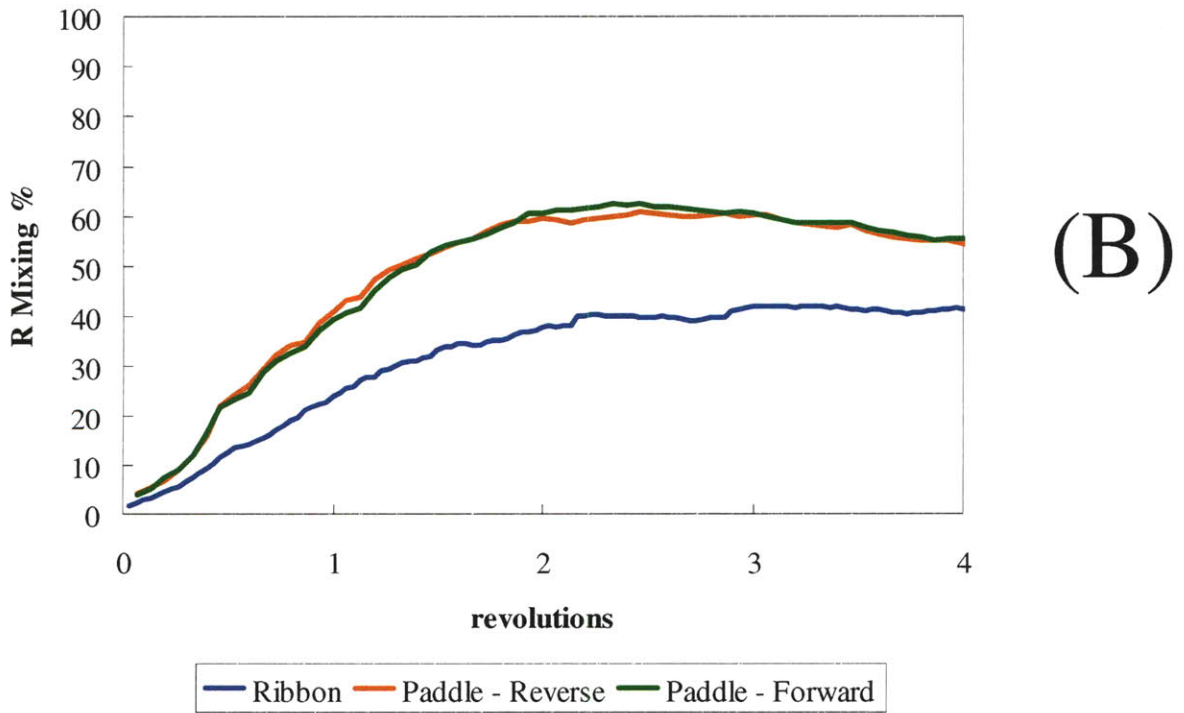
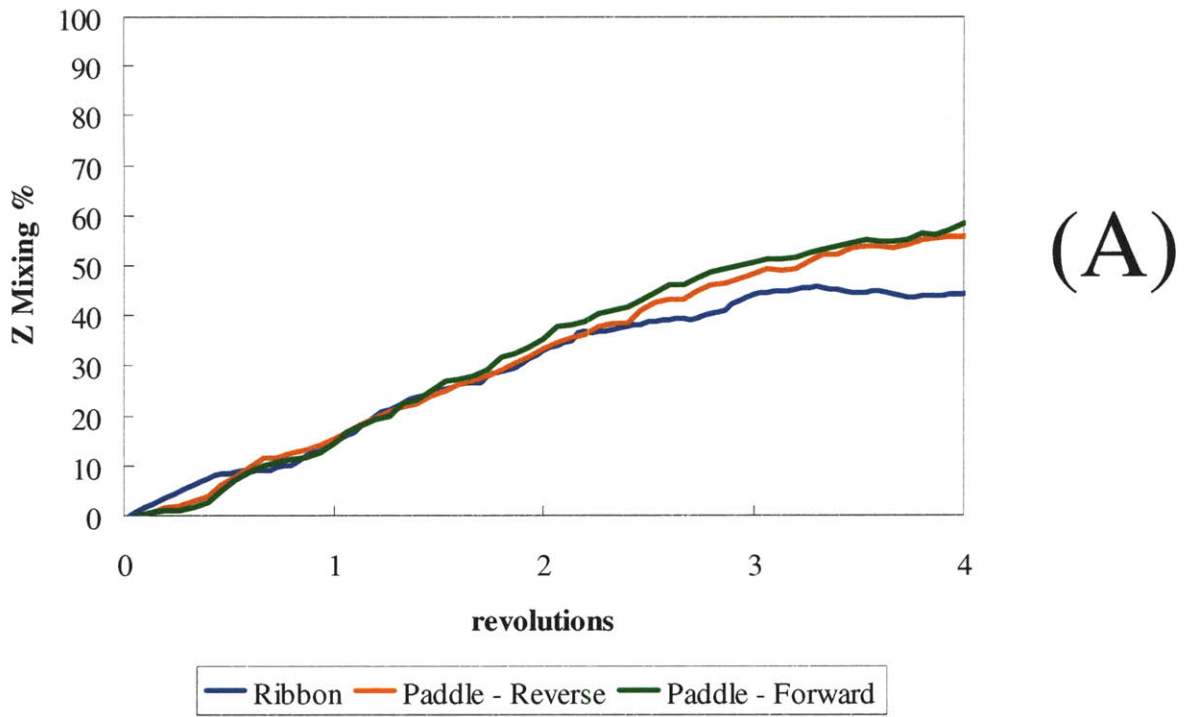


Figure 101: Homogeneity (mixing %) for Z and R initial position groups in eighth scale blenders with 300 micron lactose particles and a 0.0035 g/s inflow.

7.7 Summary of results

1. Blender size plays an important role in the flow behavior of the double helical ribbon blender. For the flow rates, there is a general trend that as the size of the blender increases the observed flow rate is greater than a volumetric scaling would predict. However, the extent to which these flow rates deviate from this volumetric scaling is different when measured in the middle of the blender compared to measurement at the exit of the blender. This seems to be caused by the cohesive properties of the particles that cause it to behave somewhat more like a fluid rather than the particle flow the Beverloo law would predict.
2. Between the eighth scale blender and the quarter scale blender, homogeneity follows a general trend that as the size of the blender increases the homogeneity of the blend decreases.
3. Between the sixteenth scale and the eighth scale blenders, the trend in homogeneity is not consistent. In some cases, the sixteenth scale blender exhibits the same or greater homogeneity over the first 2 revolutions (X and Y initial position groups), but then falls behind the eighth scale blender. In other cases (Z initial position groups), the sixteenth scale blender is generally more homogenous. Finally, there is the case where the sixteenth scale blender is never more homogenous than the eighth scale blender (R initial position groups). It is likely that the very small size of the sixteenth scale blender in relation to the particle size does not allow the particles to move freely in the radial direction and mix. It is telling that the exception to this is the mixing in the Z direction where there is the most room for the avalanching particles to rearrange.
4. The paddle blender has proven to be a resounding success for mixing pharmaceutical powders. It has shown far superior homogeneity on a per revolution basis to the double

helical ribbon blender in the X, Y and R dimensions and is comparable in homogeneity to the double helical ribbon blender in the Z dimension. When one takes into account that the paddle blender is operating at twice the rotation rate, its advantage in real world blend homogeneity is even more pronounced.

5. The paddle blender highlights the importance of transporting particles into a position where they can avalanche and diffusively mix. The wide flat paddles of the blender are very effective at lifting particles and the positioning of the paddles allows for two lifting/avalanching events to occur per revolution.
6. There was little difference in the homogeneity behavior between the paddle blender operated in the forward direction and the paddle blender operated in the reverse direction. However, there was a distinct difference in flow rates with the forward blender achieving a higher flow rate at both the middle and the exit of the blender.

8 EFFECTS OF PROCESS CONDITIONS

8.1 Rotation rate simulations

To explore the effects of rotation rate on the double helical ribbon blender on powder flow and blending performance, three simulations were conducted. The simulation operating conditions are modeled on those used by Lin [85] for residence time distribution experiments (Table 28).

Table 28: Summary of model conditions for DEM simulations comparing rotation rate.

Blender Scale	Shaft	Material	d_{particle} μm	Polydispersity	Cohesion	Ω RPM	Q_{inflow} mg/s	Fill Fraction frac
"1/8"	Ribbon	Lactose	300	Monodisperse	Standard	10	4.3	0.48
"1/8"	Ribbon	Lactose	300	Monodisperse	Standard	20	4.3	0.48
"1/8"	Ribbon	Lactose	300	Monodisperse	Standard	30	4.3	0.48

8.2 Flow behavior results for rotation rate simulations

8.2.1 Volume fraction

The rotation rate affects the axial distribution of particles. The lowest rotation rate of 10 RPM (Figure 102 A) leads to an increased volume fraction in the region near the inlet of the blender as seen by the yellow and red contours immediately below the inflow (black box in Figure 102 A). Particles move away from the inflow region and towards the exit region when the rotation rate increases to 20 RPM (Figure 102 B) and 30 RPM (Figure 102 C). This has the effect of changing fill fraction at various axial points along the blender and increasing the number of particles moving above the shaft.

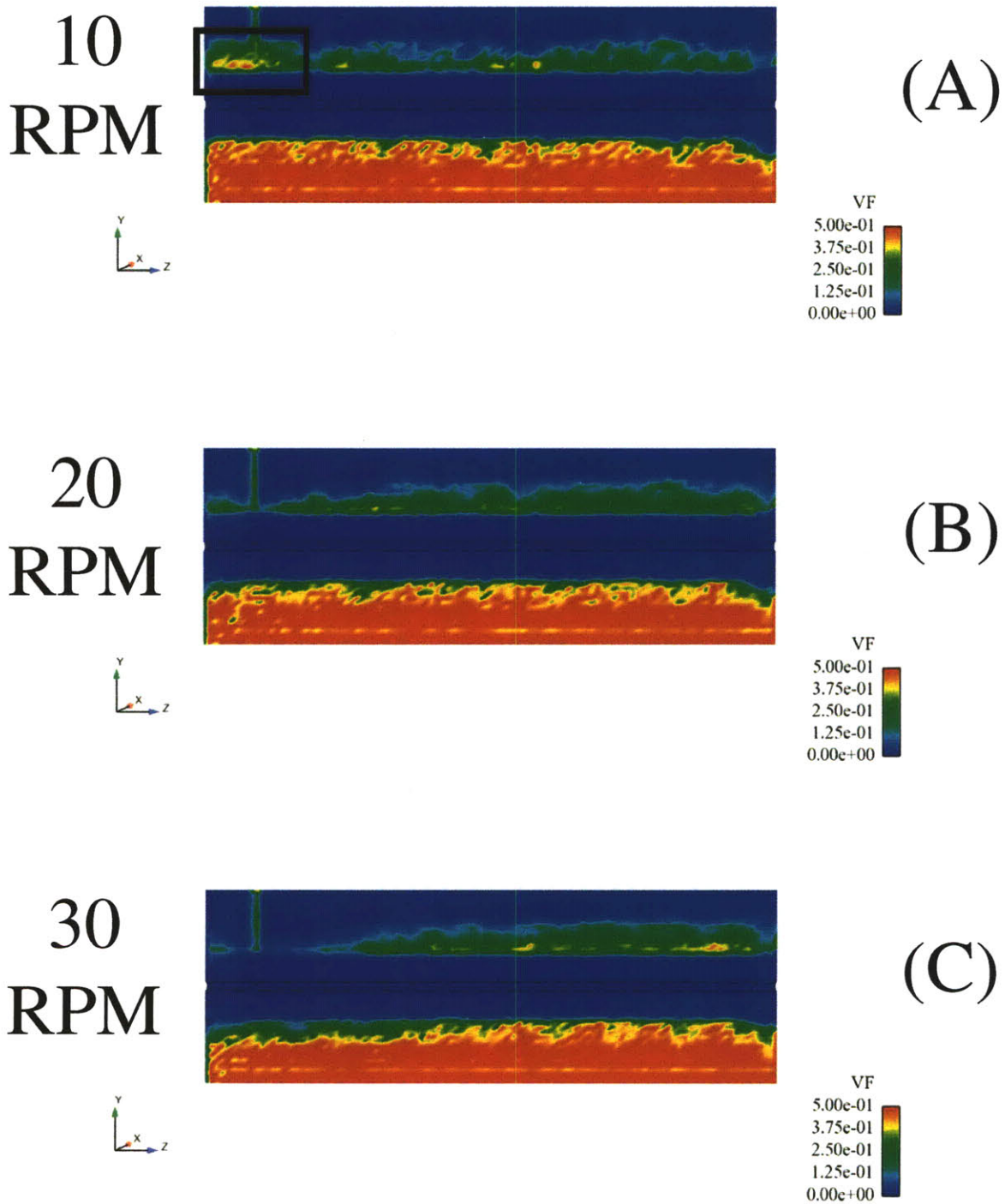
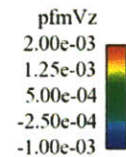
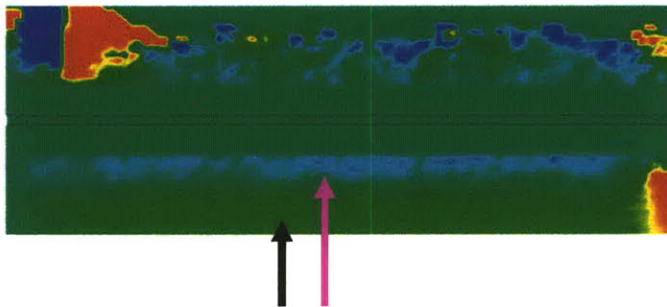


Figure 102: YZ slice showing volume fraction for an eighth scale double helical ribbon blender with 300 micron lactose particles at 10, 20 and 30 RPM and a 0.0043 g/s inflow.

8.2.2 Particle velocities

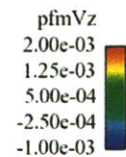
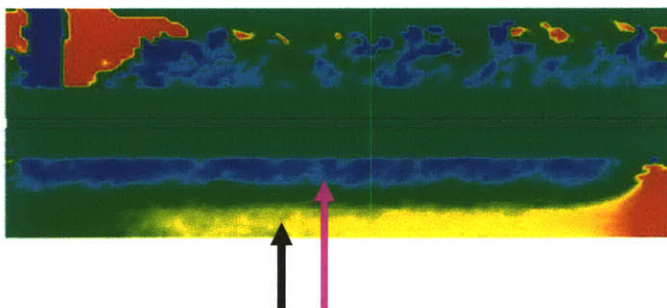
All of the simulations have the same general profile of Z velocity with a forward conveying region of positive V_z at the bottom of the blender (black arrows in Figure 103 A, B, C) and a reverse conveying region of negative V_z near the central shaft (magenta arrows in Figure 103 A, B, C). The magnitude of V_z is strongly correlated to rotation rate in both the forward and reverse conveying regions.

10
RPM



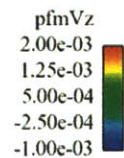
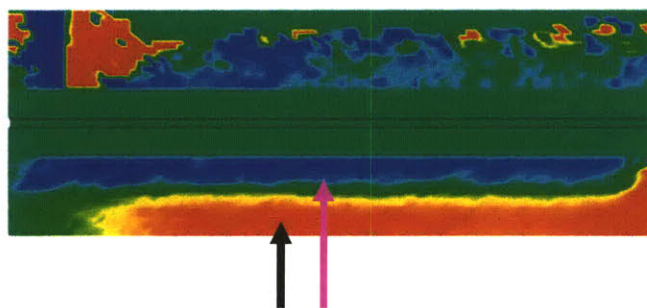
(A)

20
RPM



(B)

30
RPM



(C)

Figure 103: YZ slice showing the Z component of velocity for an eighth scale double helical ribbon blender with 300 micron lactose particles at 10, 20 and 30 RPM and a 0.0043 g/s inflow.

8.2.3 Granular temperature

The granular temperature follows the trend that higher rotation rate corresponds to a larger contour of the highest granular temperature in the XY cross section (dashed black boxes in Figure 104 A, B, C). In addition, the granular temperature increases on the lifting side of the blender as one increases rotation rate (black boxes in Figure 104 B, C). The overall higher granular temperature for the higher rotation rate simulations indicates that higher rotation rates will produce more diffusive mixing and should have greater homogeneity.

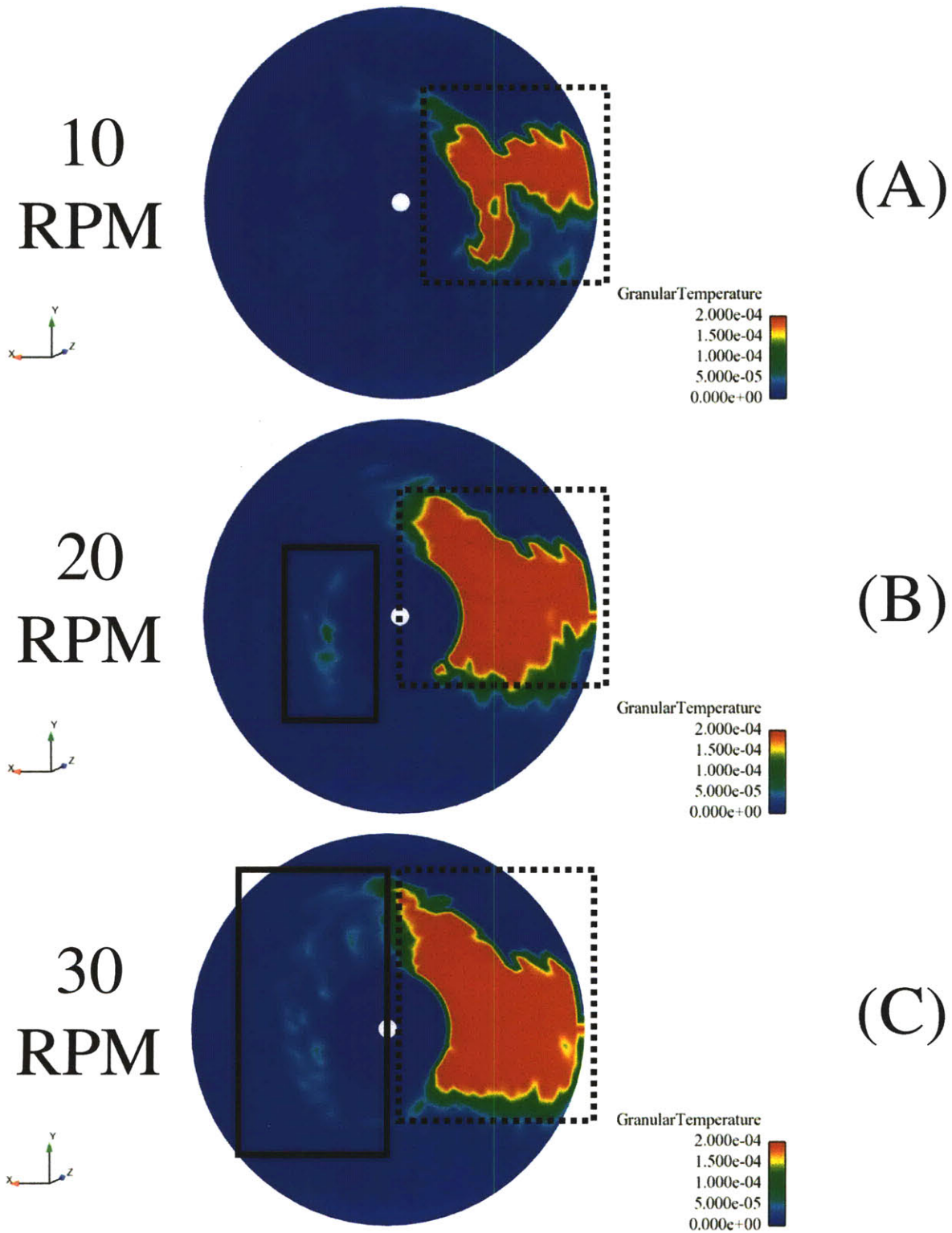


Figure 104: XY slice showing granular temperature for an eighth scale double helical ribbon blender with 300 micron lactose particles at 10, 20 and 30 RPM and a 0.0043 g/s inflow.

8.2.4 Flow rate

All of the rotation rates show some amount of periodic variation for their flow rate in the middle of the blender. While the 300 micron particles used in these simulations give the flow rate a fair amount of stochastic variation, the typical sinusoidal flow rate pattern with a period of 1 revolution is visible (Figure 105 A). Taking a 1 revolution moving average of the flow rate (Figure 105 B) indicates that in the middle of the blender the flow rate is positively correlated to the rotation rate. Like the flow rates in the middle of the blender, the exit flow rates (Figure 106 B) are also positively correlated to the rotation rate. Plotting the exit flow rates against revolutions of the shaft shows a similar periodic shape for the different rotation rates with varying amplitude. The periodic shape is characterized by two peaks of outflow per revolution (Figure 106 A): a smaller peak associated with the ribbon sweeping particles out of the top exit port and a larger peak when the blender sweeps particles out of the bottom exit port.

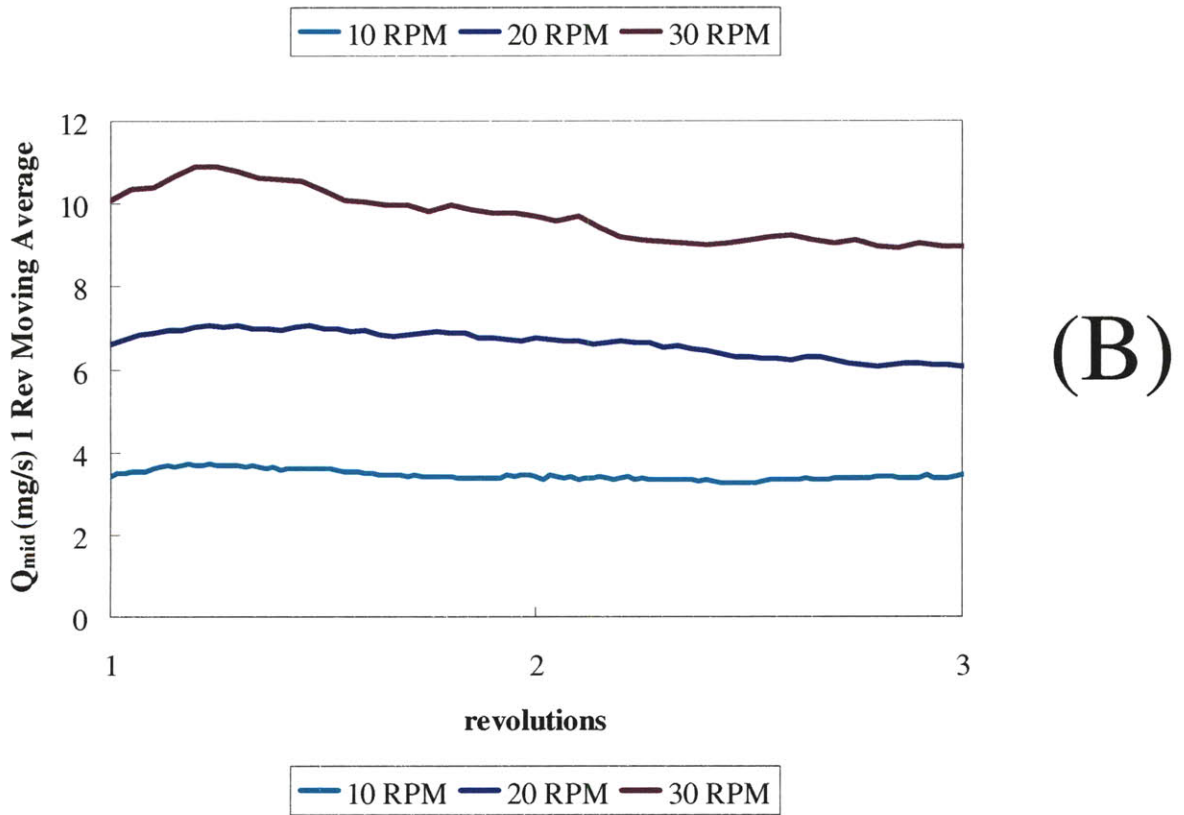
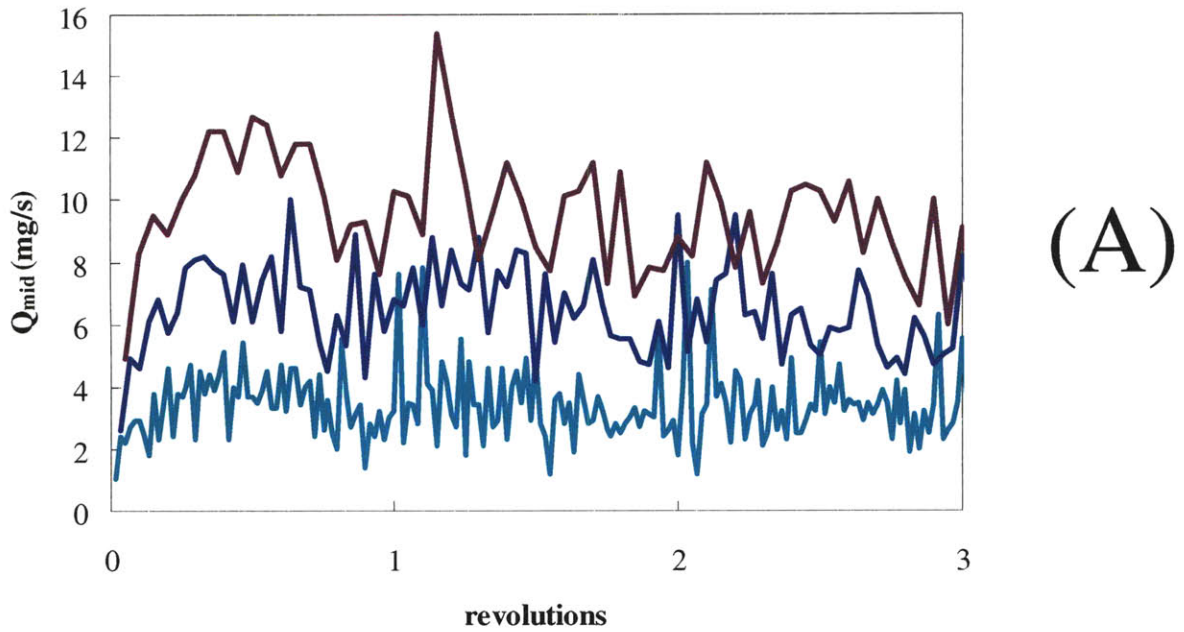


Figure 105: Flow rate in mg/s at the middle of an eighth scale double helical ribbon blender with 300 micron lactose particles operating between 10 RPM and 30 RPM and a 0.0043 g/s inflow.

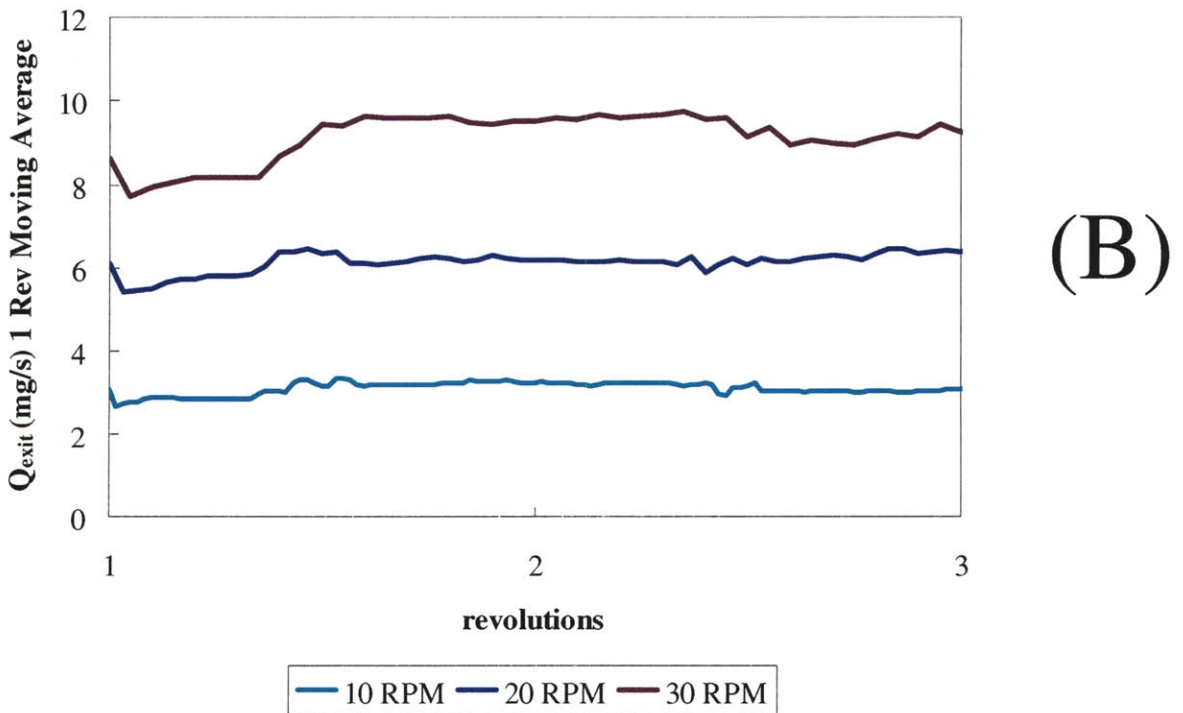
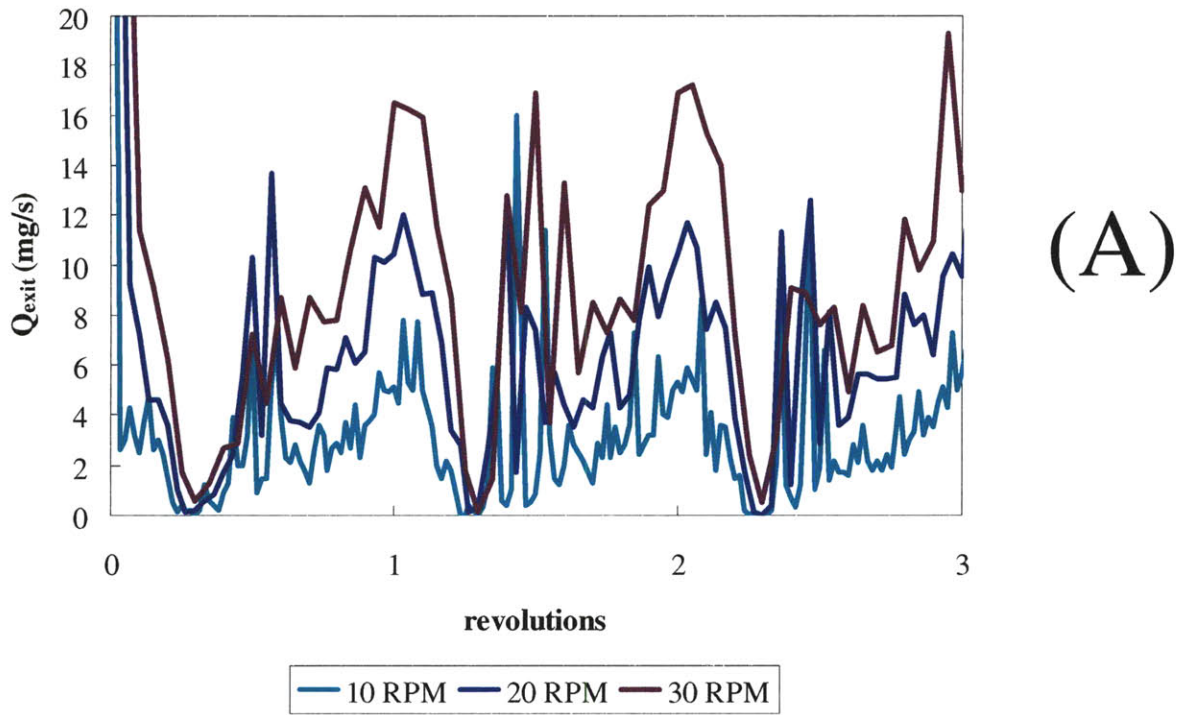


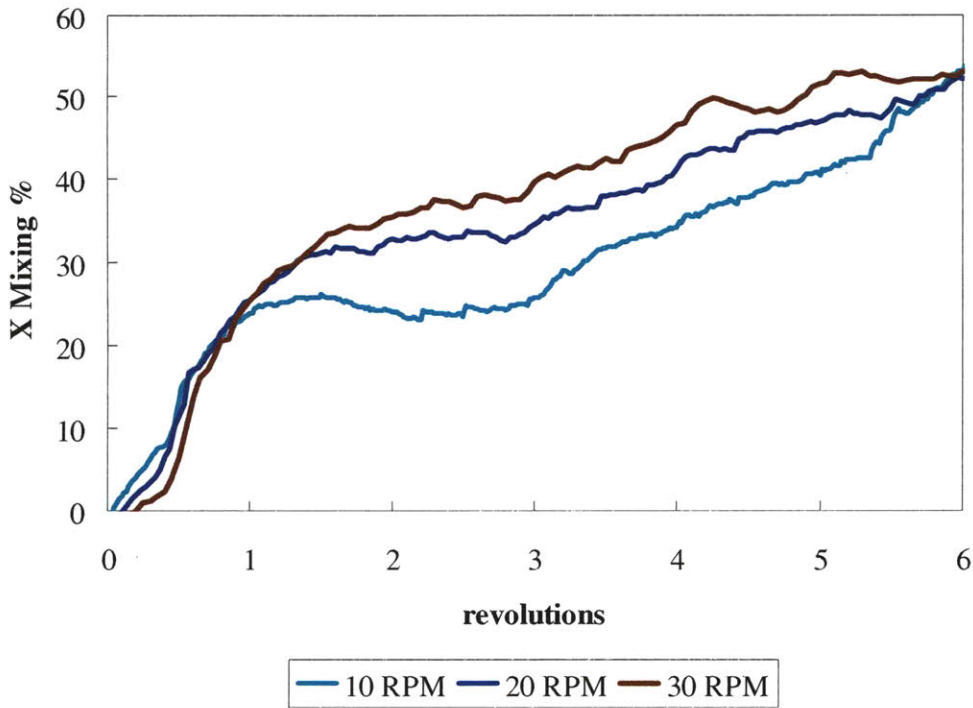
Figure 106: Flow rate in mg/s at the exit of an eighth scale double helical ribbon blender with 300 micron lactose particles operating between 10 RPM and 30 RPM and a 0.0043 g/s inflow.

8.3 Mixing results for rotation rate simulations

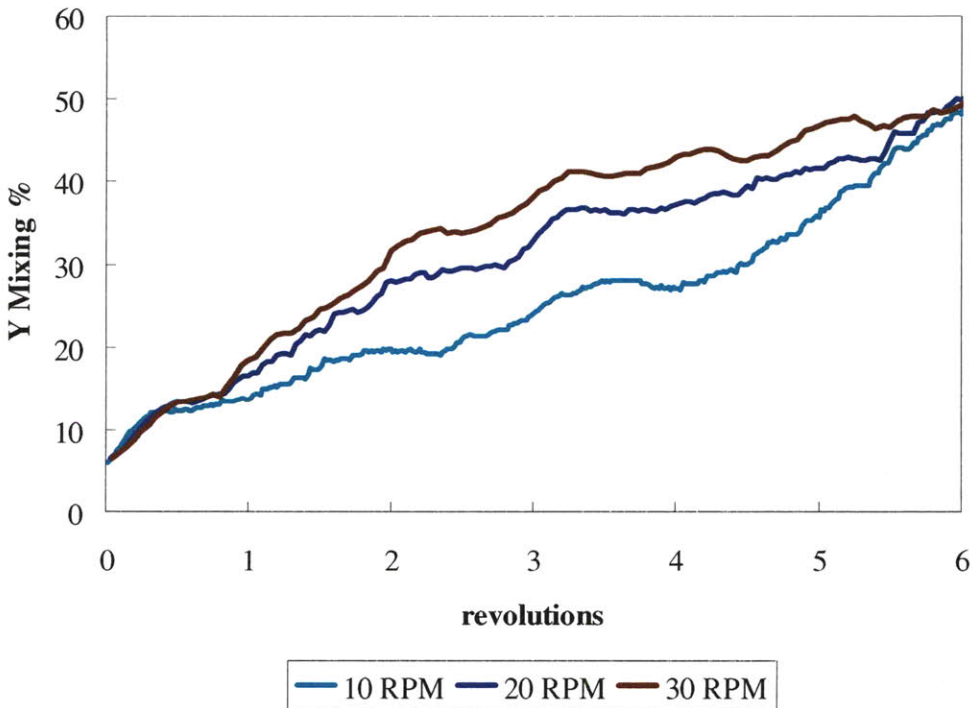
8.3.1 Particle mixing measure

The homogeneity (mixing %) of the X initial position groups (Figure 107 A) is very similar for the different rotation rates over the first revolution of the blender, but in subsequent revolutions, the higher rotation rate simulations achieve greater homogeneity. For all of the different rotation rates, the homogeneity of the Y initial position groups (Figure 107 B) is very similar up to the first revolution. However, after the first revolution, the higher rotation rates also begin to achieve greater homogeneity.

The homogeneity of the Z initial position groups (Figure 108 A) for the various process conditions is similar over the first 2 revolutions of the blender. At this point, the three rotation rates diverge over the next revolution of the blender with the 20 RPM and 30 RPM simulations achieving an asymptotic limit to their homogeneity after the third revolution. The 30 RPM simulation has a slightly higher asymptotic limit to homogeneity than the 20 RPM simulation. The 10 RPM simulation continues to increase the homogeneity of the Z initial position groups at a lower rate for revolutions 3, 4 and 5. Ultimately, the homogeneity of the Z initial position groups at the three rotation rates appears to be converging. The radial mixing (Figure 108 B) has similar behavior with the higher rotation rates demonstrating greater homogeneity after the first revolution of the blender, but then ultimately achieving the same homogeneity after 5 revolutions.

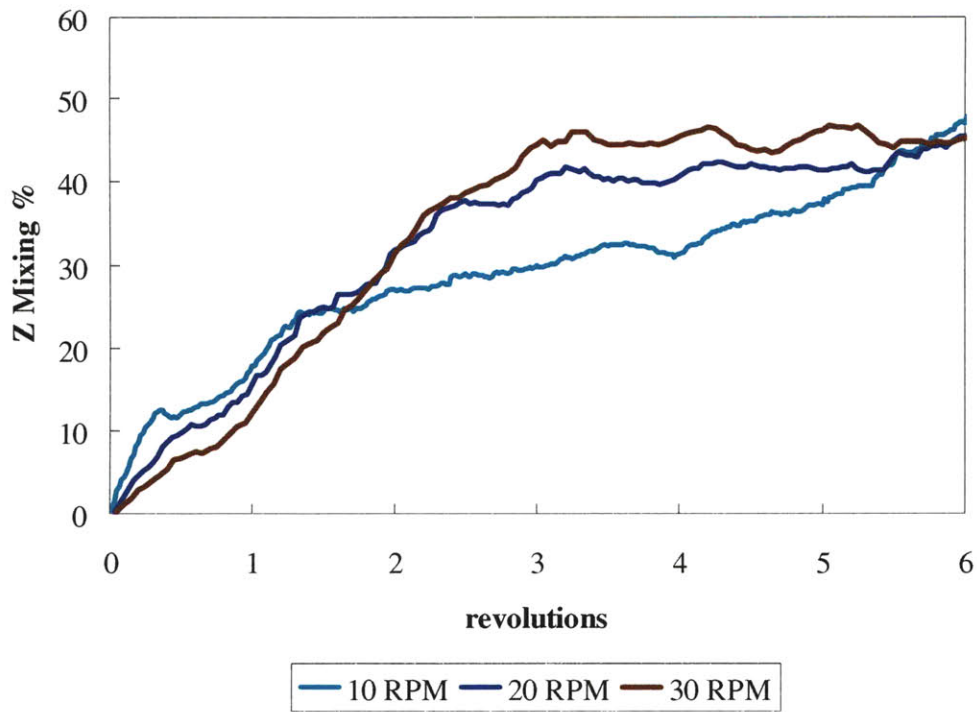


(A)

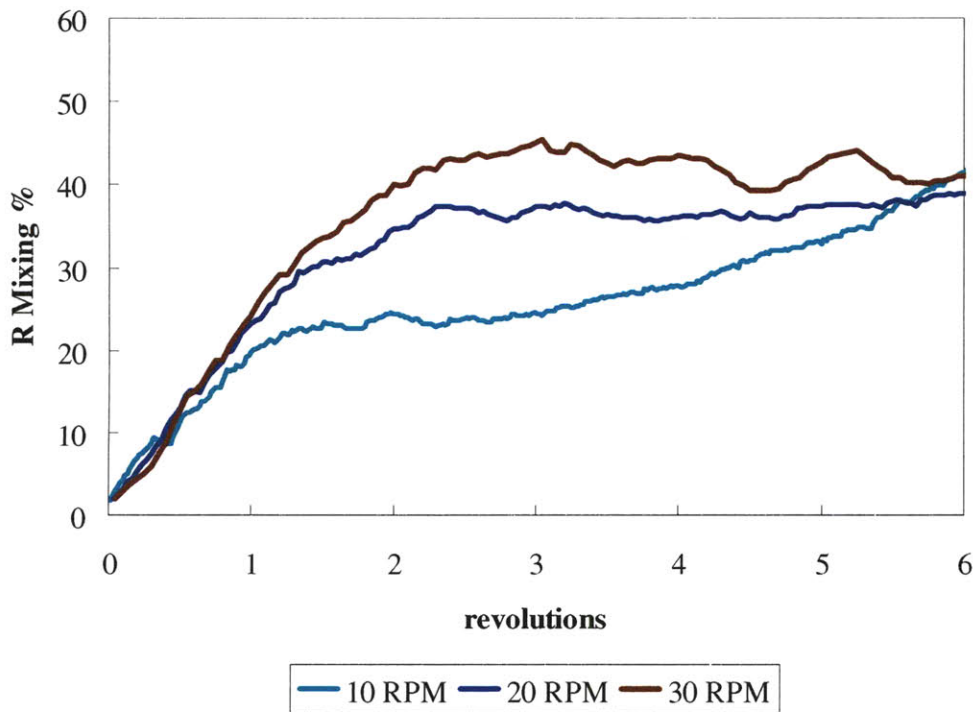


(B)

Figure 107: Homogeneity (mixing %) for X and Y initial position groups in an eighth scale double helical ribbon blender with 300 micron lactose particles operating between 10 RPM and 30 RPM and a 0.0043 g/s inflow.



(A)



(B)

Figure 108: Homogeneity (mixing %) for Z and R initial position groups in an eighth scale double helical ribbon blender with 300 micron lactose particles operating between 10 RPM and 30 RPM and a 0.0043 g/s inflow.

8.4 Fill fraction simulations

Five simulations were conducted to explore the effects of fill fraction on flow behavior and homogeneity. Fill fraction is dependent on both inflow rate and rotation rate. Both inflow rate and rotation rate need to be varied in order to create realistic simulations. The simulation operating conditions used for the residence time distribution simulations are modeled on those used by Lin [85] for residence time distribution experiments (Table 29).

Table 29: Summary of model conditions for DEM simulations comparing fill fraction.

Name	Blender Scale	Shaft	Material	d_{particle} μm	Polydispersity	Cohesion	Ω RPM	Q_{inflow} mg/s	Fill Fraction frac
-	-	-	-	-	-	-	-	-	-
Q6 R10	"1/8"	Ribbon	Lactose	300	Monodisperse	Standard	10	3.3	0.65
Q8 R10	"1/8"	Ribbon	Lactose	300	Monodisperse	Standard	10	4.3	0.67
Q8 R20	"1/8"	Ribbon	Lactose	300	Monodisperse	Standard	20	4.3	0.53
Q8 R30	"1/8"	Ribbon	Lactose	300	Monodisperse	Standard	30	4.3	0.40
Q12 R30	"1/8"	Ribbon	Lactose	300	Monodisperse	Standard	30	6.5	0.55

The simulations have been named by their inflow rate (“Q”) at the experimental scale and their rotation rate (“R”).

8.5 Flow behavior results for fill fraction simulations

8.5.1 Flow rates

Flow rates at the middle of the blender (Figure 109 A, B) are more dependent on rotation rate than fill fraction. This is apparent in the two simulations operating at 30 RPM which have the same flow rate despite having fill fractions of 0.40 and 0.55. At the exit of the blender (Figure 110 A, B), flow rates are still dominated by the differences in rotation rate. However, at the exit of the blender, the 30 RPM simulation with the higher fill fraction (0.55) actually has a higher flow rate than the simulation with a lower fill fraction (0.40).

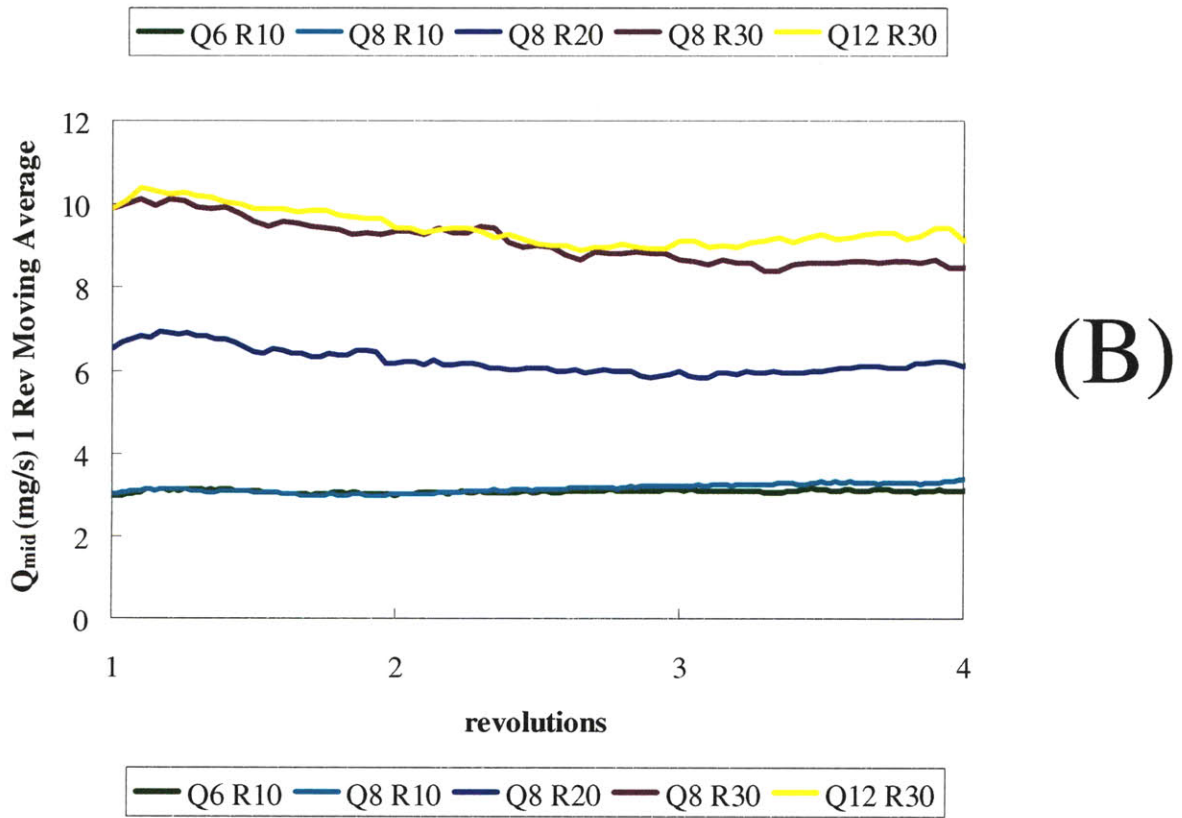
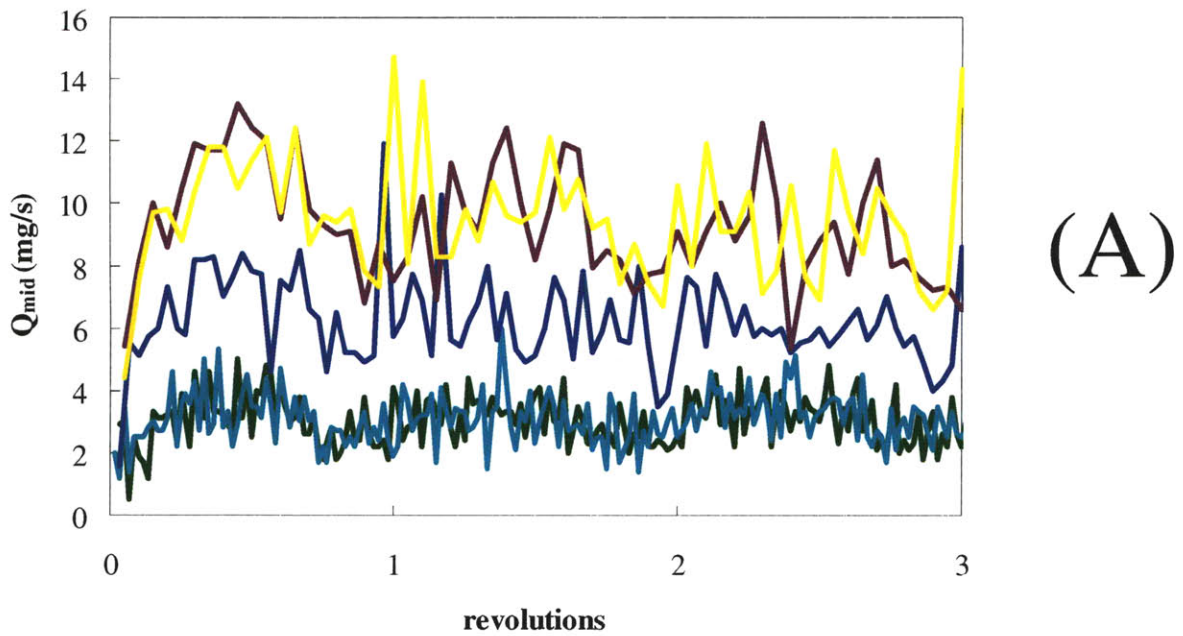


Figure 109: Flow rate in mg/s at the middle of an eighth scale double helical ribbon blender with 300 micron lactose particles operating with varying inflow, rotation rate and fill fraction.

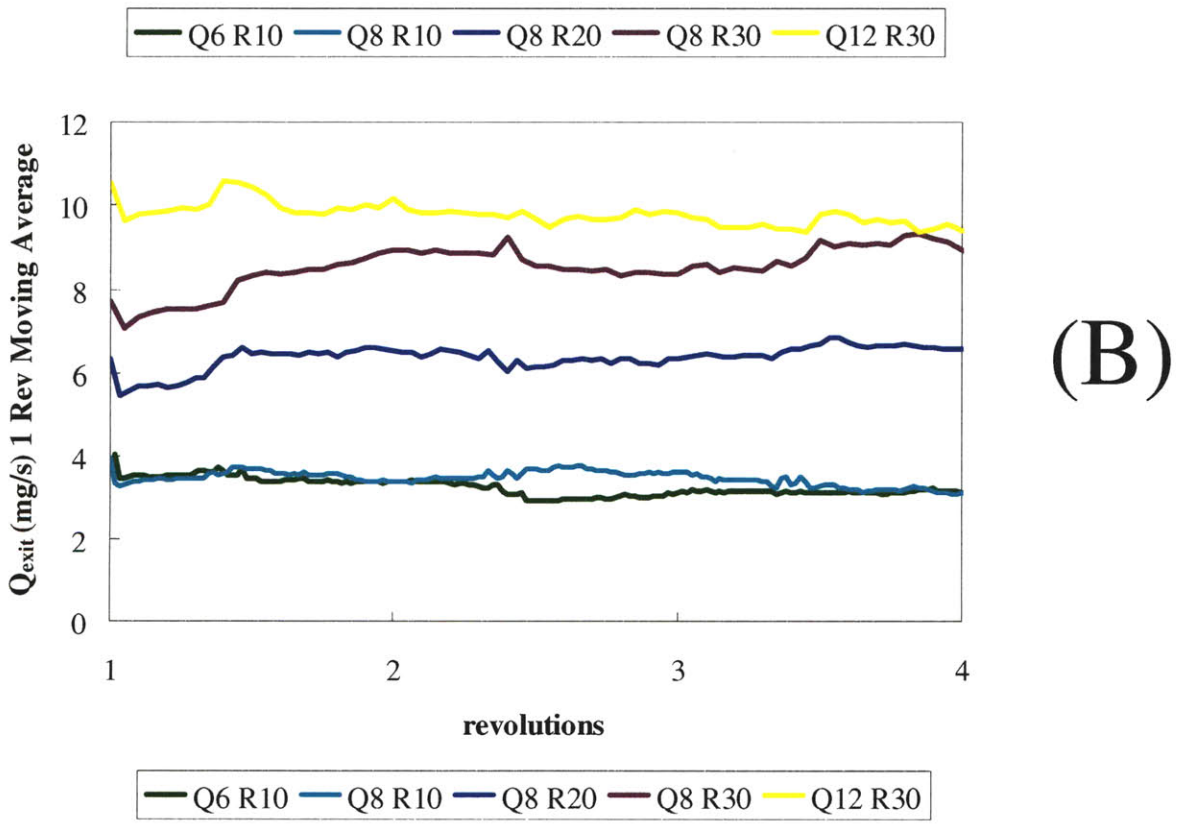
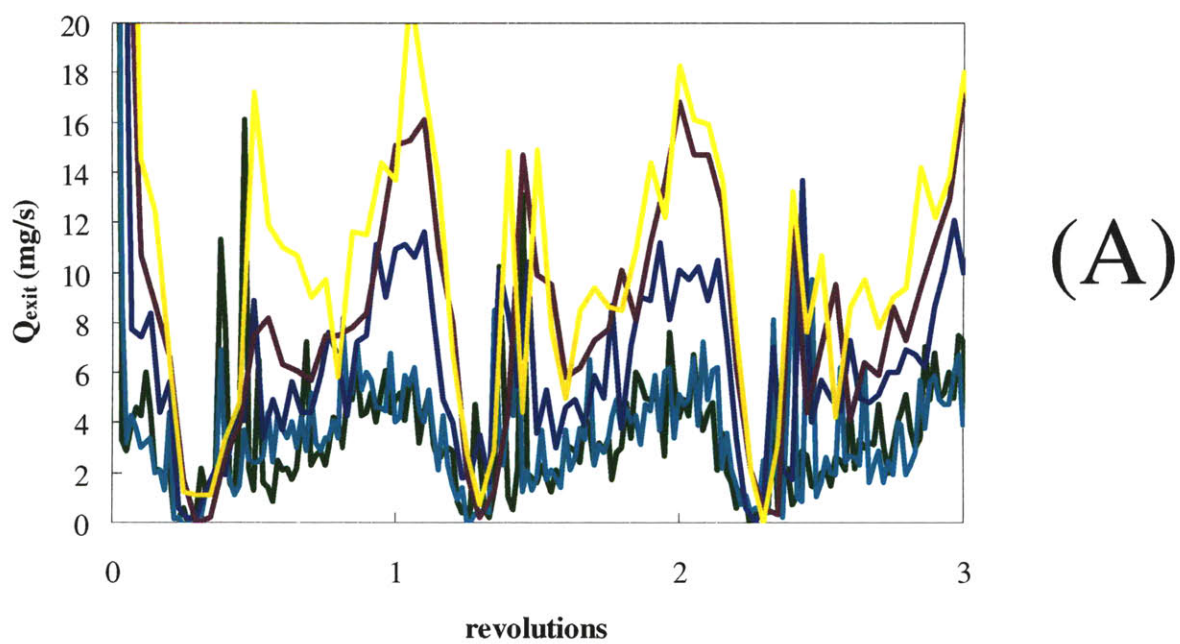


Figure 110: Flow rate in mg/s at the exit of an eighth scale double helical ribbon blender with 300 micron lactose particles operating with varying inflow, rotation rate and fill fraction.

8.6 Mixing results for fill fraction simulations

8.6.1 Quantitative mixing measure

The homogeneity of the initial position groups indicates certain fill fractions and operating conditions can have superior homogeneity in the double helical ribbon blender with these particles. The Q8 R20 (fill fraction of 0.53) and the Q12 R30 (fill fraction of 0.55) have very similar homogeneity for all of the different initial position groups. In addition, these two simulations have the highest homogeneity for the Y (Figure 111 B), Z (Figure 112 A) and R (Figure 112 B) initial position groups after the first revolution of the blender. Q8 R20 and Q12 R30 also have the highest homogeneity for the X initial position groups (Figure 111 A) after the third revolution of the blender. Increasing the fill fraction in simulations Q6 R10 (fill fraction of 0.65) and Q8 R10 (fill fraction of 0.67) and decreasing the fill fraction in simulation Q8 R30 (fill fraction of 0.40) appear to decrease the homogeneity of the blend.

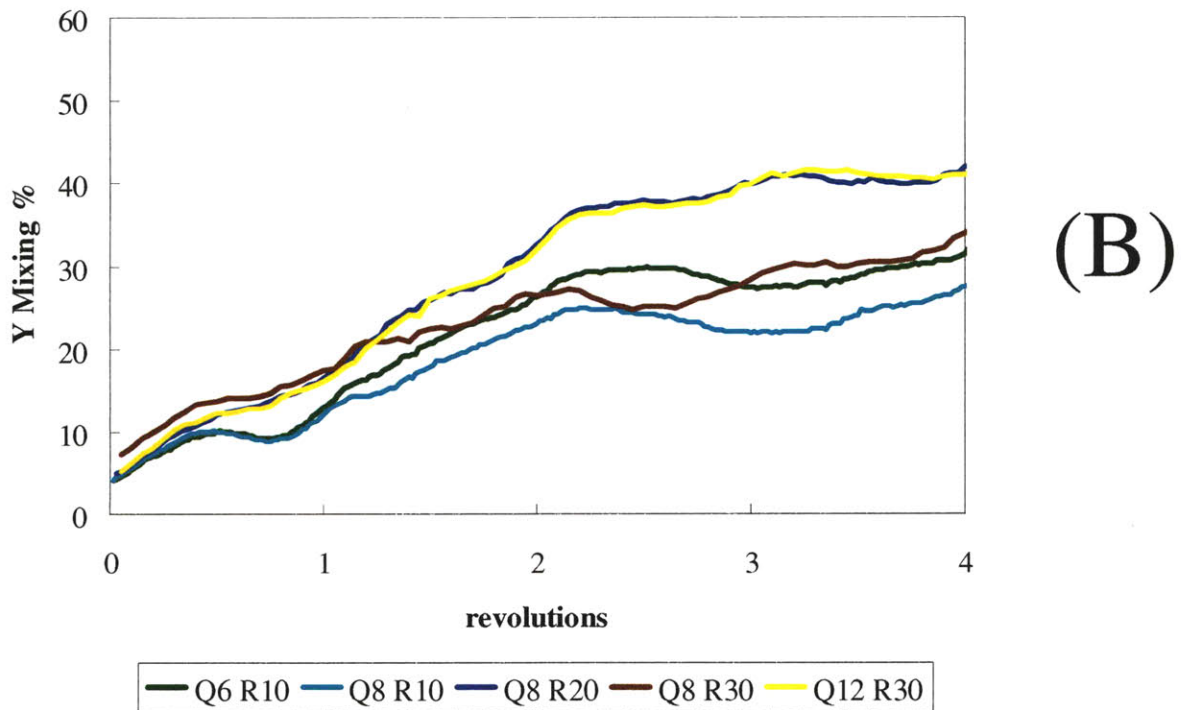
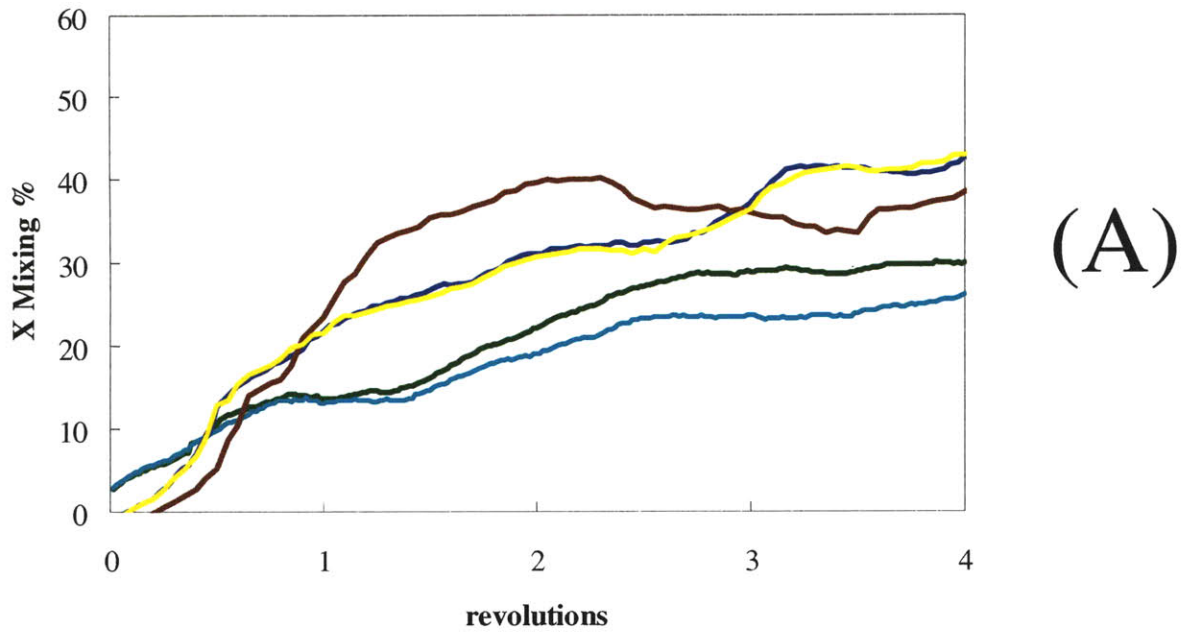


Figure 111: Homogeneity (mixing %) for X and Y initial position groups in an eighth scale double helical ribbon blender with 300 micron lactose particles operating with varying inflow, rotation rate and fill fraction.

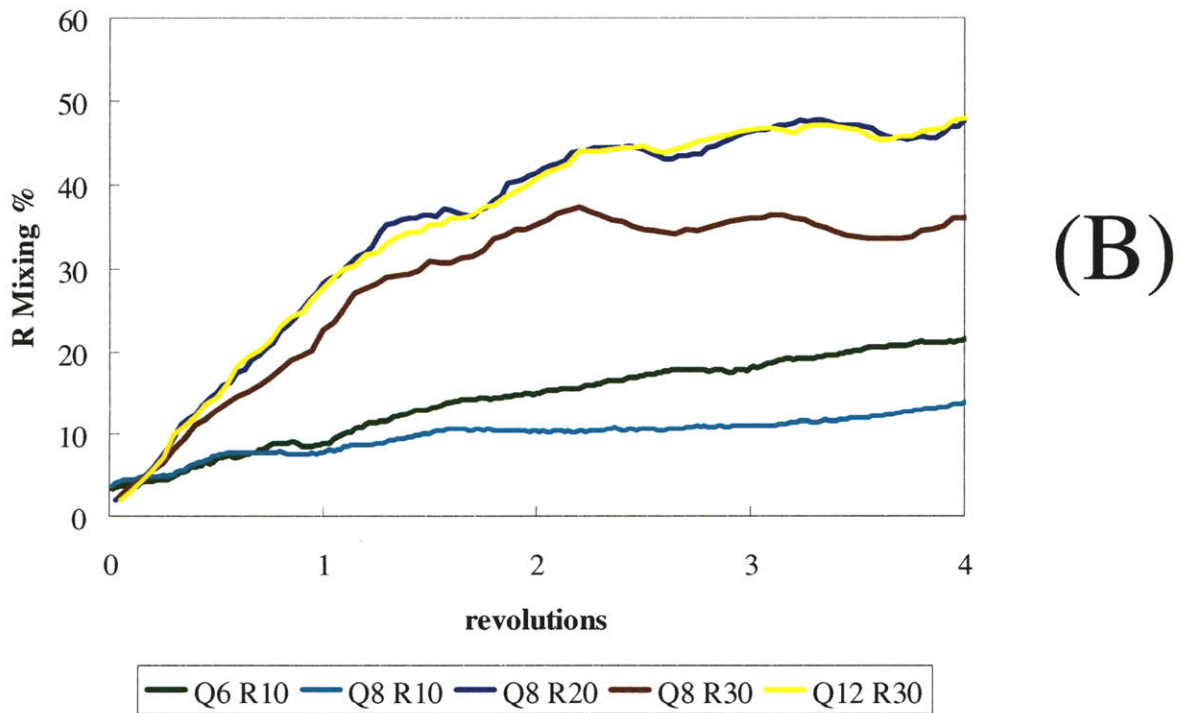
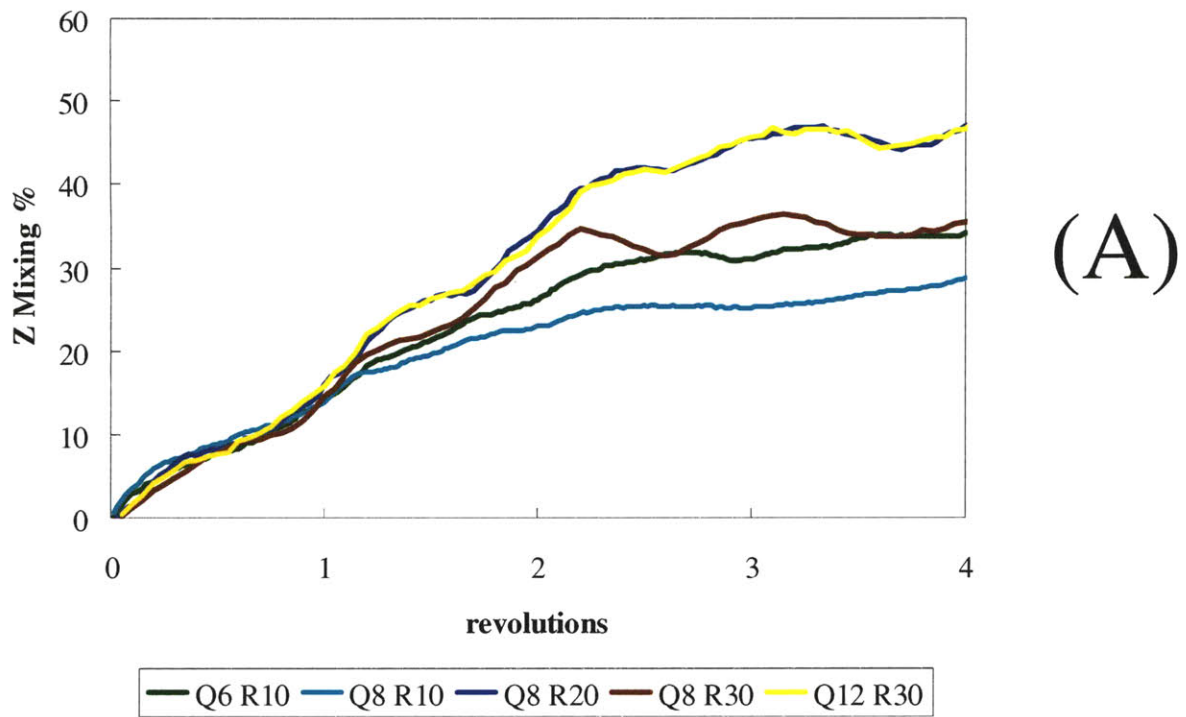


Figure 112: Homogeneity (mixing %) for Z and R initial position groups in an eighth scale double helical ribbon blender with 300 micron lactose particles operating with varying inflow, rotation rate and fill fraction.

8.7 Summary of results

1. Flow rates are well correlated to rotation rates at both the middle and exit of the blender. This is physically consistent with the fact that the rotation of the outer ribbon is the primary mechanism by which particles are moved forward.
2. Fill fractions between 0.40 and 0.67 have little effect on flow rates in the middle of the blender, but do have an effect on flow rates at the exit of the blender. In the middle of the blender, the flow rate is limited to how much particle area the inner and outer ribbon can sweep through. As the fill fraction increases over the range explored, the area of forward motion increases (outer ribbon), but is balanced by a proportional increase in the area of reverse motion (inner ribbon). At the exit of the blender, the particles in the higher fill fraction simulations can more easily flow out of the upper exit port which causes the higher flow rates.
3. Higher rotation rates lead to greater homogeneity at early times in the simulation, but ultimately all rotation rates lead to a similar homogeneity at 6 revolutions. As the residence time of the blender is approximately 14 revolutions, there should be little difference in observed homogeneity for material traveling through the blender at different rotation rates. This is seen in Lin's [85] experimental results where homogeneity at the exit of the blender is only weakly correlated to rotation rate. Ultimately, higher rotation rates offer significantly greater homogeneity when examined against time.
4. Fill fraction appears to affect the homogeneity of the double helical ribbon blender with monodisperse lactose particles. This is in line with a primarily diffusive mixing mechanism.

As fill fraction increases, the material has less time in the avalanche to randomly rearrange and mix.

9 ANALYSIS OF PHARMACEUTICAL POWDER BLENDING MODELS

The previous three chapters have demonstrated that particle properties, blender design and operating conditions can have an effect on both flow rates and homogeneity. These results can be used to test a number of the commonly reported scaling models for powder flows and blending and can be used to develop novel models for predicting flow rates and homogeneity in the double helical ribbon blender.

9.1 Summary of the effects of particle properties, blender designs and operating conditions

Five properties were seen to have significant effects on flow rate: particle size, cohesive force, blender size, rotation rate and fill fraction (Table 30). Particle size (Figure 113 A), blender size (Figure 115) and rotation rate (Figure 117 A) were all positively correlated to flow rate, while cohesive force (using surface energy as the measurement) (Figure 113 B) and fill fraction (Figure 117 B) are negatively correlated to flow rate.

Table 30: Summary of tested properties and their correlation to flow rate.

Property	Flow Rate Correlation	Chapter	Figure
Particle size	Positive	6	Figure 111
Cohesive force	Negative	6	Figure 111
Blender size	Positive	7	Figure 113
Rotation rate	Positive	8	Figure 115
Fill fraction	Negative	8	Figure 115

With the exception of cohesive force and fill fraction, all of the examined properties have a consistent trend with respect to homogeneity (Table 31). Cohesive force (Figure 114 B) is not well correlated to homogeneity. Fill fraction (Figure 118 B) has a clear negative correlation to homogeneity above fill fractions of 0.50, but is inconsistent for fill fractions lower than 0.50.

Table 31: Summary of tested properties and their correlation to homogeneity.

Property	Homogeneity Correlation	Chapter	Figure
Particle size	Positive	6	Figure 112
Cohesive force	None	6	Figure 112
Blender size	Negative	7	Figure 114
Rotation rate	Positive	8	Figure 116
Fill fraction	Negative*	8	Figure 116

**Homogeneity is negatively correlated above fill fractions of 0.50 only.*

Particle size (Figure 114 A) and rotation rate are positively correlated to homogeneity; blender size (Figure 116) is negatively correlated to homogeneity.

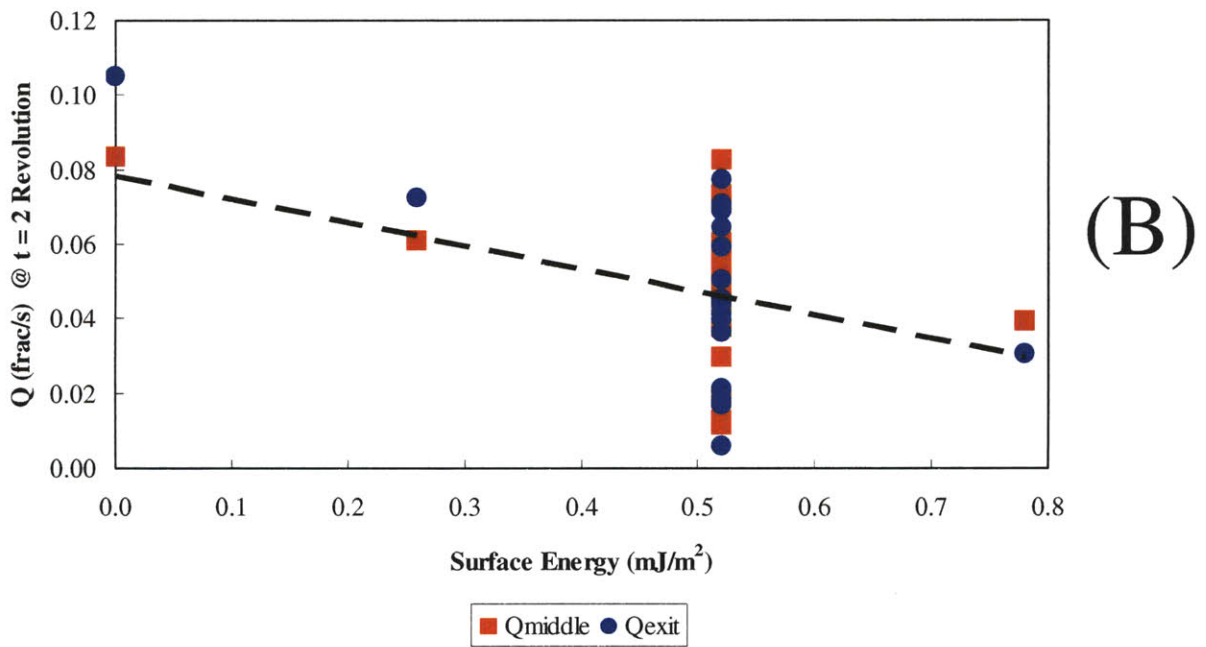
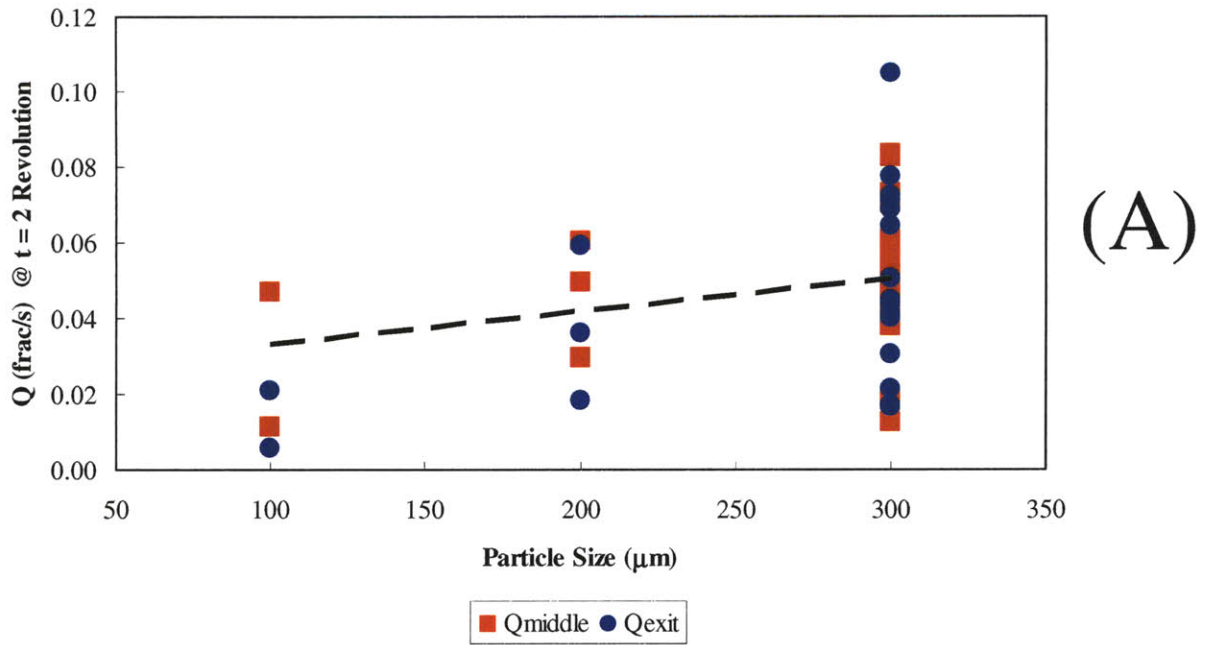


Figure 113: Effect of particle properties on 3 second moving average mass normalized flow rate at $t = 2$ revolutions for a double helical ribbon blender. Trend line fitted to Q_{middle} .

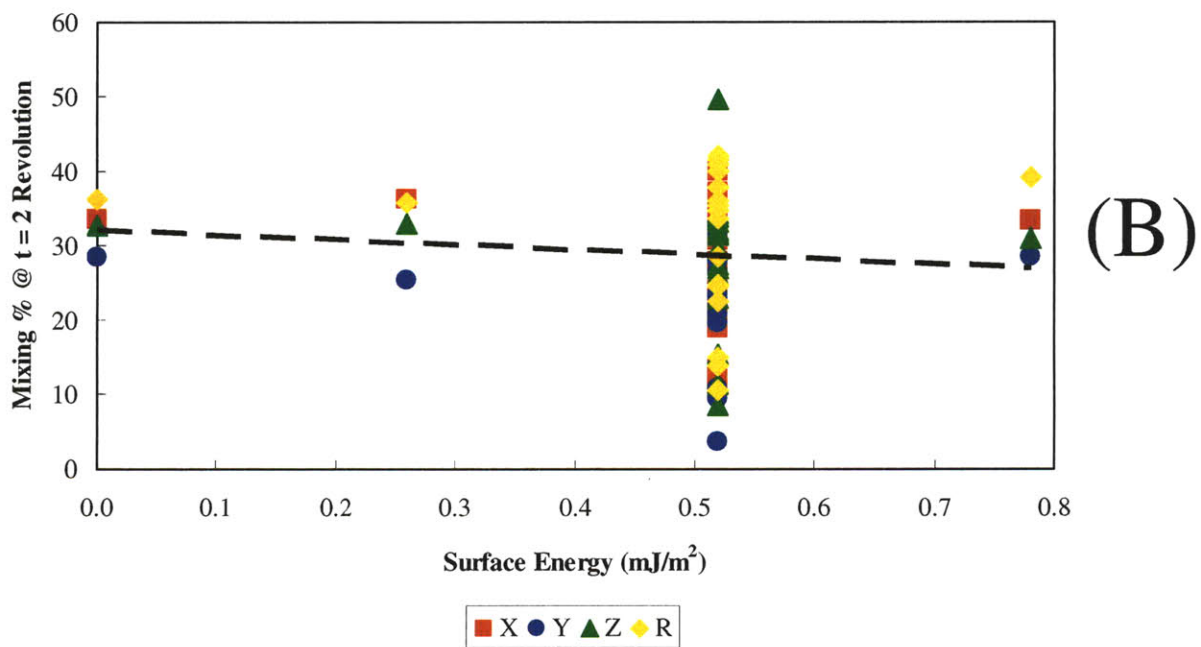
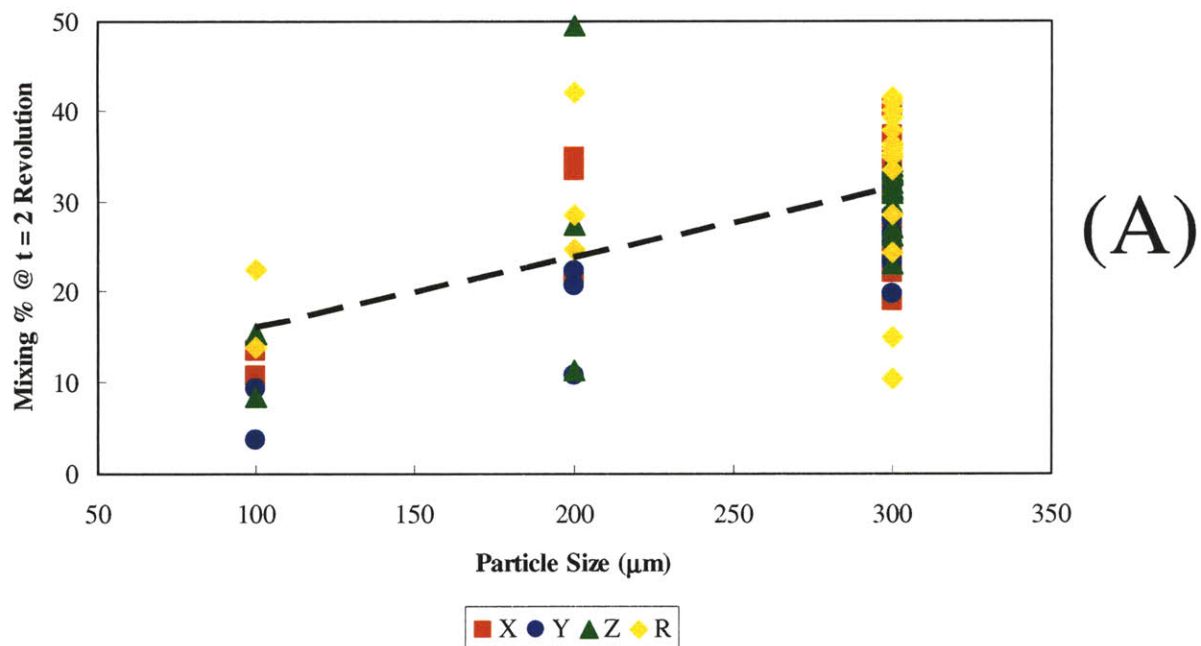


Figure 114: Effect of particle properties on initial position group homogeneity (mixing state %) at $t = 2$ revolutions for a double helical ribbon blender. Trend line fitted to Z initial position group homogeneity.

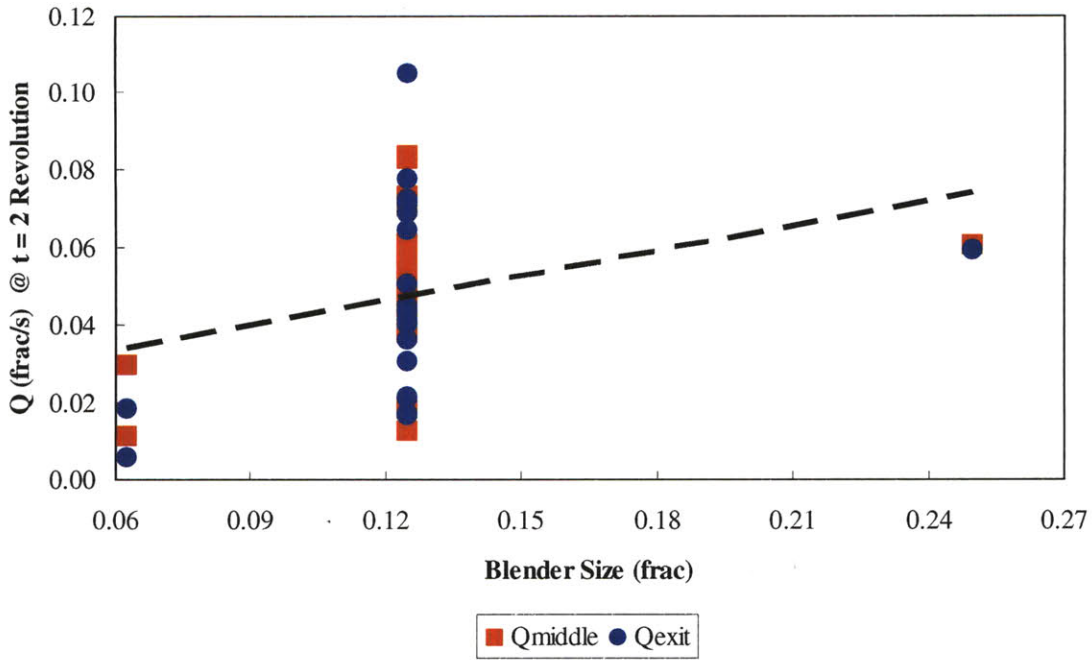


Figure 115: Effect of blender size on 3 second moving average mass normalized flow rate at t = 2 revolutions for a double helical ribbon blender. Trend line fitted to Q_{middle} .

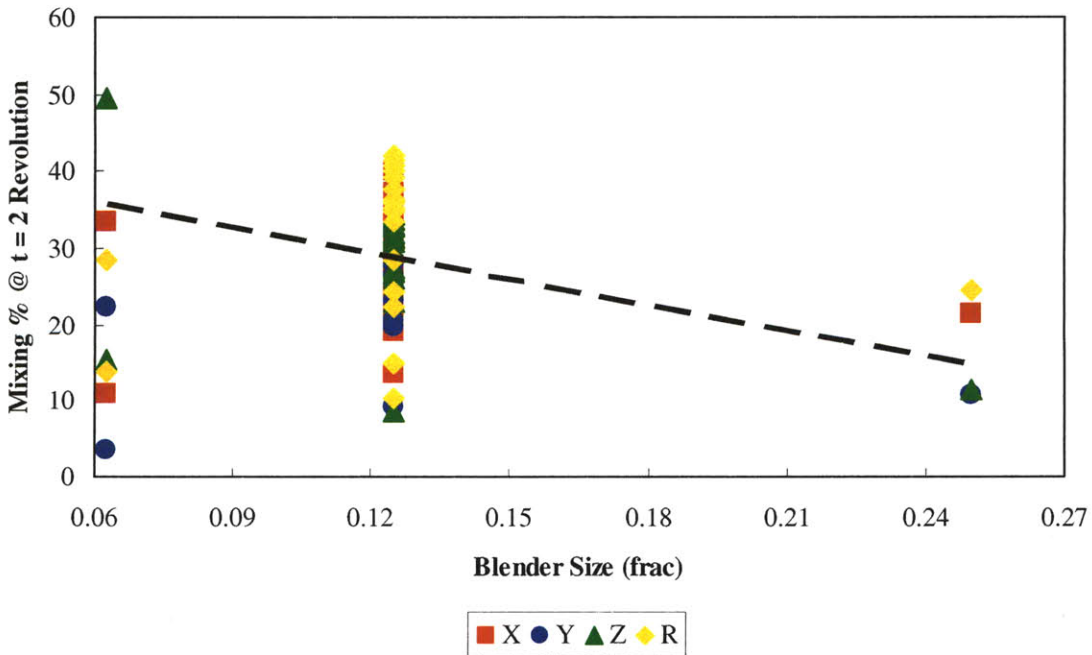


Figure 116: Effect of blender size on initial position group homogeneity (mixing state %) at t = 2 revolutions for a double helical ribbon blender. Trend line fitted to Z initial position group homogeneity.

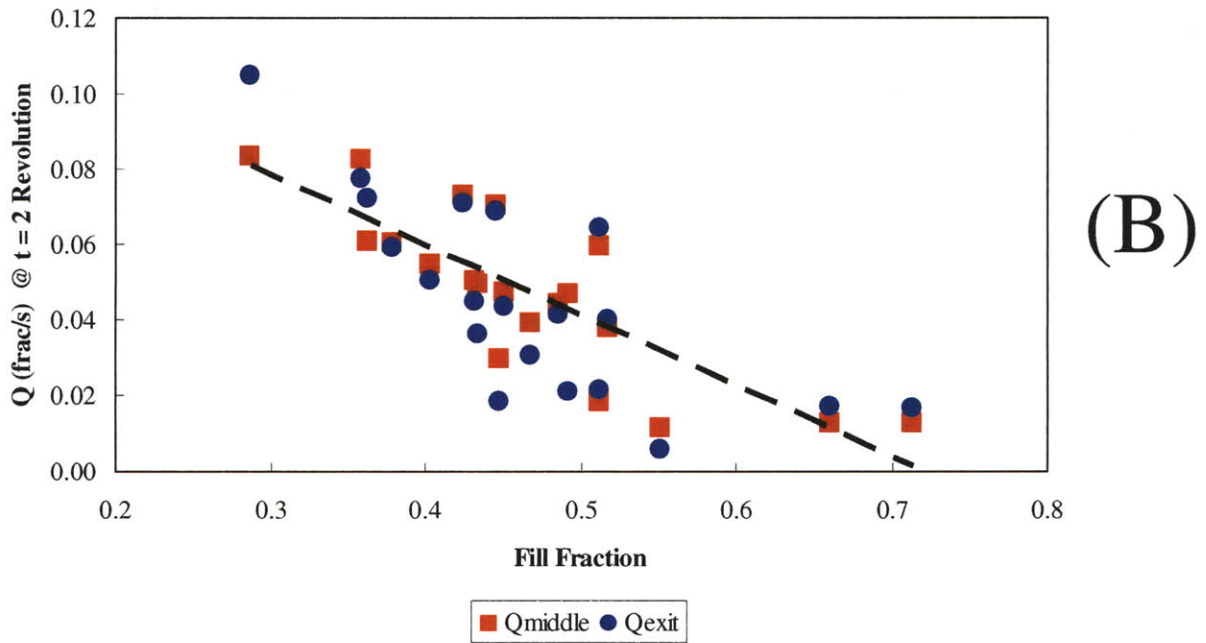
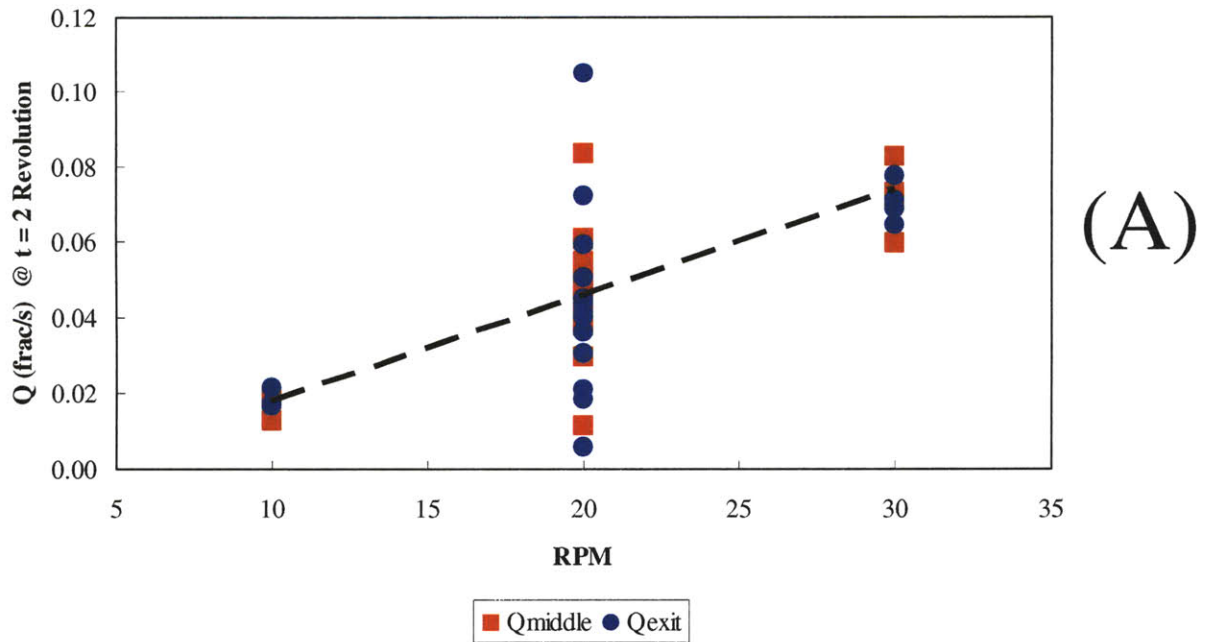


Figure 117: Effect of operating conditions on 3 second moving average mass normalized flow rate at $t = 2$ revolutions for a double helical ribbon blender. Trend line fitted to Q_{middle} .

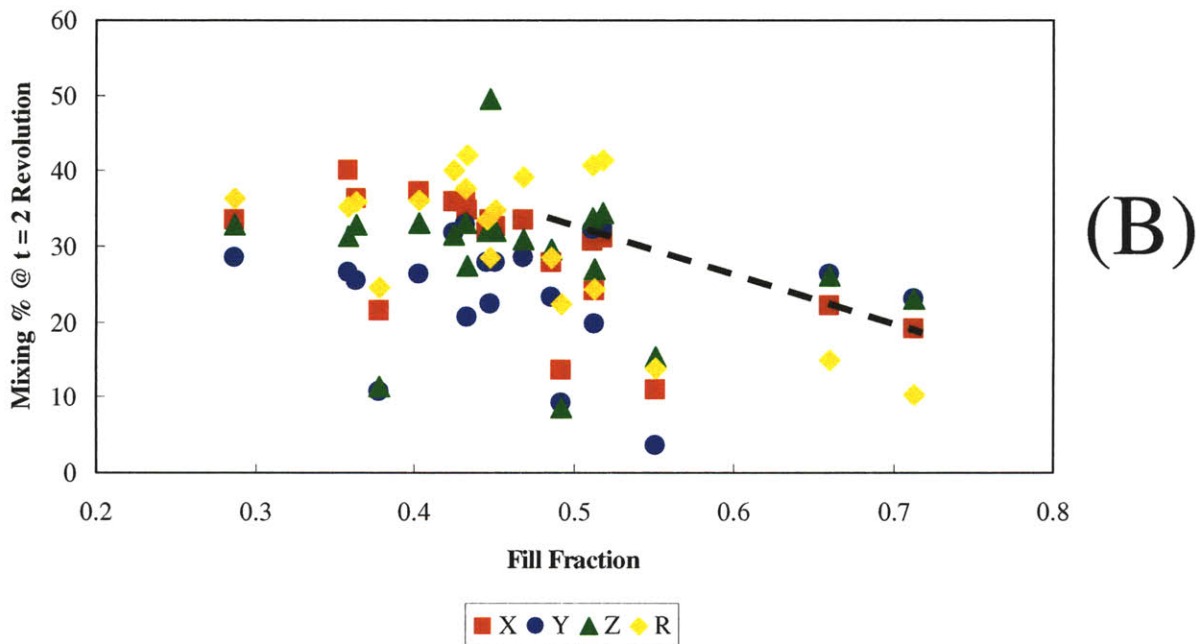
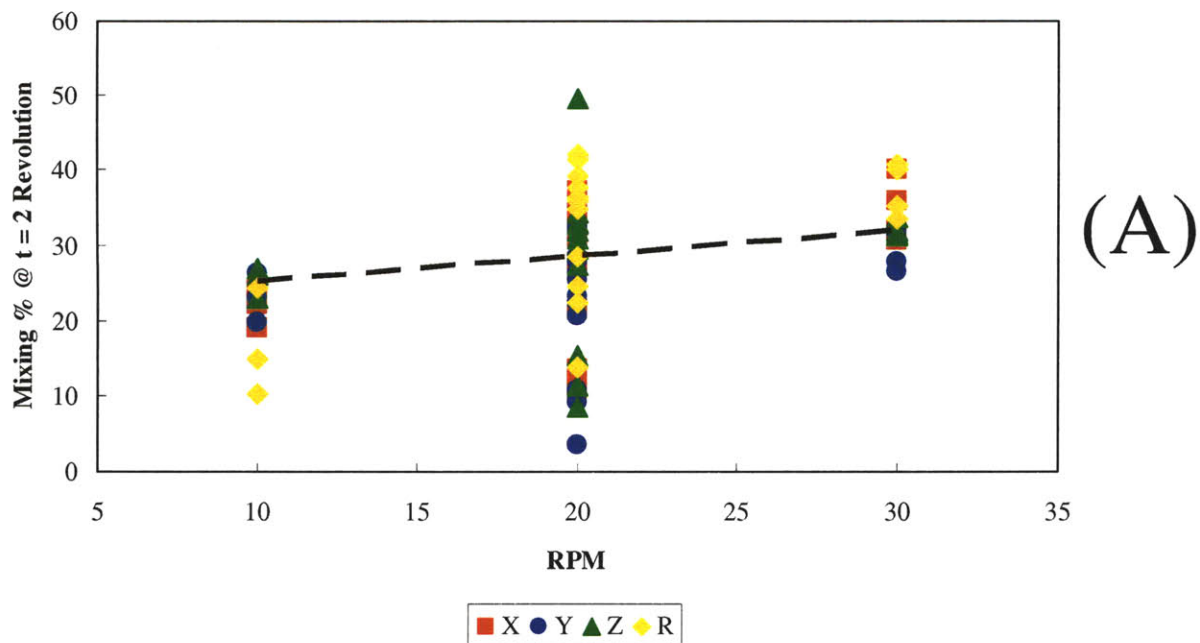


Figure 118: Effect of operating conditions on initial position group homogeneity (mixing state %) at $t = 2$ revolutions for a double helical ribbon blender. Trend line fitted to Z initial position group homogeneity.

9.2 Dimensional analysis

9.2.1 Scale ratio

Mankoc et al. [23] used a dimensionless scale ratio of orifice diameter to particle diameter to improve models predicting granular flow rates. The author's analysis using the scale ratio (Sr) was limited to materials with a common rotation rate (20 RPM), cohesion (the standard experimentally measured cohesion) and fill fraction (0.46).

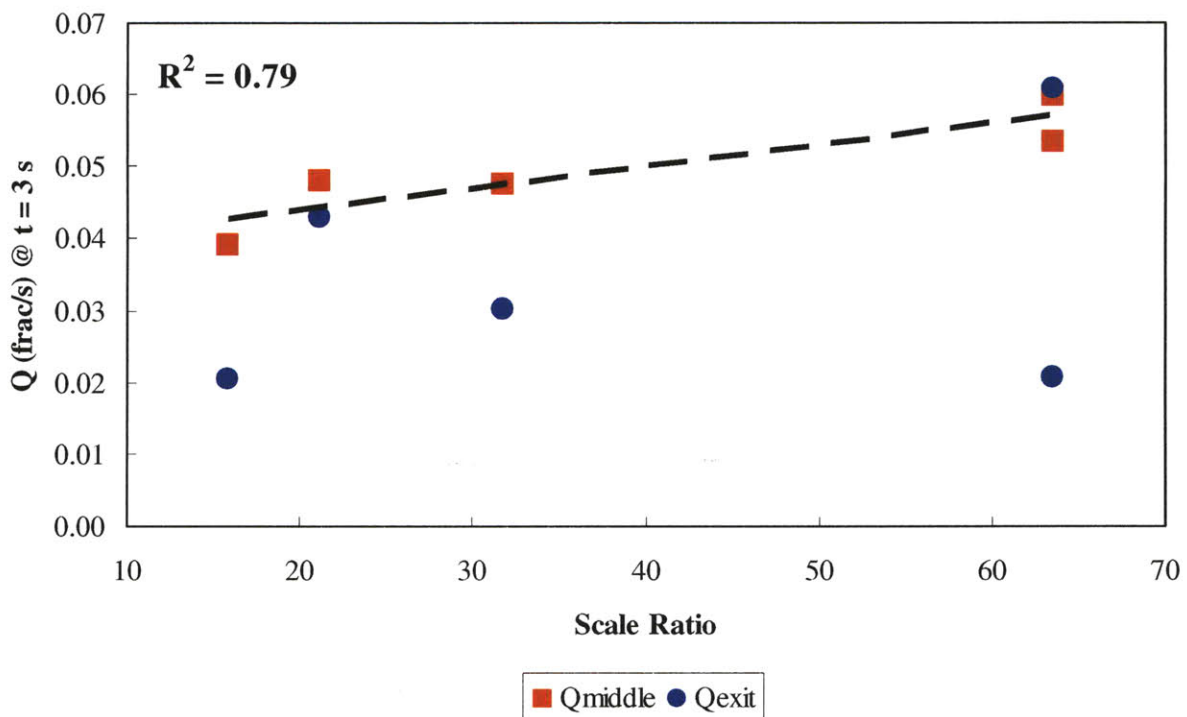


Figure 119: 3 second moving average mass normalized flow rate and scale ratio for a double helical ribbon blender with lactose particles operating at 20 RPM.

The mass normalized flow rates in the middle of the blender are well correlated (Figure 119) to the scale ratio, but weakly correlated to the exit flow rates. The weak correlation with exit flow rates indicates a greater dependence on particle size as the exit flow rate data is positively correlated with particle size, not negatively as would be the case for size ratio.

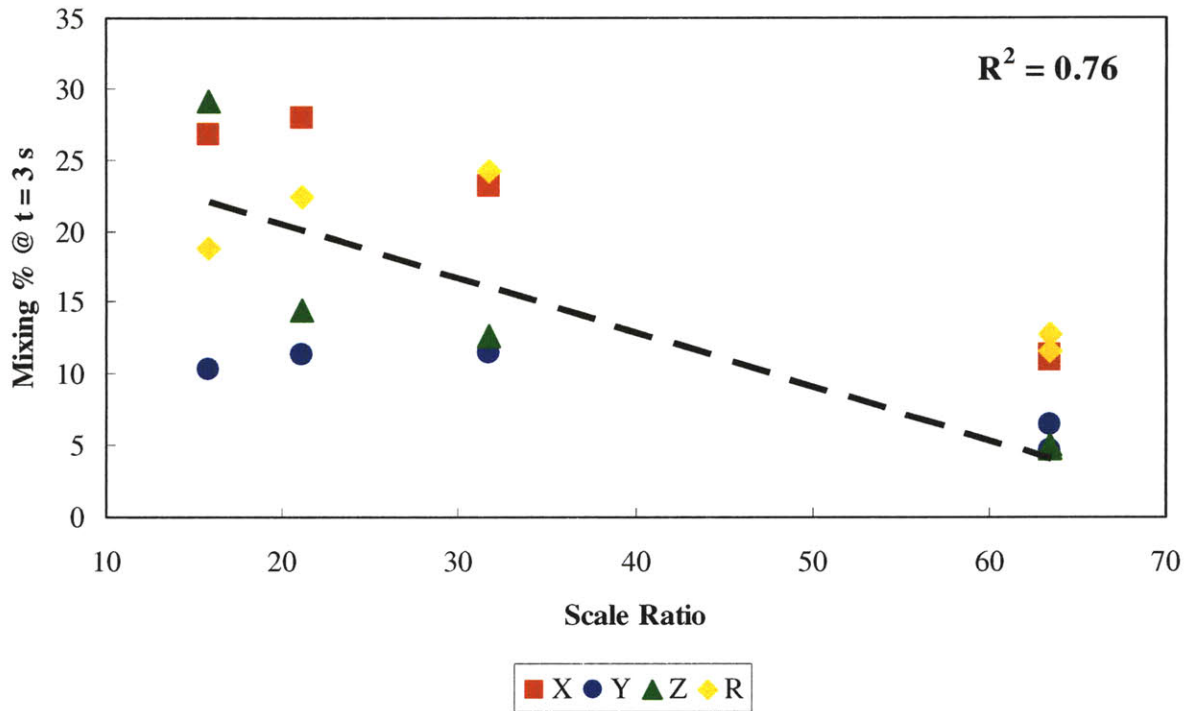


Figure 120: 3 Mixing % and scale ratio for a double helical ribbon blender with lactose particles operating at 20 RPM.

Mixing state, however, is reasonably well correlated across the particle sizes (100 micron to 300 micron) and for the blender scales explored (sixteenth, eighth and quarter scale). With the exception of the Z mixing, all of the blenders have an inflection in the 20 to 30 range indicating that there is an ideal scale ratio that maximizes homogeneity. The Z mixing does not follow this behavior as its more relevant dimension is most likely the length of the blender. The lowest length to particle diameter ratio is 48. Scale ratio does not take into account key parameters like cohesion and rotation rate that have been shown to significantly affect flow rate. However, scale ratio is effective for scaling homogeneity within a limited range and producing repeatable results at higher scales.

9.2.2 Froude number

Froude number has been suggested as an effective scaling parameter for blending and as an indicator of various flow regimes in rotating devices [13]. As Froude number now incorporates the rotational rate, the set of simulations included in its analysis has been expanded. Figure 121 and Figure 122 are comparing Froude number to flow rate and homogeneity for blenders with varying particle sizes (100 micron to 300 micron), blender sizes (sixteenth, eighth and quarter scale) and rotation rates (10 RPM to 30 RPM).

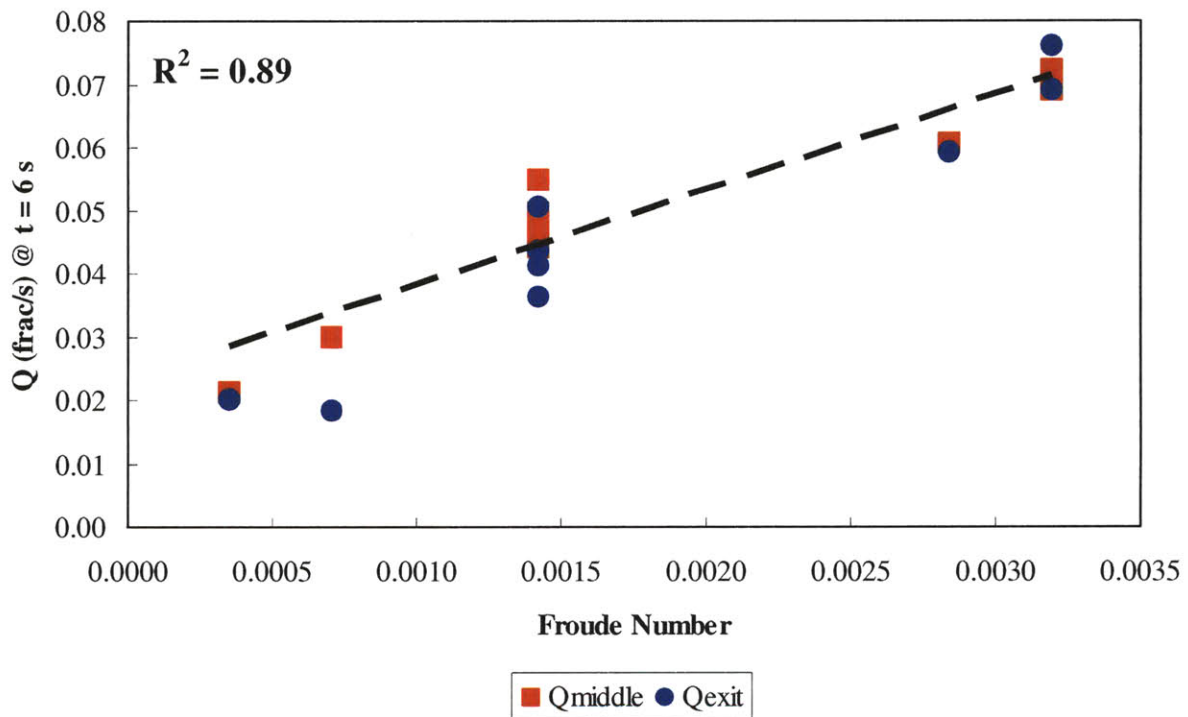


Figure 121: 3 second moving average mass normalized flow rate and scale ratio for a double helical ribbon blender with lactose particles.

Given the strong dependence of flow rate on rotation rate for the double helical ribbon blender, it is not surprising that Froude number does a reasonable job of scaling flow rates (Figure 121).

The fact that Froude number does not include a term for cohesive force, which has been shown

to significantly impact flow rate, limits the Froude number's usefulness for predicting flow rates in the double helical ribbon blender.

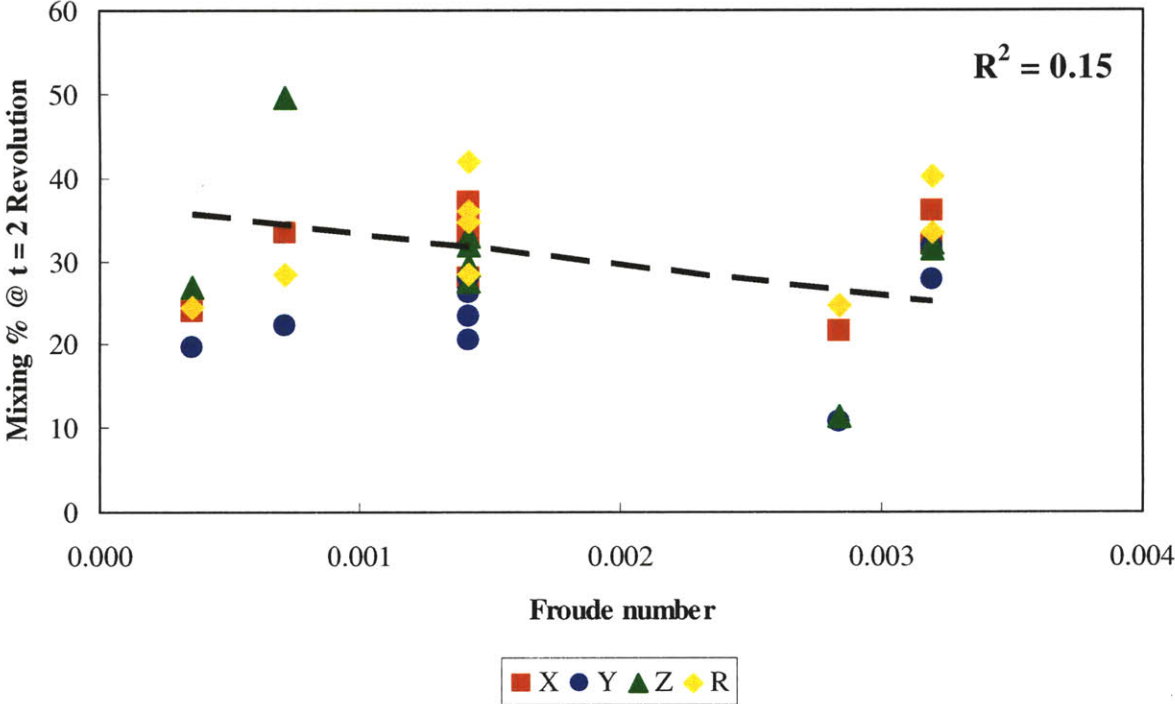


Figure 122: Mixing % and Froude number for a double helical ribbon blender with lactose particles.

Unfortunately, Froude number is almost entirely useless for scaling the blend homogeneity (Figure 122) in the double helical ribbon blender. The Froude number does not account for particle size which was demonstrated to play an important role in blend homogeneity.

9.2.3 Avalanche velocity

Diffusive mixing in avalanching particles has been shown to be an important component of mixing in the double helical ribbon blender. Alexander and Muzzio [14] believed that the velocity of this avalanche is a key factor for scaling mixing rate and blend homogeneity.

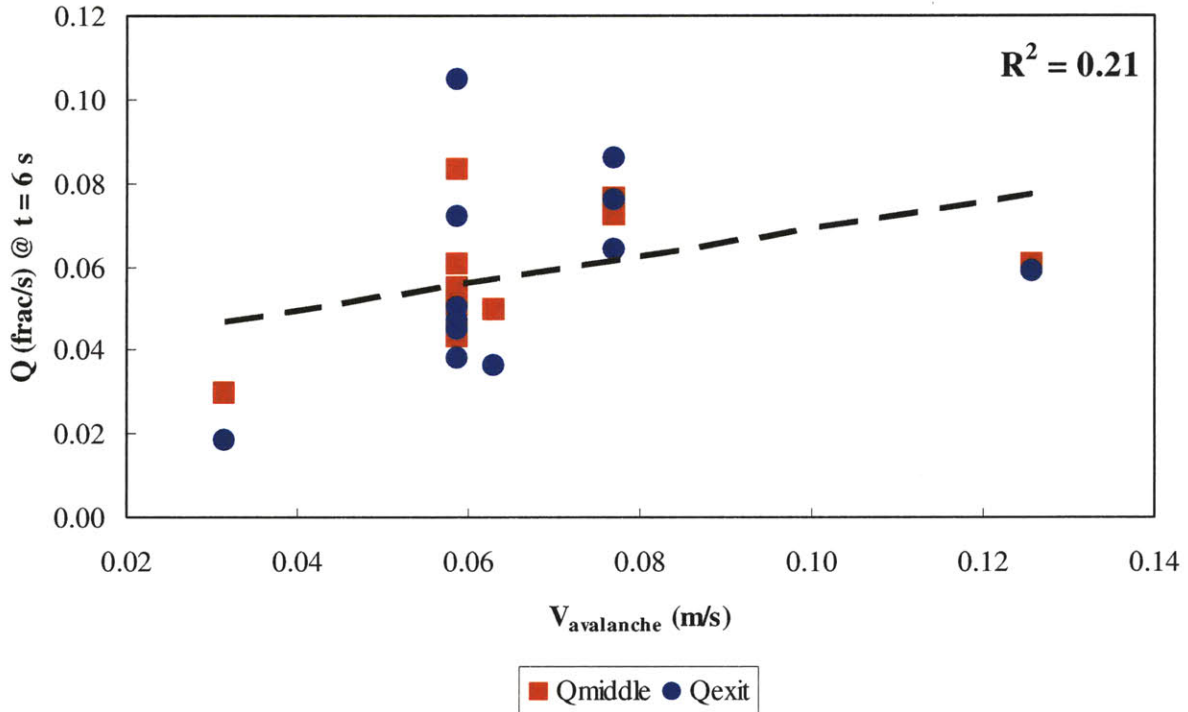


Figure 123: 3 second moving average mass normalized flow rate and avalanche velocity for a double helical ribbon blender with lactose particles.

Avalanche velocity is a poor predictor for flow rate (Figure 123). This is not surprising since avalanching particles are at best a very minor component in the axial transport of particles in the double helical ribbon blender.

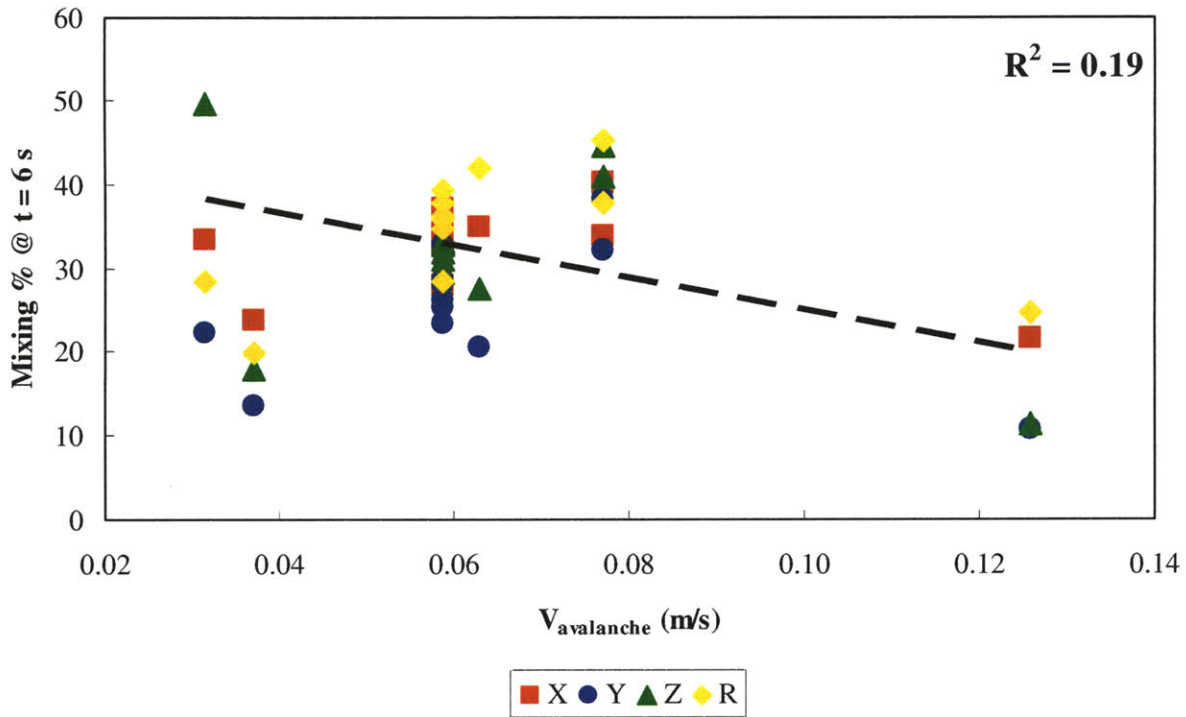


Figure 124: Mixing % and avalanche for a double helical ribbon blender with lactose particles.

Contrary to Alexander and Muzzio’s hypothesis, there appears to be very little correlation between different avalanche velocities and homogeneity (Figure 124). Avalanche velocity (Equation 6) is inversely correlated to particle size. However, the DEM simulations and experimental results [4, 85] have demonstrated that homogeneity is positively correlated to particle size.

9.2.4 Dimensional analysis of flow rate

It is clear from the analysis of single variables, Froude number and surface avalanche velocity that a reasonable correlation for flow rate would only be possible by creating an equation that included all of the parameters observed in the previous chapters to affect flow rate (Equation 23). It has been seen that flow rate is dependent on rotation rate (Ω), cohesion

(represented here by the surface energy γ), the diameter of the blender (D) and the diameter of the particles (d). The density of the particles (ρ) was assumed to be important to the mass flow rate of particles and was included in the equation although it was not tested in the DEM simulations.

$$Q \propto \Omega, \gamma, D, d, \rho$$

Equation 23: Observed relationships for mass flow rate.

Given the desired final dimensions for the normalized flow rate of inverse time (Equation 24), a dimensional model was created based on the observed behavior of the parameters (Equation 25).

$$Q[=] \frac{frac}{s}$$

Equation 24: Units for the mass normalized flow rate.

$$Q = C_{flowrate} (D^b d^{3-b})^a \left(\frac{\rho}{\gamma} \right)^a \Omega^{2a+1}$$

Equation 25: Dimensional analysis model for flow rate.

The exponents “a” and “b” were fitted to the DEM simulation data yielding Equation 26 with coefficient $C_{flowrate}$.

$$Q = C_{flowrate} (D^2 d)^{1/3} \left(\frac{\rho}{\gamma} \right)^{1/3} \Omega^{5/3}$$

Equation 26: Dimensional analysis model for flow rate with fitted exponents.

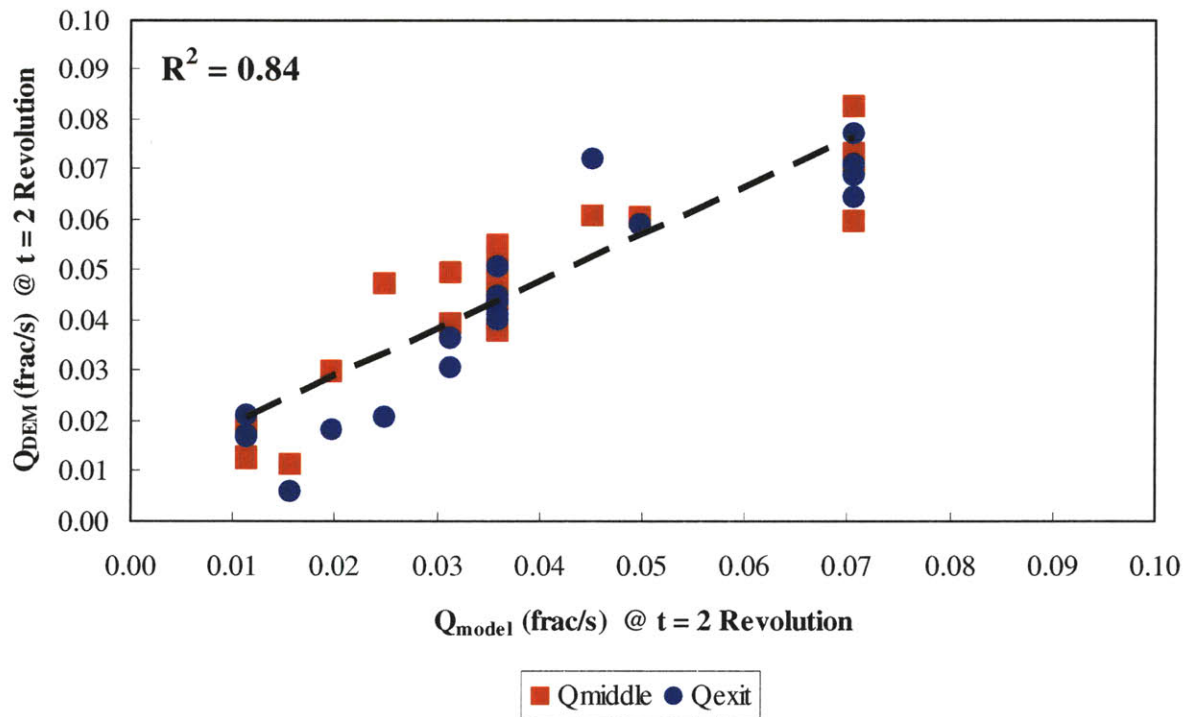


Figure 125: 1 revolution moving average mass normalized flow rate from discrete element method measurement and dimensional analysis model for a double helical ribbon blender with lactose particles.

Even with the wide range of particle and process conditions, the equation yields a reasonable correlation to the measured flow rate from the discrete element method simulation (Figure 125).

9.2.5 Dimensional analysis of homogeneity

A similar dimensional analysis was applied to the blend homogeneity. As homogeneity is a time dependent parameter, it would have to be proportional to time (t) as well as rotation rate (Ω), the diameter of the blender (D) and the diameter of the particles (d).

$$\text{Mixing} (\%) \propto t, \Omega, D, d$$

Equation 27: Observed relationships for mixing state.

A form similar to a first-order rate equation was used to develop the homogeneity model. This created a model with two constants, a rate constant (k) and a coefficient ($C_{\text{homogeneity}}$) (Equation 28).

$$\text{Mixing} (\%) = C_{\text{homogeneity}} \left(\frac{d}{D} \right)^a \left(1 - e^{(-k \cdot (t \cdot \Omega)^b)} \right)$$

Equation 28: Dimensional analysis model for homogeneity.

The exponents, “a” and “b”, in the dimensional model are fitted to the DEM homogeneity data (Equation 29).

$$\text{Mixing} (\%) = C_{\text{homogeneity}} \left(\frac{d}{D} \right)^{1/3} \left(1 - e^{(-k \cdot t \cdot \Omega)} \right)$$

Equation 29: Dimensional analysis model for homogeneity with exponents fitted from DEM simulations.

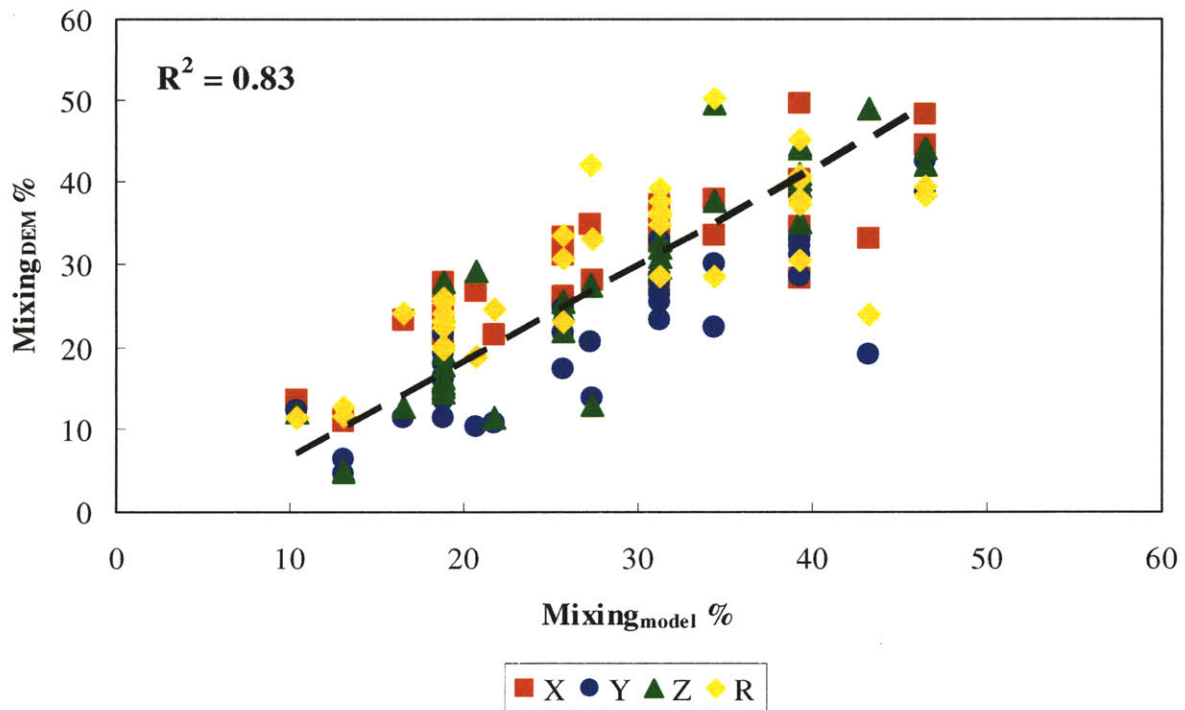


Figure 126: Homogeneity of initial position groups from DEM measurement and dimensional analysis model for a double helical ribbon blender with lactose particles.

The fit of the model is reasonable for the homogeneity of all of the initial position groups, but it is particularly good for the X and Z initial position groups (Figure 126). In general, the model tends to overestimate the homogeneity for the first revolution after which it becomes more accurate (Table 32).

Table 32: Comparison of DEM model homogeneity for Z initial position groups (mixing %) and dimensional analysis model Z homogeneity.

Z Mixing %		Z Mixing %		Z Mixing %		Z Mixing %	
DEM	Model	DEM	Model	DEM	Model	DEM	Model
4	13	16	19	28	19	36	39
5	13	16	19	29	21	38	34
5	13	16	19	30	31	39	39
8	10	18	34	31	31	40	39
8	22	18	19	31	31	40	39
9	10	19	19	31	31	41	39
11	22	20	26	32	31	42	46
12	10	21	26	32	31	44	46
13	17	22	26	33	31	44	39
13	27	22	26	33	31	44	39
14	19	23	31	33	31	44	39
14	17	24	26	33	31	45	39
14	19	25	26	34	31	46	39
14	19	26	31	34	31	46	46
14	19	26	26	35	39	49	43
15	19	27	31	36	39	50	34
15	27	27	27	36	46		

9.3 Summary of results

1. The simple dimensionless scaling ratios, like scale ratio and Froude number, are not particularly useful for the cohesive materials typically seen in the pharmaceutical industry.
2. Dimensional models that incorporate the components observed to be significant to either flow rate or homogeneity could provide some predictive capabilities. The dimensional models developed by the author have demonstrated good agreement to DEM simulations for both flow rate and homogeneity. As both the flow rate and homogeneity model have a number of nonlinear elements, they should be limited to predictions using parameters inside

the bounds explored. In addition, the dimensional analysis models are only applicable to the double helical ribbon blender.

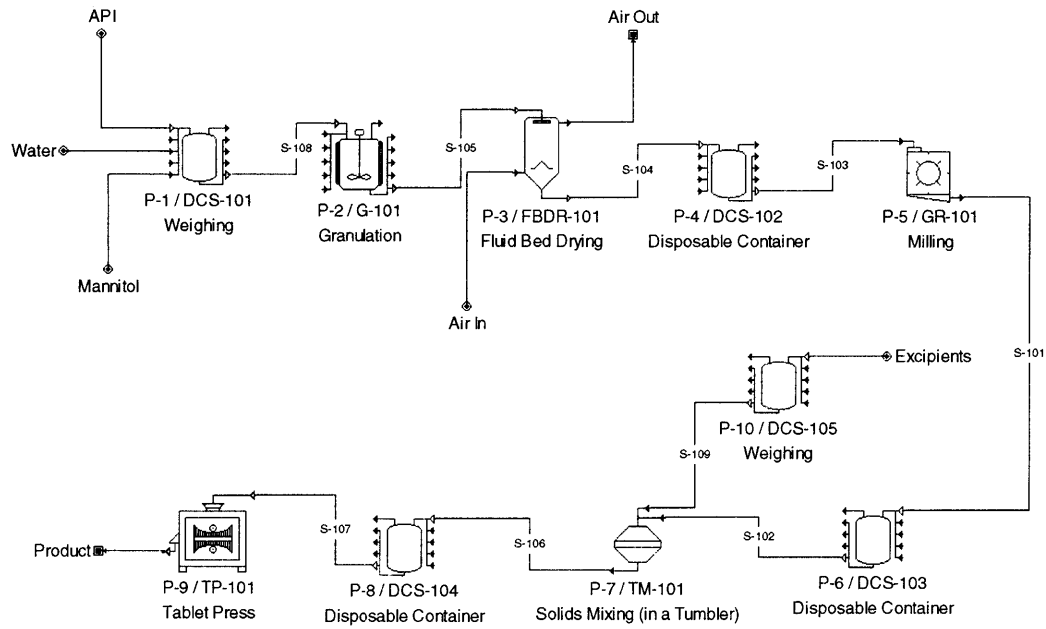
10 CONTINUOUS DOWNSTREAM PHARMACEUTICAL MANUFACTURING SYSTEMS

The successful implementation of continuous manufacturing requires integrating continuous blending into a complete pharmaceutical process. Process models allow one to explore the issues of design, scaling and costs for continuous manufacturing systems. Capital costs (CAPEX) and operating costs (OPEX) are useful metrics for comparing alternative manufacturing systems as they will decide when a continuous process is suitable for implementation. The following process system models explore how continuous manufacturing compares with batch processing for two common types of pharmaceutical manufacturing processes at different process scales. Equipment sizes, CAPEX and OPEX are calculated from the models as performance metrics.

10.1 Process models

The scope of these process models was limited to downstream pharmaceutical manufacturing, the process after the active pharmaceutical ingredient (API) synthesis. A hypothetical drug product was used in the process simulations consisting of an API, mannitol and lactose/magnesium stearate (MgSt) (excipients on the flow sheet). The API, mannitol and other excipients are used in a 1:1:1 ratio in the drug product. The materials were all assumed to be dry powders.

Batch



Continuous

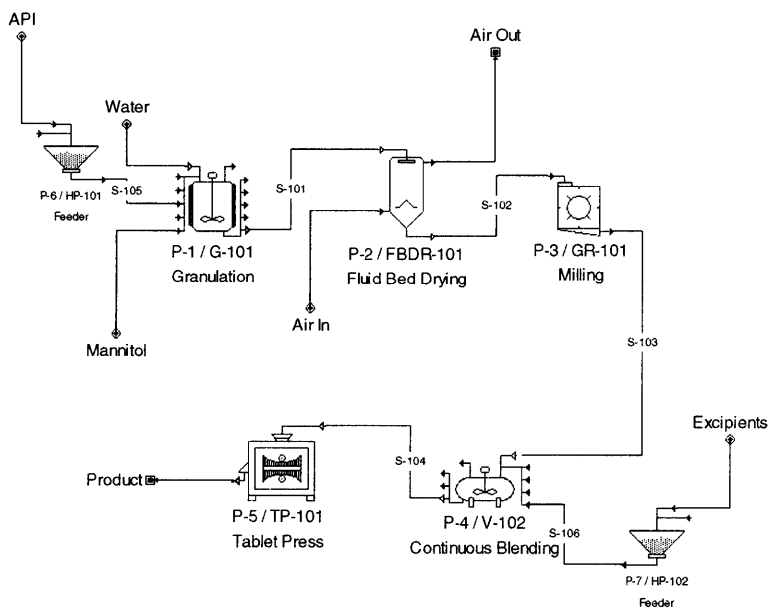
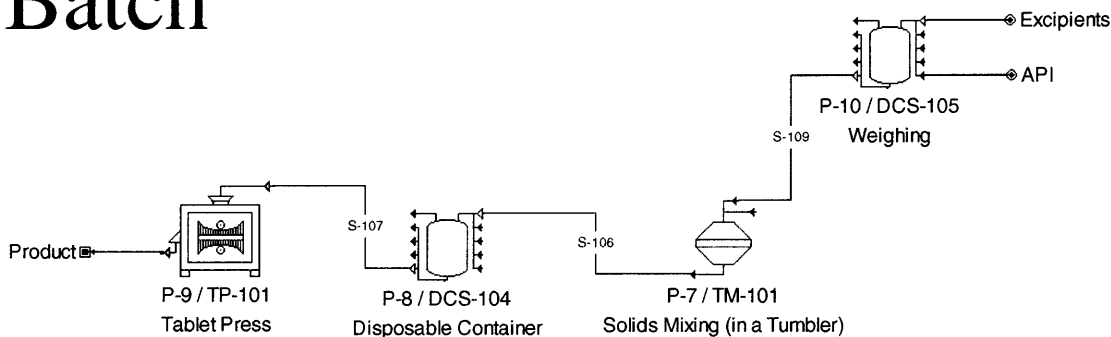


Figure 127: SuperPro Designer flow sheet for wet granulation processes.

The processes were modeled in SuperPro Designer. The first process is a wet granulation system consisting of granulation, drying, milling, blending and compression operations (Figure 127). The continuous wet granulation process system adds continuous powder feeders to deliver powder to the granulation device and the blender.

Batch



Continuous

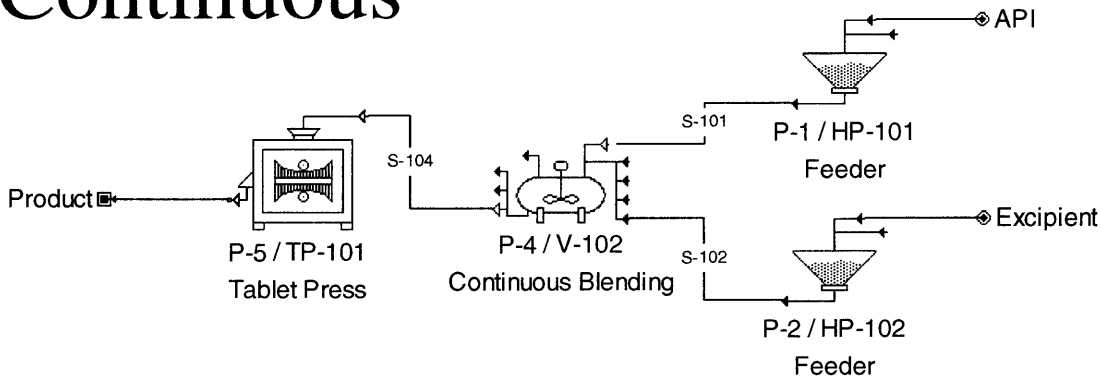


Figure 128: SuperPro Designer flow sheet for direct compression processes.

The second process is a direct compression system consisting simply of blending and compression (Figure 128). The continuous direct compression process system again adds two

continuous powder feeders to deliver materials to the blender. The manufacturing processes are operated 24/7 with 75% uptime which translates to 6570 hours of annual operation time.

Direct compression processes are less costly to build and operate than wet granulation, but not all pharmaceutical products can be manufactured with direct compression. Wet granulation is a more robust process and can be used to manufacture a wider range of pharmaceutical products. This is due to the wet granulation process being less sensitive to the quality of the input materials.

Processes were scaled using SuperPro Designer to find the optimal equipment size for process throughputs of 100 million to 1 billion tablets annually. The equipment was assumed to have a continuous size range and thus could always be optimally sized for its throughput. The exception to this was the tablet press which was limited to a maximum throughput of 200,000 tablets per hour. If this rate was exceeded, the model would substitute multiple parallel units of the appropriate size. Equipment cost estimates used the default cost model in SuperPro Designer for all of the equipment with the exception of the continuous blender and the continuous powder feeders. The continuous blender cost was estimated from a quote from Patterson-Kelley for a “Double V-Blender” examined previously by Pernenkil [4]. The cost was then scaled by volume using the 0.6 power rule (Equation 30).

$$P_{continuous_blender} = \$400,000 \left(\frac{V}{0.08(m^3)} \right)^{0.6}$$

Equation 30: Price of the modeled continuous pharmaceutical powder blender.

The automation and control equipment costs for the entire continuous manufacturing process were consolidated into the cost of the feeders. As the cost of automation and control equipment is approximately constant for different process scales, the feeder cost was approximated as being

fixed and was conservatively estimated at \$100,000 per unit. Total capital costs are calculated using a cost multiplier times the basic equipment costs. The default SuperPro Designer capital cost multipliers were used.

In the batch manufacturing system, the step of actually processing materials represents only a small amount of the time required to complete a process operation (Table 33). When new materials are introduced in the batch process for the granulation and blending operations, the operator has to weigh out the material for these operations. In addition, the operator has to transfer material into and out of the processing equipment.

Table 33: Batch process units with process times and costs for a 1 billion tablet/yr manufacturing system.

Unit	Name	Process Steps	Processing Time (min)	Cost	Quantity	Cost Type
Granulation	G-101	Weighing, Transfer In, Granulation, Transfer Out	30	\$138,000	1	Variable
Drying	FBDR-101	Transfer In, Drying, Transfer Out	60	\$27,000	1	Variable
Milling	GR-101	Transfer In, Milling	236	\$58,000	1	Variable
Blending	TM-101	Weighing, Transfer In, Mixing, Transfer Out	30	\$298,000	1	Variable
Tabletting	TP-101	Transfer In, Tabletting	300	\$753,000	2	Variable

A detailed accounting of the times associated with the process steps can be found in the Gantt charts for the wet granulation (Figure 130) and the direct compression (Figure 129) processes. The processing times for each of these operations were based on estimates from interviews with pharmaceutical engineering professionals from the Consortium for Advanced Pharmaceutical Manufacturing (CAMP).

Continuous processing does not require separate weighing or transfer steps and thus one is only concerned with the time required to actually process the material. The continuous

processing time or residence times (Table 34) were set at the same duration as the processing step times in the batch systems.

Table 34: Continuous process units with process times and costs for a 1 billion tablet/yr manufacturing system.

Unit	Name	Processing Time (min)	Cost	Quantity	Cost Type
Feeder	HP-101/HP-102	-	\$100,000	2	Fixed
Granulation	G-101	30	\$116,000	1	Variable
Drying	FBDR-101	60	\$27,000	1	Variable
Milling	GR-101	236	\$58,000	1	Variable
Blending	TM-101	30	\$215,000	1	Variable
Tabletting	TP-101	300	\$900,000	1	Variable

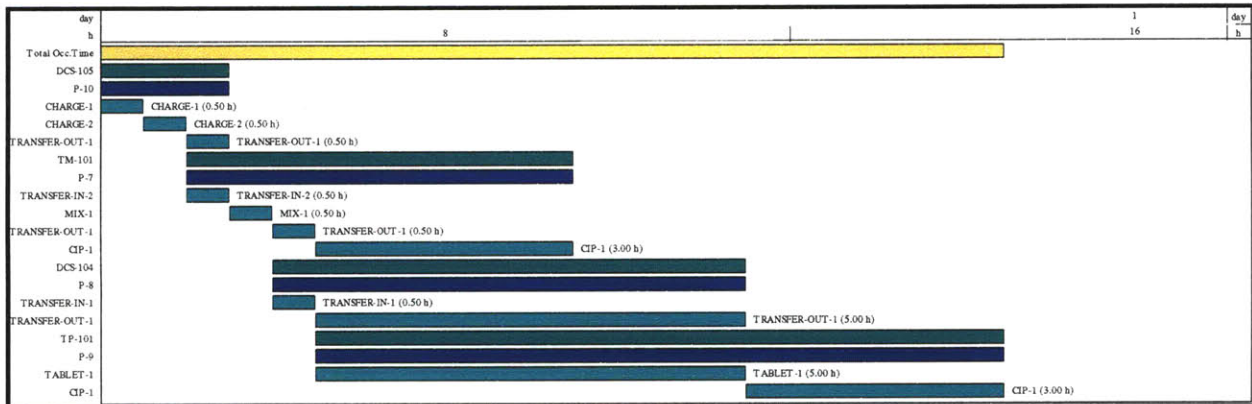


Figure 129: Gantt chart of process steps for batch direct compression process.

In the batch manufacturing systems, the different steps in an operation require different amounts of labor (Table 35). The most labor intensive steps are the weighing and transfer steps where the operator is required to handle the materials. Based on the author's experience in pharmaceutical manufacturing environments, 2 operators are required to execute these steps. The actual processing steps (granulation, mixing, compression) were assumed to require very little attention from the operator, as once the process is started, these steps are ignored under normal

conditions until they complete their operations. The drying and milling steps combine transfer steps with processing steps. Given that material is coming out of the device during the drying and milling steps, they are burdened with greater labor requirements of 0.5 operators.

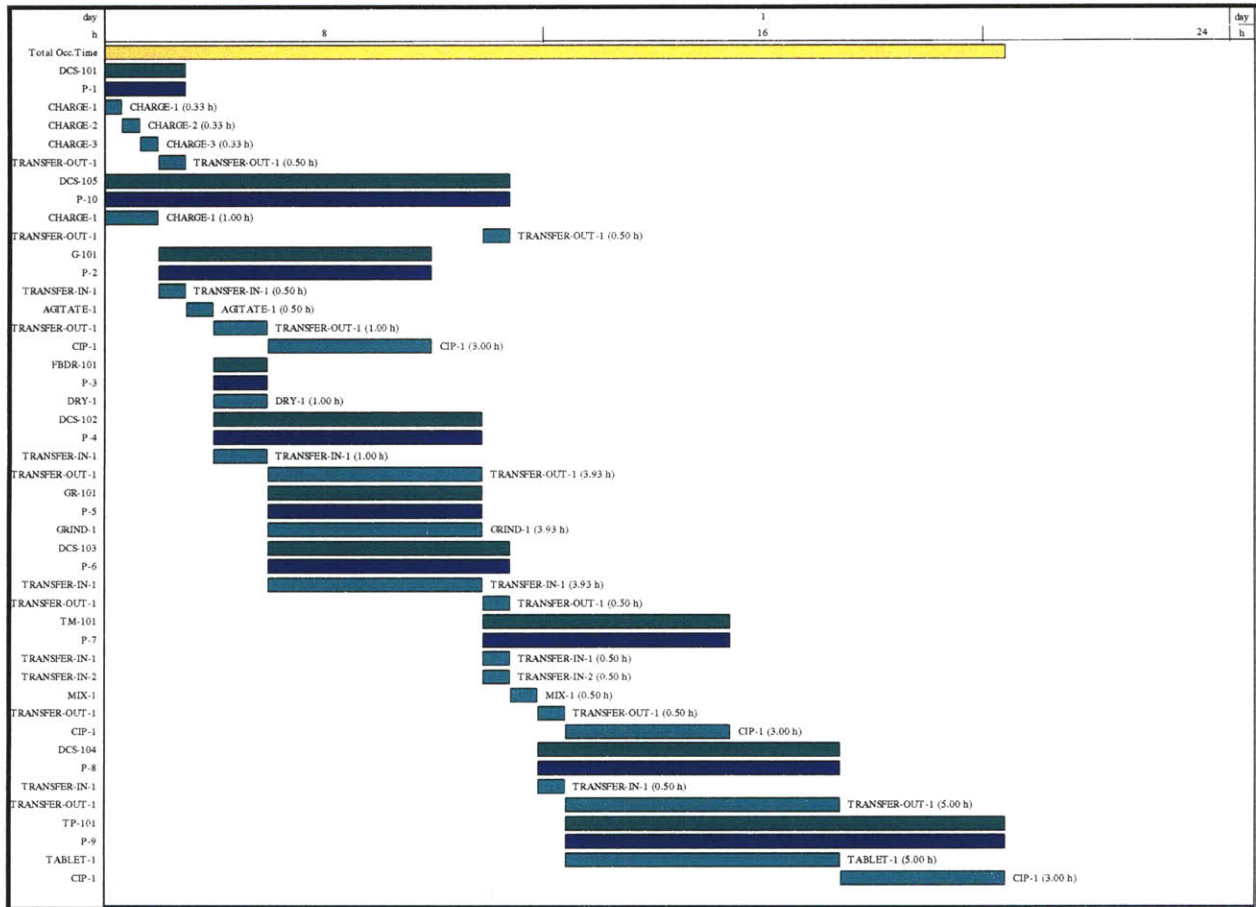


Figure 130: Gantt chart of process steps for batch wet granulation process.

Table 35: Labor hours per operating hour for batch process steps.

Process Step	Labor-hr/hr
Drying	0.5
Granulation	0.1
Milling	0.5
Mixing	0.1
Tabletting	0.1
Transfer In/Out	2.0
Weighing	2.0

All of the operations in the continuous process systems will require little attention from the operators when the system is operating normally and thus process steps were given a labor burden of 0.1 labor hours per hour of operation. Both the batch and the continuous processes were assumed to be operated in a multi-product facility where operators could be split between multiple processes for the most efficient use of labor. Labor costs associated with maintenance and cleaning were ignored for both the batch and the continuous process systems. Labor costs were \$69 per hour per operator for the batch and the continuous process systems.

10.2 Process model results

One of the advantages of continuous process systems is that they can reduce the size of process equipment through improved utilization. This is very apparent in comparing the granulation and blending equipment. In both cases, the batch system requires equipment volumes an order of magnitude greater than the continuous equipment volumes (Table 36). This translates into a smaller footprint for continuous process systems in a manufacturing facility.

Table 36: Process equipment volumes and throughputs for a 1 billion tablet/yr manufacturing system.

Unit	Name	Batch Volume (L)	Continuous Volume (L)	Batch Throughput (kg/hr)	Continuous Throughput (kg/hr)
Granulation	G-101	510	33	-	-
Drying	FBDR-101	180	250	-	-
Milling	GR-101	-	-	100	51
Blending	TM-101	800	28	-	-
Tabletting	TP-101	-	-	60 (x2)	76

Continuous process systems should enjoy cost advantages for both CAPEX and OPEX due to their smaller equipment sizes and less labor intensive operations. The CAPEX of the processes scale approximately linearly with throughput over the range examined (Figure 131 A). However, the slope and intercept of these trends are different for the batch and continuous processes. The continuous process has a smaller slope which means it costs less to increase the size of its processes. This is caused by the smaller absolute change in equipment size for continuous processes. In addition, the continuous process has a larger intercept which is caused by the fixed cost for the feeders. Comparatively this means that the CAPEX for continuous processes is greater than batch processes at low throughputs, but ultimately becomes lower than batch CAPEX at high throughputs. Once the continuous process has a lower CAPEX than the batch process, its cost advantage will continue to widen as throughput increases. For the systems simulated, the crossover where continuous CAPEX becomes less than batch CAPEX occurs at 200 million tablets per year for both the wet granulation and direct compression processes. OPEX (Figure 131 B) is consistently lower for the continuous processes at all of the simulated throughputs. Much of these savings come from the decreased labor costs of the continuous process. The range of throughputs where continuous processes enjoy a CAPEX or OPEX advantage will vary depending on the product and the design of the process system.

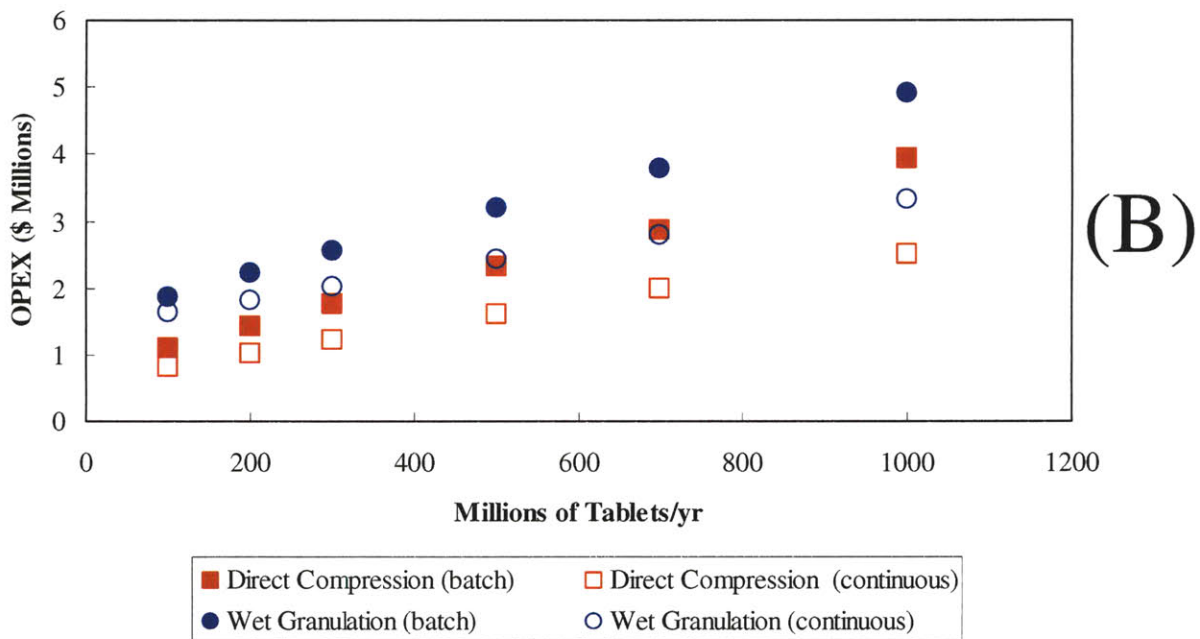
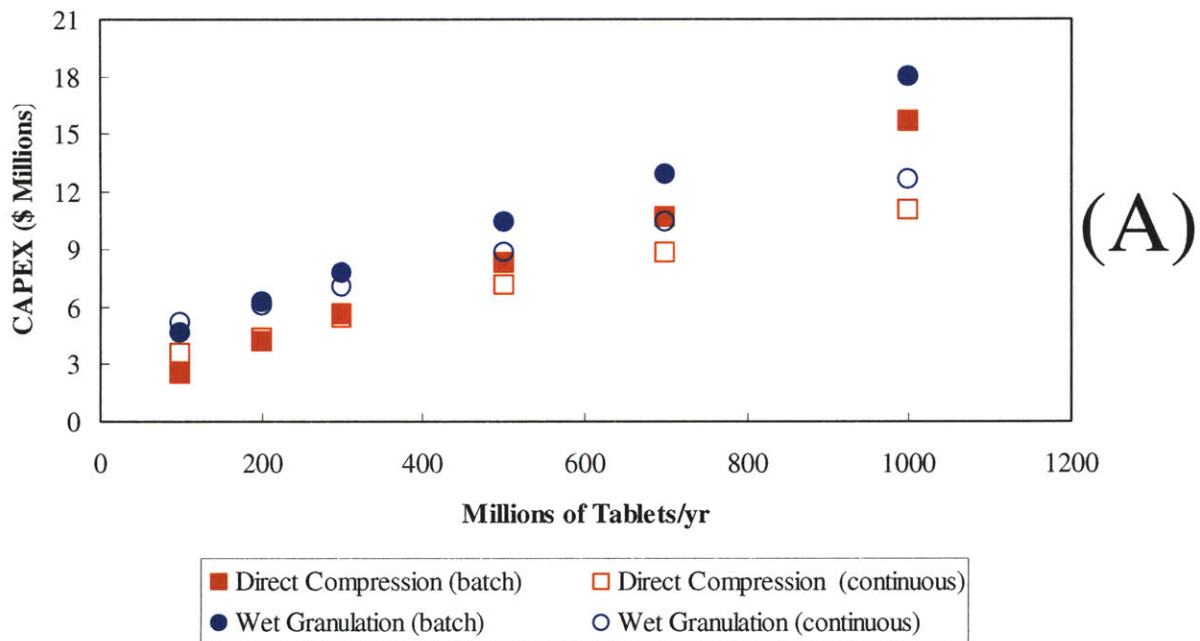


Figure 131: Capital (CAPEX) and operating (OPEX) costs for batch and continuous wet granulation and direct compression processes.

The CAPEX and OPEX can also be combined to examine the total savings for implementing a continuous manufacturing system. An example is shown for the simulated process systems with a 10 year lifespan and a weighted average cost of capital (WACC) of 10% (Figure 132). The present value (PV) of the total costs is always more favorable for the continuous process systems of the same type. Additionally, at the larger process scales, the continuous wet granulation process is less costly than the batch direct compression process. In this case, continuous manufacturing enables the implementation of the more robust wet granulation process for the same or lower cost.

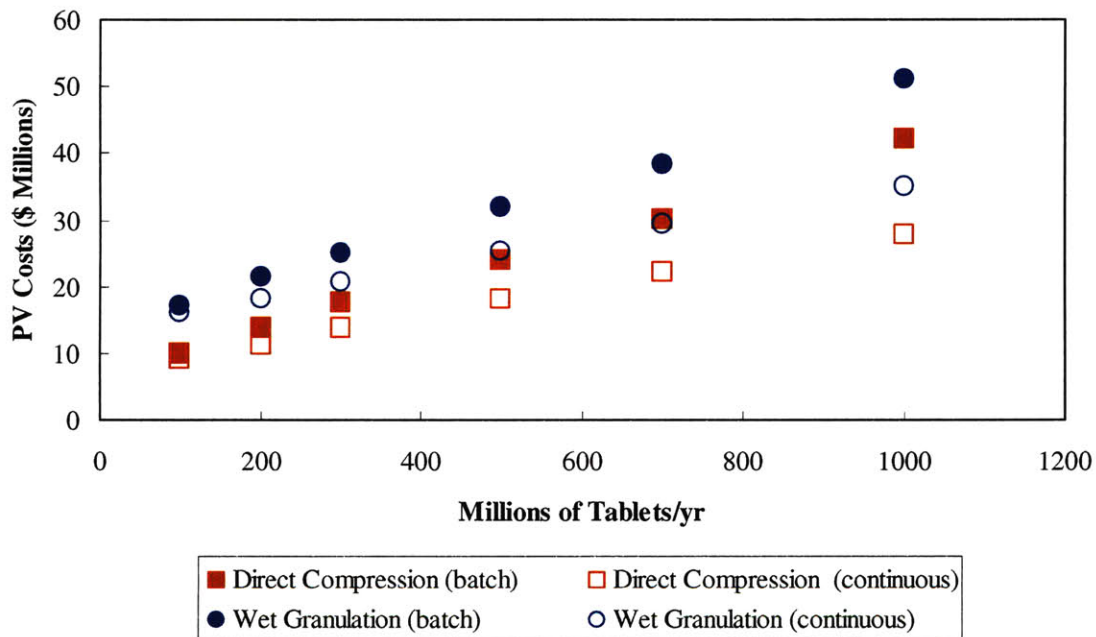


Figure 132: Present value (PV) costs for CAPEX and 10 years of OPEX with a WACC of 10%.

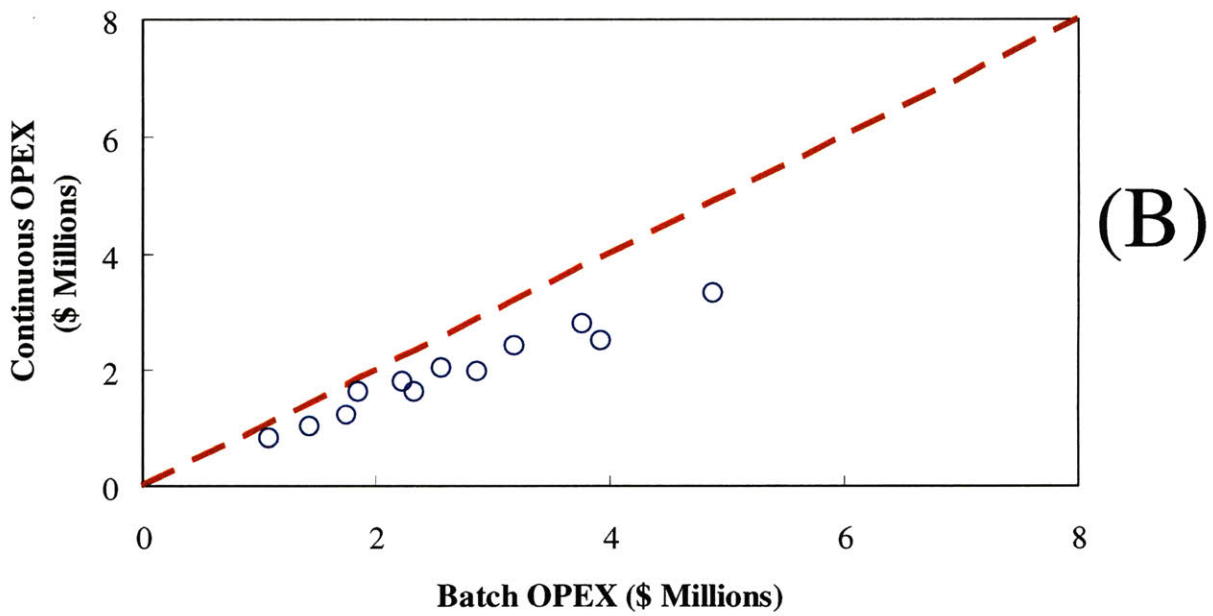
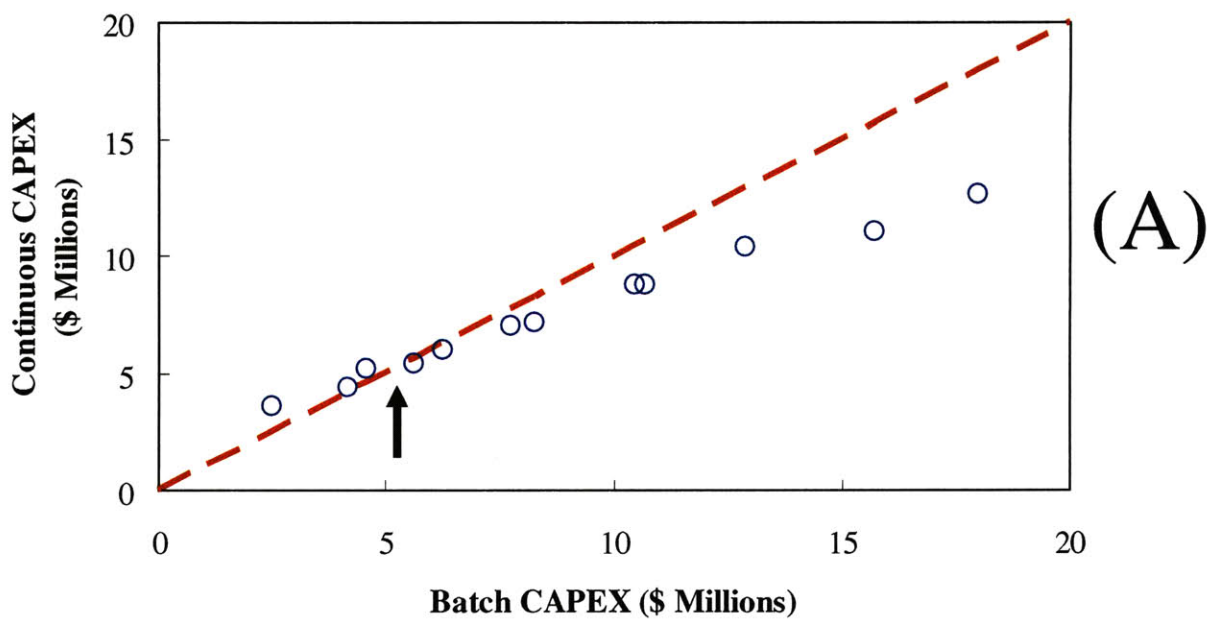


Figure 133: Capital (CAPEX) and operating (OPEX) comparison for batch and continuous wet granulation and direct compression processes.

Batch and continuous processes also can be compared on a purely cost basis. This is done by defining batch costs as the X coordinate and continuous costs as the Y coordinate for process systems of similar type and throughput, and then plotting them (Figure 133 A, B). This allows one to define a cost space where continuous process systems have more favorable costs. To assist in the visualization of this data, there is a dashed redline representing when the batch and continuous costs are equal. This method indicates that for CAPEX (black arrow in Figure 133 A) greater than \$5 million, the continuous process system will provide the lower cost and that OPEX (Figure 133 B) is always lower for the continuous system. Further populating these charts with more products and process systems will allow for a simple costing heuristic for choosing between batch and continuous process systems.

10.3 Summary of results

1. Continuous process equipment can have significantly smaller volumes than equivalent batch process equipment. This can decrease the size of the manufacturing facility required by a continuous system and decreases the CAPEX for process equipment and facilities.
2. Continuous process systems enjoy a CAPEX advantage at process throughputs greater than 200 million tablets/yr in the model systems. Conversely, batch process systems have lower CAPEX at process throughputs less than 200 million tablets/yr in the modeled systems.
3. Continuous process systems have lower OPEX for all of the process throughputs simulated in the model systems.
4. The present value (PV) of the costs for the model system are lower for the continuous process for all the scales and systems simulated.

5. Continuous manufacturing allows for the implementation of more robust process systems for the same or lower costs.

11 FUTURE WORK

11.1 Parallel discrete element method simulation

The current simulation efforts have been limited to discrete element method (DEM) model sizes less than and equal to one quarter of the lab scale blender using the true particle size distributions. However, these quarter scale simulations are intractably slow using a single processor with estimated run times on the order of a year to see any dynamic behavior. An obvious solution shown by Cleary and Sawley [44] is the use of parallel computation. Cleary and Sawley demonstrated that computation time decreases nearly linearly with the number of processors. Given this, it is not impossible to imagine a two order of magnitude reduction in computation time with a moderate (100 processor) sized computer cluster. The parallel computing algorithms for the discrete element method software are currently under development at CSIRO and are planned to be available within the next two years.

When the software has been developed, a further analysis of blender size to half the size of the lab scale blender should be performed, as well as continued simulation of the quarter and eighth scale for longer simulation times. In addition, performing a series of simulations to mimic Lin's [85] operational parameter sensitivity at the half scale would also be worthwhile for comparison. Ultimately, this could bring DEM simulation into the domain of a practical analysis tool for pharmaceutical process system development and improvement.

11.2 Non-spherical particles

While many aspects of particle properties were explored (size, polydispersity, cohesion) another area of interest is shape. While some pharmaceutical materials, like spray dried lactose,

are nearly spherical, other common pharmaceutical materials, like microcrystalline cellulose (MCC) and many active pharmaceutical ingredients, have a more elongated needle like shape. Cleary and Sawley [44] have shown that shape properties (aspect ratio and blockiness) can have a significant effect on behaviors of 2D hopper flows. It would be worthwhile to test these shape properties for their effects on flow behavior and homogeneity in a 3D blender. A first step could be to examine the homogeneity of microcrystalline cellulose blends with both spherical particles and particles that better represent its true shape. This can be done by modifying the particle's aspect ratio and blockiness. Continued efforts could examine an intermediate aspect ratio and blockiness between the spherical and true particle shape to better understand the sensitivity of flow behavior and mixing performance to these parameters.

11.3 New active pharmaceutical ingredients

Most of the current DEM simulation work has examined the behavior of blending while varying the properties of the excipients, but continued work could shift the focus to varying the properties of active pharmaceutical ingredients (API). The sole active pharmaceutical ingredient used in the blending simulations was caffeine, but there is a wide variety of other active ingredients that have very different size, shape and cohesive properties. Extensive experimental work has been performed at the Massachusetts Institute of Technology and elsewhere with acetaminophen. Acetaminophen is thus the most logical API to examine next. In addition to examining the blending performance of acetaminophen, it would be worthwhile to examine the performance of either wet or dry granulated acetaminophen. The preliminary work on particle size has shown improved blending performance as one increases the particle size, but it would be interesting to further quantify this for a granulated active ingredient. This would help to provide

a better understanding of the true value of granulation steps as one can economically weigh the cost of the granulation processes (OPEX and CAPEX) versus the benefits of improved blending performance/reliability.

11.4 Paddle blender design optimization

The paddle blender proved to be a sound design improvement over the ribbon blender even on its first iteration, but further optimization would almost certainly improve the blender's performance. There are three main areas that would seem to yield the most gains from a further optimization of the paddle blender design: the geometry of the blender shell, the shape and position of the inflow and outflow ports and the design of the paddles.

11.4.1 Blender geometry

The geometry of the current paddle blender was carried over from the original ribbon paddle blender, but modifying the aspect ratio of the blender might yield improved performance. The ribbon blender shell was 6" long and had a diameter of 2" giving it an aspect ratio of 3:1. Lin [85] has shown for the lactose and caffeine system that a ribbon blender at half the scale with the same aspect ratio improves the VRR. In addition, the DEM simulations indicate that shorter paddle blenders might be able to achieve similar homogeneity to longer blenders.

While shortening the blender will certainly reduce its cost, it will need to be tested whether or not this will adversely affect blend homogeneity. In addition, shrinking the diameter of the blender certainly gives the potential for faster mixing, but this will decrease the blenders throughput. Any homogeneity advantage gained by reducing blender diameter needs to be

balanced against lack of future flexibility in process design. In both cases, a model integrating costs and quantitative mixing performance is required to truly find the optimal blender geometry.

11.4.2 Inflow and outflow ports

The discrete element method simulations have indicated that inflow and outflow ports are both very important to the flow rate and homogeneity. Further research could be done to optimize their positions and shapes to improve blend homogeneity. It is unclear whether the inflow port's centerline position is optimal. Either an experimental or computational study would be worthwhile to find the inflow port's optimal position along the X axis. An examination of two other points, one on the positive side of the X origin and one on the negative side, should be sufficient to indicate whether any substantial advantage can be gained by moving the inflow port. The combination of the position of the exit ports on the end plate and a rotating mixing element produce a very pulsatile flow. These flow characteristics might be problematic from an implementation stand point for continuous pharmaceutical manufacturing. It would be worthwhile to explore moving the exit port to the bottom of the blender, so gravity could assist the outflow and hopefully create a more consistent exit flow rate.

11.4.3 Paddle design and orientation

The other main area for optimization is the pitch and number of paddles. Portillo et al. [24] has experimentally examined the basic effect of paddle angle on homogeneity. Of the paddle angles Portillo et al. tested, they found the best blend homogeneity with the 60° paddle offset. The paddles in the author's design are 87.5° offset from perpendicular to the central shaft. However, Portillo et al.'s blender design was incapable of operating at the 90° offset in a

horizontal position. This leaves the author to believe that if one were limited to a single blade angle, it would exist somewhere between the 60° and 90° offset. Continued discrete element method simulations with controlled fill weights and variable inflow could be planned to further refine the optimal blade angle in this range.

While there is certainly an advantage to be gained by uniformly optimizing the paddle angle, there is possibly greater advantage to optimizing the paddle angle for each individual set of paddles. The author's blender has 8 pairs of paddles and thus even the simplest exploration of pitch sensitivity (forward, neutral and reverse) yields a somewhat daunting 6561 combinations. Even if one applied a practical reduction in experimental combinations that the first and last pair of paddles had to be pitched forward, one would still be left with 729 combinations. This is a large number of combinations for either an experimental or a computational analysis. This design optimization could be most effectively handled using a more iterative and qualitative approach using the velocity and granular temperature data to guide design improvements.

Finally, there is the question of the number of paddles. It would be worthwhile to explore a sensitivity for the number of paddle pairs in the axial position using 4 pairs of paddles (50% less) or 12 pairs of paddles (50% more), but maintaining the same paddle area. This would show the influence of material spilling off the paddle on mixing rate as well as give indication on the importance of paddle spacing in the axial direction. Next, it would be interesting to explore a blender with three paddles per axial position (compared to the current two) as the previous data shows that increasing the number of paddle passes per revolution improves mixing performance.

12 CONCLUSION

Continuous manufacturing offers a number of operational and financial benefits to pharmaceutical companies. This research has examined the critical blending step for continuous pharmaceutical manufacturing and the characteristics of continuous downstream pharmaceutical manufacturing systems. Discrete element method (DEM) simulations were used to develop novel insights into the mechanism of mixing for continuous blending of cohesive pharmaceutical powders and to examine the effects of particle properties, blender design and operating conditions on blend homogeneity. The scope of the analysis was then expanded to examine an entire downstream pharmaceutical manufacturing system using process simulations to quantify the potential advantages of continuous manufacturing.

DEM simulations were used to study the mechanisms of mixing in continuous blenders with pharmaceutical powders. The continuous double helical ribbon blender produces complex particle flows that blend using both diffusive mixing in a tumbling avalanche and convective mixing driven by its oppositely pitched helical ribbons. The particles are not evenly distributed in the blender with more particles towards the outflow region and on the positive X side of the blender (in the direction of rotation). Throughout the blender, though, there are distinct regions of forward and reverse flow driven by the outer and inner helical ribbons respectively that induce the convective axial mixing. However, the diffusive mixing from the avalanching particles appears to be the dominant mechanism of mixing in both the axial and radial direction.

If diffusive mixing in avalanching particles is the dominant mixing mechanism, then the efficient lifting of particles is essential for rapid mixing. The more efficient the mixing elements (ribbons, paddles) are at lifting particles, the greater number of particles will move to positions

where they can avalanche. These avalanching particles can then diffusively mix when they fall. The paddle blender has demonstrated superior homogeneity on a per revolution basis when compared to the double helical ribbon blender in the X, Y and R dimensions and is comparable in homogeneity in the Z dimension. The improved blend homogeneity in the paddle blender appears to be a product of more efficient lifting of particles due to the paddles' shape, greater surface area and more frequent passes through the particle bed. The paddle blender also creates new mixing zones between the paddles where particles spill off. Improved homogeneity due to more efficient particle transport was also observed in the set of simulations with different sized double helical ribbon blenders. Here it was observed that blender size was negatively correlated to homogeneity as the smaller blenders were more efficient at transporting a greater percentage of the total particles to a position where they can avalanche.

The uneven axial distribution of particles in the double helical ribbon blender creates regions of greater and lesser diffusive mixing. As fill fraction increases above a certain threshold, diffusive mixing and homogeneity decreases. This was observed in both entire blenders with higher fill fractions and in the regions of higher fill fraction near the outflow of blenders. It is believed that higher fill fractions limit the duration of particle avalanches and decrease mixing.

This understanding of mixing mechanisms will be very useful when guiding the design of future continuous pharmaceutical powder blenders. The mixing elements need to be optimized to increase the amount of particles transported to a position where they can avalanche/flow and diffusively mix. The mixing elements need to be appropriately pitched and the outflow ports need to be optimally sized and positioned to maintain an even fill fraction throughout the blender and maximize the utility of the blender's volume. Further DEM simulations can offer the insight

necessary to develop and test improved designs and create a superior continuous pharmaceutical powder blending device.

A range of particle properties and operating conditions were examined for their effects on flow behavior and blend homogeneity. Three particle properties were examined: particle size, polydispersity and cohesive force. Particle size was observed to be positively correlated to both flow rates and blend homogeneity. Polydispersity had no effect on flow rate and was negatively correlated to homogeneity. Cohesive force was negatively correlated to flow rate and had little to no effect on homogeneity. Two operating parameters were also studied: rotation rate and fill fraction. Rotation rate was positively correlated to both flow rate and homogeneity. Fill fraction had the interesting result of being positively correlated to the absolute flow rate, but negatively correlated to the fill mass normalized flow rate. In addition, fill fraction has a clear negative correlation to homogeneity above fill fractions of 0.55, but is inconsistent for fill fractions lower than this.

This research on particle properties and operating conditions will help to guide the operation of continuous blending pharmaceutical blenders and the design of continuous pharmaceutical manufacturing systems. A striking feature of this analysis is the very weak correlation between flow rates and blend homogeneity in the double helical ribbon blender. This presents a significant problem for designing blending processes in the pharmaceutical industry as powders are frequently characterized based on their flow properties (angle of repose). The blending scaling solutions reported in the literature based on particle properties and operating conditions (scale ratios [30], Froude number [29], avalanche velocity [14]) were also shown to have limited application for correlating homogeneity across different scales, materials and operating conditions for the double helical ribbon blender. However, calibrated dimensional

analysis models for homogeneity offer a reasonable method for estimating blend homogeneity and optimizing blending processes. From these models and the experimental results, one can see that increasing particle size appears to offer tangible benefits to blend homogeneity. This makes a case for the inclusion of a granulation step in a pharmaceutical manufacturing system as the required residence time required to achieve a homogeneous blend will be reduced. However, the added cost and complexity of a granulation step will have to be weighed against the respective decrease in volume of the blending device. Operationally, increasing rotation rate shows a moderate improvement in blend homogeneity on a per revolution basis, but offers a significant homogeneity advantage on a time basis. This indicates that the optimal operating condition from a cost perspective will be the one with the highest rotation rate that does not degrade the particles or fundamentally change the flow regime of the blender. Finally, the blender should be operated at a fill fraction below the threshold where blend homogeneity decreases.

With the increased understanding of continuous pharmaceutical blender design and operation and the existing continuous pharmaceutical unit operations (roller compaction, milling, compression), a continuous process is a legitimate option for a downstream pharmaceutical manufacturing system. Process simulations comparing model batch and continuous downstream pharmaceutical manufacturing systems have quantified some of the potential size, cost and performance benefits of continuous processes. The models showed significant reductions in process equipment sizes for continuous manufacturing particularly in the blending step. The model's continuous blending equipment was more than an order of magnitude smaller in volume than the model's batch blending equipment. This reduction in equipment size translates to capital cost (CAPEX) savings for the both the process equipment and the facilities. The steady state operation of continuous processing also reduces the labor requirements for continuous processes

and gives the continuous processes an operating cost (OPEX) advantage over batch processes. Finally, these cost advantages for continuous processing allow for the implementation of more robust continuous processes for the same or lower costs. By decreasing the costs of more robust processes, continuous manufacturing could shorten process development times and increase manufacturing reliability.

This research has contributed to the understanding of continuous pharmaceutical powder blending and quantified some of the benefits of continuous downstream pharmaceutical manufacturing. This research has demonstrated that:

- Continuous manufacturing offers a number of benefits (safety, operational, financial) to pharmaceutical companies.
- DEM simulation can be used to study novel aspects of the flow and mixing in pharmaceutical powder blenders. The DEM simulations found that diffusive mixing during the avalanching of particles appears to be the dominant mechanism of mixing for the double helical ribbon blender in both the axial and radial direction. This diffusive mixing mechanism drives some of the improved blend homogeneity in the paddle blender.
- Current blender scaling techniques (scale ratio, Froude number, avalanche velocity) have limited applicability to continuous blending of pharmaceutical powders. However, calibrated dimensional analysis models offer a reasonable technique for estimating flow rate and blend homogeneity, as well as optimizing blending processes.

Through the findings of this research, continuous pharmaceutical manufacturing has been brought closer to reality, but there is considerable work left to be done. This work is being

continued by the Novartis-MIT Center for Continuous Manufacturing whose work is providing the foundation for future industrial scale pharmaceutical continuous manufacturing systems.

REFERENCES

- 1 Fortune. Global 500 2009: Industry: Pharmaceuticals.
<http://money.cnn.com/magazines/fortune/global500/2009/industries/21/index.html>
- 2 J. Kossik. Think Small: Pharmaceutical facilities could boost capacity and slash costs by trading in certain batch operations for continuous versions. *PharmaManufacturing.com*
<http://www.pharmamanufacturing.com/articles/2002/6.html> **2002**.
- 3 Food and Drug Administration. Guidance for Industry: PAT — A Framework for Innovative Pharmaceutical Development, Manufacturing, and Quality Assurance.
<http://www.fda.gov/downloads/Drugs/GuidanceComplianceRegulatoryInformation/Guidances/UCM070305.pdf> **2004**.
- 4 L. Pernenkil. Continuous Blending of Dry Pharmaceutical Powders. *PhD dissertation, Massachusetts Institute of Technology, Department of Chemical Engineering*. May **2008**.
- 5 CAMP workshop on Continuous Manufacturing. April **2004**.
- 6 M.J. Mollan and M. Lodaya. Continuous Processing in Pharmaceutical Manufacturing.
PharmaManufacturing.com <http://www.pharmamanufacturing.com/whitepapers/2004/11.html>
2004.
- 7 J. A. DiMasi, R.W. Hansen and H.G. Grabowski. The price of innovation: new estimates of drug development costs. *Journal of Health Economics* **22** (2003) 151-185.
- 8 Pfizer Inc. Pfizer 10-K (period: December 31, 2008).
- 9 P. Basu, G. Joglekar, S. Rai, P. Suresh and J. Vernon. Analysis of Manufacturing Costs in Pharmaceutical Companies. *Journal of Pharmaceutical Innovation* **3** (2008) 30-40.

- 10 R.G. Sherritt, J. Chaouki, A.K. Mehrotra and L.A. Behie. Axial dispersion in the three-dimensional mixing of particles in a rotating drum reactor. *Chemical Engineering Science* **58** (2003) 401-415.
- 11 O.S. Sudah, A.W. Chester, J.A. Kowalski, J.W. Beeckman and F.J. Muzzio. Quantitative characterization of mixing processes in rotary calciners. *Powder Technology* **126** (2002) 166-173.
- 12 A. Ingram, J.P.K. Seville, D.J. Parker, X. Fan and R.G. Forster. Axial and radial dispersion in rolling mode rotating drums. *Powder Technology* **158** (2005) 76-91.
- 13 J.M. Ottino and D.V. Khakhar. Mixing and Segregation of Granular Materials. *Annual Review of Fluid Mechanics* **32** (2000) 55-91.
- 14 A.W. Alexander and F.J. Muzzio. "Batch Size Increase in Dry Blending", in: M. Levin (Ed.), *Pharmaceutical Process Scale-Up, Second Edition*. CRC Press, Boca Raton, **2006**.
- 15 M. Zlokarnik. "Dimensional Analysis and Scale-Up in Theory and Industrial Application", in: M. Levin (Ed.), *Pharmaceutical Process Scale-Up, Second Edition*. CRC Press, Boca Raton, **2006**.
- 16 V. Kehlenbeck and K. Sommer. Possibilities to improve the short-term dosing constancy of volumetric feeders. *Powder Technology* **138** (2003) 51-56.
- 17 K. Marikh, H. Berthiaux, V. Mizonov and E. Barantseva. Experimental study of the stirring conditions taking place in a pilot plant continuous mixer of particulate solids. *Powder Technology* **157** (2005) 138-143.
- 18 W.A. Beverloo, H.A. Leniger and J. Van de Velde. The flow of granular material through orifices. *Chemical Engineering Science* **15** (1961) 260-296.

- 19 T. M. Verghese and R. M. Nedderman. The discharge of fine sands from conical hoppers. *Chemical Engineering Science* **50** (1995) 3143-3153.
- 20 I. Zuriguel, L.A. Pagnaloni, A. Garcimartin and D. Maza. Jamming during the discharge of grains from a silo described as a percolating transition. *Physical Review E* **68** (2003) 030301 1-4.
- 21 G.D.R. MiDi. On dense granular flows. *European Physical Journal E* **14** (2004) 341-365.
- 22 A. N. Faqih, A.W. Alexander, F.J. Muzzio and M.S. Tomassone. A method of predicting hopper flow characteristics of pharmaceutical powders. *Chemical Engineering Science* **62** (2007) 1536-1542.
- 23 C. Mankoc, A. Janda, R. Arévalo, J.M. Pastor, I. Zuriguel, A. Garcimartín, D. Maza. The flow rate of granular materials through an orifice. *Granular Matter* **9** (2007) 407-414.
- 24 P.M. Portillo, M.G. Ierapetritou and F.J. Muzzio. Characterization of continuous convective powder mixing processes. *Powder Technology* **182** (2008) 368-378.
- 25 L. Pernenkil and C.L. Cooney. A review on the continuous blending of powders. *Chemical Engineering Science* **61** (2006) 720-742.
- 26 D.M. Kremer and B.C. Hancock. Process simulation in the pharmaceutical industry: A review of some basic physical models. *Journal of Pharmaceutical Sciences* **95** (2006) 517-529.
- 27 C.S. Campbell. Rapid Granular Flows. *Annual Review of Fluid Mechanics* **22** (1990) 57-92.
- 28 J.M.N.T. Gray. "Rapid Granular Avalanches", in: K. Hutter and N. Kirchner (Ed.), *Dynamic Response of Granular and Porous Materials under Large and Catastrophic Deformations*. Springer, Berlin, **2003**.

- 29 Y.L. Ding, R. Forster, J.P.K. Seville and D. J. Parker. Granular motion in rotating drums: bed turnover time and slumping–rolling transition. *Powder Technology* **124** (2002) 18-27.
- 30 Y.L. Ding, R.N. Forster, J.P.K. Seville and D.J. Parker. Scaling relationships in rotating drums. *Chemical Engineering Science* **56** (2001) 3737-3750.
- 31 T.S. Majmudar TS and R.P. Behringer. Contact force measurements and stress-induced anisotropy in granular materials. *Nature* **435** (2005) 1079-1082.
- 32 D. Ramkrishna and A.W. Mahoney. Population balance modeling. Promise for the future. *Chemical Engineering Science* **57** (2002) 595-606.
- 33 H. Berthiaux, K. Marikh, V. Mizonov, D. Ponomarev and E. Barantzeva. Modeling continuous powder mixing by means of the theory of Markov chains. *Particulate Science and Technology* **22** (2004) 379-389.
- 34 P.M. Portillo, F.J. Muzzio and M.G. Ierapetritou. Characterizing powder mixing processes utilizing compartment models. *International Journal of Pharmaceutics* **320** (2006) 14-22.
- 35 D. Brone, A. Alexander and F.J. Muzzio. Quantitative characterization of mixing of dry powders in V-blenders. *AIChE Journal* **44** (1998) 271-278.
- 36 P.M. Portillo, F.J. Muzzio and M.G. Ierapetritou. Using Compartment Modeling to Investigate Mixing Behavior of a Continuous Mixer. *Journal of Pharmaceutical Innovation* **3** (2008) 161-174.
- 37 G.C. Barker. “Computer Simulations of Granular Materials”, in: A. Mehta (Ed.), *Granular Matter: An Inter-Disciplinary Approach*. Springer, Berlin, **1994**.
- 38 P.A. Cundall and O.D.L. Strack. Discrete-numerical models for granular assemblies. *Geotechnique* **29** (1979) 47-65.

- 39 P.W. Cleary. Discrete Element Modelling of Industrial Granular Flow Applications. *TASK. Quarterly - Scientific Bulletin*. **2** (1998) 385-416.
- 40 W.R. Ketterhagen, M.T.A. Ende and B.C. Hancock. Process Modeling in the Pharmaceutical Industry using the Discrete Element Method. *Journal of Pharmaceutical Sciences* **98** (2009) 442-470.
- 41 H.P. Zhu and A.B. Yu. A theoretical analysis of the force models in discrete element method. *Powder Technology* **161** (2006) 122-129.
- 42 P.W. Cleary and M.L. Sawley. Three dimensional modelling of industrial granular flows. *Proceedings of the 2nd International Conference on CFD in the Minerals and Processing Industries*. Melbourne, December **1999**.
- 43 L.E. Silbert, J.W. Landry and G.S. Grest. Granular flow down a rough inclined plane: Transition between thin and thick piles. *Physics of Fluids* **15** (2003) 1-10.
- 44 P.W. Cleary and M. Sawley. DEM modelling of industrial granular flows: 3D case studies and the effect of particle shape on hopper discharge. *Applied Mathematical Modelling*. **26** (2002) 89-111.
- 45 F. Bertrand, L.A. Leclaire and G. Levecque. DEM-based models for the mixing of granular materials. *Chemical Engineering Science* **60** (2005) 2517-2531.
- 46 P.W. Cleary. Large scale industrial DEM modeling. *Engineering Computations*. **21** (2004) 169-204.
- 47 S.T. Nase, W.L. Vargas, A.A. Abatan and J. J. McCarthy. Discrete characterization tools for cohesive granular material. *Powder Technology* **116** (2001) 214-223.

- 48 H.P. Zhu, Z.Y. Zhou, R.Y. Yang and A.B. Yu. Discrete particle simulation of particulate systems: Theoretical developments. *Chemical Engineering Science* **62** (2007) 3378-3396.
- 49 M.W. Weber, D.K. Hoffman and C.M. Hrenya. Discrete-particle simulations of cohesive granular flow using a square-well potential. *Granular Matter* **6** (2004) 239-254.
- 50 S.H. Ngai. Multiscale analysis and simulation of powder blending in pharmaceutical manufacturing. *PhD dissertation, Massachusetts Institute of Technology, Department of Chemical Engineering*. August **2005**.
- 51 A.W. Alexander, B. Chaudhuri, A. Faqih, F.J. Muzzio, C. Davies and M.S. Tomassone. Avalanching flow of cohesive powders. *Powder Technology* **164** (2006) 13-21.
- 52 R.D. Domike. Pharmaceutical powders in experiment and simulation: Towards a fundamental understanding. *PhD dissertation, Massachusetts Institute of Technology, Department of Chemical Engineering*. September **2003**.
- 53 P.W. Cleary. DEM simulation of industrial particle flows: case studies of dragline excavators, mixing in tumblers and centrifugal mills. *Powder Technology* **109** (2000) 83-104.
- 54 R.L. Stewart, J. Bridgwater, Y. C. Zhou and A. B. Yu. Simulated and measured flow of granules in a bladed mixer - a detailed comparison. *Chemical Engineering Science* **56** (2001) 5457-5471.
- 55 H.P. Kuo, P.C. Knight, D.J. Parker, Y. Tsuji, M. J. Adams and J.P.K. Seville. The influence of DEM simulation parameters on the particle behaviour in a V-mixer. *Chemical Engineering Science* **57** (2002) 3621-3638.

- 56 P.E. Arratia, Nhat-hang Duong, F.J. Muzzio, P. Godbole and S. Reynolds. A study of the mixing and segregation mechanisms in the Bohle Tote blender via DEM simulations. *Powder Technology* **164** (2006) 50-57.
- 57 M. Kwapinska, G. Saage and E. Tsotsas. Mixing of particles in rotary drums: A comparison of discrete element simulations with experimental results and penetration models for thermal processes. *Powder Technology* **161** (2006) 69-78.
- 58 G.J. Finnie, N.P. Kruyt, M. Ye, C. Zeilstra and J.A.M. Kuipers. Longitudinal and transverse mixing in rotary kilns: A discrete element method approach. *Chemical Engineering Science* **60** (2005) 4083-4091.
- 59 K. Yamane. Discrete-element method application to mixing and segregation model in industrial blending system. *Journal of Materials Research* **19** (2004) 623-627.
- 60 M. Lemieux, F. Bertrand, J. Chaouki and P. Gosselin. Comparative study of the mixing of free-flowing particles in a V-blender and a bin-blender. *Chemical Engineering Science* **62** (2007) 1783-1802.
- 61 M. Lemieux, G. Léonard, J. Doucet, L.-A. Leclaire, F. Viens, J. Chaouki and F. Bertrand. Large-scale numerical investigation of solids mixing in a V-blender using the discrete element method. *Powder Technology* **181** (2008) 205-216.
- 62 C.S. Campbell. Granular material flows – An overview. *Powder Technology* **162** (2006) 208-229.
- 63 P.W. Cleary, G. Metcalfe and K. Liffman. How well do discrete element granular flow models capture the essentials of mixing processes?. *Applied Mathematical Modelling*. **22** (1998) 995-1008.

- 64 G. Metcalfe, T. Shinbrot, J.J. McCarthy and J.M. Ottino. Avalanche Mixing of Granular Solids. *Nature* **374** (1995) 39-41.
- 65 P.W. Cleary and M.D. Sinnott. Assessing mixing characteristics of particle-mixing and granulation devices. *Particuology* **6** (2008) 419-444.
- 66 D. Hirshfeld and D.C. Rapaport. Granular flow from a silo: Discrete-particle simulations in three dimensions. *European Physical Journal E* **4** (2001) 193-199.
- 67 P.M. Portillo, F.J. Muzzio and M.G. Ierapetritou. Hybrid DEM-compartment modeling approach for granular mixing. *AIChE Journal* **53** (2007) 119-128.
- 68 C.H. Rhycoft, M.Z. Bazant, G.S. Grest and J.W. Landry. Dynamics of random packings in granular flow. *Physical Review E* **73** (2006) 051306 1-7.
- 69 K. Kamrin and M.Z. Bazant. Stochastic flow rule for granular materials. *Physical Review E* **75** (2007) 041301 1-28.
- 70 C.H. Rycroft, K. Kamrin and M.Z. Bazant. Assessing continuum postulates in simulations of granular flow. *Journal of the Mechanics and Physics of Solids* **57** (2009) 828-839.
- 71 Intelligen Inc. Company Information. <http://www.intelligen.com/compinfo.shtml>
- 72 D. Petrides, A. Koulouris and P.T. Lagonikos. The Role of Process Simulation in Pharmaceutical Process Development and Product Commercialization. *Pharmaceutical Engineering* **22** (2002) 1-8.
- 73 R.G. Harrison, P.W. Todd, S.R. Rudge and D. Petrides. *Bioseparations Science and Engineering*. Oxford University Press, Oxford, **2003**.
- 74 AspenTech. aspenONE for Process Manufacturers. <http://www.aspentech.com/core/aspen-one.cfm>

- 75 J.C. Toebermann, J. Rosenkranz, J. Werther and G. Gruhn. Block-oriented process simulation of solids processes. *Computers & Chemical Engineering* **23** (2000) 1773-1782.
- 76 J.N. Michaels. Toward rational design of powder processes. *Powder Technology* **138** (2003) 1-6.
- 77 K.M. Ng. Design and development of solids processes - a process systems engineering perspective. *Powder Technology* **126** (2002) 205-210.
- 78 V. Kulikov, H. Briesen, R. Grosch, A.D. Yang, L. von Wedel and W. Marquardt. Modular dynamic simulation for integrated particulate processes by means of tool integration. *Chemical Engineering Science* **60** (2005) 2069-2083.
- 79 A. Gerstlauer, C. Gahn, H. Zhou, M. Rauls and M. Schreiber. Application of population balances in the chemical industry — current status and future needs. *Chemical Engineering Science* **61** (2006) 205-217.
- 80 Process System Enterprise Ltd. gProms. <http://www.psenterprise.com/gproms/>
- 81 Numerica Technology. Jacobian. <http://www.numericatech.com/jacobian.htm>
- 82 C. Wibowo and K.M. Ng. Synthesis of bulk solids processing systems. *AIChE Journal* **45** (1999) 1629-1648.
- 83 K.Y. Fung and K.M. Ng. Product-centered processing: Pharmaceutical tablets and capsules. *AIChE Journal* **49** (2003) 1193-1215.
- 84 Hosokawa Micron B.V. Modulomix – Working Principle.
<http://www.hosokawamicron.nl/template.asp?paid=223>

- 85 B.C.P. Lin. Exploration of Parameters for Continuous Blending of Pharmaceutical Powders.
PhD dissertation in preparation, Massachusetts Institute of Technology, Department of Chemical Engineering. Expected **2010**.
- 86 B.F.C. Laurent and J. Bridgewater. Performance of single and six-bladed powder mixers.
Chemical Engineering Science **57** (2002) 1695-1709.
- 87 B.F.C. Laurent. Scaling factors in granular flow - analysis of experimental and simulation results. *Chemical Engineering Science* **61** (2006) 4138-4146.
- 88 K. Johnson, K. Kendall and A. Roberts. Surface energy and the contact of elastic solids.
Proceedings of the Royal Society of London. Series A, Mathematical and Physical Sciences **324** (1971) 301-313.
- 89 R.B. Bird, W.E. Stewart and E.N. Lightfoot. *Transport Phenomenon*. John Wiley & Sons, New York, **2001**.